SIZE EFFECT AND ANISOTROPY

IN TRANSVERSELY ISOTROPIC ROCKS

LI KAIHUI

PhD

The Hong Kong Polytechnic University

2019

The Hong Kong Polytechnic University
Department of Civil and Environmental Engineering

Size Effect and Anisotropy in Transversely Isotropic Rocks

LI Kaihui

A thesis submitted in partial fulfillment of the requirements for the degree of Doctor of Philosophy

July 2019

CERTIFICATE OF ORIGINALITY

I hereby declare that this thesis is my own work and that, to the best of my knowledge and belief, it reproduces no material previously published or written, nor material that has been accepted for the award of any other degree or diploma, except where due acknowledgement has been made in the text.

_____ (Signed)

LI Kaihui (Name of student)

ABSTRACT

Transversely isotropic rocks, making up around 75% of the earth's surface, are widely encountered in civil, mining, petroleum, geothermal and radioactive-waste disposal engineering. In Hong Kong, the rock cavern development plan has commenced in recent years to increase the land supply and improve the environment. Some strategic cavern areas are also inevitably located in anisotropic formations. Anisotropy, as one of the most distinct features possessed by these kind of rocks, generally originates from the mineral foliation in metamorphic rocks, the stratification in sedimentary rocks, and the discontinuities in rock masses due to stress and geological history. Size effect is another important characteristic owned by brittle and semi-brittle rocks. Numerous investigations into size effect in isotropic rocks have been conducted, and many size-effect models have been proposed for isotropic rocks. However, considering the influence of anisotropy, size effect in transversely isotropic rocks is very different from that in isotropic rocks. To date, there are few studies in relation to size effect in transversely isotropic rocks.

In this study, a transversely isotropic slate rock from a quarry was obtained as the test material. The first principal objective is to investigate the anisotropy and size effect in slate under indirect tensile conditions. A series of Brazilian tests were performed on slate samples with different diameters at different anisotropic angles. Size effects on elastic properties, indirect tensile strength and fracture pattern were analysed. Size effect on indirect tensile strength was found to be correlated with the anisotropy. A unified size-effect relation was proposed and validated against the experimental data to capture the ascending and descending size-effect trends and the relationship among indirect tensile strength, sample size and anisotropic angle. Furthermore, the influence of three-dimensional anisotropy on the tensile behaviour of transversely isotropic rock was

investigated using a particle-based discrete element approach. Considering various foliation orientations relative to loading direction and sample axis, the tensile strength, fracture mechanism and micro-cracking were systematically studied.

The second principal objective is to investigate the anisotropy and size effect in slate under compressive conditions. A series of uniaxial and triaxial compression tests were conducted on slate samples. In response to the test results, a size-effect model developed from coal was extended to the transversely isotropic rock. Both uniaxial and triaxial compressive strengths were found to follow a cosine relation. It was also found that the size-effect behaviours in uniaxial and triaxial compressive strengths were similar. Two size-dependent failure criteria were proposed by incorporating the size-effect model for uniaxial compressive strength into the modified Hoek-Brown and Saeidi failure criteria, respectively, and were verified against the experimental data. For the first time, the relationship among compressive strength, specimen size, anisotropic angle and confining pressure was comprehensively captured for transversely isotropic rock. Lastly, without evident size effect, the anisotropic triaxial residual strength was captured well by an improved cohesion loss model. Two equations delineating the range for ratio of residual to peak strength were proposed for transversely isotropic rocks.

Overall, these findings in slate may be applicable to other transversely isotropic rocks.

PUBLICATIONS

PUBLICATIONS ARISING FROM THE THESIS

1. **Li K.H.**, Cheng Y.M.*, Fan X. (2018) Roles of model size and particle size distribution on macro-mechanical properties of Lac du Bonnet granite using flat-joint model. Computers and Geotechnics 103:43-60.
2. Fan X, **Li K.H.***, Lai H., Xie Y., Cao R., Zheng J. (2018) Internal stress distribution and cracking around flaws and openings of rock block under uniaxial compression: A particle mechanics approach. Computers and Geotechnics 102:28-38.
3. **Li K.H.**, Cheng Y.M.*, Yin Z., Han D., Meng J. Size effects in a transversely isotropic rock under Brazilian tests: laboratory testing. Rock Mechanics and Rock Engineering (Under review).
4. **Li K.H.***, Yin Z., Cheng Y.M., Cao P., Fan X., Meng J. Size-effect and anisotropy in a transversely isotropic rock under compressive conditions. International Journal of Rock Mechanics and Mining Sciences (Under review).
5. **Li K.H.**, Yin Z.*, Cheng Y.M, Cao P., Meng J. Three-dimensional discrete element simulation of indirect tensile behaviour of a transversely isotropic rock. International Journal for Numerical and Analytical Methods in Geomechanics (Under review).

OTHER PUBLICATIONS

1. Meng J., Huang J., Lin H., Laue J., **Li K.H.** (2019) A static discrete element method with discontinuous deformation analysis. International Journal for Numerical Methods in Engineering 2019;1–18.
2. Meng J., Cao P., Huang J., Lin H., **Li K.H.**, Cao R. (2019) Three-dimensional spherical discontinuous deformation analysis using second-order cone programming. Computers and Geotechnics 112:319-328.
3. Lin Q., Cao P., **Li K.H.**, Cao R., Zhou K., Deng H. (2018) Experimental study on acoustic emission characteristics of jointed rock mass by double disc cutter. Journal of Central South University 25:357-367.
4. Fan X., **Li K.H.**, Lai H., Zhao Q., Sun Z. (2018) Experimental and Numerical Study of the Failure Behaviour of Intermittent Rock Joints Subjected to Direct Shear Load.

Advances in Civil Engineering 2018.

5. Zhang K., Cao P., Ma G., Wang W., Fan W., **Li K.H.** (2016) Strength, fragmentation and fractal properties of mixed flaws. Acta Geotechnica 11:901-912.
6. Zhang K., Cao P., Ma G., Ren F., **Li K.H.** (2016) Stability analysis of rock slope controlled by major geological discontinuities based on the extended kinematical element method. Rock Mechanics and Rock Engineering 49:2967-2975.
7. Zhang K., Cao P., Ma G., Fan W., Meng J., **Li K.H.** (2016) A new methodology for open pit slope design in Karst-Prone ground conditions based on integrated stochastic-limit equilibrium analysis. Rock Mechanics and Rock Engineering 49:2737-2752.
8. **Li K.H.**, Cao P., Zhang K., Zhong Y. (2015) Macro and meso characteristics evolution on shear behaviour of rock joints. Journal of Central South University 22:3087-3096.

ACKNOWLEDGEMENTS

First of all, I would like to express my deepest gratitude to my chief supervisor, Prof. Yung-Ming Cheng, for providing me the opportunity to pursue a Ph.D. degree in The Hong Kong Polytechnic University. His patient guidance, constant encouragement and support are indispensable for the completion of this thesis. My sincere thanks also go to my second chief supervisor, Dr. Zhen-Yu Yin. He has invested a great amount of time reading my thesis draft and offered many good thoughts and suggestions.

Secondly, I gratefully acknowledge other professors at the Department of Civil and Environmental Engineering in The Hong Kong Polytechnic University for teaching me different fields of professional knowledge. My special thanks also give to Dr. Xiang Fan in Chang'an University and Mr. Raymond Leung at Rock Mechanics Laboratory in The Hong Kong Polytechnic University for offering great help in the experimental part of this work.

Moreover, I own my heartfelt gratitude to my friends and members of the research group in The Hong Kong Polytechnic University, Dr. Yi Yang, Dr. Leilei Liu, Dr. Na Li, Dr. Tao Zhou, Mr. Lei Huang, Mr. Dongya Han, Ms. Hui Yang, Ms. Na Yang, Mr. Jian Li and others for their help and kindness in both my life and research work.

Last but not least, I am deeply indebted to my wife, Zi, and my parents for their unconditional love and wordless support. I would also like to thank my newborn son, Yuqian, who has added joys to my life.

TABLE OF CONTENTS

LIST OF FIGURES

LIST OF TABLES

LIST OF NOTATIONS

A	a constant in the cosine relation
A_0, A_M	A constants for specimen size approaching zero and infinite
a	a Hoek–Brown parameter
a_{ij}	compliance matrix
B	a material constant in Size Effect Law
c	cohesion
D	a constant in the cosine relation
D_0, D_M	D constants for specimen size approaching zero and infinite
d	specimen diameter
d_0	maximum aggregate size
d_f	fractal dimension
d_i	specimen diameter at which the maximum tensile strength reaches
d_L	large scale
d_S	representative volume element
E, E'	elastic moduli parallel to and perpendicular to the plane of transverse isotropy
E_β	apparent elastic modulus
F	applied force
f_c, f_t	strength of a specimen with an infinitesimal size
G'	shear modulus normal to the transversely isotropic plane
g	a constant in the modified cohesion loss model

H	sample height
k	a material parameter in the statistical size-effect model
k_β	a parameter describing the anisotropy effect
l_{ch}	an intrinsic material length
m, m_i	a Hoek–Brown parameter
m_1	a material constant in Aubertin et al.'s size-effect model
P, Q	material constants in Rafiai's failure criterion
q_{xx}, q_{yy}, and q_{xy}	stress concentration factors
R_c	degree of anisotropy
R_0	radius of the failure surface in the meridian plane
r	distance from the centre of the disk
s	a Hoek–Brown parameter
T_m, T_b	tensile strength of the rock matrix and the weak plane
T_{REV}	tensile strength of representative elementary volume
T_0	uniaxial tensile strength
T_{b0}, T_{m0}	tensile strength of the weak plane and the rock matrix when $d \to 0$
T_{bM}, T_{mM}	tensile strength of the weak plane and the rock matrix when $d \to \infty$
$T(\beta)$	tensile strength of a specimen at the loading-foliation angle β
$T_1(d)$, $T_2(d)$	tensile strength of specimen with the diameter of d
$T_1(d,\beta)$, $T_2(d,\beta)$	tensile strength of specimen with a diameter d and a loading-foliation angle β

t	thickness of the disk-shaped specimen
$V_{\max}$, $V_{\min}$, V_{mean}	Maximum, minimum and average ultrasonic wave velocities
x, y, z	global co-ordinate system
x', y', z'	local co-ordinate system
α_{β}	reduction factor of strength associated with the rock anisotropy
β	anisotropic angle
β_{f}	inclination of failure plane
$\beta_{\min}$	angle at which the strength is minimum
β^{*}	a material parameter corresponding to a critical angle
γ_{xy} , γ_{yz} , γ_{zx}	shear strain components
δ	foliation spacing
ε_{x} , ε_{y} , ε_{z}	axial strain components
η_{β}	elliptical coordinate of the maximum tensile stress at a specified angle β
λ	a material constant in Size Effect Law
λ_{i}	a dimensionless parameter in the cohesion loss model for isotropic rocks
λ_{0} , λ_{m} , λ_{β}	parameters in the modified cohesion loss model for transversely isotropic rocks
ν , ν'	Poisson's ratios parallel to and normal to the transverse isotropic plane
ν_{c}	a parameter controlled by the ratio of the major axis to the minor axis of the idealized ellipse of crack
σ_{0}	strength of a specimen with an infinitesimal size

σ_1, σ_3	maximum and minimum principal stresses
σ_{c50}	uniaxial compressive strength obtained from a specimen with diameter in 50 mm
σ_{ci}, σ_c	uniaxial compressive strength of intact rock
σ_d	uniaxial compressive strength of the specimen with a diameter of d
$\sigma_{c\beta}$, σ_β	uniaxial compressive strength at β
$\sigma_{c\beta d}$	uniaxial compressive strength of specimen with d at β
$\sigma_{c(90)}$	compressive strength at $\beta = 90°$
$\sigma_{c(\min)}$	minimum compressive strength commonly at $\beta = 30—45°$
σ_M	compressive strength when $d \to \infty$
σ_N	nominal strength, e.g., tensile strength, uniaxial compressive strength and point-load strength
σ_n	normal stress on the shearing plane
σ_L	minimum strength of a sample in the large scale
σ_p	peak strength
σ_r	residual strength
σ_S	maximum strength of a sample with the representative volume element
σ_t	tensile strength
σ_t^m	measured tensile strength by experiment
σ_t^{p1}, σ_t^{p2}	tensile strength predicted by the size-dependent modified Hoek-Brown and Saeidi failure criteria

σ_x, σ_y, σ_z	stress components in the x-axis, y-axis, z-axis
σ_{xx}, σ_{yy}	horizontal and vertical stresses
$\sigma_{\theta\theta}$, σ_{rr}	tensile and compressive stresses
τ_n	shear stress on the shearing plane
φ	angle of friction
χ	a reduction factor of strength indicating the fracture degree of the rock mass
ψ	angle between sample axis and weak plane
AARE	Average absolute relative error
AE	acoustic emission
BTS	Brazilian tensile strength
DEM	Discrete Element Method
DFN	discrete fracture network
FFSEL	fractal fracture size effect law
FJM	flat-joint model
MARE	maximum absolute relative error
MFSL	multifractal scaling relation
MPE	mean prediction error
PBM	parallel-bond model
PFC	particle flow code
SD	standard deviation
SE	standard error
SEL	size-effect law
SJM	smooth-joint model

SPW	single plane of weakness
TCS	triaxial compressive strength
TRS	triaxial residual strength
UCS	uniaxial compressive strength
USEL	unified size-effect law
VA	velocity anisotropy index

CHAPTER 1 INTRODUCTION

1.1 Research motivation

Size effect is an important characteristic of brittle and semi-brittle materials such as rock and concrete; the term refers to the influence of sample size on measured mechanical properties. Although large-scale in situ tests can accurately estimate the strength and deformation properties of the surrounding rocks or rock masses of underground structures (e.g., tunnels, caverns, mining stopes), they are not always practical or economical considering the difficulty of performing such tests or the time and economic costs incurred by doing so. A particularly promising alternative method involves scaling up the strength and elasticity properties of intact rocks tested in the laboratory to match those of rocks or rock masses in practical engineering. At this point, a proper size-effect model is essential.

There have been a great many investigations into size effect in concrete or intact rocks under different stress conditions, including uniaxial compressive, indirect tensile, point load and triaxial compressive testing. Four classical types of size-effect models have been established based on the theories of statistics, fracture energy, multifractality and mixed fractals with fracture energy. **Masoumi et al. (2015)** presented another size-effect model, viz., the unified size-effect law (USEL), capturing both the ascending and descending uniaxial compressive strength trends of six rock types.

Nevertheless, these size-effect models have a limitation: the rock is assumed to be isotropic. Natural rocks, however, are more or less anisotropic. The anisotropy in rocks is reflected by the different physical and mechanical properties in different directions. Typical anisotropic rocks include sedimentary rocks (shale, siltstone, claystone, sandstone, etc.) and metamorphic rocks (slate, phyllite, schist, gneiss, etc.). Because of their stratified or foliated structures, these rocks can further be treated as transversely isotropic material, in which one privileged direction exists and material behaviour has rotational symmetry with regard to that direction. Although the earth's crust is composed of approximately 95% igneous rocks and 5% sedimentary and metamorphic rocks, sedimentary and metamorphic rocks make up around 75% of the earth's surface. As a

result, transversely isotropic rocks are widely encountered in civil, mining, petroleum, geothermal, geo-environmental and radioactive waste disposal engineering. In Hong Kong, to increase land supply and improve local environment, a plan for rock cavern development has commenced in recent years, and some strategic cavern areas are also, inevitably, located in anisotropic formations **(Sewell 2000; Wallace and Ng 2016)**.

Anisotropy in the strength and deformation behaviours of transversely isotropic rocks has been extensively studied for decades using analytical, experimental and numerical approaches. Five independent elastic constants are employed to describe the different deformation behaviours in directions along and perpendicular to the plane of transverse isotropy. Moreover, numerous failure criteria have been proposed to capture the anisotropic tensile strength of transversely isotropic rocks, such as the Hobbs–Barron criterion and Lee–Pietruszczak criterion, which are based on the Griffith crack theory and the single plane of weakness theory, respectively. In regard to uniaxial and triaxial compressive strength, a great many failure criteria have been proposed using mathematical, empirical and discontinuous approaches. For example, the empirical equation developed initially by **Jaeger (1960)** and improved by **Donath (1961)** is used most commonly in uniaxial compression conditions. The modified Hoek–Brown criterion and Saeidi failure criterion **(Saeidi et al. 2014)** can provide good predictions for many transversely isotropic rocks in conventional triaxial conditions. In contrast, the failure criteria for transversely isotropic rocks subject to true triaxial stress states are less investigated because of the complexity. Until recently, **Pei et al. (2018)** proposed a failure criterion with which to describe anisotropic strength in true triaxial conditions by combining the anisotropic Matsuoka–Nakai criterion and the Coulomb criterion. This has been validated by true triaxial test data on chlorite schist and Chichibu greenschist. However, none of these proposed failure criteria for transversely isotropic rocks incorporate the size effect. Also, no proposed failure criteria have involved the residual strength of transversely isotropic rocks.

Is there a relationship between size effect and anisotropy in transversely isotropic rock? How do size effect and anisotropy in transversely isotropic rocks alter with stress conditions? These questions must be answered. However, to the author's knowledge, scarcely any studies have focused on the size effect while considering the influence of anisotropy in transversely isotropic rocks. Additionally, no size-dependent failure criteria

have been proposed with which to predict the strength of transversely isotropic rocks subject to different stresses. Accordingly, the research presented in this thesis aims to fill these gaps.

1.2 Research objectives

This thesis is intended to conduct a systematic study of size effect and anisotropy in transversely isotropic rock under different stress conditions, including indirect tensile, uniaxial and triaxial compressive loading. The main objectives of this thesis are as follows:

1. To propose a size-dependent failure criterion for predicting the anisotropic tensile strength of transversely isotropic rocks. Comprehensive indirect tensile tests are conducted to obtain the laws governing variations in elastic properties, indirect tensile strength, fracture patterns and transverse strains of transversely isotropic rock with sample size and anisotropic angle.
2. To propose size-dependent failure criteria for predicting the anisotropic uniaxial and triaxial compressive strength of transversely isotropic rocks, and to discuss their applicabilities. Comprehensive uniaxial and triaxial compression tests are performed to obtain the laws governing variations in compressive strength of transversely isotropic rock with sample size, anisotropic angle and confining pressure.
3. To put forward a viable failure criterion describing the residual strength of transversely isotropic rocks by incorporating the size dependency while also establishing the relationship among the residual strength, peak strength and confining pressure for transversely isotropic rocks.
4. To investigate the roles of model size and particle size distribution in the mechanical properties of isotropic rock using flat-joint model, allowing further study of the three-dimensional effect of anisotropy on the tensile behaviour of transversely isotropic rock using a combination of the flat-joint and smooth-joint models. Also, to establish a commonly accepted standard for the selection of model size and particle size distribution for three-dimensional discrete element simulation.

1.3 Thesis outline

The entire thesis is divided into seven chapters, organized as follows:

Chapter 1 introduces the research motivation, clarifies the research objectives and presents the thesis outline.

Chapter 2 reviews extensively the literature related to this research, which includes the existing size-effect models for rocks, tensile and compressive strength failure criteria for transversely isotropic rocks.

Chapter 3 systematically investigates the pure effects of model size and particle size distribution on mechanical properties of isotropic rock simulated by a flat-joint model. Comparisons with other bonded-particle models are made to illustrate the flat-joint model's capability to simulate hard rock. The coefficients of variation in mechanical properties obtained from specimens with different model sizes and particle size distributions are fully discussed.

Chapter 4 concentrates on size effect and anisotropy in the transversely isotropic rock under indirect tensile conditions. The effects of specimen size on elastic properties, tensile strength, fracture pattern and transverse strain of a transversely isotropic rock are systematically studied in laboratory tests. A tensile failure criterion is suggested with which to capture the anisotropic tensile strength. Furthermore, questions about the correlated relationship between size effect and anisotropy in indirect tensile strength are answered.

Chapter 5 incorporates the size dependency into two failure criteria, the modified Hoek–Brown and Saeidi criteria. A series of uniaxial and triaxial compression tests are conducted on a transversely isotropic slate with different sample sizes at different loading directions and confining pressures. The obtained uniaxial and triaxial test data are further used to validate the proposed size-dependent failure criteria. Additionally, the size effect and anisotropy on the triaxial residual strength are investigated to deduce a failure criterion for describing the residual strength of transversely isotropic rocks. The relationship among residual strength, peak strength and confining pressure is also studied.

Chapter 6 extends the experimental results in Chapter 4 to numerically investigate the three-dimensional effect of anisotropy on the tensile behaviour of transversely isotropic rocks using a discrete element method in three dimensions. A calibration procedure for this three-dimensional modelling of transversely isotropic rocks is proposed. The

coupling effect of loading–foliation and foliation orientation on the tensile behaviour, including tensile strength and fracture pattern, is further studied from the microscale perspective.

Chapter 7 summarises the main findings and conclusions of the thesis and presents some recommendations for future research.

CHAPTER 2 LITERATURE REVIEW

2.1 Review of existing size-effect models for rocks

In general, the term *size effect* refers to the influence of sample size (i.e., diameter or width) on mechanical characteristics **(Masoumi 2013)**, which is different from the shape effect (i.e., length-to-diameter ratio) **(Rong et al. 2018)**. Size effect is dependent on the deformation processes, so that it changes with loading condition and testing approach **(Hudson and Harrison 2000; Jaeger et al. 2009)**. Numerous researchers have studied the size effect in brittle and quasi-brittle materials such as concrete and rock under different stress states, including uniaxial compressive **(Darbor et al. 2018; Darlington et al. 2011; Elkadi et al. 2006; Hawkins 1998; Hoek and Brown 1980; Masoumi et al. 2015; Nishimatsu et al. 1969; Pierce et al. 2009; Quiñones et al. 2017; Song et al. 2018; Thuro et al. 2001; Yoshinaka et al. 2008; Zhang et al. 2011)**, indirect tensile **(Bažant 1997; Carpinteri et al. 1995; Elkadi et al. 2006; Masoumi et al. 2018; Masoumi et al. 2015; Masoumi et al. 2017; Rocco et al. 1999a; Rocco et al. 1999b; Thuro et al. 2001)**, point load **(Broch and Franklin 1972; Hawkins 1998; Masoumi 2013; Masoumi et al. 2018; Thuro and Plinninger 2001)** and triaxial compressive testing **(Aubertin et al. 2000; Hoek and Brown 1980; Masoumi et al. 2016; Medhurst and Brown 1998)**. Both descending models **(Bažant 1984; Carpinteri et al. 1995; Hoek and Brown 1980)** and ascending models **(Bažant 1997)** have been proposed to describe the results that are observed. **Masoumi et al. (2015)** further divided the descending models into four categories: those based on statistics, fracture energy and multifractals and those involving empirical and semi-empirical models. A unified size-effect law (USEL) including both the ascending and descending trends was proposed based on uniaxial compression data obtained from six sedimentary rocks. Recently, based on a statistical model and the strength anisotropy, a universal size-effect equation (USEE) describing the relationship among anisotropic angle, sample size and uniaxial compressive strength (UCS) was put forward by **Song et al. (2018)** for coal, which can be modelled as an orthotropic material **(Amadei 1996)**. Because the statistical models, fracture energy models, fractal and multifractal models, and empirical and semi-empirical models have been reviewed very extensively in the literature **(Masoumi 2013; Masoumi et al. 2015)**, they are not repeated here. Instead, the latest proposed USEL and USEE and

the size-effect models in relation to triaxial stress conditions are reviewed in the following.

2.1.1 Unified size-effect law

The development of the unified size-effect law was motivated by the observation that both ascending and descending size-effect trends are simultaneously observed in some sedimentary rocks. As shown in Figure 2.1, the uniaxial compressive strengths of seven sedimentary rocks increase initially and then decrease with the sample size reported by **Hawkins (1998)**. To reproduce this unique UCS response, **Masoumi et al. (2015)** proposed the USEL by incorporating an ascending model into a descending model.

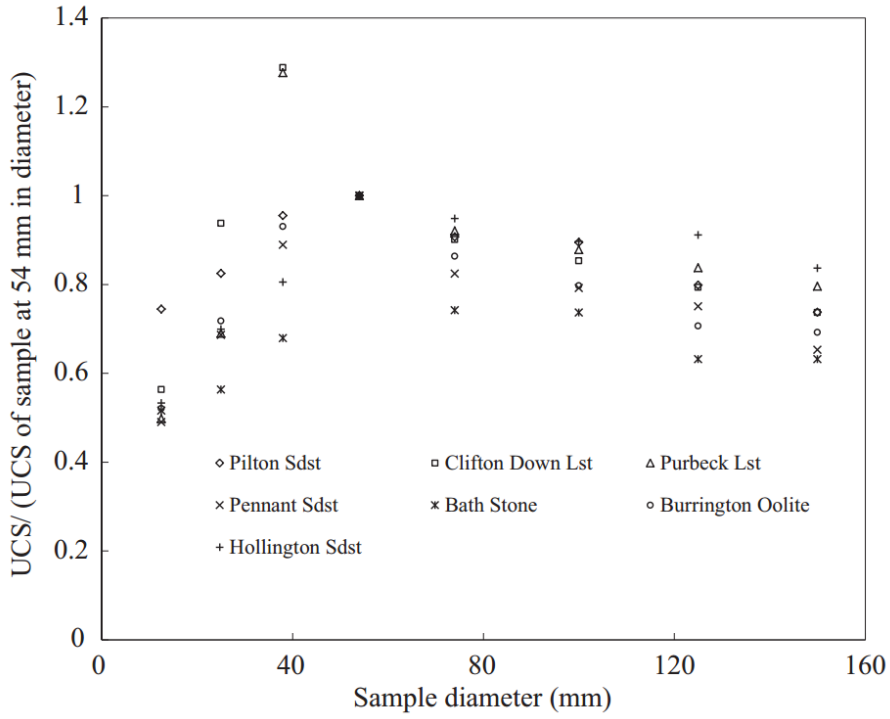

Figure 2.1 Variations of uniaxial compressive strengths with sample size obtained from seven sedimentary rocks by **Hawkins (1998)**.

The two components of USEL originate from the works of **Bažant (1984, 1997)**. Firstly, **Bažant (1984)** introduced the fracture energy theory, in which crack initiation and propagation require that the total potential energy within the materials and loading systems reduces or stays constant with increasing crack length to derive a size-effect model, called the size effect law (SEL). The size effect is regarded as being induced by the blunting of microcracking prior to the fracture, resulting in a lower stress required for

the failure of a larger structure. The SEL is expressed in the form

$$\sigma_N = \frac{Bf_t}{\sqrt{1+\frac{d}{\lambda d_0}}} \tag{2.1}$$

where σ_N is the nominal strength (e.g., tensile strength, uniaxial compressive strength and point-load strength), d denotes the specimen diameter, B and λ are dimensionless material constants, f_t represents the strength of a specimen with an infinitesimal size and d_0 represents the maximum aggregate size.

Subsequently, **Bažant (1997)** put forward another size-effect model, viz. the fractal fracture size effect law (FFSEL), by incorporating the concept of fractals into fracture energy. It was illustrated that the fracture surfaces in many brittle or quasi-brittle materials, such as concrete, rock and ceramics, to some degree present fractal characteristics in a certain range of sizes. The fractal characteristics were defined by the fractal dimension, d_f. More specifically, $d_f = 1$ presents the non-fractal characteristics, whereas $d_f \neq 1$ presents the fractal characteristics. The form of FFSEL is given as

$$\sigma_N = \frac{\sigma_0 d^{\frac{d_f - 1}{2}}}{\sqrt{1+\frac{d}{\lambda d_0}}} \tag{2.2}$$

This is similar to the expression of SEL, in particular when $d_f = 1$. The parameter σ_0 has the same meaning with f_t, representing the strength of a sample with an infinitesimal size. The other parameters are the same as those in the SEL. When $d_f > 1$, the FFSEL can reproduce the ascending size-effect response of UCS data at small sample sizes.

Combining the SEL and FFSEL models, **Masoumi et al. (2015)** proposed the USEL, in which it is always the minimum strength between that predicted by SEL and FFSEL throughout the size range that characterizes the nominal strength of material, as illustrated in Figure 2.2. The maximum nominal strength is attained at a sample size of d_i, corresponding to the intersection between SEL and FFSEL models, according to

$$d_i = \left(\frac{Bf_t}{\sigma_0} \right)^{2/(d_f - 1)} \tag{2.3}$$

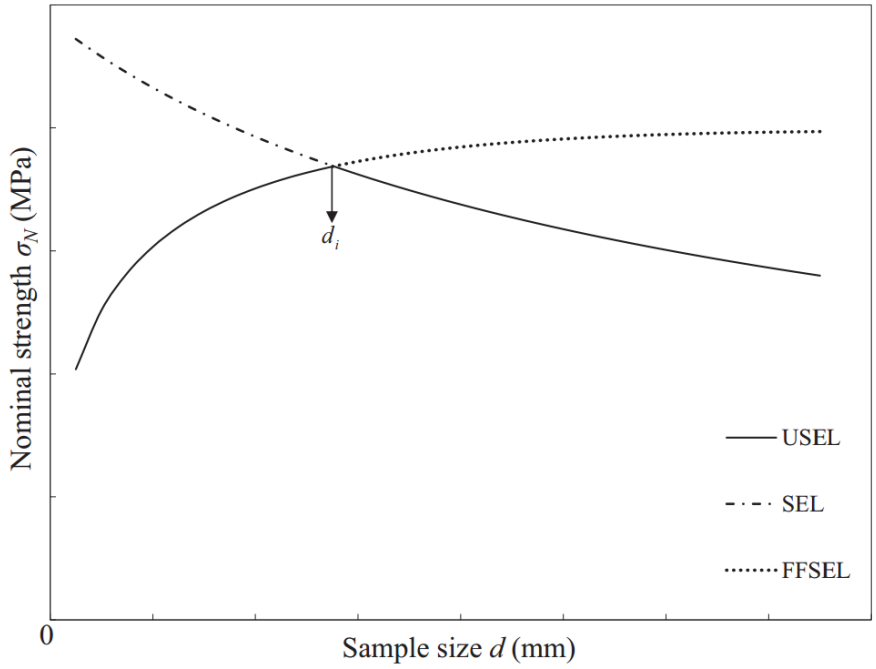

Figure 2.2 Schematic representation of USEL, combining SEL and FFSEL **(Masoumi et al. 2015)**.

The USEL model was verified against UCS data obtained from five sedimentary rocks reported by **Hawkins (1998)** as well as those obtained from Gosford sandstone reported by **Masoumi et al. (2015)**. The USEL model was also demonstrated to be capable of describing the variations of UCS, crack-initiation and crack-damage stresses of an igneous rock, Blanco Mera granite, with varying sample size. Furthermore, the applicability of this model to the triaxial data was proved in Gosford sandstone by **Masoumi et al. (2016)**. However, further study is needed to demonstrate the viability of the USEL model for rocks subject to other stress conditions, such as tensile and true triaxial stress states.

2.1.2 Universal size-effect equation

In the aforementioned size effect models, rocks are postulated to be isotropic. Nevertheless, natural rocks are more or less anisotropic, exhibiting different mechanical characteristics in different directions as a result of stresses and geological history **(Abad**

et al. 2003). However, to date there have been few size-effect studies considering the influence of anisotropy. Until recently, **Song et al. (2018)** investigated the relationship between size effect and anisotropy in the UCS of coal, an orthotropic material, and proposed a universal size-effect equation (USEE) involving the strength anisotropy and sample size. Firstly, three principles were suggested for defining the size-effect response in the UCS of coal:

1. The relationship between sample size and UCS is determined by the mechanical properties of materials.
2. The UCS decreases with increasing specimen size.
3. For samples of a prescribed shape, the UCS remains constant for coal samples having sizes beyond or below the threshold values.

Based on the three principles, a statistical size-effect model was put forward, expressed as

$$\sigma_d = \sigma_M + (\sigma_0 - \sigma_M)e^{-kd} \tag{2.4}$$

where σ_d is the UCS of the specimen with a diameter of d; σ_0 and σ_M characterize the UCS when $d \to 0$ and $d \to \infty$, respectively; and k is a material parameter. The applicability of this size-effect model to coal was validated against the UCS data obtained from coal specimens having different shapes (cylindrical and cubic).

Next the strength anisotropy of coal was captured by an empirical equation developed initially by **Jaeger (1960)** and improved by **Donath (1961)**, which is used most commonly in uniaxial compression conditions. The empirical equation is in the form

$$\sigma_\beta = A - D\cos 2(\beta - \beta_{\min}) \tag{2.5}$$

where σ_β is the UCS at the anisotropic angle of β, $\beta_{\min}$ corresponds to the angle at which UCS is minimum; and A and D are two constants.

Lastly, the USEE model was obtained by incorporating the strength anisotropy into the statistical size-effect model, replacing σ_0 and σ_M in Eq. (2.4) with Eq. (2.5). The proposed USEE model is given as

$$\sigma_{c\beta d} = A_M - D_M \cos 2(\beta - \beta_{\min}) + \left[(A_0 - A_M) - (D_0 - D_M)\cos 2(\beta - \beta_{\min})\right] e^{-kd} \qquad (2.6)$$

where $\sigma_{c\beta d}$ is the UCS of specimen with the diameter of d at the anisotropic angle of β; A_0 and D_0, A_M and D_M are A and D constants for specimen size approaching zero or infinite, respectively; and $\beta_{\min}$ is the average of β at which UCS is minimum.

The advantage of USEE model is that material strength, sample size and anisotropic angle are all combined to get a mechanistic description of behaviour. Correspondingly, its limitation is that many tests are required to be conducted on samples with different sizes at different anisotropic angles for a certain material. The USEE model has been proved to be viable for coal, which behaves as a rock mass with preferentially oriented cleats under the uniaxial condition. However, further investigations are needed to explore its applicability to other rocks, such as transversely isotropic rock, and in other stress conditions.

2.1.3 Size-effect models in relation to triaxial stress conditions

Because the Hoek–Brown criterion **(Hoek and Brown 1980)** is the most well-known, trusted, and commonly used triaxial criterion in rock mechanics and rock engineering, it has been selected as a basic step in deducing size-effect models applicable in triaxial conditions. The generalized Hoek–Brown failure criterion for rock masses is expressed by

$$\sigma_1 = \sigma_3 + \sigma_{ci}\left(m\frac{\sigma_3}{\sigma_{ci}} + s\right)^a \qquad (2.7)$$

where σ_1 and σ_3 are the maximum (peak strength) and minimum (confining pressure) principal stresses, respectively; σ_{ci} is the UCS of intact rock; and m, s and a are material constants. For intact rocks, $s = 1$ and $a = 0.5$.

The first notable size-effect model considering triaxial confinement was developed by **Hoek and Brown (1980)**, who introduced a statistical descending size-effect model to the well-known Hoek–Brown failure criterion according to

$$\sigma_1 = \sigma_3 + \sigma_{c50}\left(\frac{50}{d}\right)^{0.18}\left(m\frac{\sigma_3}{\sigma_{c50}\left(\frac{50}{d}\right)^{0.18}} + 1\right)^{0.5} \tag{2.8}$$

where σ_{c50} denotes the UCS obtained from a specimen of 50 mm diameter and d is the sample diameter. Afterwards **Medhurst and Brown (1998)** succeeded in applying the Hoek–Brown size-effect model to estimate the compressive strength of coal specimens with diameters of 61, 101, 146 and 300 mm under confining pressures in the range of 0–10 MPa.

Subsequently, **Masoumi et al. (2016)** observed that both uniaxial and triaxial compressive strengths of Gosford sandstone samples with diameters of 25, 50 and 96 mm followed the ascending and then descending size-effect trend. They incorporated the USEL **(Masoumi et al. 2015)** into the original Hoek–Brown failure criterion according to

$$\sigma_1 = \sigma_3 + \min\left(\frac{\sigma_0 d^{(d_f-1)/2}}{\sqrt{1+(d/\lambda d_0)}}, \frac{Bf_t}{\sqrt{1+(d/\lambda d_0)}}\right)\left(m\frac{\sigma_3}{\min\left(\frac{\sigma_0 d^{(d_f-1)/2}}{\sqrt{1+(d/\lambda d_0)}}, \frac{Bf_t}{\sqrt{1+(d/\lambda d_0)}}\right)} + 1\right)^{0.5} \tag{2.9}$$

where the parameters are as described for Eqs. (2.1) and (2.2). The size-dependent failure criterion describes the relationship among compressive strength, confining pressure and specimen size and is verified against the experimental results for Gosford sandstone.

Notably, the underlying assumption for the two size-dependent failure criteria described is that the size-effect behaviours in uniaxial and triaxial conditions are similar, supported by experimental results. Owing to the adoption of the Hoek–Brown failure criterion, the two size-dependent criteria inherit its shortcoming of limited applicability in the brittle regime.

Another size-effect model taking the triaxial confinement into account was developed by **Aubertin et al. (2000)**, who stated that with increasing confinement, size effects are reduced progressively when going from a brittle to a semi-brittle regime and fully

disappear in the ductile regime. The proposed size-effect model follows a generalization of power-law functions in a complicated form according to

$$\sigma_N = \sigma_S - x_1\left(\sigma_S - \sigma_L\right)\left(\frac{d - d_S}{d_L - d_S}\right)^{m_1} \qquad (2.10)$$
$$x_1 = e^{(x_0\sigma_3/T_0)}$$

where σ_N is the nominal strength of a sample with size (d); σ_S is the maximum strength of a sample with the representative volume element (d_S); σ_L is the minimum strength of a sample in the large scale (d_L); x_0 and m_1 denote two material constants; and T_0 denotes the uniaxial tensile strength, taken as a negative value. The use of this size-effect model is very limited due to the complexity involved in determining its required parameters.

In summary, it should be noted that none of the reviewed size-effect models in relation to triaxial compressive conditions take into account the strength anisotropy of rocks.

2.2 Review of failure criteria for transversely isotropic rocks

Anisotropy in the strength of transversely isotropic rocks has been extensively studied for decades using analytical, experimental and numerical approaches. Numerous failure criteria have been proposed to capture the anisotropic tensile strength of transversely isotropic rocks, such as the Hobbs–Barron, Pietruszczak–Mroz, Nova–Zaninetti and Lee–Pietruszczak criteria. With respect to the uniaxial and triaxial compressive strength, a great many failure criteria have been proposed using mathematical, empirical and discontinuous approaches. For example, the criterion developed by **Jaeger (1960)** based on the theory of single plane of weakness (SPW) is used most commonly in uniaxial compression conditions. The modified Hoek–Brown criterion and Saeidi failure criterion **(Saeidi et al. 2014)** can provide good predictions for many transversely isotropic rocks in conventional triaxial conditions. The Anisotropic Matsuoka–Nakai (AMN)–Coulomb failure criterion proposed by **Pei et al. (2018)** is capable of describing both the strength and failure mode of transversely isotropic rocks under true triaxial stress conditions.

2.2.1 Failure criteria in tensile conditions

The tensile strength of transversely isotropic rocks can be determined using direct or indirect tensile tests. In the direct tensile test, the requirement for experimentation is high but the tensile strength of rocks is directly equal to the applied stress. Among indirect tensile tests, which require less testing equipment and sample preparation, the Brazilian test is a very common method for measuring the tensile strength of rocks, but a formula is required to indirectly calculate the tensile strength. For isotropic rocks, the suggested formula was proposed by **Akazawa (1943)** and **Carneiro (1943)** independently; it is expressed as

$$\sigma_t = \frac{2F}{\pi dt} \tag{2.11}$$

where F is the force at failure and d and t are the diameter and thickness of the disk-shaped specimen, respectively. Two prerequisites for this formula are that (1) the material be isotropic and (2) the fracture be initiated by tensile crack from the centre of the disk-shaped specimen. However, for the transversely isotropic rock of interest in this thesis, the strength obtained from this formula cannot represent the true tensile strength for most cases. Accordingly, based on the elastic constants, **Claesson and Bohloli (2002)** proposed a reasonably accurate approximate formula for calculating the tensile strength of transversely isotropic rocks,

$$\begin{aligned} \sigma_t &= \frac{2P}{\pi dt}\left[(\sqrt[4]{E/E'})^{(-\cos 2\beta)} - \frac{\cos 4\beta}{4}(b-1) \right] \\ b &= \frac{\sqrt{EE'}}{2}\left(\frac{1}{G'} - \frac{2\nu'}{E'}\right) \end{aligned} \tag{2.12}$$

where E and E' are the elastic moduli parallel to and normal to the transversely isotropic plane, respectively, and G' and ν' represent the shear modulus and the Poisson's ratio in the direction perpendicular to the plane of transverse isotropy, respectively. It requires that the failure should start at the center of disc, but not requires that the failure plane must be along the loaded diameter. In this section, the tensile failure criteria of transversely isotropic rocks, which are applicable to both direct and indirect tensile strength, are reviewed as follows.

2.2.1.1 Hobbs-Barron criterion

Regarding the tensile strength variation of transversely isotropic rocks with loading direction, **Hobbs (1967)** put forward the first failure criterion based on the Griffith crack theory. Afterwards, an anisotropic tensile strength criterion was proposed by **Barron (1971)** using the modified Griffith's theory. In essence, the two criteria are consistent and can be combined as the Hobbs–Barron (H-B) criterion,

$$T(\beta)=\begin{cases}\dfrac{2T_b}{\cos\beta(1+\cos\beta)}, & 0^\circ\le\beta\le\beta^*\\ T_m, & \beta^*\le\beta\le 90^\circ\end{cases} \qquad (2.13)$$
$$\text{with } \cos\beta^*(1+\cos\beta^*)=\frac{2T_b}{T_m}$$

where $T(\beta)$ represents the tensile strength of a specimen when the angle between the tensile loading direction and the normal of the transversely isotropic plane is β; T_m and T_b represent the tensile strength of the rock matrix and the weak plane (e.g., bedding plane, foliation plane and discontinuity plane), respectively. β^* is a material parameter, corresponding to a critical angle.

2.2.1.2 Liao et al. criterion

Liao et al. (1997) observed that the Hobbs–Barron criterion cannot provide a good strength description when the angle between the tensile loading direction and the normal of the bedding plane is high ($\beta^*\le\beta\le 90^\circ$). Accordingly, they extended the Hobbs–Barron criterion and proposed a second formula for describing the tensile failure stress according to

$$T(\beta)=\begin{cases}\dfrac{2T_b}{\cos\beta(1+\cos\beta)}, & 0^\circ\le\beta\le\beta^*\\ T_m\left(1-h\cos^2\beta\right), & \beta^*\le\beta\le 90^\circ\end{cases} \qquad (2.14)$$

where h and β^* are material parameters and the value of β^* is determined as in Eq. (2.13). Notably, the Liao et al. criterion involves three parameters.

2.2.1.3 Nova-Zaninetti criterion

Subsequently, based on the direct tensile strength obtained from the Luserna gneiss, **Nova and Zaninetti (1990)** presented a continuous tensile strength criterion, called the Nova–Zaninetti (N-Z) criterion. The form of the N-Z criterion is given as

$$T(\beta) = \frac{T_b T_m}{T_b \sin^2 \beta + T_m \cos^2 \beta} \tag{2.15}$$

Correspondingly, the inclination of failure plane (β_f) can be predicted by

$$\tan \beta_f = \frac{(T_m - T_b)\sin \beta \cos \beta}{T_b \sin^2 \beta + T_m \cos^2 \beta} \tag{2.16}$$

Although the N-Z criterion is deduced from the direct tensile strength data of gneiss, its applicability to indirect tensile strength data has been validated by various transversely isotropic rocks, such as shale, sandstone, slate, gneiss, schist and marl.

2.2.1.4 Li-Aubertin criterion

Firstly, **Li and Aubertin (2000)** put forward an empirical failure criterion based on direct tensile strength data of anisotropic rocks and succeeded in applying it into the description of indirect tensile strength of gneiss and schist. As in the Liao et al. criterion, this criterion also has three parameters in the form

$$T(\beta) = T_b + (T_m - T_b)\sin^n \beta \tag{2.17}$$

where *n* is a material parameter that can be approximately taken as $n = T_m / T_b$.

Furthermore, the weak planes embedded in rocks are idealized as series of preferentially oriented elliptical cracks, and the tensile strength of transversely isotropic rocks is postulated to be dependent on the maximum tensile local stress along the boundary of elliptical cracks. Accordingly, based on Inglis's analytical solution, **Li and Aubertin (2002)** proposed another failure criterion including two formulations to describe both direct and indirect tensile strength of transversely isotropic rocks, expressed by

$$T(\beta)=\frac{T_m\left[\left(1+\nu_c^{\,2}\right)\left(1-\nu_c^{\,2}\right)\cos 2\eta_\beta\right]}{2\nu_c+\left(1-\nu_c^{\,2}\right)\cos 2\beta+\left(1+\nu_c^{\,2}\right)\cos 2\left(\beta-\eta_\beta\right)} \tag{2.18}$$

$$T(\beta)=\frac{T_m\left[\left(1+\nu_c^{\,2}\right)\left(1-\nu_c^{\,2}\right)\cos 2\eta_\beta\right]}{4\left[-\nu_c+\left(1-\nu_c^{\,2}\right)\cos 2\beta+\left(1+\nu_c^{\,2}\right)\cos 2\left(\beta-\eta_\beta\right)\right]} \tag{2.19}$$

where ν_c is a parameter controlled by the ratio of the major axis to the minor axis of the idealized ellipse of crack ($\nu \geq 1$) and η_β represents the elliptical coordinate of the maximum tensile stress at a specified angle β. Eqs. (2.18) and (2.19) correspond to the failure criteria for direct and indirect tensile strength of transversely isotropic rocks, respectively, and they have three parameters as well.

2.2.1.5 Lee-Pietruszczak criterions

A tensile failure criterion was proposed by **Lee and Pietruszczak (2015)** employing the single plane of weakness (SPW) theory, so the criterion is called the SPW criterion; it is stated as

$$T(\beta)=\begin{cases}\dfrac{T_b}{\cos^2\beta}, & 0^\circ \leq \beta \leq \beta^* \\ T_m, & \beta^* \leq \beta \leq 90^\circ\end{cases} \tag{2.20}$$
$$\text{with } \beta^*=\cos^{-1}\sqrt{\frac{T_b}{T_m}}$$

It is noted that the value of critical angle (β^*) defined here is different from that in Eqs. (2.13) and (2.14). Meanwhile, based on the tensile strength tensor, **Lee and Pietruszczak (2015)** also presented another tensile failure criterion, named the Lee–Pietruszczak (L-P) criterion, which tends to oversimplify the real tensile strength features. The formulation of the L-P criterion is

$$T(\beta)=\frac{T_m+T_b}{2}-\frac{T_m-T_b}{2}\cos 2\beta \tag{2.21}$$

2.2.1 Failure criteria in compressive conditions

2.2.1.1 Modified Hoek-Brown failure criterion

To consider the strength anisotropy of intact anisotropic rocks in triaxial conditions, **Saroglou and Tsiambaos (2008)** built on the work of **Hoek and Brown (1980)** by incorporating an anisotropic parameter k_β in the form,

$$\sigma_1 = \sigma_3 + \sigma_{c\beta}\left(k_\beta m_i \frac{\sigma_3}{\sigma_{c\beta}} + 1\right)^{0.5} \tag{2.22}$$

where $\sigma_{c\beta}$ represents the UCS of rock at the anisotropic orientation with respect to the loading direction (β), k_β is a parameter describing the anisotropy effect, and m_i is a material constant independent of the loading direction. The parameter $\sigma_{c\beta}$ mainly controls the upward and downward movement of the criterion (Figure 2.3a), while k_β influences the curvature of the criterion (Figure 2.3b). The modified Hoek–Brown failure criterion has been widely used to predict the failure of various transversely isotropic rocks.

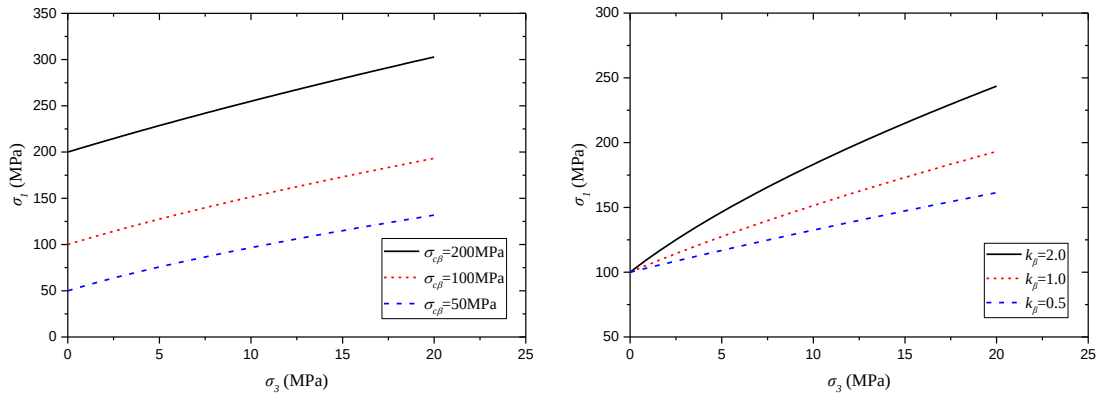

(a) (b)

Figure 2.3 Schematic representation of Hoek-Brown failure criterion: (a) at different $\sigma_{c\beta}$ values and identical k_β of 1.0 and m_i of 10; and (b) at different k_β values and identical $\sigma_{c\beta}$ of 100MPa and m_i of 10.

2.2.1.2 *Saeidi failure criterion*

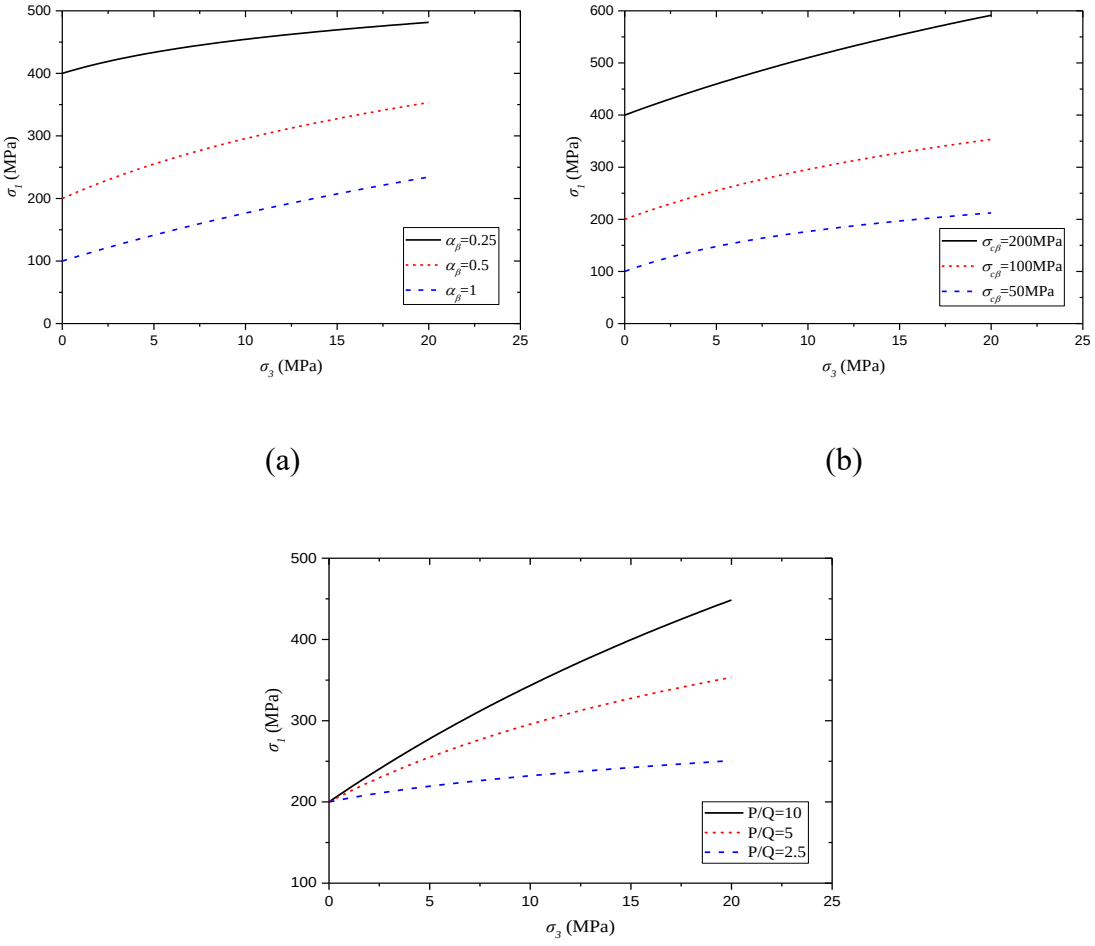

Figure 2.4 Schematic representation of Saeidi failure criterion: (a) at different α_β values and identical $\sigma_{c\beta}$ of 100MPa, P of 10 and Q of 2; (b) at different $\sigma_{c\beta}$ values and identical α of 0.5, P of 10 and Q of 2; and (c) at different ratios of P/Q and identical $\sigma_{c\beta}$ of 100MPa, α of 0.5 and P of 10.

To overcome the limitations of the Hoek–Brown failure criterion in the brittle regime, **Rafiai (2011)** proposed an empirical failure criterion for isotropic rocks which is capable of estimating the strength of rocks in the ductile failure regime according to

$$\frac{\sigma_1}{\sigma_{ci}} = \frac{\sigma_3}{\sigma_{ci}} + \left[\frac{1+P(\sigma_3/\sigma_{ci})}{1+Q(\sigma_3/\sigma_{ci})}\right] - \chi \qquad (2.23)$$

where P and Q are two material constants ($P \geq Q \geq 0$); χ is a reduction factor of strength indicating the fracture degree of the rock mass. Subsequently, **Saeidi et al. (2014)** extended the failure criterion developed by **Rafiai (2011)** and put forward a criterion applicable for transversely isotropic rocks, called the Saeidi failure criterion, which is expressed as

$$\sigma_1 = \sigma_3 + \sigma_{c\beta}\left[\frac{1+P(\sigma_3/\sigma_{c\beta})}{\alpha_\beta + Q(\sigma_3/\sigma_{c\beta})}\right] \tag{2.24}$$

where α_β is the reduction factor of strength associated with the rock anisotropy. In the failure criterion, α_β and $\sigma_{c\beta}$ control the upward and downward movement of the criterion (Figure 2.4a and b) and P/Q influences the curvature of the criterion (Figure 2.4c).

2.2.1.3 AMN-Coulomb failure criterion

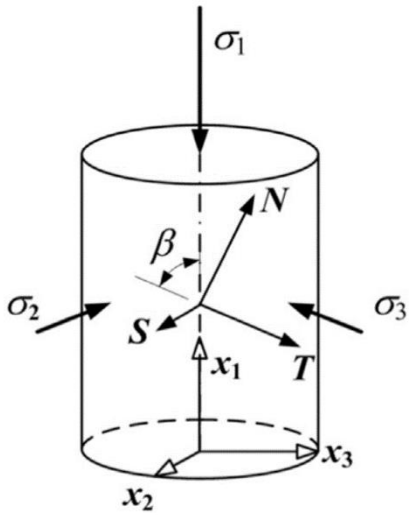

Figure 2.5 Relative orientation of the material system (*STN*) with respect to the principal stress system ($x_1x_2x_3$) **(Pei et al. 2018)**.

Pei et al. (2018) introduced a normal stress space, which incorporates the principal stress system in the material system, as shown in Figure 2.5, into the well-known isotropic Matsuoka–Nakai criterion to describe the anisotropic shear strength of transversely isotropic rocks. Moreover, to examine the failure surface geometry in the normal stress

space, the Cartesian coordinates $(\sigma_s, \sigma_t, \sigma_n)$ was transformed into the polar coordinates (r, θ, Z) as per the followings:

$$
\begin{aligned}
&Z = \frac{\sigma_s + \sigma_t + \sigma_n}{\sqrt{3}};\\
&r = \sqrt{\frac{1}{3}\left[(\sigma_s - \sigma_t)^2 + (\sigma_t - \sigma_n)^2 + (\sigma_n - \sigma_s)^2\right]};\\
&\tan\theta = \frac{\sqrt{3}(\sigma_t - \sigma_s)}{2\sigma_n - \sigma_s - \sigma_t};\\
&\sigma_n = \frac{\sqrt{3}}{3}\left[Z + \sqrt{2}r\cos\theta\right];\\
&\sigma_s = \frac{\sqrt{3}}{3}\left[Z - \sqrt{2}r\sin\left(\frac{\pi}{6} + \theta\right)\right];\\
&\sigma_s = \frac{\sqrt{3}}{3}\left[Z - \sqrt{2}r\sin\left(\frac{\pi}{6} - \theta\right)\right];\\
&r_{240} = \frac{1}{\sqrt{6}}\left(2\sigma_s - \sigma_t - \sigma_n\right);\\
&r_{120} = \frac{1}{\sqrt{6}}\left(-\sigma_s + 2\sigma_t - \sigma_n\right);\\
&r_0 = \frac{1}{\sqrt{6}}\left(-\sigma_s - \sigma_t + 2\sigma_n\right)
\end{aligned}
\tag{2.25}
$$

The resulting anisotropic Matsuoka–Nakai (AMN) criterion is formulated as

$$
\begin{aligned}
&(1-\rho)r'^3\cos 3\theta - \left(1 - \rho + \rho^2\right)r'^2 + \rho^2 - 2\left(1 - \rho + \rho^2\right)\left(\sigma'^2_{tn} + \sigma'^2_{ns} + \sigma'^2_{st}\right) - \kappa\left(\sigma'^2_{tn} + \sigma'^2_{ns}\right)\\
&+\alpha\left(1 - r'_0\right) - 6(1-\rho)\left(r'_{240}\sigma'^2_{tn} + r'_{120}\sigma'^2_{ns} + r'_0\sigma'^2_{st}\right) + 6\sqrt{6}(1-\rho)\sigma'_{tn}\sigma'_{ns}\sigma'_{st} = 0
\end{aligned}
\tag{2.26}
$$

where ρ describes the roundness of the failure surface; σ'_{st}, σ'_{tn} and σ'_{ns} are normalized shear stresses; r'_0, r'_{120} and r'_{240} are normalized r_0, r_{120} and r_{240}, respectively; the two terms, $-\kappa\left(\sigma'^2_{tn} + \sigma'^2_{ns}\right)$ and $\alpha\left(1 - r'_0\right)$, are used to characterize the transversely isotropic failure. The more details can be found in the literature **(Pei et al. 2018)**.

Furthermore, because natural rocks are different from frictional soils for which the assumption of linear pressure dependence is acceptable, the radius of the failure surface

in the meridian plane (R_0) should be a function of the polar coordinate *Z*, expressed by

$$R_0 = R_0(Z) \tag{2.27}$$

Consequently, Eqs. (2.26) and (2.27) together constitute the complete formulation of AMN failure criterion with non-linear pressure dependence. In transversely isotropic rocks, there are two basic types of failure modes – that occurring in the rock matrix and that occurring along discontinuities (e.g., cleavage, bedding and foliation planes). The AMN failure criterion can describe only the failure of a homogeneous transversely isotropic material without discontinuities. Moreover, it is known that failure along the discontinuities usually obeys the traditional Coulomb criterion,

$$\tau_n - \sigma_n \tan\varphi - c = 0 \tag{2.28}$$

where τ_n and σ_n are the applied shear and normal stresses on the transversely isotropic plane and φ and c are the friction angle and cohesion along the transverse planes of isotropy. Accordingly, the lower bound envelope of the AMN criterion and the Coulomb criterion controls the failure of transversely isotropic rocks under a true triaxial condition. The applicability of the AMN–Coulomb failure criterion to predict the failure strength and failure mode of transversely isotropic rocks has also been validated against the true triaxial data on chlorite schist and Chichibu greenschist.

CHAPTER 3 EFFECTS OF MODEL SIZE AND PARTICLE SIZE DISTRIBUTION IN THE ISOTROPIC ROCK

3.1 Introduction

The strength and deformation characteristics of rocks are critical to various engineering applications such as the stability of slopes, tunnels, caverns, dam foundations and radioactive waste storages **(Witherspoon et al. 1981)**. Among the numerous factors which control the behaviour of rock, the size effect of rocks must be considered when applying the laboratory strength and elasticity properties to the practical engineering design.

Most researchers investigated the size effect by varying the diameter of the specimen while keeping the length-to-diameter ratio of 2:1 under compression tests **(Hawkins 1998; Quiñones et al. 2017; Rong et al. 2018)** or 1:2 under the Brazilian tests **(Simpson et al. 2014; Tavallali and Vervoort 2010)**. To date, both descending model **(Bažant 1984; Carpinteri et al. 1995; Hoek and Brown 1980)** and ascending model **(Bažant 1997)** have been proposed to describe the results that are observed. Recently, a unified size-effect law (USEL) including both the ascending and descending trends was proposed, based on the uniaxial compressive strengths (UCS) obtained from six sedimentary rocks **(Masoumi et al. 2015)**. Sometimes, such size-effect relation also shows good agreement for igneous rock, i.e., Blanco Mera granite **(Quiñones et al. 2017)**. As for the large variation of the size effect, **Darlington et al. (2011)** gave several possible reasons: the differences between (a) testing method/apparatus used, (b) specimen preparation method and (c) type of materials (i.e., sedimentary rocks, igneous rocks and metamorphic rocks). In essence, the size effect is associated with the discontinuities, pre-existing flaws or pores within the specimen **(Ju et al. 2013)**, the surface flaws or imperfections **(Vutukuri et al. 1974)**, and the rock types **(Pierce et al. 2009; Yoshinaka et al. 2008)** at macro scale. While in the microscale term, it is related to micro defects, mineral composition, mineral shape, mineral size distribution etc. The aforementioned two discrepancies of (a) and (b)

can be avoided when numerical methods are adopted. Moreover, the use of numerical method is also a promising tool to study the size effect of rocks, especially considering the convenience of investigation at microscale using numerical models and the difficulty in preparation and testing of large size specimens in laboratory, such as 300mm diameter or more which is of crucial importance to give a representative result for the study of the size effect **(Darlington et al. 2011)**.

For rock mechanics problems, the most commonly adopted numerical approaches are classified into three categories: continuum methods, discontinuum methods and hybrid continuum/dicontinuum methods **(Jing 2003)**. Conventional continuum approaches, such as the Finite Element Method (FEM) or the Finite Difference Method (FDM), are mesh-based and suffer the shortcomings of (a) complicated re-meshing and remapping of variables, and (b) causing drastic errors in simulating large-deformation problems **(Li and Liu 2002)**. To overcome the weaknesses, many mesh-free continuum approaches have been developed, including the Smooth Particle Hydrodynamics (SPH) **(Gingold and Monaghan 1977)**, Material Point Method (MPM) **(Soga et al. 2016)**, Element-free Galerkin (EFG) **(Lu et al. 1994)** and so forth. Up to date, these mesh-free techniques have achieved success in modelling large-deformation problems in geomechanics (e.g., landslides, deformations in tunnels) **(Manchao et al. 2015; Soga et al. 2016)**, but conventional continuum approaches still remain the mainstream numerical tool in rock engineering computations because of the advantage in computational efficiency **(Jing 2003)**. Compared with conventional continuum approaches, discontinuum approaches (e.g., Discrete Element Method (DEM), Discrete Fracture Network (DFN)) have the advantages of (a) avoiding discretization around fractures, (b) explicitly presenting fracture initiation and propagation processes and (c) capable of simulating large discontinuous deformation **(Bai et al. 2016; Donzé et al. 2013; Karampinos et al. 2015; Zhang and Wong 2012)**, while have the limitations of (a) time-consuming calibration process of microscopic parameters and (b) huge demand for computing power for large-scale engineering applications **(Hofmann et al. 2015; Koyama and Jing 2007; Potyondy and Cundall 2004)**. Also, to make a brief comparison between mesh-free continuum and discontinuum approaches, taking MPM and DEM as an example, the DEM is more capable of explicitly presenting the cracks initiating, propagating and

nucleating process but sacrifices a lot of time in calibrating microscopic parameters.

The particle flow code (PFC) **(Itasca Consulting Group 2014)**, including PFC2D and PFC3D, based on DEM, have been widely used for solving various rock mechanics and rock engineering problems **(Fan et al. 2018; Potyondy 2015)**. Some researchers **(Bahrani and Kaiser 2016; Esmaieli et al. 2010; Zhang et al. 2011)** have applied PFC in the study of size effect on rocks by introducing pre-existing joints or fractures, and the results can capture the typical descending trend of UCS with the sample size. However, in these studies, the packing effect of particle models was ignored. In other words, the porosity of generated models following the standard PFC procedure **(Potyondy and Cundall 2004)** cannot be controlled even if the same micro-parameters and particle size distribution are assigned. Generally, the porosity of model decreases with the model size increasing **(Ding et al. 2014)**, which will result in a great variation in the strength and elastic properties **(Schöpfer et al. 2009)**. To eliminate the packing effect, **Esmaieli et al. (2010)** assigned different micro-parameters for models of different sizes; **Scholtès et al. (2011)** fixed the initial average coordination number (i.e., average number of contacts per particle) by varying the interaction range of connecting discrete elements, and **Ding et al. (2014)** directly controlled the porosity using a deletion method. It is also noted that the model size and particle size are usually interrelated **(Hofmann et al. 2015; Koyama and Jing 2007; Peng et al. 2017a)**. Either the model size is varied when grain size is fixed, or the grain size is varied while the model size will vary in the size effect study. **Potyondy (2017)** confirmed that the two methods could obtain similar results. In addition, contact constitutive model and particle size distribution, in a way corresponding to mineral composition and mineral size distribution respectively, also play vital roles in the size effect in the PFC models **(Koyama and Jing 2007)**. The effects of model size and particle size distribution on parallel-bonded models have been investigated under uniaxial compression tests by PFC2D **(Koyama and Jing 2007)** and PFC3D **(Ding et al. 2014)**. **Peng et al. (2017a; 2017b)** and **(Zhou et al. 2017)** explored the two effects on grain-based models using PFC2D. Nevertheless, even nowadays, there is not yet a systematic study on the flat-jointed models.

In this chapter, the roles of model size and particle size distribution on flat-jointed models

are systematically investigated under uniaxial compression and Brazilian tests using PFC3D. An insight into these effects assists to establish a commonly accepted standard for the selection of model size and particle size for the flat-jointed PFC3D models. It is also a basic step for the further size-effect study of rocks, since there is still no single numerical approach capable of capturing the USEL response observed in laboratory **(Masoumi et al. 2015; Quiñones et al. 2017)**.

3.2 Research methodology

The Lac du Bonnet (LdB) granite, which has been extensively investigated either in laboratory **(Kelly et al. 1994; Martin 1993)** or in numerical simulation **(Ding et al. 2014; Lan et al. 2010; Liu et al. 2018; Potyondy and Cundall 2004; Scholtès and Donzé 2013)**, is cited as the reference in this numerical study. Firstly, the mechanical properties of LdB granite are summarised. Then the adopted constitutive model, flat-joint model (FJM), is introduced exhaustively from the fundamental principles, microscopic parameters and the inherent advantages in application. The generation methods for the standard and same-porosity PFC3D models are further presented to prepare for the following calibration and parametric study. To accurately reproduce the mechanical behaviours of LdB granite, the micro-parameters of FJM are calibrated from as many macro-properties as possible. These macro-properties cover a range of UCS, Young's modulus, Poisson's ratio, compressive strengths and crack-initiation stresses under various confining stresses, and Brazilian tensile strength (BTS). Lastly, the influences of the model size and particle size distribution are investigated under uniaxial compression and Brazilian tests.

3.2.1 Mechanical characteristics of LdB granite

A great number of laboratory tests have been carried out on the LdB granite, which is mainly composed of K-feldspar, plagioclase, quartz and biotite. The grain structures and size distributions of the four mineral compositions are shown in Figure 3.1. From the viewpoint of two-dimensional thin section image, the grain structures can be represented by means of polygon. The minimum grain size is in the range of 0.2-0.5mm, while the maximum grain size ranges from 2 to 6mm. The mean grain size, which is often used as

an analogue of particle size in numerical models, covers a range of 0.7-4.3mm and follows a power function. Thus the average grain diameter (d) of 2.5mm is chosen for controlling the particle size distribution in this study. Moreover, the short-term laboratory properties **(Martin 1993)** of LdB near surface (0-200m) granite obtained from specimens of 63-mm diameter and length-to-diameter ratio of 2.5 are listed in the second column of Table 3.1. The Young's modulus was obtained by the tangent at the 50% peak strength under uniaxial compression test. The crack-initiation stress, which indicates the onset of cracking, is determined to be approximately one-third of UCS by the volumetric strain method **(Martin and Chandler 1994; Martin 1997)** for the LdB granite. It is found to be dependent on the confining stress in the form of $\frac{1}{3}q_u + 1.5\sigma_3$, where q_u and σ_3 are UCS and confining stress respectively **(Martin 1997)**.

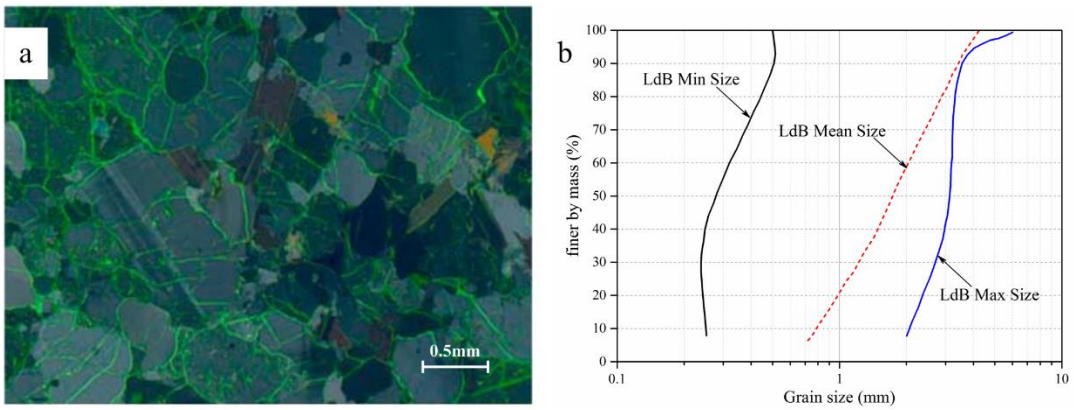

Figure 3.1 Mineral grain structures and grain size distributions of a sample of LdB granite from Underground Research Laboratory (URL). (a) Polarized and fluorescent microscopic image **(Lan et al. 2010)**. (b) Grain size distribution **(Kelly et al. 1994)**. The solid black and blue lines envelop the distributions of minimum and maximum grain sizes, respectively. The dashed red line represents the mean grain size distribution.

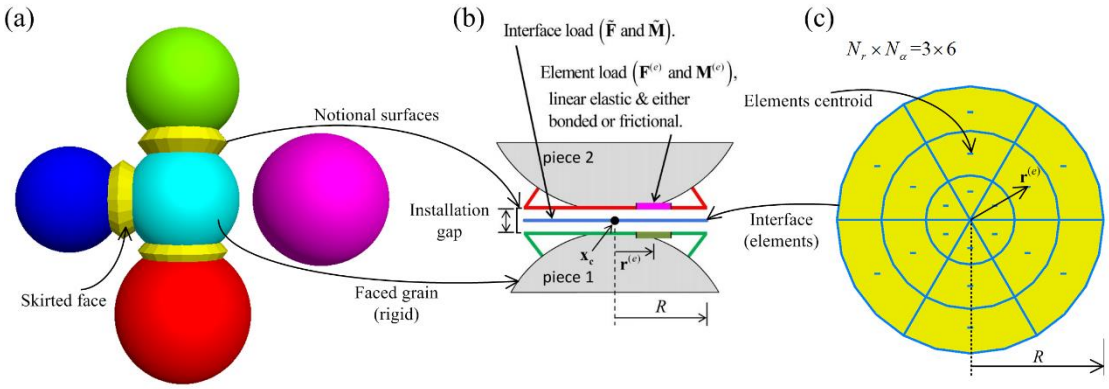

Figure 3.2 3D flat-joint model. (a) Installation of flat-joint contacts. (b) Mechanical behaviour of flat-joint model **(Potyondy 2016)**. (c) Interface discretization of flat-joint model.

Table 3.1 Macro-properties of LdB granite, calibrated PBM and FJM specimens.

Property	LdB granite from **(Martin 1993)**	PBM results from **(Potyondy and Cundall 2004)**	FJM results **(This study)**
Young's modulus, E (GPa)	69±5.8 (n = 81)	69.2±0.8 (n = 10)	68.6±0.3 (n = 10)
Poisson's ratio, ν	0.26±0.04 (n = 81)	0.256±0.014 (n = 10)	0.254±0.004 (n = 10)
UCS, q_u (MPa)	200±22 (n = 81)	198.8±7.2 (n = 10)	201.2±1.3 (n = 10)
BTS, σ_t (MPa)	9.3±1.3 (n = 39)	27.8±3.8 (n = 10)	9.5±0.3 (n = 10)
Crack-initiation stress, σ_{ci} (MPa)	$\frac{1}{3}q_u + 1.5\sigma_3$	$0.35q_u + 1.9\sigma_3$	$0.32q_u + 2.8\sigma_3$
HB parameter σ_c (MPa)	210	199.1	210.7
HB parameter m_i	28.9	3.3	28.2
Specimen size (mm)	157.5×63	63.4×31.7×31.7	125×62.5
D(W)/d ratio	25	21	25

Note that, the first four macro-properties are expressed in the form of mean ± standard deviation (number of samples). In laboratory, n is the total number of samples undergone tests, while in simulations, n represents the number of realizations with different particle

packing arrangements.

3.2.2 Flat-joint constitutive model

Prior to FJM, bonded-particle models (BPMs), including the contact-bond model (CBM) and parallel-bond model (PBM), have been widely employed to study the mechanical behaviours of adhesiveless materials (i.e., soil) **(Cundall and Strack 1979)** and adhesive materials (i.e., rock) **(Potyondy and Cundall 2004)**. However, when either the CBM or PBM is used to simulate the hard rock, there exist three intrinsic problems **(Wu and Xu 2016)**: (a) low ratio of uniaxial compression strength to tensile strength, (b) low friction angle and (c) linear failure envelop. To overcome these problems, **Potyondy (2012)** first developed the FJM in 2012 and sanctioned the model for rock by using a typical hard rock (Äspö diorite). After that, FJM has successfully simulated various rocks, such as granite **(Castro-Filgueira et al. 2017; Vallejos et al. 2016)**, marble **(Cheng et al. 2015; Wu and Xu 2016)**, tuff **(Xu et al. 2016)**, limestone **(Chen 2017)**, sandstone **(Imani et al. 2017; Potyondy 2017)** and phyllite **(Xu et al. 2017)**.

Flat-joint contacts are installed between grains with a gap equal to or less than the installation gap (Figure 3.2a). That varies among different interaction grains, defined as the installation gap ratio (g_{ratio}) multiplying the smaller radius of the two connecting grains. It is noted that $0 \le g_{ratio} < R_{\min} / R_{\max}$ to prevent grains from being embedded in adjoining pairs **(Scholtès and Donzé 2013)**. The FJM describes the bond as a discretized interface between two notional surfaces (Figure 3.2b), each of which is attached to a rigid grain. The interface is divided into $N_r \times N_\alpha$ elements (N_r and N_α are the number of elements in radial and circumferential directions respectively), every of which is either bonded or unbonded (Figure 3.2c). The strength envelops of bonded and unbonded elements are illustrated in Figure 3.3. For a bonded element, it breaks either in tensile or shear mode when the exerted stress exceeds the corresponding tensile-strength ($\bar{\sigma}_b$) or shear strength ($\left|\tau^{(e)}\right| = \bar{c}_b - \sigma^{(e)} \tan(\bar{\phi}_b)$). Once the element is unbonded, it follows a slip envelop that only the shear stress ($\left|\tau^{(e)}\right| = -\mu\sigma^{(e)}$) can be sustained.

Each element bearing a force ($\mathbf{F}^{(e)}$) and moment ($\mathbf{M}^{(e)}$) at the element centroid (Figure 3.2b) obeys the force-displacement law **(Potyondy 2016)** to update the force, moment and bond state. Combined the contributions of all elements, the interface presents an emergent behaviour that evolves from the linear elastic and fully bonded state to a partially damaged state to the finally frictional state, when gapped contact and slit contact are not introduced in the model. The collective behavior of interacting mechanism in elements of bonded and unbonded states is similar to that in the disturbed state concept (DSC) model **(Desai 1976; Desai 2016)**. Both gapped ($\varphi_G \neq 0$) and slit contacts ($1\text{-}\varphi_G\text{-}\varphi_B \neq 0$) belong to the unbonded contact, which presents a frictional behaviour when notional surfaces being in contact. The element force can be regarded as the resultant of normal and shear forces, while the element moment is the resultant of twisting and bending moments, expressed by

$$\begin{cases} \mathbf{F}^{(e)} = -F_n^{(e)}\hat{\mathbf{n}}_\mathbf{c} + \mathbf{F}_\mathbf{s}^{(e)} \\ \mathbf{M}^{(e)} = M_t^{(e)}\hat{\mathbf{n}}_\mathbf{c} + \mathbf{M}_\mathbf{b}^{(e)} \end{cases} \tag{3.1}$$

where $F_n^{(e)} < 0$ represents compression and $M_t^{(e)}$ is assumed to be equal to zero for simplification. For FJM in three-dimension (FJM3D), this simplification is based on the assumption that the shear stress induced by relative twist rotation keeps constant in the whole element so that the induced twisting moment at the element centroid is zero. In fact, the shear stress changes linearly along the radial direction over the element and the equivalent twisting moment is not equal to zero. Furthermore, the normal stress arising from the relative deflection also varies along the radial direction in the element. Thus a similar inaccuracy also exists for the bending moment. However, these errors tend to vanish with the refinement of discretization. As a result, the number of elements of a contact has influence on the behaviour of FJM and even the mechanical behaviour of synthetic flat-jointed material **(Wang et al. 2017a)**.

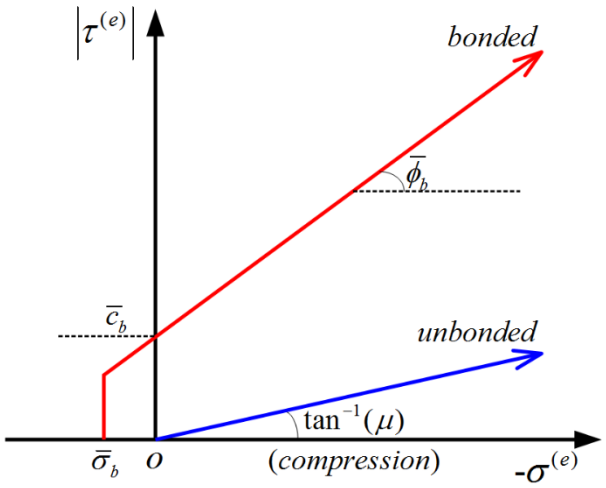

Figure 3.3 Failure and slip envelops of elements of FJM.

Table 3.2 The requirements of dimension and number of specimens in the current versions of ASTM and ISRM.

Type of test	ASTM	ISRM
Uniaxial compressive test	$\begin{cases} L/D = 2.0 \sim 2.5 \\ D \geq 47mm \\ D/d_{\max} \geq 10 \\ n \geq 5^{*} \end{cases}$ **(ASTM 2014)**	$\begin{cases} L/D = 2.0 \sim 3.0 \\ D \geq 50mm \\ D/d_{\max} \geq 20 \\ n \geq 5 \end{cases}$ **(Fairhurst and Hudson 1999)**
Brazilian test	$\begin{cases} L/D = 0.2 \sim 0.75 \\ D \geq 54mm \\ D/d_{\max} \geq 10 \\ n \geq 10 \end{cases}$ **(ASTM 2016)**	$\begin{cases} L/D = 0.5 \\ D \geq 54mm \\ n \geq 10 \end{cases}$ **(ISRM 1978)**

*ASTM does not give this number directly but suggests 5 is usually adopted. Parameters of L, D, $d_{\max}$ and n refer to the length, diameter of specimen, maximum grain diameter and required number of specimens, respectively.

3.2.3 Flat-jointed model of LdB granite

3.2.3.1 Calibration procedure

The calibration of microscopic parameters from macro-properties obtained in laboratory or in situ is regarded as a key process for PFC simulations. For simplicity and direct comparison, the uniform particle size distribution similar to other researchers **(Ding et al. 2014; Potyondy and Cundall 2004)** was adopted. For each group of micro-parameters, ten cylindrical FJM3D models of 62.5mm-diameter with different particle packing configurations by varying the seed of random-number generator are created, and the diameter of which is 25 times the average grain diameter and 20 times the maximum grain diameter. For uniaxial, confined compression and Brazilian test simulations, the length-diameter-ratios of the specimens were 2.0 and 0.5 respectively, following the suggestions (listed in Table 3.2) of the American Society for Testing and Materials (ASTM) **(2014; 2016)** and the International Society for Rock Mechanics (ISRM) **(Fairhurst and Hudson 1999; ISRM 1978)**. The number of ten realizations is also based on the requirements of ASTM and ISRM, and is used in the subsequent parametric study.

When uniaxial and confined compression test simulations are performed, the loading velocity, exerted by moving the upper and bottom platens towards each other, was always controlled at 0.125 m/s, which is in the range of 0.016-0.2 m/s adopted by many researchers **(Cho et al. 2007; Ding et al. 2014; Potyondy and Cundall 2004)**. They have confirmed that this velocity range is slow enough to ensure the specimen in a quasi-static state throughout the test. For the Brazilian test simulations, the loading velocity of 0.0075 m/s is chosen for all the specimens, and the loading platen width is kept at one average grain diameter (2.5 mm), as suggested by **Xu et al. (2016)**.

Based on previous parametric studies **(Castro-Filgueira et al. 2017; Wu and Xu 2016)** on FJM micro-parameters, it is found that local tensile-strength ($\bar{\sigma}_b$) is proportional to the macroscopic tensile strength, and local friction angle ($\bar{\phi}_b$) depends linearly on the macroscopic friction angle or Hoek-Brown (*HB*) strength parameter m_i. Referring to the calibration procedures defined by **Itasca (2014)** and **Wu and Xu (2016)**, a different calibration process was employed as summarised in the flowchart (Figure 3.4a) and

described in the following steps:

Step 1: Choice of installation gap ratio (g_{ratio}) and number of elements ($N_r \times N_\alpha$) aiming to achieve a reasonable coordination number (CN) and calculation efficiency. As a first approximation, the bond cohesion, $\bar{c}_b$, and tensile-strength, $\bar{\sigma}_b$, were taken to be equal to the laboratory properties of UCS and BTS respectively. Meanwhile, other unknown parameters were set to arbitrary values.

Step 2: Calibration on tensile strength: Brazilian test simulations were run on specimens with parameters obtained from step one, by adjusting $\bar{\sigma}_b$ to match the BTS.

Step 3: Calibration on UCS, Young's modulus, Poisson's ratio and post-peak response: uniaxial compression test simulations were carried out. The UCS of the model is correlated to $\bar{\sigma}_b$ and $\bar{c}_b$. The Young's modulus and Poisson's ratio of model were found to be correlated to the bond and particle moduli ($\bar{E}_c$ and E_c), and the ratios of bond and particle normal to shear stiffness ($\bar{k}_n / \bar{k}_s$ and k_n / k_s), respectively. The residual strength of the model was also found to be interrelated to the bond and particle friction coefficients (μ and μ_p). These macro-properties were matched by iteratively adjusting the micro-parameters, except for the bond tensile-strength which had been calibrated in step 2.

Step 4: Calibration on the confined strength and macroscopic friction angle or *HB* strength parameter m_i: confined compression test simulations were performed on FJM models with previously calibrated micro-parameters. The two macroscopic behaviours were matched by adjusting the FJ bond friction angle ($\bar{\phi}_b$). If after 5 loops the calibration results were still not converging to the target values, the calibration needed to be redone from Step 1.

(a)

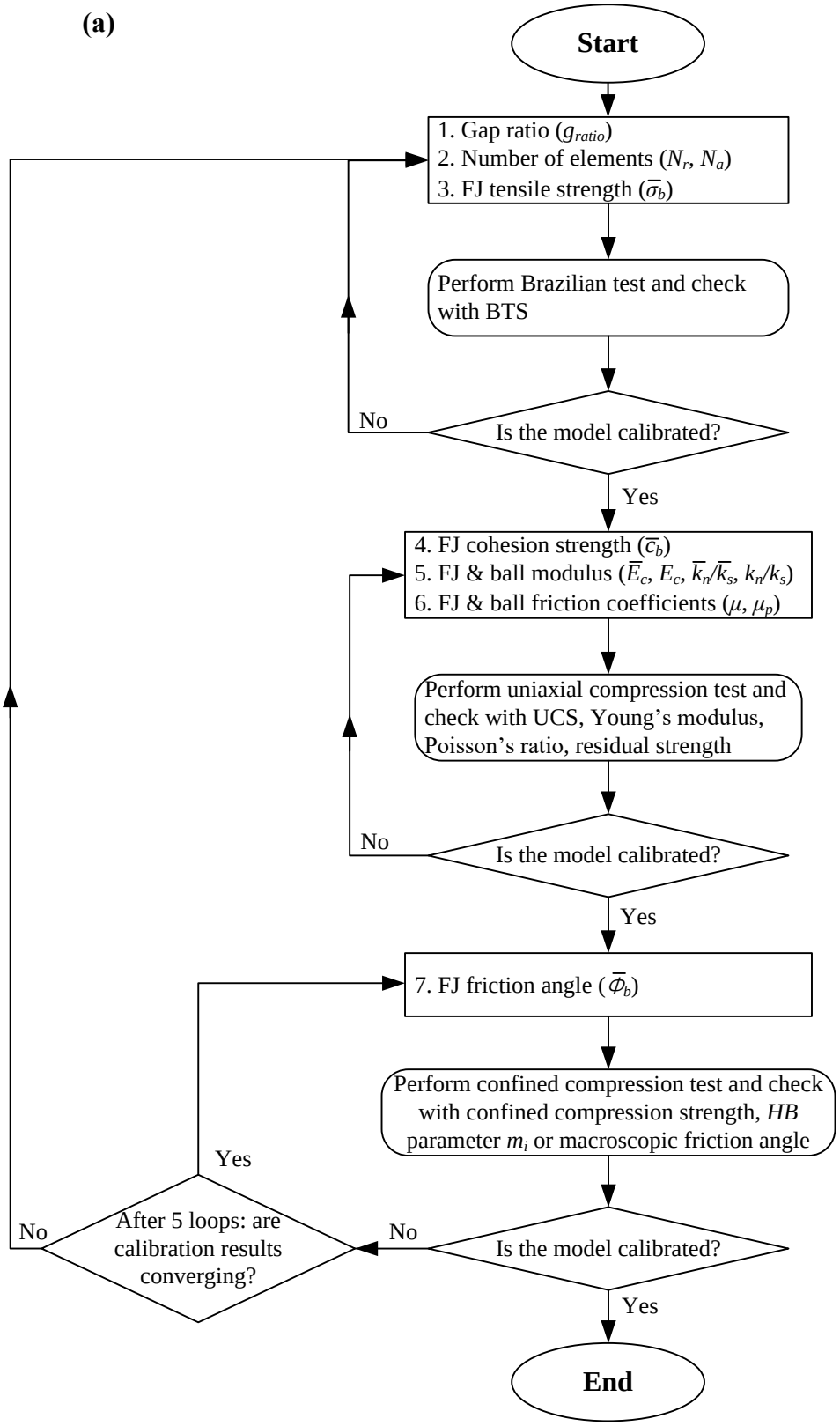
Start
1. Gap ratio (g_{ratio})
2. Number of elements (N_r, N_a)
3. FJ tensile strength ($\overline{\sigma}_b$)
Perform Brazilian test and check with BTS
No
Is the model calibrated?
Yes
4. FJ cohesion strength ($\overline{c}_b$)
5. FJ & ball modulus ($\overline{E}_c$, E_c, $\overline{k}_n/\overline{k}_s$, k_n/k_s)
6. FJ & ball friction coefficients (μ, μ_p)
Perform uniaxial compression test and check with UCS, Young's modulus, Poisson's ratio, residual strength
No
Is the model calibrated?
Yes
7. FJ friction angle ($\overline{\Phi}_b$)
Perform confined compression test and check with confined compression strength, *HB* parameter m_i or macroscopic friction angle
Yes
No
After 5 loops: are calibration results converging?
No
Is the model calibrated?
Yes
End

(b)

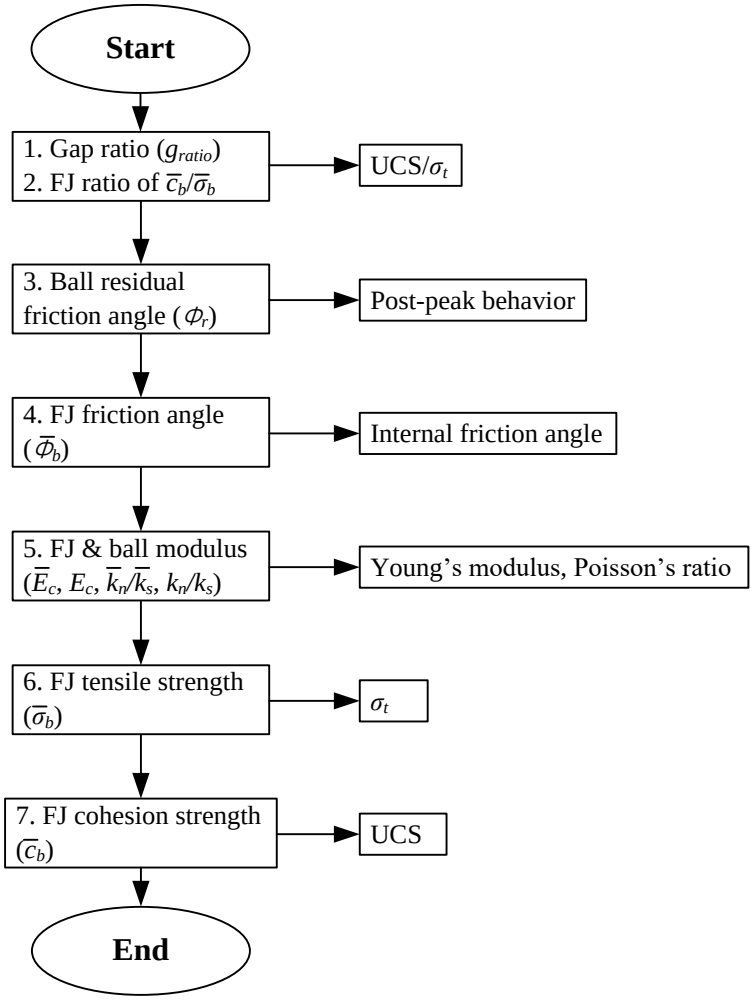

Figure 3.4 Flowcharts of calibration process for flat-jointed models (FJ represents the flat-joint bond): (a) proposed in this study; (b) defined by **Wu and Xu (2016)**.

Since the calibration procedure defined by **Itasca (2014)** only considers three macro-properties (UCS, Young's modulus and Poisson's ratio), it cannot accurately reproduce the mechanical behaviours of rocks. In addition, compared with the calibration methodology provided by **Wu and Xu (2016)**, as shown in Figure 3.4, the proposed calibration process makes improvements in: (1) increasing the calibration efficiency by taking advantage of the correspondences between the bond tensile-strength and the macroscopic tensile strength, and between the bond friction angle and the macroscopic friction angle or Hoek-Brown (*HB*) strength parameter m_i, (2) reducing the number of simulations by grouping together the microscopic parameters which can be calibrated in the same test, (3) enhancing the feasibility of calibration method by performing

simulations in a more logic order.

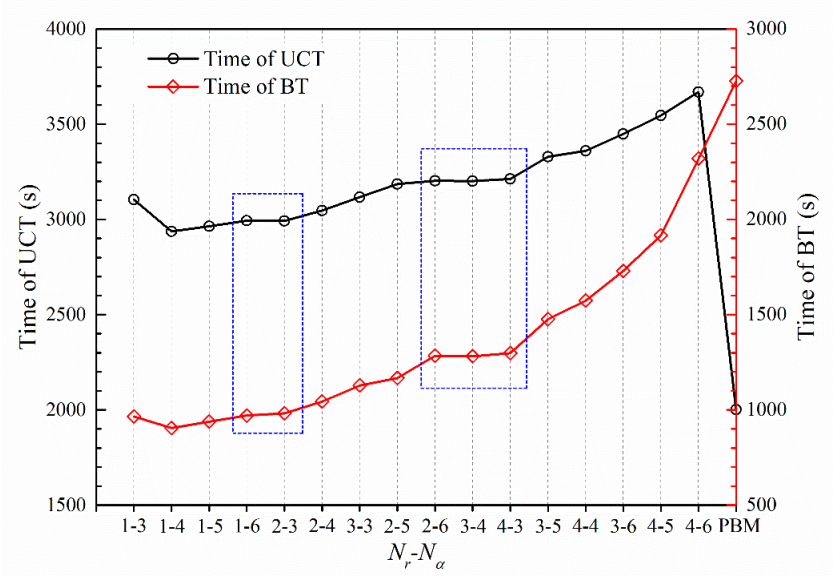

Figure 3.5 Calculation time for FJM models with different numbers of elements and PBM models measured by conducting UCT and BT simulations on the 62.5mm-diameter specimens. The total number of elements of a contact is identical, enclosed by the blue dashed line.

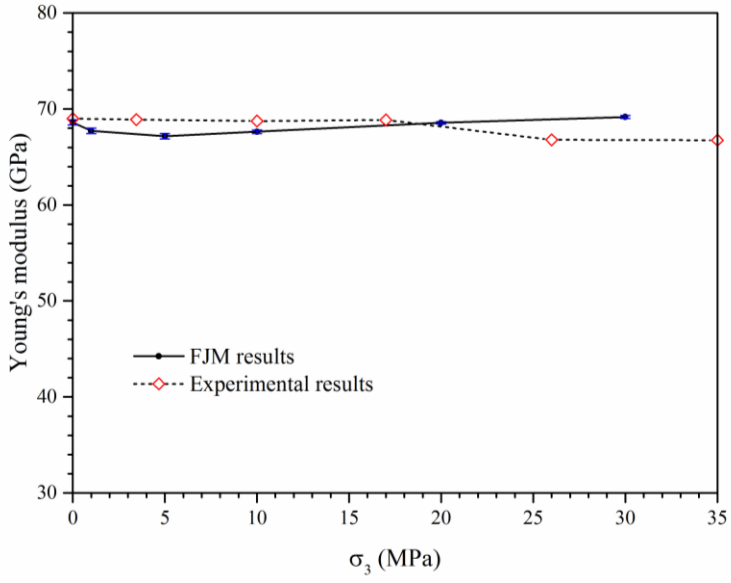

Figure 3.6 Comparisons between the Young's modulus of FJM numerical simulation and laboratory test results. The error bar of FJM results is equal to one standard deviation.

It should be noted that the determination of the installation gap ratio considers two factors: CN and $R_{\min} / R_{\max}$. The g_{ratio} of 0.15 results in an average CN of the model equal to 7.8, among the range of 6-10 found in the dense states of homogeneous, two-mixed and multi-mixed assemblies **(Oda 1977)**. In this work, the minimum ratio of $R_{\min}$ to $R_{\max}$ is 1:6, thus g_{ratio} of 0.15 was adopted lastly. In order to determine the number of elements, the calculation time for FJM models with different N_r (1, 2, 3, 4) and N_α (3, 4, 5, 6) was measured through conducting uniaxial compression test (UCT) and Brazilian test (BT) simulations one by one on a desktop computer with 3.5GHz quad-core i7-4770K CPU. As a reference, the calculation time for PBM models with the same model size, particle size distribution and UCS was also measured under the two kinds of simulations. All the calculation time was recorded from the initial start to the peak strength, the mean value of which based on 10 realizations is shown in Figure 3.5. The results show that the calculation efficiencies for both UCT and BT increase first and then decrease with increasing number of elements, reaching the best when $N_r \times N_\alpha$ equals to 1×4. Hence, this combination was adopted in our work. It is also found that the calculation efficiency nearly keeps unchanged if the total number of elements of a contact is identical. Compared with the PBM, the FJM requires longer calculation time for simulating the specimens with the same strength (e.g., UCS), which is consistent with the finding of **Vallejos et al. (2016)**. It is worth noting that the more calculation time of BT needed for PBM models results from the higher BTS (nearly twice) than that for FJM models. Moreover, since the intact rock is the research object, unbonded contacts (gapped and slit contacts) are not introduced by setting the bonded element fraction (φ_B) equal to 1.0.

3.2.3.2 Model genesis

There are two categories of sample preparation methods for DEM simulations: dynamic and constructive **(Bagi 2005; Schöpfer et al. 2009)**. The dynamic approach has been used extensively, which is the default method in PFC. The procedure of standard PFC model-genesis method is **Potyondy and Cundall (2004)**: (1) Particles of radii in a specified range are generated randomly within a vessel with frictionless walls. (2) System is adjusted by rearranging the particles until the equilibrium state under zero friction. (3) A

low isotropic stress within the particle assembly is achieved by reducing the radii of all particles iteratively and simultaneously. (4) The number of contacts of each particle reaches at least three by only modifying the positions and radii of particles with less than three contacts. (5) Contact bonds are installed between particles in near proximity which is defined by users. Although at beginning, the vessel porosity (default value is 35% in PFC3D) is fixed, the porosity of the populated model is still varying even if the same model size and particle size distribution are assigned. To eliminate this packing effect, the particle deletion method, one constructive method, is utilised in this study. Based on the specimens generated by the standard PFC procedure, the particle deletion method follows the process: (1) A random position within the vessel is chosen and the corresponding nearest particle is selected. (2) The selected particle and all its neighbors are checked whether they have been selected. If yes, go back to step one; if no, continue. (3) The volume of all selected particles is deducted to update the model porosity. If it does not attain the required porosity, go back; if it does, continue. (4) All selected particles are deleted and the new model is saved. As the deleted particles are selected randomly, the original particle size distribution is marginally affected **(Ding et al. 2014)**.

In this study, the specimens are generated by these two methods which are called the standard and the same-porosity FJM3D models, respectively.

3.2.3.3 Calibration results

Table 3.3 summarises the micro-parameters of FJM for simulating the LdB granite obtained through the calibration process. The coefficient of variation (CV), defined as the ratio between the standard deviation and the mean, for the FJ bond tensile-strength and cohesion is set to 0.23 to compare directly with the published numerical simulation results obtained using PBM **(Ding et al. 2014; Potyondy and Cundall 2004)**. Interestingly, owing to the special micro-structure of FJM, the post-peak response of the model was calibrated by assigning a relative low value (0.1) to the friction coefficients (μ and μ_p).

Table 3.3 Calibrated micro-parameters of the FJM for simulating LdB granite.

Micro-parameter	Definition	Value
ρ_v	Bulk density (kg/m^3)	2640
$d_{\min}$	Minimum particle diameter (mm)	1.88
$d_{\max} / d_{\min}$	Ratio of maximum to minimum particle diameter	1.66
g_{ratio}	Installation gap ratio	0.15
N_r	Number of elements in radial direction	1
N_α	Number of elements in circumferential direction	4
φ_B	Bonded element fraction	1.0
φ_G	Gapped element fraction	0
$\overline{E}_c$	Effective modulus of bond (GPa)	100
$\overline{k}_n / \overline{k}_s$	Ratio of bond normal to shear stiffness	2.7
$\overline{\sigma}_b$	Mean bond tensile-strength ± SD (MPa)	22 ± 5
$\overline{c}_b$	Mean bond cohesion strength ± SD (MPa)	215 ± 49
$\overline{\phi}_b$	Friction angle of bond (degrees)	55
μ	Friction coefficient of bond	0.1
E_c	Effective modulus of particle contact (GPa)	100
k_n / k_s	Ratio of particle normal to shear stiffness	2.7
μ_p	Friction coefficient of particle	0.1

All the calibrated macro-properties are listed in the fourth column of Table 3.1, relative errors of which except the crack-initiation stress fall within 3%. The Young's modulus of FJM specimens varies scarcely with the confining stress increasing, in line with the experimental results (Figure 3.6). Moreover, comparisons of the results with the laboratory tests, FJM and PBM numerical simulations were made as shown in Figure 3.7 and Table 3.1. Contrary to the low UCS/BTS (equal to 7.2) of PBM specimens, the UCS/BTS of the calibrated FJM specimens is very high (21.2), capturing the brittleness of the hard rock (21.5 in laboratory). In addition, unlike a linear failure envelop for PBM

specimens, the failure envelops for both FJM and experimental specimens are nonlinear. Furthermore, the *HB* failure criterion was used to fit the peak confined strengths of FJM and PBM specimens, compared with the failure envelope obtained by **Martin (1993)**. The *HB* failure criterion for intact rocks is given by

$$\sigma_1 = \sigma_3 + \sigma_c(m_i \frac{\sigma_3}{\sigma_c} + 1)^{0.5} \tag{3.2}$$

where σ_c and m_i are two parameters determined by statistical analysis **(Hoek and Brown 1997)**. It is found that the *HB* parameters m_i for FJM and experimental specimens are far larger than that for the PBM specimen. At this point, the FJM successfully solves the three intrinsic shortcomings of classical DEM as aforementioned. It is also noted that the curve-fitted *HB* failure envelops for FJM and experimental results underestimate the peak strength in the tension zone (Figure 3.7), which is in agreement with the conclusion of **Cai (2010)** that m_i in high confinement is about 1.5 times that in tension zone for brittle rocks (e.g., crystalline rocks).

The crack-initiation stress (CIS) is one characteristic material parameter **(Martin and Chandler 1994)**, often used as an estimated onset point of spalling around underground excavations **(Li et al. 2019; Nicksiar and Martin 2014)**. The variation of crack-initiation stress (the axial stress corresponding to about 5% of the number of cracks at the peak stress) with confining stress is presented in Figure 3.7, and it is well fitted by the linear relationship:

$$\sigma_{ci} = 0.32q_u + 2.8\sigma_3 \tag{3.3}$$

Although Eq. (3.3) differs slightly from the experimental result made by **Martin (1997)** ($\sigma_{ci} = \frac{1}{3}q_u + 1.5\sigma_3$), it however agrees with the experimental observations from various brittle rocks **(Brace et al. 1966; Pestman and Van Munster 1996)** with regard to damage initiation. Also, Eq. (3.3) is very similar to the numerical results obtained by Potyondy and Cundall ($\sigma_{ci} = 0.35q_u + 1.9\sigma_3$) using PBM **(Potyondy and Cundall 2004)**, and by Scholtès and Donzé ($\sigma_{ci} = 0.3q_u + 2.6\sigma_3$) using a novel DEM model **(Scholtès and**

Donzé 2013).

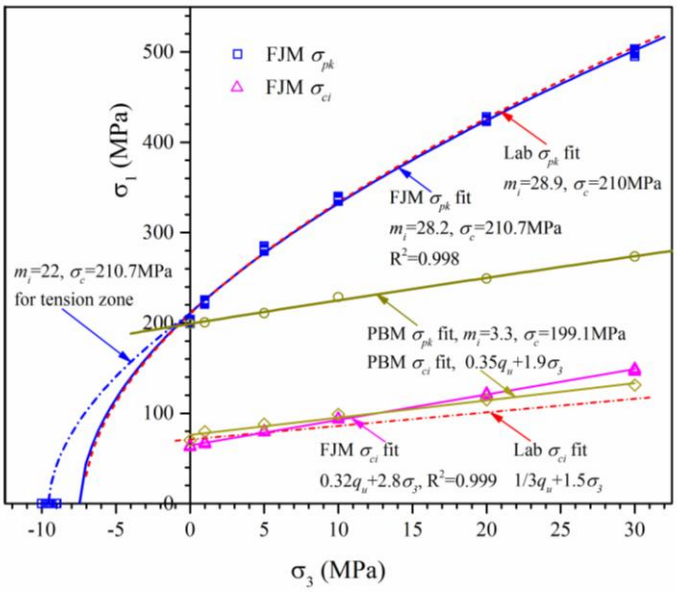

Figure 3.7 Comparisons among unconfined, confined peak and crack-initiation strengths and Brazilian tensile strengths obtained from FJM and PBM **(Potyondy and Cundall 2004)** numerical simulation and laboratory **(Martin 1993)** tests. The fitted *HB* failure envelop curves and crack-initiation stress lines are plotted.

In summary, the calibrated FJM specimen as developed well captures the mechanical behaviours of LdB granite. However, there are still some limitations existing in the FJM: (1) it requires longer simulation time than the PBM; and (2) the predicted CIS is overestimated with increasing confining stress. The calculation time required is associated with the number of constitutive contacts in the synthetic models. When the model size, particle size distribution and installation gap are the same, the number of contacts in the FJM models is $N_r \times N_\alpha$ times of that in the PBM models.

3.2.4 Parametric study

Based on the calibrated micro-parameters, the cylindrical FJM3D models with different model sizes and particle size distributions were created to investigate their influences on macro-mechanical properties by conducting uniaxial compression and Brazilian tests. The schematic view of generation procedure of the models is shown in Figure 3.8. Seven

model sizes and four particle size distributions were adopted, and for each case ten realizations were generated. It is worth noting that the length-diameter-ratios of these models for uniaxial compression and Brazilian tests are 2.0 and 0.5 respectively. Therefore, there are totally 280 models used for either UCT or BT. The loading fashions and loading velocities for the two tests have been given in detail in section 3.2.3.2.

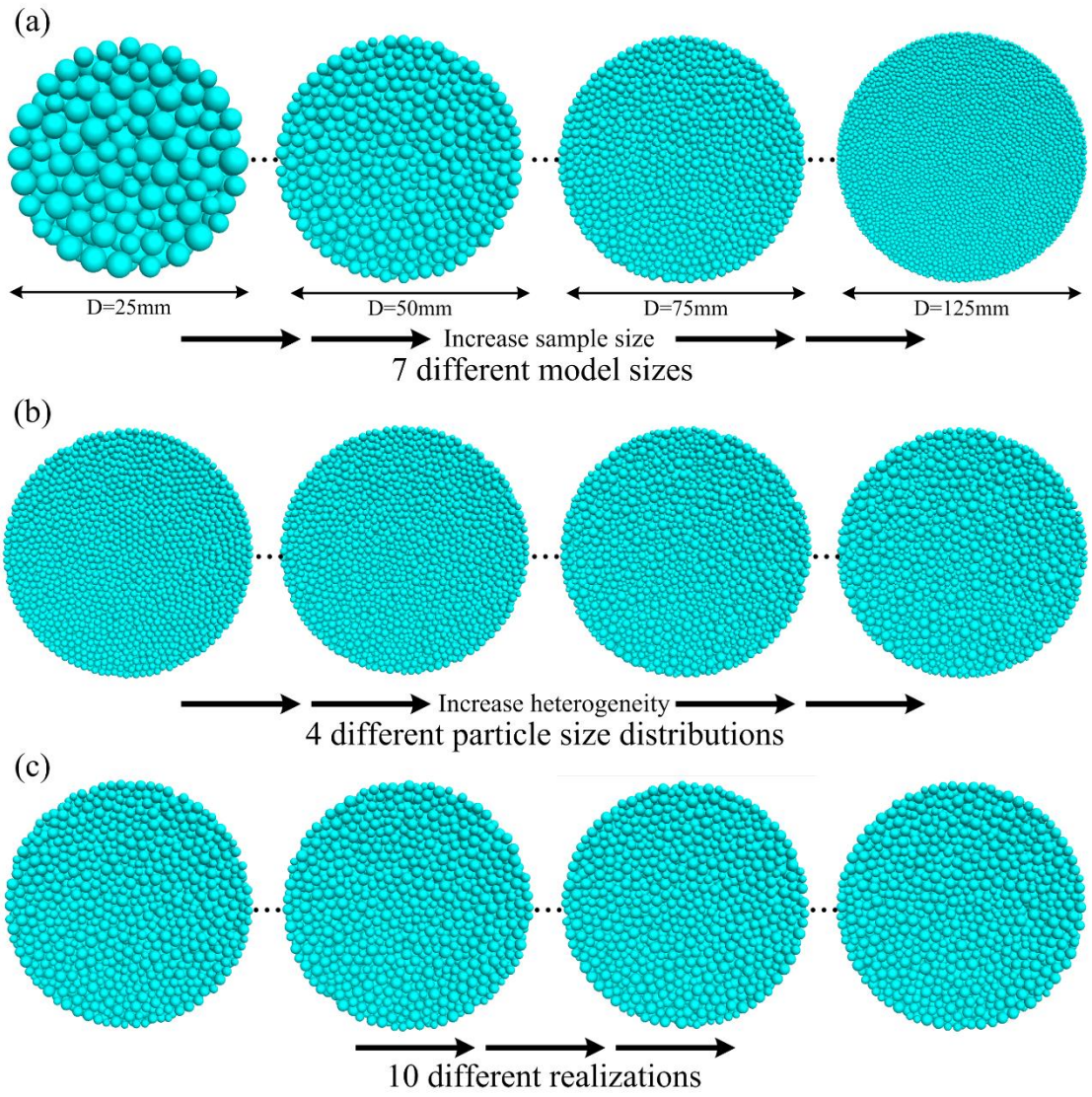

Figure 3.8 The schematic view of generation procedure of FJM3D models used in this study. The particles were randomly generated in (a) a cylinder domain of length-diameter-ratio of 2.0 or 0.5 with diameter varying from 25 to 125 mm; (b) four different particle size distributions; (c) 10 realizations for each model by varying the seed of random-number generator, and a total of 280 models were created.

Table 3.4 shows the specific parameters of model size and particle size distribution used for the analysis. The four particle size distributions, following the uniform distribution, are labelled as Case I, II, III and IV, corresponding to d_{max}/d_{min} of 1, 1.66, 3 and 6 respectively. To ensure the average particle diameter of the assembly roughly identical (~ 2.5 mm), the minimum particle diameters (d_{min}) for Case I, II, III and IV are 2.5, 1.88, 1.25 and 0.72 mm respectively. Meanwhile, the model diameters (D) cover a range of 25, 37.5, 50, 62.5, 75, 87.5, 125 mm, corresponding to D/d of 10, 15, 20, 25, 30, 35 and 50 respectively.

Table 3.4 Properties for model size and particle size distribution.

Property and description	Case I	Case II	Case III	Case IV
Particle size ratio: d_{max}/d_{min}	1	1.66	3	6
Average particle diameter: d (mm)	2.5	2.5	2.5	2.5
Minimum particle diameter: d_{min} (mm)	2.5	1.88	1.25	0.72
Particle size distribution type	Uniform			
Model diameter: D (mm)	25 37.5	50 62.5	75 87.5	125

3.3 Simulation Results

3.3.1 The standard FJM3D model

In this section, the simulation results obtained from the standard FJM3D models under UCT and BT are given.

3.3.1.1 Effect of model size

Figure 3.9 shows the simulation results of UCS, Young's modulus, Poisson's ratio and BTS for Case II from 10 realizations. The calculated values scatter widely when the mode size is small (e.g. D/d = 10), and then concentrates with increasing model size (D/d). Although the particle size distributions are different, the effects of the model size on the simulation results of Cases I-IV are similar. Figures similar to Figure 3.9 can also be plotted for Cases I, III and IV, but are not given for avoiding repetitions.

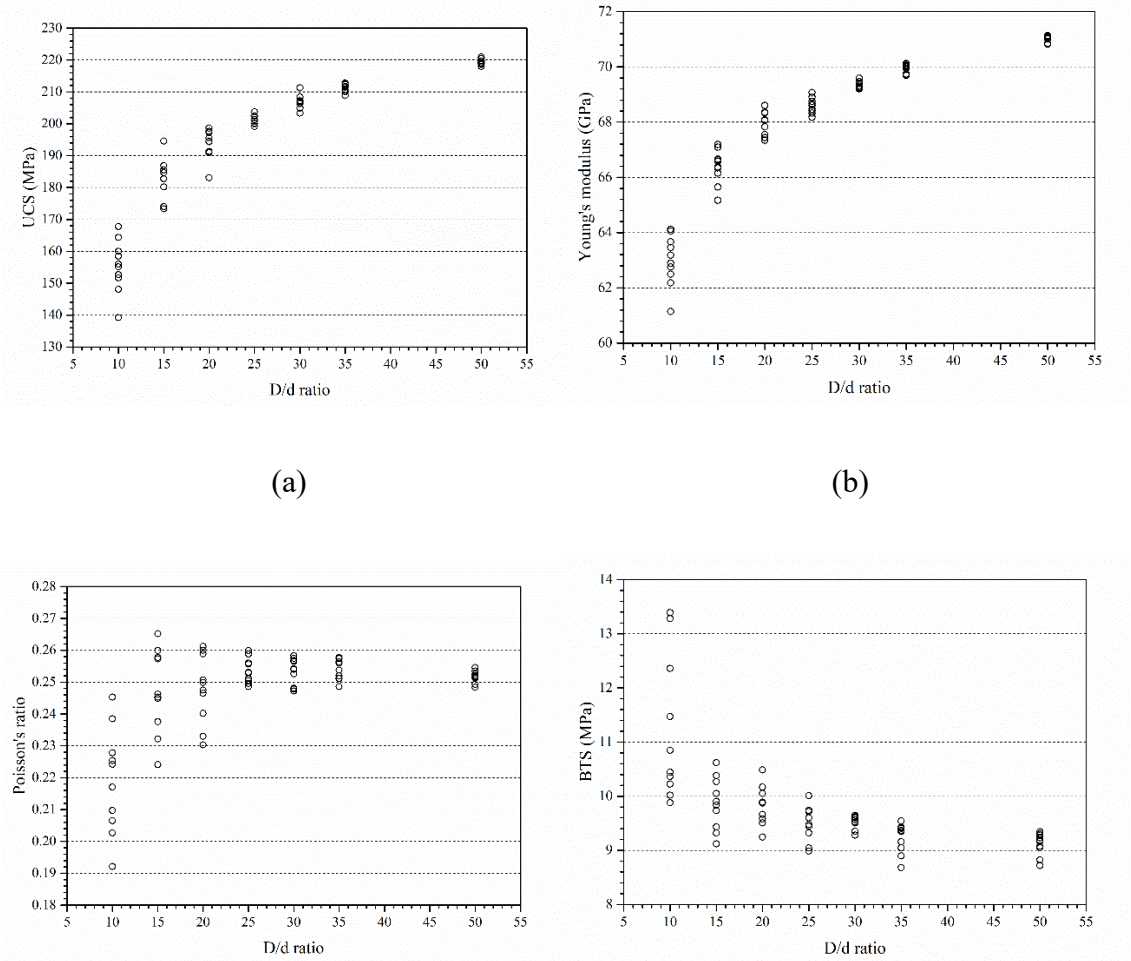

Figure 3.9 Results of the simulated macro-mechanical properties for Case II obtained from 10 realizations. (a) UCS, (b) Young's modulus, (c) Poisson's ratio and (d) BTS.

Table 3.5 Model size (D/d_{max}) determination on the basis of coefficient of variation.

Acceptable variation (%)	Case I	Case II	Case III	Case IV
10	15	12	10	9
5	20	16	17	15
3	30	24	20	18

The mean values and coefficients of variation (CV) of these four macro-properties are presented in Figures 3.10 and 3.11 to analyze the variation trends and levels with the model size. Unless otherwise stated, the data in the following figures represented the

mean values. As the sample size increases, UCS and Young's modulus grow rapidly first and then gradually, increasing by around 40% and 13% respectively. Poisson's ratio only increases in small size models (from D/d = 10 to D/d = 15) and then fluctuates at a certain value. Contrary to UCS and Young's modulus, BTS reduces by approximately 20% with a decreasing rate when the model size increases.

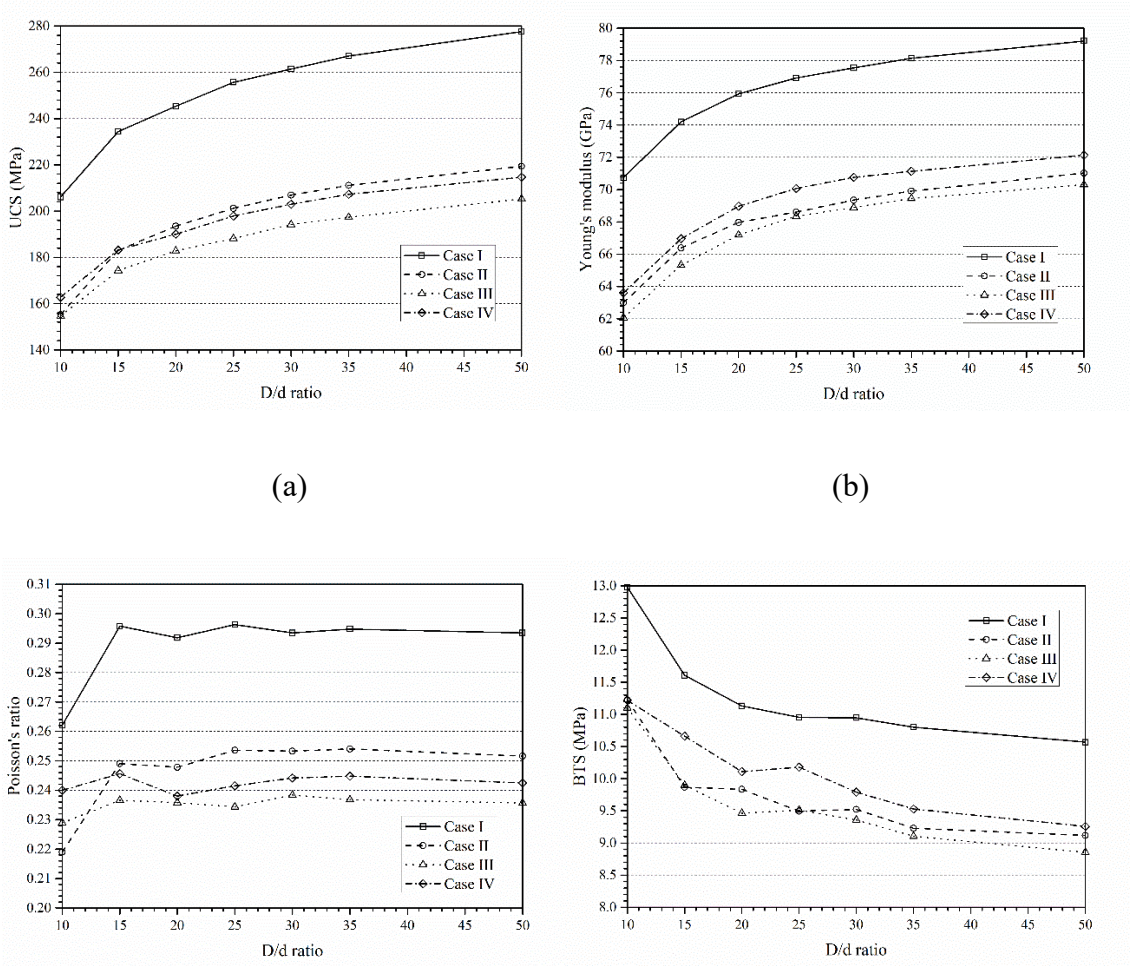

Figure 3.10 Effect of the model size on (a) UCS, (b) Young's modulus, (c) Poisson's ratio and (d) BTS for the standard FJM3D model.

Referring to Figure 3.11, CVs of the macro-properties are functions of the model size with four different particle size distributions, decreasing with increasing model size. The CV of BTS is the largest because the minimum dimension of the specimen for BT

simulations is the length (thickness), rather than the diameter as that for the UCT simulations. For rock engineering applications, a zero CV cannot be achieved, instead a small acceptable variation should be chosen to limit the uncertainties of the results. Table 3.5 shows the model sizes determined by three acceptable variations of 10%, 5% and 3% for the four cases. A 5% acceptable variation is usually adequate in practice, and that corresponds to D/d of 20, 20, 25 and 25 and $D/d_{\max}$ of 20, 16, 16.7 and 14.6 for Cases I-IV respectively.

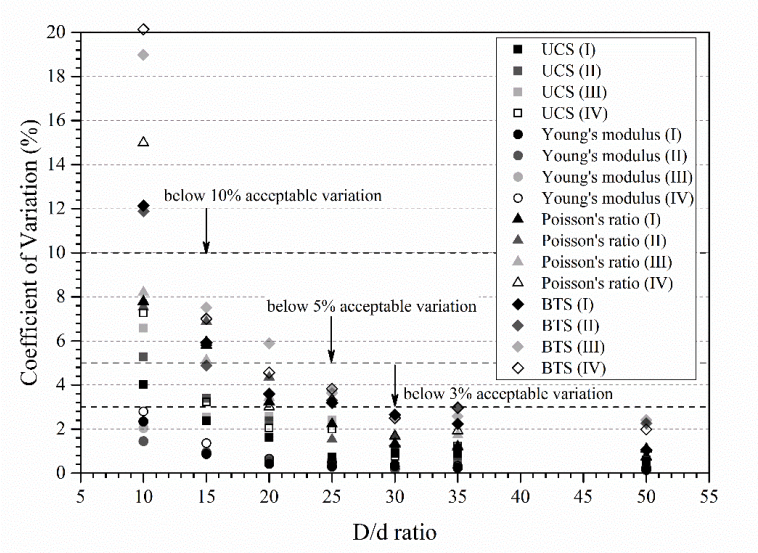

Figure 3.11 Effect of the model size on the coefficients of variation of UCS, Young's modulus, Poisson's ratio and BTS for the standard FJM3D model.

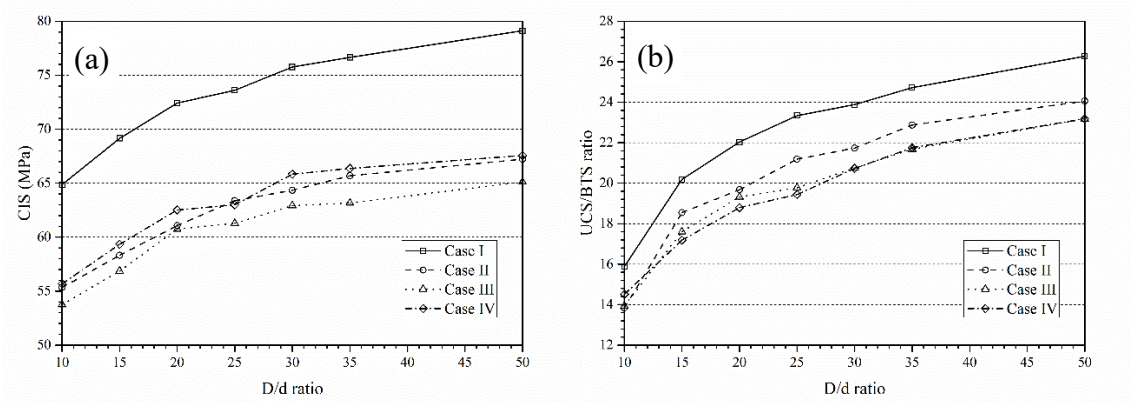

Figure 3.12 Effect of the model size on (a) CIS and (b) UCS/BTS ratio for the standard FJM3D model.

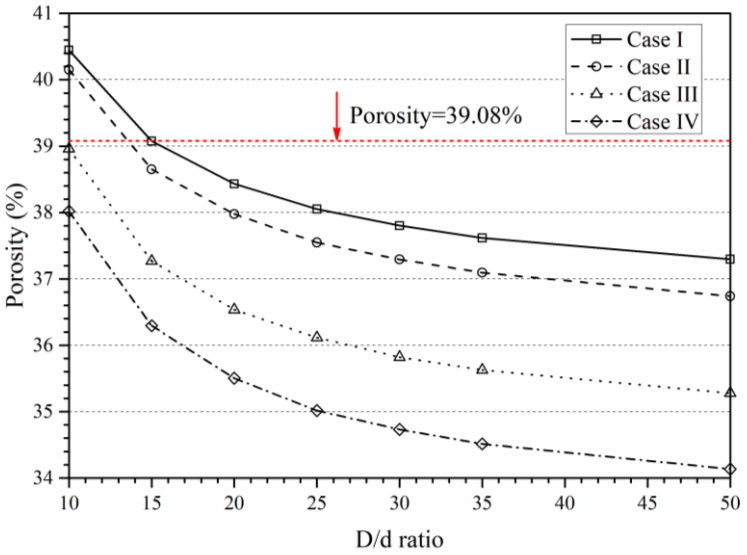

Figure 3.13 Effect of the model size on the porosity of the standard FJM3D models.

The mean values of CIS and UCS/BTS ratio are also functions of the model size shown in Figure 3.12. The CIS keeps increasing, by average 21.5% for the four cases, as the model size increases. Since the variation trend of UCS is opposite to that of BTS, the increase of UCS/BTS ratio is far greater than the rate of change of any of them, and is exceeding 60%. However, the variations of all these macro-properties are attributed to not only the model size change, but also the porosity variation with model size as illustrated in Figure 3.13. It is noted that the model porosity is usually larger than that of the real rocks, which are typically comprised of non-spherical grains packed more tightly than spheres **(Schöpfer et al. 2009)**. Besides, the contact bond analogous to cement in real rocks is not considered in the porosity calculation.

3.3.1.2 Effect of particle size distribution

Figure 3.14 presents the effect of particle size distribution (PSD) on UCS, Young's modulus, Poisson's ratio and BTS. All of them decrease first, reaching the lowest point at d_{max}/d_{min} equal to 3, and then increase slightly with the particle size heterogeneity (d_{max}/d_{min}). The results are some different from the others' research **(Liu et al. 2018; Peng et al. 2017b)** that strengths of specimens keep decreasing as the particle size heterogeneity increases. It is because the difference in the porosity of specimens plays a

role in the particle size effect, as indicated in Figure 3.13.

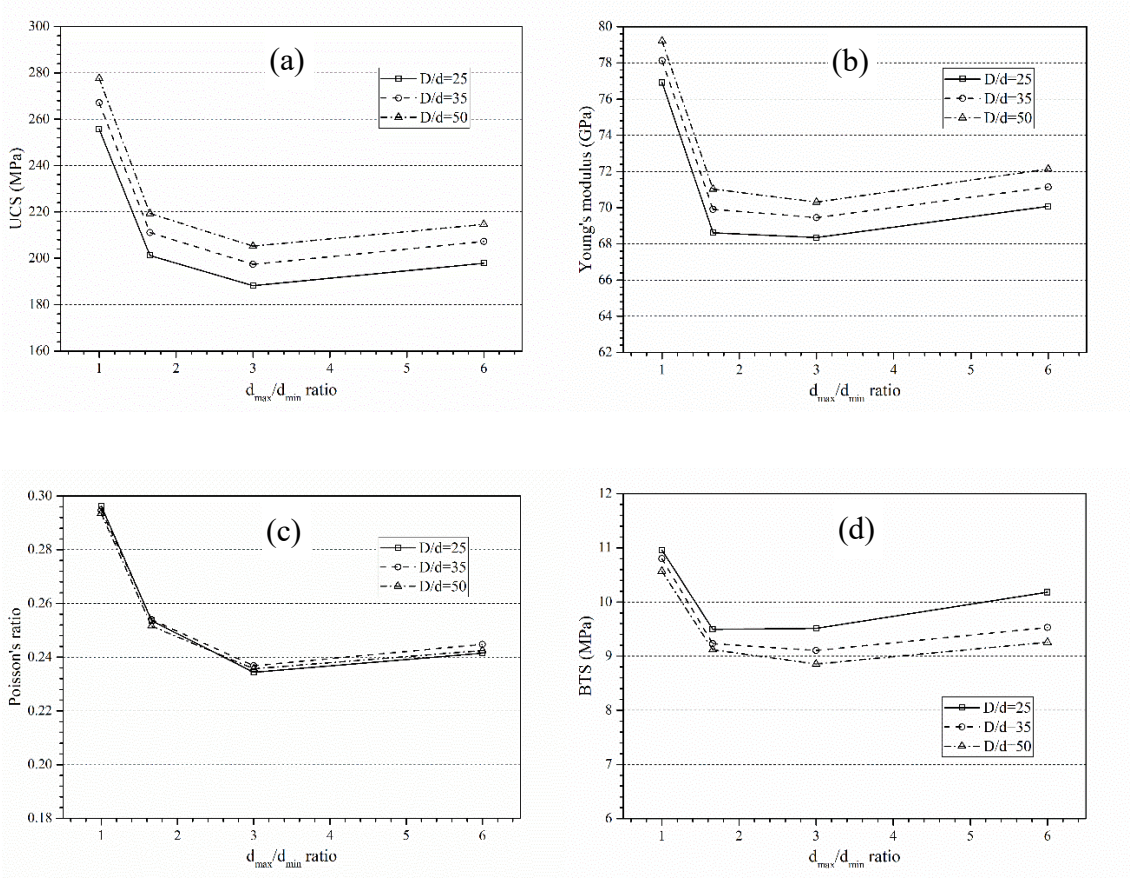

Figure 3.14 Effect of PSD on (a) UCS, (b) Young's modulus, (c) Poisson's ratio and (d) BTS for the standard FJM3D model.

3.3.2 The same-porosity FJM3D model

As pointed out in Section 3.3.1, the model porosity plays a pivotal influence on the effects of the model size and particle size distribution. To capture their true effects on simulation results, the porosity of all specimens with different model sizes and PSDs is controlled at a same value using the described deletion method. In our study, the model porosity for Case II at D/d=15 is chosen to be the target porosity (39.08%), as shown in Figure 3.13. In the section, the simulation results for the same-porosity FJM3D models under UCT and BT are presented, and meanwhile compared with results for the standard FJM3D models.

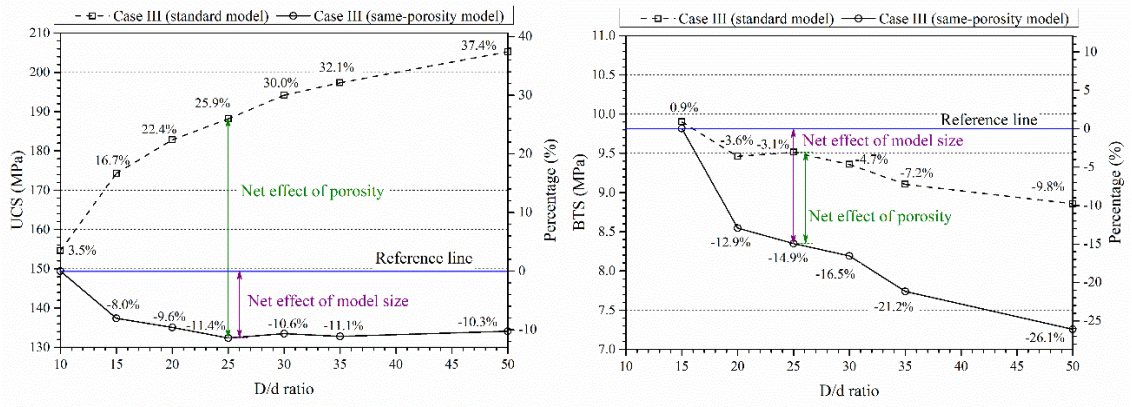

(a) (b)

Figure 3.15 Comparisons of (a) UCS and (b) BTS for Case III between based on the standard and same-porosity FJM3D models. The percentages in the figure are calculated based on the reference line, and signs "+" and "-" represent increase and decrease respectively.

3.3.2.1 Net effect of model size

For each model size and PSD, the simulated values of the macro-properties, including UCS, Young's modulus, Poisson's ratio and BTS, are obtained from 10 realizations. The results (considering the limited space, are not presented here) imply the scatter and CV of simulated macro-properties follow the same patterns with those for the standard FJM3D models as shown in Figures 3.9 and 3.11.

Taking an example, UCS and BTS for Case III obtained from standard and same-porosity FJM3D models are compared in Figure 3.15. The calculated values of UCS for standard and same-porosity FJM3D models present two opposing variation trends. Compared to the reference line, the UCS of standard models increases by 33.9% while that of the same-porosity models decreases by around 10% with increasing model size. Although the calculated values of BTS for the two models show the same trend, the change rates of them are very different. These discrepancies arise from the difference of porosity between the two models, as demonstrated by the net effect of porosity in Figure 3.15. The net effect of the model size is also illustrated in Figure 3.15, which is regarded as the difference between the reference line and the line connecting results based on the same-porosity

models.

Thus, for one same particle size distribution, the variation of the macro-properties for standard models is the combined action of porosity (n) and model size (D/d). Because the net effect of the model size is negative, the relationship between porosity and UCS (BTS) is obtained through combining the corresponding magnitude of net effect of model size on UCS (BTS) of the standard FJM3D models, as shown in Figure 3.16. As the model porosity increases, both UCS and BTS decrease nearly linearly. It is in good agreement with the trends of simulation results using parallel-bond models in three-dimension (PBM3D) provided by **Schöpfer et al. (2009)** and **Ding et al. (2014)**.

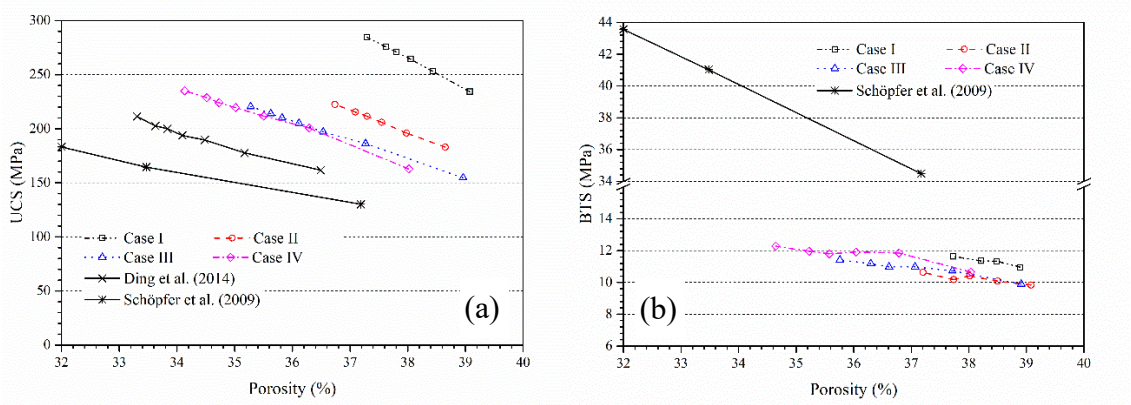

Figure 3.16 Plots of (a) UCS and (b) BTS vs. porosity. The simulation results using PBM3D by **Schöpfer et al. (2009)** and **Ding et al. (2014)** are also plotted to compare.

The variations of the calculated values of macroscopic properties (UCS, Young's modulus, Poisson's ratio and BTS) with model size are given in Figure 3.17. The UCS, Young's modulus, and Poisson's ratio slightly decrease until the model size increases to 50mm (D/d = 20), afterwards they keep nearly unchanged. Meanwhile, BTS reduces as the model size increases. Moreover, Figure 3.18 shows the size effect on CIS and UCS/BTS ratio. It is found that CIS only decreases slightly in small size specimens ($D \leq 50mm$) and then remains nearly constant with increasing model size. But the model size has an evident positive effect on the UCS/BTS ratio, which is mainly attributed to the sharp reduction of BTS.

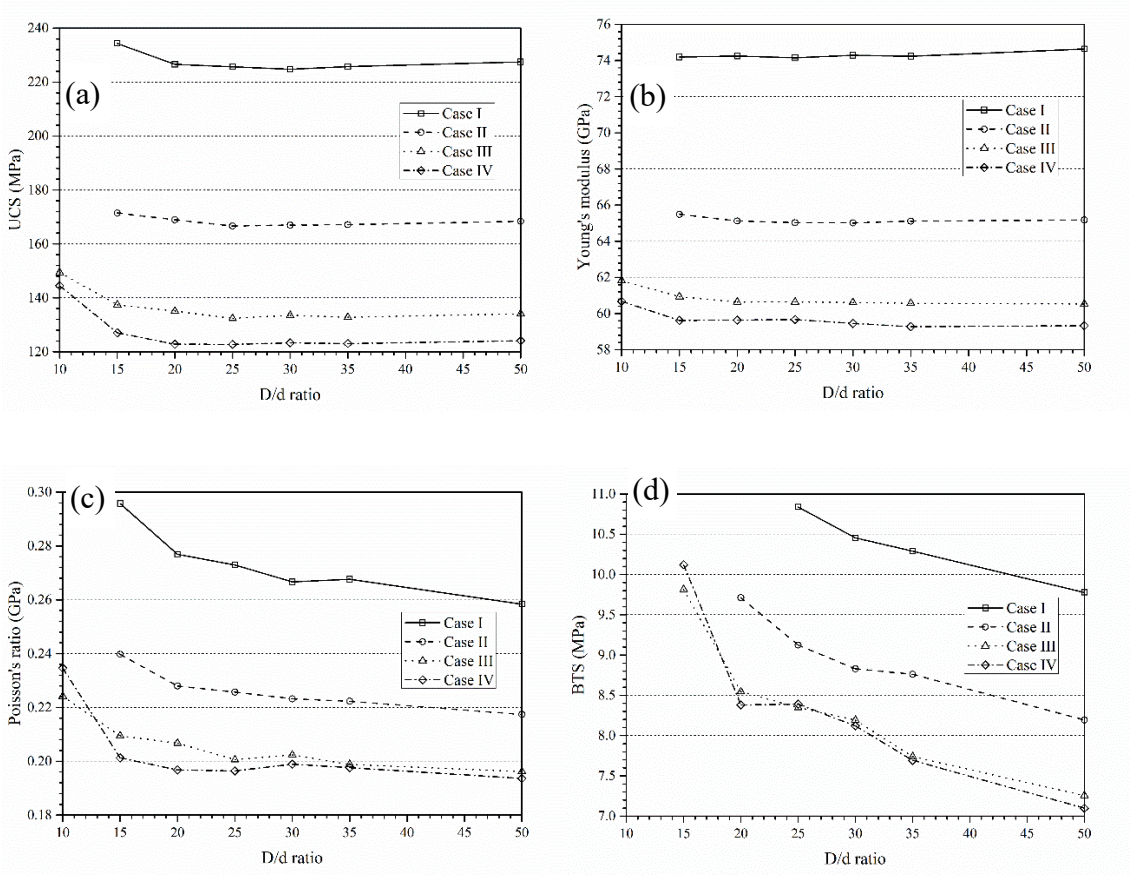

Figure 3.17 Effect of the model size on (a) UCS, (b) Young's modulus, (c) Poisson's ratio and (d) BTS obtained from the same-porosity FJM3D model simulations.

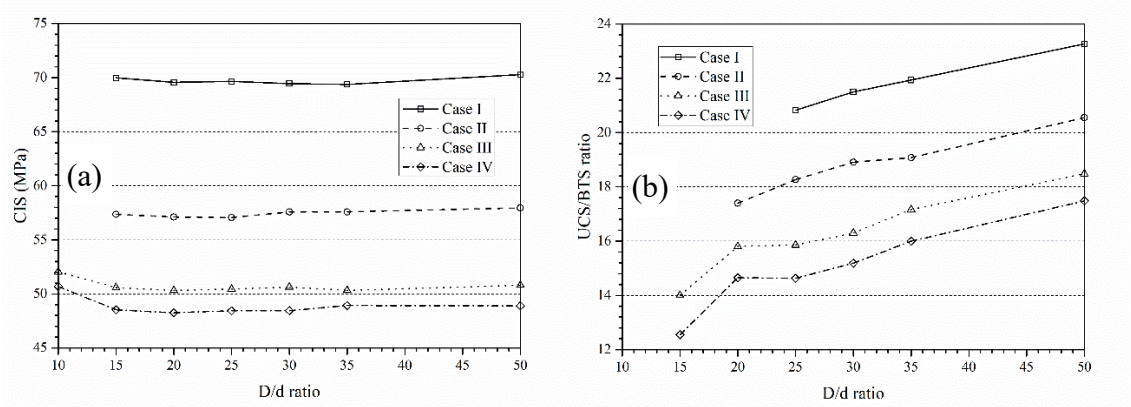

Figure 3.18 Effect of the model size on: (a) CIS, (b) UCS/BTS ratio for the same-porosity FJM3D model.

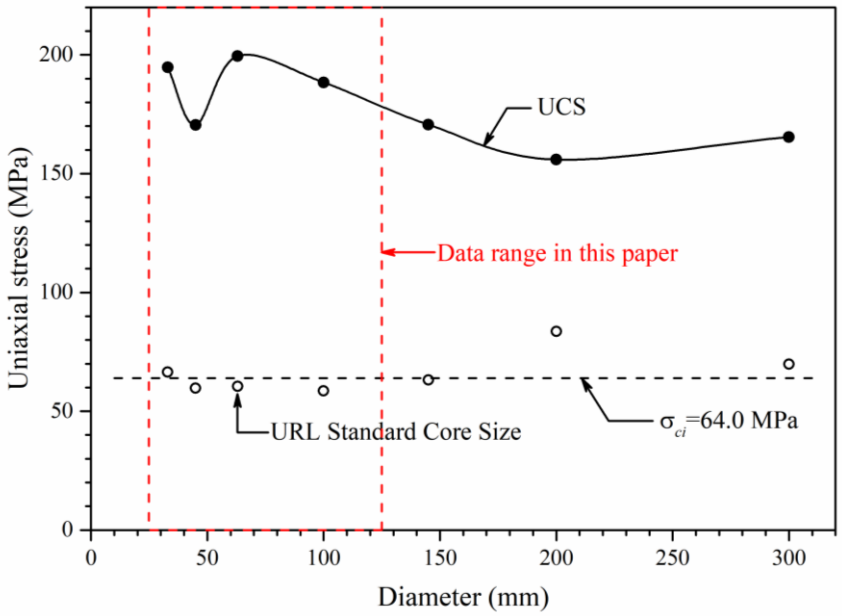

Figure 3.19 Effect of the sample size on UCS and CIS from URL for LdB granite (the red dashed lines enclose the data range in this paper, 25-125mm) **(Martin 1993)**.

Additionally, compared with the experimental results **(Martin 1993)** from URL depicted in Figure 3.19, the trends of CIS for same-porosity models and LdB granite specimens follow a similar pattern in the data range of this study (25-125mm), decreasing slightly and then reaching a minimum value. In the data range, UCS fluctuates with no evident trend, which is in some sense close to the trend of UCS for same-porosity models.

3.3.2.2 Net effect of particle size distribution

Having eliminated the effect of porosity, the pure influence of the particle size distribution on macro-properties is investigated, as plotted in Figure 3.20. Interestingly, the variations of UCS, Young's modulus, Poisson's ratio and BTS are the same, decreasing first dramatically and then gradually with increasing grain size heterogeneity ($d_{\max}/d_{\min}$). Similarly, the particle size distribution also has a significant impact on CIS and UCS/BTS which reduce with increasing $d_{\max}/d_{\min}$, as given in Figure 3.21. Consequently, our results are also in line with the findings from **Peng et al. (2017b)** and **Liu et al. (2018)** that the strengths of intact rocks decrease as the grain size heterogeneity increases.

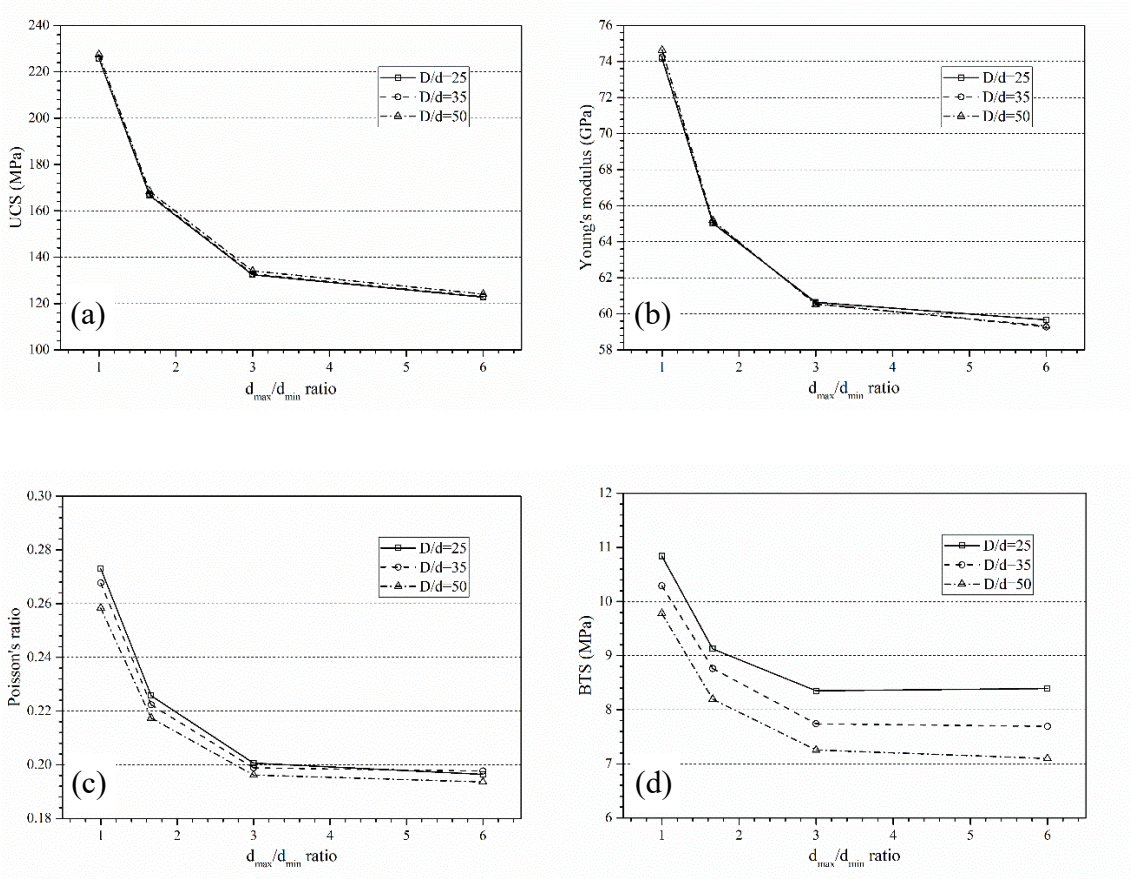

Figure 3.20 Effect of PSD on (a) UCS, (b) Young's modulus, (c) Poisson's ratio and (d) BTS for the same-porosity FJM3D model.

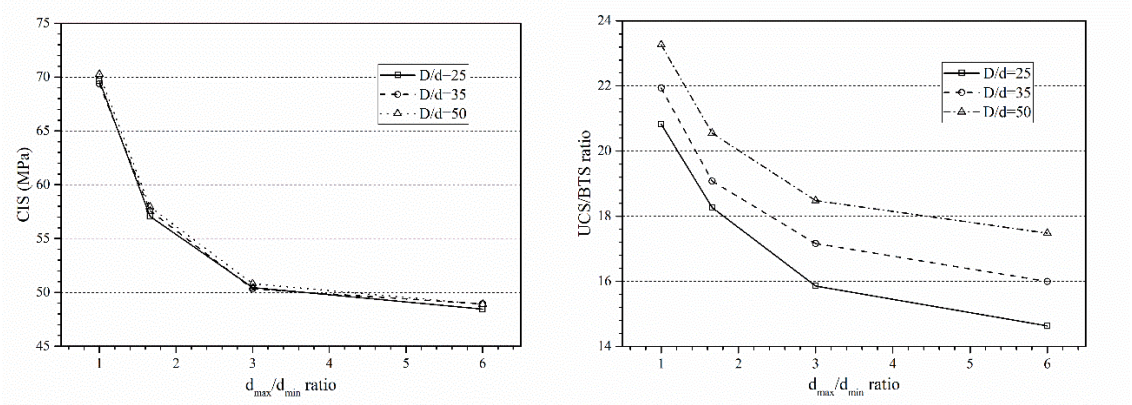

(a) (b)

Figure 3.21 Effect of PSD on (a) CIS and (b) UCS/BTS ratio the same-porosity FJM3D model.

3.3.3 Comparisons of simulation results using FJM3D and PBM3D

Figure 3.22 compares the variations of UCS, Young's modulus and Poisson's ratio with model size (D/d) for same-porosity FJM3D and PBM3D models **(Ding et al. 2014)** with $d_{max}/d_{min}=6$ (Case IV). As D/d increases, the Young's modulus and Poisson's ratio for the two kinds of specimens follow a similar pattern, decreasing first and then reaching a minimum. The variations of the UCS for FJM3D models also give such a trend, but that for PBM3D models is very different, for which the UCS increasing steadily with increasing model size. Since the effects of porosity and PSD are eliminated, the trend difference of UCS between FJM3D and PBM3D models can only be attributed to the difference of the adopted contact models.

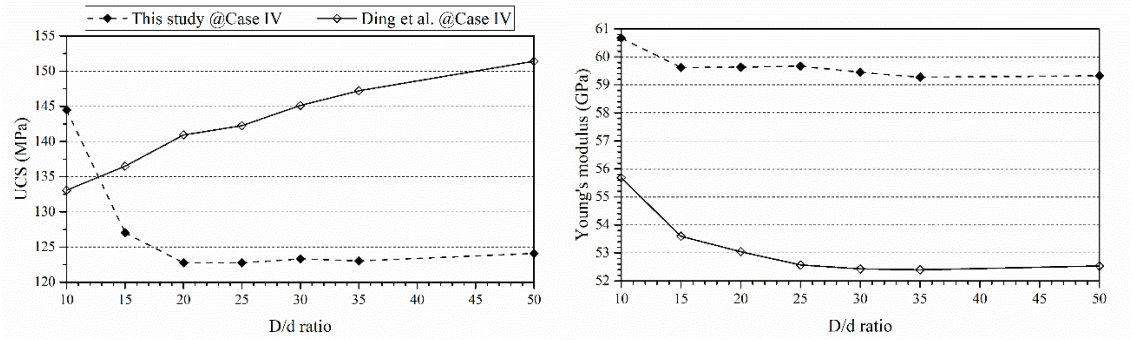

(a) (b)

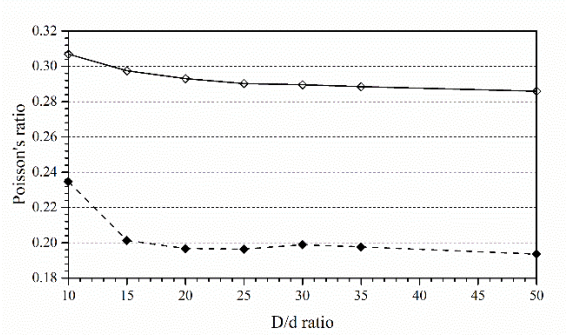

(c)

Figure 3.22 Comparison of the model size effect on (a) UCS, (b) Young's modulus and (c) Poisson's ratio for FJM3D and PBM3D models **(Ding et al. 2014)** with $d_{max}/d_{min}=6$.

Similarly, the effects of PSD on UCS, Young's modulus and Poisson's ratio for the FJM3D and PBM3D models are compared (considering the space, pictures are not provided here). The results indicate that the variations of UCS and Young's modulus except Poisson's ratio with grain size heterogeneity ($d_{\max} / d_{\min}$) are the same for the two models. The discrepancy of the Poisson's ratio is also due to the different contact models.

In addition, CVs of UCS, Young's modulus and Poisson's ratio for FJM3D and PBM3D models are compared and plotted in Figure 3.23. All of them decrease as a function of the model size. For each D/d, the CVs of UCS and Young's modulus for the two models are comparable, while CV of the Poisson's ratio for FJM3D models is far larger than that for the PBM3D models. This difference probably arises from the special microstructure of FJM which leads to the big variability of diametrical strain under uniaxial compression.

As a result, it is further confirmed that the contact constitutive model plays a role in the effects of model size and PSD.

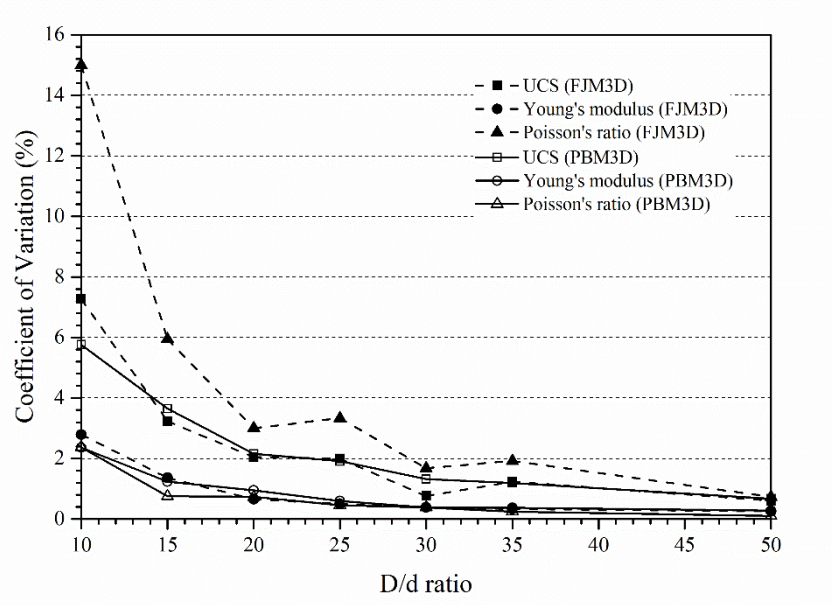

Figure 3.23 Comparison of the model size effect on CVs of UCS, Young's modulus and Poisson's ratio for FJM3D and PBM3D models **(Ding et al. 2014)** with $d_{\max} / d_{\min} = 6$.

3.4 Discussion

So far, there have been three major size-effect models put forward for brittle or quasi-brittle materials, such as rocks and concrete, based on statistics **(Weibull 1951)**, fracture energy **(Bažant 1984)** and multifractals **(Carpinteri et al. 1995)**. As a statistical model, the strength size-effect relation established by **(Hoek and Brown 1980)** is suitable for crystalline rocks rather than for sedimentary rocks **(Hawkins 1998)**, expressed by

$$\sigma_{cd} = \sigma_{c50}(\frac{50}{d})^{0.18} \tag{3.4}$$

where σ_{cd} and σ_{c50} are UCS of a sample with diameter of d and 50mm, respectively.

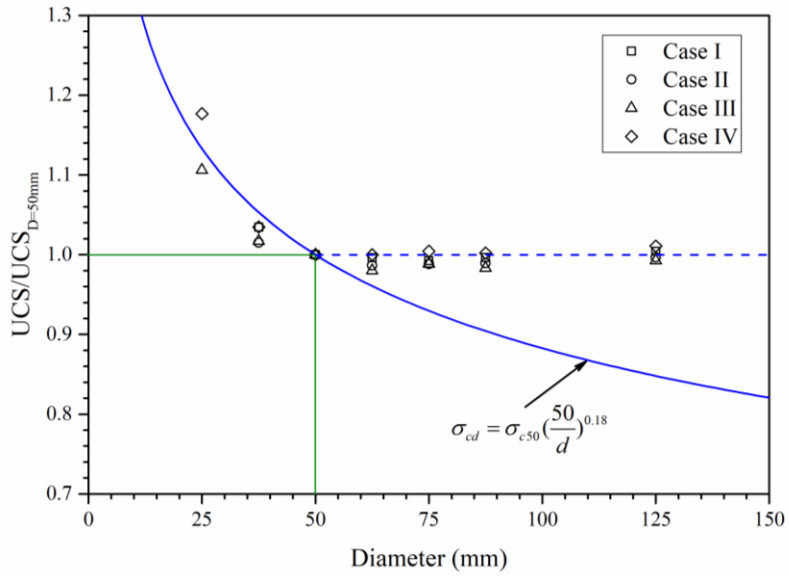

Figure 3.24 Size-effect on the mean UCS obtained from the same-porosity FJM3D models using Eq. (3.4).

This formula is used to fit the nondimensionalized UCS of same-porosity FJM3D models as shown in Figure 3.24. The results indicate that the size-effect relation well captures the variation of UCS when the sample diameter is less than or equal to 50mm, but it begins to underestimate UCS which remains nearly invariable with increasing diameter. Thus, it is suggested that considering the influence of the model size using FJM, the special

treatment, such as introduction of initial micro-fractures **(Zhang et al. 2011)** and discrete fracture network (DFN) **(Bahrani and Kaiser 2016; Esmaieli et al. 2010)**, is only needed if *D/d* of the specimen is above 20.

Bažant (1984) pointed out that the size effect in concrete and rock was induced by the blunting of the microcracking zone at the fracture front, and proposed a size-effect relation (SEL), Eq. (2.1). After that, on the basis of the topological concept of geometrical multifractality, the multifractal scaling relation (MFSL), Eq. (3.5), was put forward by **Carpinteri et al. (1995)**.

$$\sigma_N = f_c\sqrt{1+\frac{l_{ch}}{d}} \tag{3.5}$$

in which σ_N is the nominal strength (e.g. UCS, BTS and point-load strength); d is the sample diameter; f_t is a strength parameter; f_c and l_{ch} are constants that represent the strength of an infinitely large sample and an intrinsic material length, respectively.

The mean BTS indices for same-porosity FJM3D models are depicted in Figure 3.25. All the fitting constants are listed in Table 3.6, and are compared with those obtained from Gosford Sandstone **(Masoumi et al. 2018)**. According to the coefficient of multiple determination (R^2) values, both SEL and MFSL provide a good fit to the tensile strength data from the same-porosity FJM3D models. Therefore, in good agreement with experimental findings, the BTS indices obtained from same-porosity FJM3D models also follow the generalized size-effect trend where the strength decreases with increasing size. Additionally, as the grain size heterogeneity ($d_{\max}/d_{\min}$) increases, Bf_t (except for Case I) and l_{ch} ascend gradually, while $\lambda_0 d_{\max}$ and f_c keep descending. This result appears to be new to the authors' knowledge, as such variation rule has not been reported up to now, which should be supported by experiments in future.

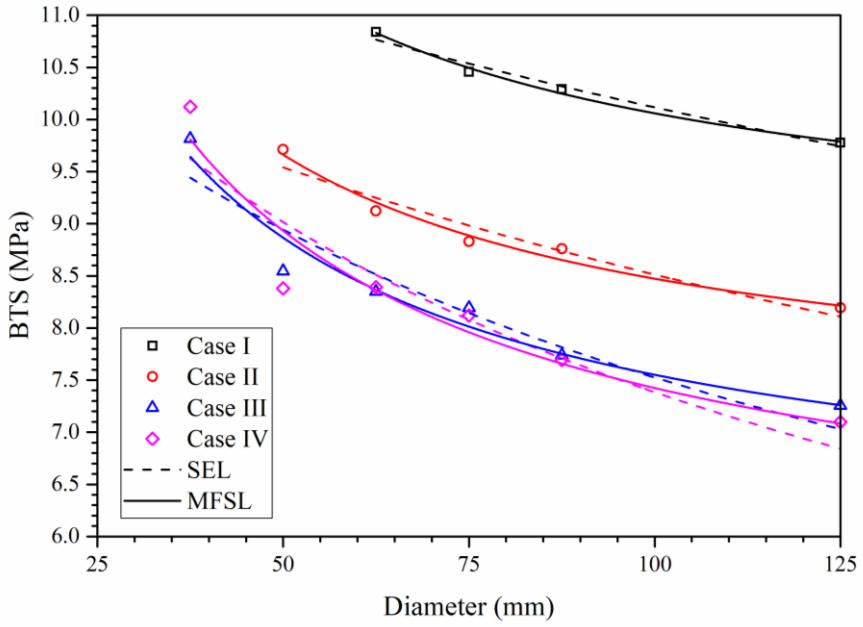

Figure 3.25 Comparisons of the size-effects on the mean BTS obtained from the same-porosity FJM3D models using Eqs. (2.1) and (3.5).

Table 3.6 List of fitting constants for SEL and MFSL obtained from BTS of same-porosity FJM3D models and Gosford Sandstone **(Masoumi et al. 2018)**.

Specimen	SEL			MFSL		
	Bf_t (MPa)	$\lambda_0 d_{\max}$ (mm)	R^2	f_c (MPa)	l_{ch} (mm)	R^2
Case I	12.19	221.12	0.98	8.62	36.15	0.99
Case II	11.06	145.07	0.94	7.09	42.96	0.98
Case III	11.66	71.32	0.90	5.95	60.90	0.96
Case IV	12.64	51.86	0.86	5.52	81.06	0.92
Gosford Sandstone	3.85	77.50	0.94	2.36	24.59	0.77

3.5 Summary

In this chapter, a new calibration process was put forward to calibrate the micro-parameters of FJM, and $N_r \times N_\alpha$ equal to 1×4 was suggested to be the combination for the best calculation efficiency. The calibrated FJM specimen well captures the mechanical behaviours of LdB granite by overcoming the three intrinsic problems in the

classical DEM models. Based on the calibrated microscopic parameters, a suite of standard and same-porosity FJM3D models were created to investigate the effects of model size and particle size distribution on the macroscopic properties under uniaxial compression and Brazilian tests. The main conclusions are as follows:

(1) As the model size increases, the simulated results begin to converge. Combining the requirements of ASTM and ISRM for both uniaxial compression and Brazilian tests, $D/d_{\max}$ should be greater than or equal to 20. The requirement ensures an adequate reliability of the results, since $D/d_{\max}$ of the models for Cases I-IV correspond to 20, 16, 16.7 and 14.6, respectively, under 5% acceptable variation.

(2) The model porosity has a significant influence on strengths of FJM3D models, UCS and BTS of which decrease linearly with increasing porosity. Having eliminated the influence of the model porosity, the pure effects of the model size and particle size distribution are captured. With increasing model size, UCS, CIS, Young's modulus and Poisson's ratio first decrease and then reach a minimum, while BTS follows a descending trend and UCS/BTS maintains increasing gradually. Moreover, all the macro-properties decrease with the grain size heterogeneity ($d_{\max}/d_{\min}$), which are in agreement with the findings from **Peng et al. (2017b)** and **Liu et al. (2018)**.

(3) Comparing the results obtained from FJM3D and PBM3D models, it is also demonstrated that the constitutive contact model plays a role in the effects of model size and particle size distribution.

(4) Only when D/d of the specimen is less than or equal to 20, the UCS follows the decreasing trend. In the range ($D/d = 10 \sim 50$) in this research, BTS follows the generalized descending trend, best fitted by fracture energy and multifractal size-effect models for which fitting constants are functions of grain size heterogeneity.

CHAPTER 4 SIZE EFFECT AND ANISOTROPY IN A TRANSVERSELY ISOTROPIC ROCK UNDER INDIRECT TENSILE CONDITIONS

4.1 Introduction

In recent years, the behaviour of transversely isotropic rocks, e.g., gneiss, schist, slate, phyllite, shale, mudstone and layered sandstone, has attracted an increased attention **(Fu et al. 2018; Kundu et al. 2018; Sesetty and Ghassemi 2018; Setiawan and Zimmerman 2018; Xu et al. 2018)**. In general, the anisotropic characteristics originate from the stratification in the sedimentary rock, mineral foliation in metamorphic rocks and discontinuities in rock masses **(Cho et al. 2012)**. The anisotropy is one of the most distinct features that has to be considered in this kind of rocks which are widely encountered in civil, mining, petroleum, geothermal and geo-environmental engineering **(Ma et al. 2018)**.

The tensile strength plays an important role, and is often the most vital role in rock engineering, because rocks usually are weaker in tension than compression or shear **(Dan et al. 2013)**. Moreover, tensile failure has great influence in many rock engineering activities, such as drilling, cutting and blasting of rocks, hydraulic fracturing of a wellbore or a tunnel, exploitation of rock slopes, and excavation of underground structures **(Chen and Hsu 2001; Goodman 1989)**. Hence, for engineering practice, the determination of tensile strength of rocks is indispensable. Compared to the high requirement for experimentation with the direct tensile tests **(Liao et al. 1997; Shang et al. 2016)** or the high requirement for sample preparation with the ring tests **(Barla and Innaurato 1973; Chen and Hsu 2001)**, the Brazilian test is a more common and easy method for measuring the tensile strength of rock. However, the use of the formula for the Brazilian tensile strength requires the material to be isotropic. To improve the Brazilian test so that it can be useful for determining the tensile strength of transversely isotropic rocks, much work has been done by theoretical, experimental and numerical methods **(Aliabadian et al. 2017; Cai and Kaiser 2004; Chen et al. 1998; Claesson and Bohloli 2002; Exadaktylos and Kaklis 2001)**. Among these, a reasonably accurate equation for the principal tension at the rock disc center based on elastic constants and anisotropic angle

was proposed **(Claesson and Bohloli 2002)**, which approximates well to the tensile strength of transversely isotropic rocks.

The pioneering work on the anisotropy of tensile strength for transversely isotropic rocks was done by **Hobbs (1964)**, who conducted Brazilian tests on laminated siltstone, sandstone and mudstone to measure their tensile strengths. Since then, many researches have been carried out on this issue **(Ma et al. 2018)**. The published results showed that the tensile strength of transversely isotropic rocks greatly depended on the angle (β) between the loading direction and the transversely isotropic plane. Based on Brazilian test results of various transversely isotropic rocks, **Vervoort et al. (2014)** classified four trends for the variation of the tensile strength with β: (1) trend I for which the tensile strength almost keeps constant; (2) trend II for which the tensile strength increases first and then remains constant; (3) trend III for which the tensile strength increases systematically, and (4) trend IV for which the tensile strength stays constant first and then increases linearly. Recently, a U-shaped distribution exhibited by a slate was added into the classification as trend V **(Xu et al. 2018)**. In addition, three typical failure modes have been observed **(Dan et al. 2013; Tavallali and Vervoort 2010; Tavallali and Vervoort 2013)**: (1) fractures along the transversely isotropic planes in the low β range; (2) fractures across the isotropic planes in the high β range and (3) mixed fractures along and across the isotropic planes in the intermediate β range. Further, **Hu et al. (2017)** revealed the main cause for the three failure modes by means of scanning electron microscopy (SEM). The results indicated that with β increasing, the fracture morphology transforms from an intergranular fracture pattern along the bedding plane to across the rock matrix, and is a coupled intergranular with transgranular fracture when $\beta = 45°$.

When upscaling the strength and elasticity properties obtained from laboratory to practical engineering design, the size effect must be taken into consideration **(Li et al. 2018)**. As a key input parameter in engineering applications, the size effect on the tensile strength of transversely isotropic rocks must be understood. Nevertheless, the existing size effect relations are almost all derived from the isotropic rock or rock-like materials **(Bažant 1984; Bažant 1997; Carpinteri et al. 1995; Hoek and Brown 1980; Masoumi et al. 2015)**, neglecting the influence of rock anisotropy. Consequently, a suitable relation capturing both the size effect and the anisotropy of the tensile strength of transversely isotropic rocks is urgent to be unveiled. For this purpose, Brazilian tests were conducted

on slate specimens of six different sizes (25-100 mm) with seven various β (0-90°) in this study. During the test, the load and strain data were recorded. On the basis of the observed information, size effects on elastic properties and tensile strength were investigated in detail.

4.2 Theoretical background

4.2.1 Constitutive model of transversely isotropic rocks

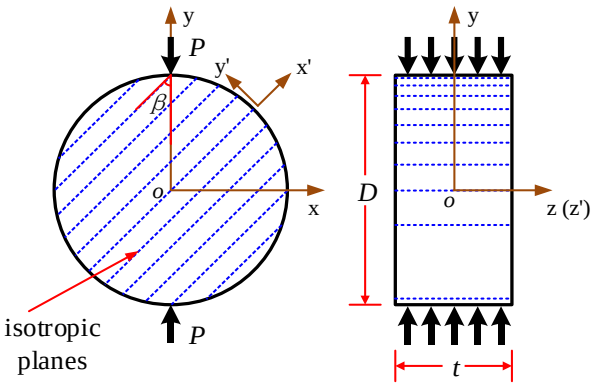

Figure 4.1 The disc geometry of a transversely isotropic material under diametral loading.

As presented in Figure 4.1, the disc of a transversely isotropic material under diametral loading (Brazilian test) has a diameter D and a thickness t. The angle between global (x, y, z) and local (x', y', z') co-ordinate systems is $\pi/2-\beta$, as shown in Figure 4.1. The local system is attached to the transversely isotropic plane, with x'-axis and y'-axis parallel to and perpendicular to the isotropic plane, respectively, and the z'-axis coinciding with the z-axis. If the disc is loaded with force P, the stresses σ_x, σ_y, and τ_{xy} within the disc can be expressed in the form of stress concentration factors (SCFs) q_{xx}, q_{yy}, and q_{xy} **(Amadei 1996)**:

$$\begin{cases} \sigma_x = \dfrac{P}{\pi D t} q_{xx} \\ \sigma_y = \dfrac{P}{\pi D t} q_{yy} \\ \tau_{xy} = \dfrac{P}{\pi D t} q_{xy} \end{cases} \tag{4.1}$$

A generalized plane stress formulation was used, then the constitutive law is expressed as,

$$\frac{\pi Dt}{P}\begin{Bmatrix}\varepsilon_x\\ \varepsilon_y\\ \gamma_{xy}\end{Bmatrix}=\begin{bmatrix}a_{11} & a_{12} & a_{16}\\ a_{12} & a_{22} & a_{26}\\ a_{16} & a_{26} & a_{66}\end{bmatrix}\begin{Bmatrix}q_{xx}\\ q_{yy}\\ q_{xy}\end{Bmatrix} \tag{4.2}$$

As the medium in the direction parallel to the transversely isotropic plane is postulated to be linearly elastic, homogeneous and continuous, **(Amadei 2012)** put forward the expression of a_{ij} as,

$$\begin{aligned}
a_{11} &= \frac{\sin^4\beta}{E}+\frac{\cos^4\beta}{E'}+\frac{\sin^2 2\beta}{4}\left(\frac{1}{G'}-\frac{2\nu'}{E'}\right)\\
a_{12} &= \frac{\sin^2 2\beta}{4}\left(\frac{1}{E}+\frac{1}{E'}-\frac{1}{G'}\right)-\frac{\nu'}{E'}\left(\sin^4\beta+\cos^4\beta\right)\\
a_{16} &= \sin 2\beta\left[\left(\frac{\cos^2\beta}{E'}-\frac{\sin^2\beta}{E}\right)-\left(\frac{1}{2G'}-\frac{\nu'}{E'}\right)\cos 2\beta\right]\\
a_{22} &= \frac{\sin^4\beta}{E'}+\frac{\cos^4\beta}{E}+\frac{\sin^2 2\beta}{4}\left(\frac{1}{G'}-\frac{2\nu'}{E'}\right)\\
a_{26} &= \sin 2\beta\left[\left(\frac{\sin^2\beta}{E'}-\frac{\cos^2\beta}{E}\right)+\left(\frac{1}{2G'}-\frac{\nu'}{E'}\right)\cos 2\beta\right]\\
a_{66} &= \sin^2 2\beta\left(\frac{1}{E}+\frac{1}{E'}+\frac{2\nu'}{E'}\right)+\frac{\cos^2 2\beta}{G'}
\end{aligned} \tag{4.3}$$

where E and E' represent the elastic moduli parallel to and perpendicular to the plane of transverse isotropy, respectively; ν' and G' are the Poisson's ratio and the shear modulus in the direction normal to the transversely isotropic plane, respectively. Note that the parameters a_{ij} in Eq. (4.3) only depend on E, E', ν' and G', and are independent of ν which is the Poisson's ratio in the plane of transverse isotropy.

4.2.2 Determination of elastic constants for transversely isotropic rocks

Loureiro-Pinto (1979) first determined the elastic constants of anisotropic rocks by means of Brazilian tests. Later, the Loureiro-Pinto's procedure was revised by **Amadei (1996)**, and a more accurate solution was given by **Chen et al. (1998)** who combined the Brazilian test and the generalized reduced gradient (GRG) method. However, the theorem

and mathematical computation procedure in the approach proposed by **Chen et al. (1998)** are rather complicated. To overcome the problem, **Chou and Chen (2008)** developed a more convenient method. This approach combines the Brazilian test and a commercial numerical program (e.g. finite difference program, finite element program or boundary element program), and the iterative solution procedure is shown in Figure 4.2 and described briefly as follows:

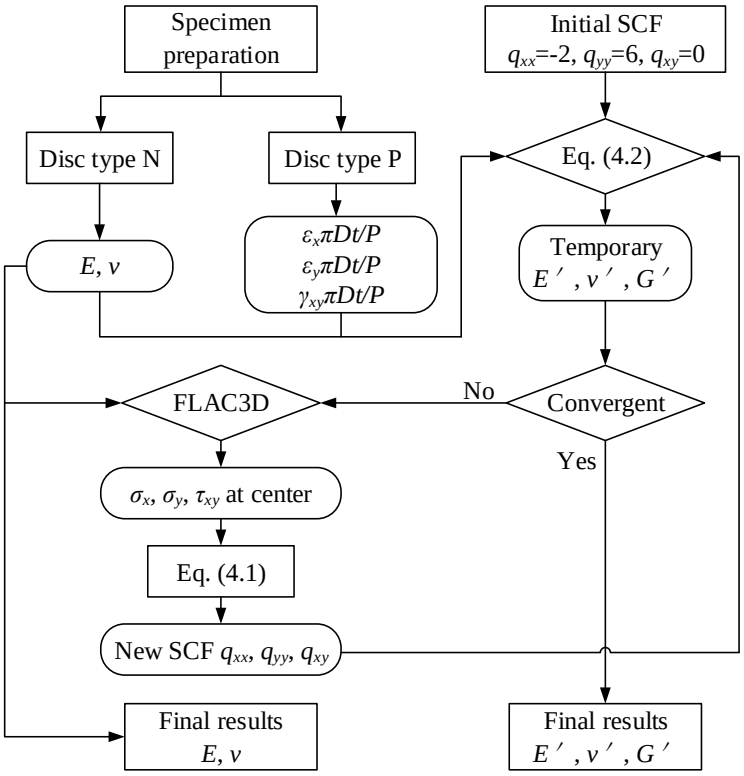

Figure 4.2 Flowchart of iteration for calculating the elastic constants modified from **Chou and Chen (2008)**.

(1) Brazilian tests are performed on two types of specimens: Type N (the central axis normal to the transversely isotropic plane) and Type P (the central axis parallel to the transversely isotropic plane). The strains at the disc center are obtained by Eq. (4.4), and ε_H, ε_{45} and ε_V are measured by 45° strain rosettes in test. The E and ν are calculated by Eq. (4.5).

(2) The temporary E', ν' and G' are computed by substituting $\varepsilon_x \pi Dt/P$, $\varepsilon_y \pi Dt/P$, $\gamma_{xy} \pi Dt/P$ and SCFs into Eq. (4.2).

(3) The five elastic constants obtained by previous steps are applied in the numerical simulation of Brazilian tests, and FLAC3D adopted in this study. The new SCFs are computed by Eq. (4.1).

(4) Steps (2) and (3) are repeated until E', ν' and G' have converged, and the difference between two successive cycles below 0.1% is adopted as the termination criterion.

$$\begin{Bmatrix} \varepsilon_x \\ \varepsilon_y \\ \gamma_{xy} \end{Bmatrix} = \begin{bmatrix} 1 & 0 & 0 \\ 0 & 0 & 1 \\ -1 & 2 & -1 \end{bmatrix} \begin{Bmatrix} \varepsilon_H \\ \varepsilon_{45} \\ \varepsilon_V \end{Bmatrix} \tag{4.4}$$

$$\begin{aligned} E &= \frac{16P}{\pi Dt(3\varepsilon_y + \varepsilon_x)} \\ \nu &= -\frac{3\varepsilon_x + \varepsilon_y}{3\varepsilon_y + \varepsilon_x} \end{aligned} \tag{4.5}$$

Meanwhile, to determine the elastic constants for a transversely isotropic medium, E, ν, E', ν' and G' must satisfy the following thermodynamic constraints **(Amadei 1996; Chen et al. 1998)**:

$$\begin{aligned} &E,\ E',\ G' > 0 \\ &-1 < \nu < 1 \\ &1 - \nu - 2\frac{E}{E'}(\nu')^2 > 0 \end{aligned} \tag{4.6}$$

4.3 Material and methods

4.3.1 Sample preparation

To minimize the influence of discreteness, five blocks of slate were taken from the same location in a slate quarry in Jiujiang, Jiangxi Province, China. The slate is a metamorphic Precambrian rock from sedimentary rocks. The slate possesses a well-developed slaty structure, with the layers of which being very straight (Figure 4.3a), as compared to the ripple layers of shale which exhibits dark grey to light grey colours. Moreover, a thin section of the slate normal to the foliation planes is observed by an optical microscopy and shown in Figure 4.3b. It is observed that the sample has a layered texture comprised

of granular calcite (5%), flaky sericite (25-30%), angular feldspar and quartz (65-70%), with a very fine grain size in the range of 0.01-0.05mm. Figure 4.3c further displays that the slate is tightly packed with strongly oriented rock fragments using SEM. The natural density of the slate is 2759±5 kg/m^3.

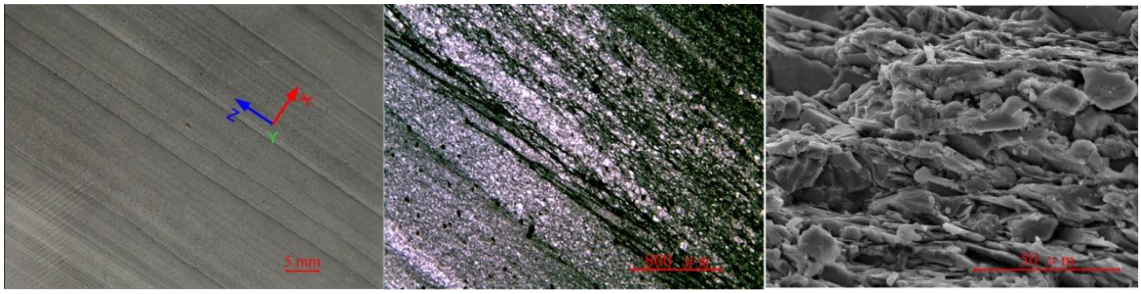

(a) (b) (c)

Figure 4.3 (a) The appearance of the slate; (b) a thin section image of the slate; (c) a SEM image of the slate.

The core specimens were drilled parallel to the foliations (Type P) and perpendicular to the foliations (Type N) with diameters of 25, 38, 50, 63, 75 and 100 mm, and were then cut into disc specimens. The thickness (t) of each disc specimen was fixed at 0.5 diameter (D) of the specimen. The end surfaces of the disc specimens were polished to satisfy the standard for tests **(ASTM 2016)**. The prepared disc slate samples of six different diameters are shown in Figure 4.4. Additionally, the P-wave velocities of slate samples were tested with inclination angle (β) 0°, 15°, 30°, 45°, 60°, 75° and 90° by using a Tektronix DPO 2012B Oscilloscope, OLYMPUS 5077PR wave pulser/receiver and two OLYMPUS V195 ultrasound probes. The variation of the P-wave velocities (v_p) with β is depicted in Figure 4.5. The results indicate that v_p decreases from 6002 to 4760 m/s with increasing β because of the increased influence of foliations on the ultrasound transmitting within the slate sample. Based on the anisotropy classification proposed by **Tsidzi (1997)**, using a velocity anisotropy index (VA) expressed as Eq. (4.7), the slate (VA=22.9) is classified as a highly anisotropic rock.

$$VA = \frac{V_{\max} - V_{\min}}{V_{mean}} (\%) \tag{4.7}$$

in which V_{max}, V_{min} and V_{mean} are the maximum, minimum and average ultrasonic wave velocities, respectively.

Figure 4.4 Preparation of disc slate samples of various diameters

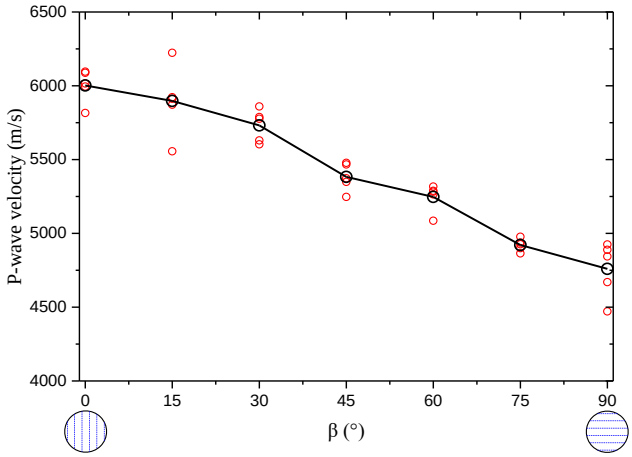

Figure 4.5 The variation of P-wave velocities of slate specimens with β.

4.3.2 Test procedure

The layout of the test devices is shown in Figure 4.6a. To ensure accuracy, a VJ tech machine with a low loading capacity of 100 kN was employed to conduct the Brazilian tests. The loading rate was controlled at 0.3 mm/min. Among the typical loading configurations suggested by **ASTM (2016)** and **ISRM (1978)**, the flat loading platens were chosen for this size-effect study. The reason behind is that the ratio of steel rod

diameter to specimen diameter (for flat loading platens with two small-diameter steel rods) or the contact angle (for curved loading jaws) is a function of the specimen diameter which will greatly affect the measured tensile strength **(Komurlu and Kesimal 2015; Markides and Kourkoulis 2012; Rocco et al. 1999a)**. In addition, strains at the disc center of the specimen were obtained by a 45° strain rosette with a length of 3mm (Figure 4.6b), which should not exceed 10% of the diameter of the disc **(Chen et al. 1998)**. During the test, the load and strains were recorded simultaneously using a Kyowa datalogger. Moreover, the AE signals were monitored by a PAC PCI-2 AE detection system **(Li et al. 2015)**, and two PICO sensors were used, arrangements of which are showed in Figure 4.6b. Meanwhile, the fracture conditions of specimens in the test were recorded through a Photron FASTCAM SA-Z high-speed camera with the LED lighting.

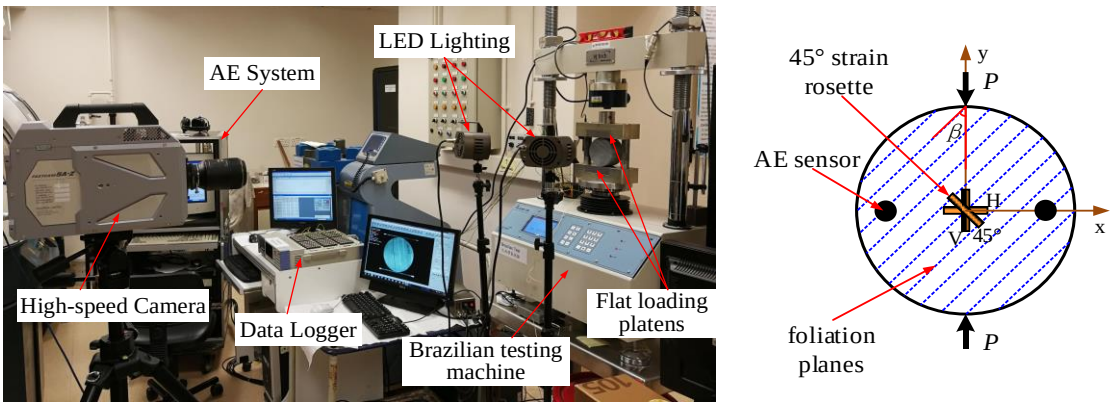

(a) (b)

Figure 4.6 (a) The test setup for Brazilian tests; (b) the arrangements of strain gauges and AE sensors.

4.4 Results and discussion

4.4.1 Size-effect on the elastic properties

As an illustrative example, Figure 4.7a and 4.7b show the typical stress-strain curves of disc slate samples of Type N and Type P, respectively. The $\varepsilon_x \pi Dt/P$, $\varepsilon_y \pi Dt/P$ and

$\gamma_{xy}\,\pi Dt/P$ used in section 4.2.2 to compute E', ν' and G' correspond to the secant values at 50% peak stress as depicted by the green lines in Figure 4.7.

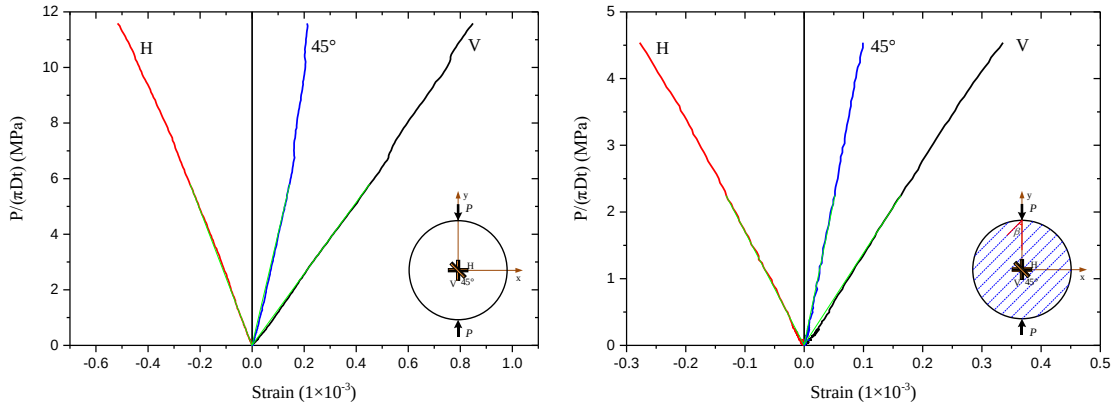

(a) (b)

Figure 4.7 Typical stress-strain curves of slate specimens under Brazilian tests (strains measured at the centre of the disk): (a) Type N and (b) Type P.

Table 4.1 Mean values of elastic constants determined on slate with different diameters using Brazilian tests.

Diameter of specimen (mm)	No. of tests	E (GPa)	E' (GPa)	ν	ν'	G' (GPa)	E/E'
25	28	56.3	68.1	0.29	0.28	31.2	0.83
38	24	81.4	41.9	0.28	0.30	26.5	1.94
50	25	78.7	55.8	0.28	0.27	30.2	1.41
63	30	71.2	45.2	0.23	0.30	19.4	1.58
75	33	70.1	39.2	0.16	0.20	19.6	1.29
100	29	89.8	28.1	0.32	0.21	16.2	3.19

Theoretically, only two disc samples are needed to determine the five elastic constants of transversely isotropic rocks by the Brazilian tests. To ensure accuracy, in this study, more than two specimens were employed to measure the elastic constants of slate for each size, as listed in Table 4.1. E, E', G', ν and ν' results for each size slate specimens are listed in Table 4.1 and plotted in Figure 4.8. E dramatically increases as the sample diameter increases from 25 to 38 mm, then fluctuates when the sample diameter is in the range of 38-75 mm, and finally increases again until the sample diameter reaches 100 mm.

The total trend of E is increase with specimen size, which is similar with that observed in the Blanco Mera granite **(Quiñones et al. 2017)** and Stanstead granite **(Walton 2017)**. It is because E and ν are obtained by Type N samples, in which the foliation planes have little influence on the deformability of transversely rocks under Brazilian tests. At this point, the slate of Type N and the two granites are treated as isotropic rocks, irrespective of rock anisotropy. The ascending size-effect on E can be attributed to the near-surface damage during sample preparation. The bigger specimens have a less surface area-to-volume ratio ($4/R$ for Brazilian discs), so the bigger specimens can be expected to be more rigid with less damage densities. In contrast, E', ν' and G' were determined by Type P samples, in which the foliation planes have a great influence on the deformability of transversely rocks under the Brazilian tests. Moreover, the stiffness of the foliation plane is far smaller than that for the rock matrix. The increasing number or volume of foliation planes per unit volume in the loading direction with increasing sample diameter reduces the rigidity of the sample, which can explain the decrease with the sample diameter as shown in Figure 4.8a for E' and G'. The singularities of E' for 38-mm-diameter sample and of G' for 50-mm-diameter sample may be induced by the higher effect of the surface damage in sample preparation than the foliation plane. Additionally, ν and ν' do not present an evident size effect as depicted in Figure 4.8b.

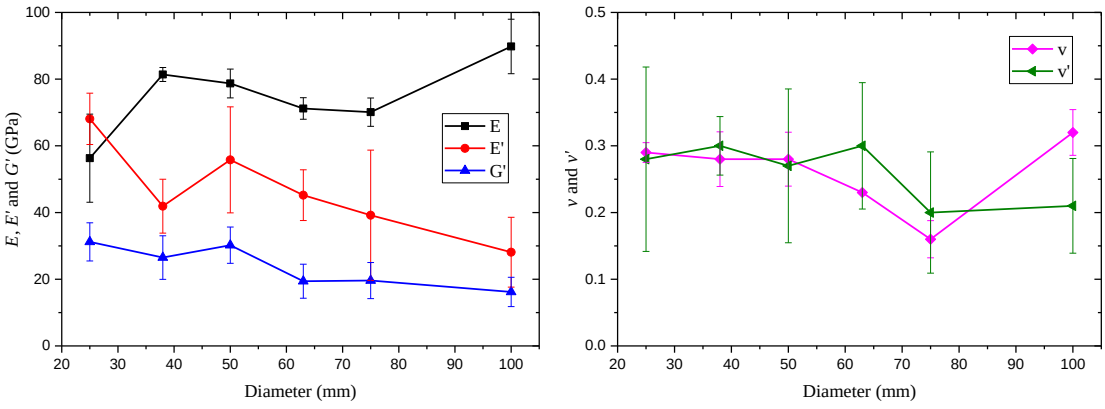

(a) (b)

Figure 4.8 (a) E, E', G' and (b) ν, ν' results for slate specimens of different diameters. The error bar represents one standard deviation.

The shear modulus G' is often obtained **(Togashi et al. 2017)** using the Saint-Venant's

empirical relation **(Saint Venant 1863)**:

$$\frac{1}{G'_{SV}} = \frac{1}{E} + \frac{1}{E'} + 2\frac{\nu'}{E'} \tag{4.8}$$

Cho et al. (2012) investigated the validity of the empirical equation and found that the equation did not agree well with the experimental data obtained from Asan gneiss, Boryeong shale and Yeoncheon Schist. With respect to this issue, results of G' obtained from experiment and theory for the slate of various diameters are compared and shown in Figure 4.9. The results demonstrate that with the sample diameter increasing, the difference between G' measured by experiment and that predicted by theory decreases gradually, almost equal to zero when D=100mm.

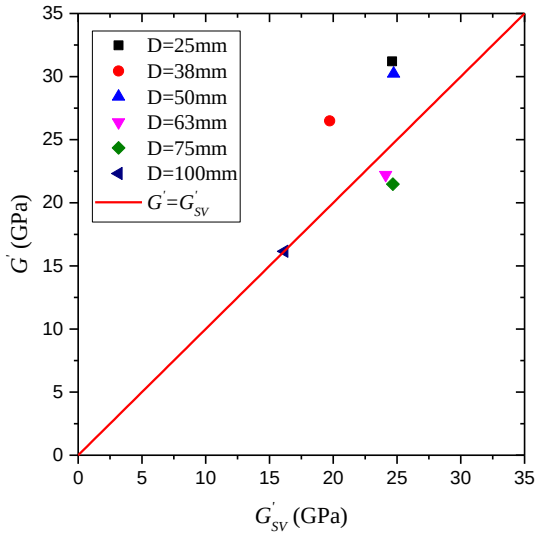

Figure 4.9 The comparison between Saint-Venant's empirical values (G'_{SV}) and experimental ones (G').

4.4.2 Size-effect on the tensile strength

As mentioned in section 2.2.1, the indirect tensile strength (σ_t) is well approximated as the principal tension at the disc center **(Claesson and Bohloli 2002)**.

For each condition (a prescribed size and β), there are three to five slate samples being tested. The tensile strength results for each of sample tested are plotted in Figure 4.10.

The results indicate that the variation of σ_t with β for specimens of different sizes mostly exhibits trend III: σ_t increasing systematically with β. Sometimes the minimum σ_t occurs at 15° or 30° which is consistent with those observed in other transversely isotropic rocks **(Khanlari et al. 2015; Mighani et al. 2016)**.

4.4.2.1 Assessment of tensile failure criteria

In order to assess the performance of existing typical tensile failure criteria as mentioned in section 2.2.1, three different assessment indicators are employed **(Ma et al. 2017)**. They are the maximum absolute relative error (*MARE*), the average absolute relative error (*AARE*), and the standard error (*SE*), defined by the following formulae:

$$MARE = \max\left\{\left|\frac{T_P(\beta)-T_E(\beta)}{T_E(\beta)}\right|\right\} \tag{4.9}$$

$$AARE = \frac{\sum\left|\frac{T_P(\beta)-T_E(\beta)}{T_E(\beta)}\right|}{N} \tag{4.10}$$

$$SE = \sqrt{\frac{\sum\left[T_P(\beta)-T_E(\beta)\right]^2}{N}} \tag{4.11}$$

The three assessment indicators can reflect the reliability or misfit of each failure criterion that the higher *MARE*, *AARE* and *SE* illustrate the lower reliability and higher misfit, and vice versa. The order of failure criteria is sorted according to the magnitude of *MARE*, *AARE* and *SE* when the four failure criteria are evaluated. Note that the *SE* is recommended as the final assessment indicator in case that the order of *MARE*, *AARE* and *SE* is not same for a certain failure criterion.

The comparisons between the predicted and test results are given in Figure 4.10, and the evaluation results using *MARE*, *AARE* and *SE* are listed in Table 4.2. The results indicate the orders of the reliability of the failure criteria are: (1) N-Z > L-P > H-B > SPW for the 25-, 38- and 50-mm-diameter specimens, (2) N-Z > H-B > L-P > SPW for the 63- and 100-mm-diameter specimens, and (3) L-P > SPW > N-Z > H-B for the 75-mm-diameter specimens. Except for the 75-mm-diameter specimens, the predicted results by N-Z

criterion are the most in line with those from the experiments. Therefore, the N-Z criterion is recommended to describe the anisotropy of the tensile strength of the slate.

Table 4.2 Assessment indicators (*MARE*, *AARE* and *SE*) of slate specimens with different diameters.

Diameter of specimen (mm)	Indicators	Results of the Assessment			
		H-B	N-Z	SPW	L-P
25	MARE	0.923	0.493	0.923	0.666
	AARE	0.208	0.107	0.258	0.168
	SE	3.801	1.995	4.270	2.832
38	MARE	0.454	0.159	0.643	0.369
	AARE	0.117	0.062	0.184	0.167
	SE	2.568	0.863	3.576	2.386
50	MARE	0.511	0.381	0.558	0.434
	AARE	0.192	0.166	0.232	0.201
	SE	3.011	2.080	3.888	2.945
63	MARE	0.531	0.203	0.770	0.521
	AARE	0.185	0.116	0.261	0.234
	SE	2.199	0.983	3.073	2.271
75	MARE	0.322	0.330	0.339	0.186
	AARE	0.147	0.119	0.120	0.090
	SE	1.593	1.420	1.362	0.868
100	MARE	0.206	0.195	0.393	0.323
	AARE	0.091	0.089	0.129	0.140
	SE	0.930	0.818	1.591	1.092

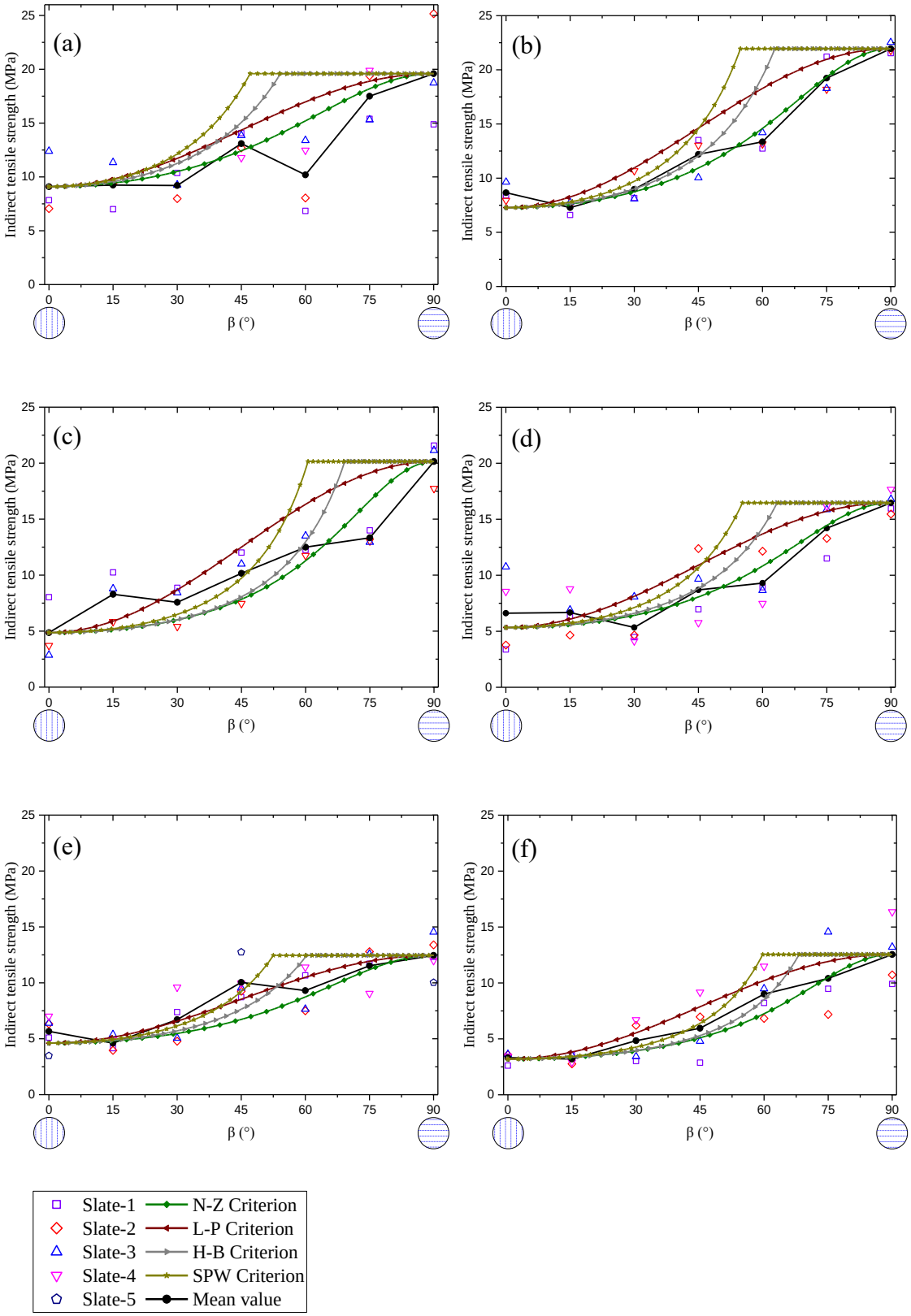

Figure 4.10 The relationship between indirect tensile strength and β for slate specimens of different diameters: (a) d=25mm; (b) d=38mm; (c) d=50mm; (d) d=63mm; (e) d=75mm and (f) d=100mm.

4.4.2.2 Anisotropic size-effect of tensile strength

Based on the existing size-effect models referring to section 2.1 and the experimental data of this study as shown in Figure 4.11, three principles defining the size-effect response are as follows:

(1) The relationship between tensile strength and specimen size depends on the mechanical properties of the material.
(2) The variation of tensile strength with specimen size shows both ascending and descending trends, and is correlated with the loading-foliation angle.
(3) For samples of a prescribed shape, the tensile strength has the upper and lower boundaries with the sample size varying.

Thus, the SEL and FFSEL are recommended to describe the size dependency of tensile strength of the slate. This combination has the advantages in capturing the increasing and decreasing trends with the common parameters (λd_0).

Based on the SEL, when the upper and lower boundaries are considered, the size-effect relation is transformed as,

$$T_1(d) = \sigma_M + \frac{(\sigma_0 - \sigma_M)}{\sqrt{1+\frac{d}{\eta}}} \tag{4.12}$$

where $T_1(d)$ is the tensile strength of specimen with the diameter of d; η=λd_0 with unit of length; σ_0 and σ_M are the tensile strength when $d \to 0$ and $d \to \infty$, respectively.

Correspondingly, the FFSEL is transformed as,

$$T_2(d) = \frac{\bar{\sigma}_0 d^{\frac{d_f - 1}{2}}}{\sqrt{1+\frac{d}{\eta}}} \tag{4.13}$$

where, $T_2(d)$ has the same meaning with $T_1(d)$; d_f represents the fractal dimension;

$\bar{\sigma}_0$ is the tensile strength when $d \to 0$.

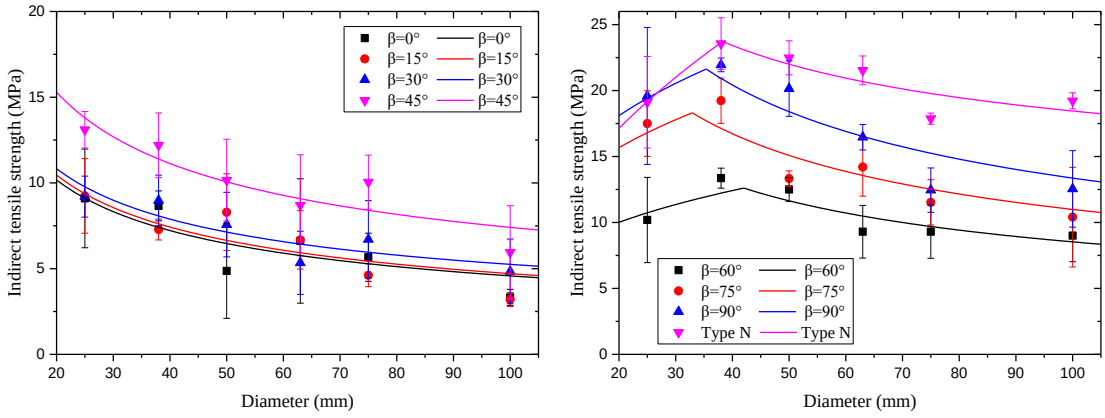

(a) (b)

Figure 4.11 The size effects on the indirect tensile strength of slate samples with different loading-foliation directions. The error bar represents one standard deviation.

The curved fitted results of Eqs. (4.12) and (4.13) are shown in Figure 4.11, and the fitting parameters (σ_0, σ_M, η, $\bar{\sigma}_0$ and d_f) of the equations in every loading-foliation direction are listed in Table 4.3. The fitted curves are in agreement with the experimental data, and correlation coefficients of Eqs. (4.12) and (4.13) are greater than 0.73. The results indicate that with specimen diameter increasing, the tensile strength maintains decreasing when β lies within 0-45°, and the tensile strength increases first and then decreases when β is in the range of 60-90° or the specimen belongs to Type N. The transition occurs at β lies within 45-60°, which may be attributed to the change of failure modes in this range. The results are elaborated in the following. When β lies within 0-45°, the tensile strength of slate is mainly dependent on the strength of the foliation planes, displaying the failure mostly along the foliation plane. When β lies within 60-90° or the specimen belongs to Type N, the tensile strength of the slate is primarily determined by the strength of rock matrix, exhibiting the failure mostly across the foliation plane. The typical descending size-effect can be attributed to the Fairhust's theory **(Fairhurst 1971)**, originated from elastic energy principles, that the product of the length of the critical flaw and the square of strength of tested sample is constant. The length of the critical flaw is proportional to the specimen size. Thus, the strength is reduced as the specimen diameter increases. On the other hand, the reverse size effect observed in the slate specimens can

be explained that the smaller specimens have the lower strength because of the higher surface damage density or the developing cracks more inclining to intersect the free sample surface in smaller specimens **(Quiñones et al. 2017)**.

Table 4.3 Fitting parameters in Eqs. (4.12) and (4.13) when the slate specimen is loaded in various directions.

β (°)	0	15	30	45	60	75	90	Type N
σ_0 (MPa)	76.45	78.63	77	108.76	127.21	167.16	205.43	153.66
σ_M (MPa)	0	0	0.68	0.95	0.97	1.04	1.13	9.84
σ_0-σ_M (MPa)	76.45	78.63	76.32	107.81	126.24	166.12	204.3	143.82
η					0.36			
R^2	0.73	0.75	0.80	0.81	0.85	0.80	0.83	0.76
$\bar{\sigma}_0$	-	-	-	-	6.75	10.57	12.21	6.54
d_f	-	-	-	-		2.61		2.99
R^2	-	-	-	-	0.79	0.86	0.89	0.88

Referring to Table 4.3, σ_0 and σ_M exhibit an almost increasing trend with β; $\bar{\sigma}_0$ also keeps increasing as β increases from 60° to 90°; but the parameters of η and d_f are basically constant. It is worth noting that the curve fitting parameters for the Type N specimen are greatly different from those obtained for Type P specimens, except for η. The results also suggest that the loading direction plays an important role in the size-effect response.

In addition, in order to compare the anisotropy of the size effect on the tensile strength of the slate, the derivative of Eq. (4.12) is deduced as,

$$T_1'(d) = -\frac{(\sigma_0 - \sigma_M)}{2\eta(1+\frac{d}{\eta})^{1.5}} \tag{4.14}$$

where $T_1'(d)$ is the derivative of $T_1(d)$. Values of $T_1'(d)$ are negative since $\sigma_0 - \sigma_M$

and η are positive as listed in Table 4.3. The values of $T_1'(d)$ are comparable when β = 0-30°, reaching the maximum value. $T_1'(d)$ is the minimum value when β = 90°. It implies that the downward size effect on the tensile strength of the slate is strongly increasing with β, reaching the strongest value when β=90°.

Table 4.4 The predicted T_{REV} by Eq. (4.12) for the slate specimen of d = 300 mm loaded in various directions.

β (°)	0	15	30	45	60	75	90
T_{REV} (MPa)	2.65	2.72	3.32	4.68	5.34	6.79	8.20

Table 4.5 The variation of parameters T_b and T_m with specimen size increasing.

Diameter (mm)	25	38	50	63	75	100	300
T_b (MPa)	8.25	7.60	6.32	5.46	5.82	3.80	2.79
T_m (MPa)	18.51	21.58	18.21	16.01	12.55	12.55	8.00
R^2	0.82	0.98	0.88	0.94	0.88	0.97	0.98

4.4.2.3 Anisotropy of tensile strength

Darlington et al. (2011) found that the results of specimens of 300-mm-diameter, at which asymptotic strength is met, are of crucial importance to large scale design. Thus, the tensile strength of 300-mm-diameter specimen is recommended to be taken as the tensile strength of representative elementary volume (REV), which is termed as T_{REV}. The predicted T_{REV} by Eq. (4.12) are listed in Table 4.4, which increases steadily with increasing β. Furthermore, the experimental data as fitted by Eq. (2.15) are plotted in Figure 4.12, and the curve fitting parameters T_b and T_m are listed in Table 4.5. T_b characterizing the tensile strength of weak planes decreases gradually, and T_m characterizing the tensile strength of the rock matrix, increases first and then decreases with increasing specimen size. The variation rules correspond to the two kinds of size-effect responses as depicted in the previous section (see Figure 4.11). It further illustrates that the transition of size-effect trends is closely related to the change of the failure modes.

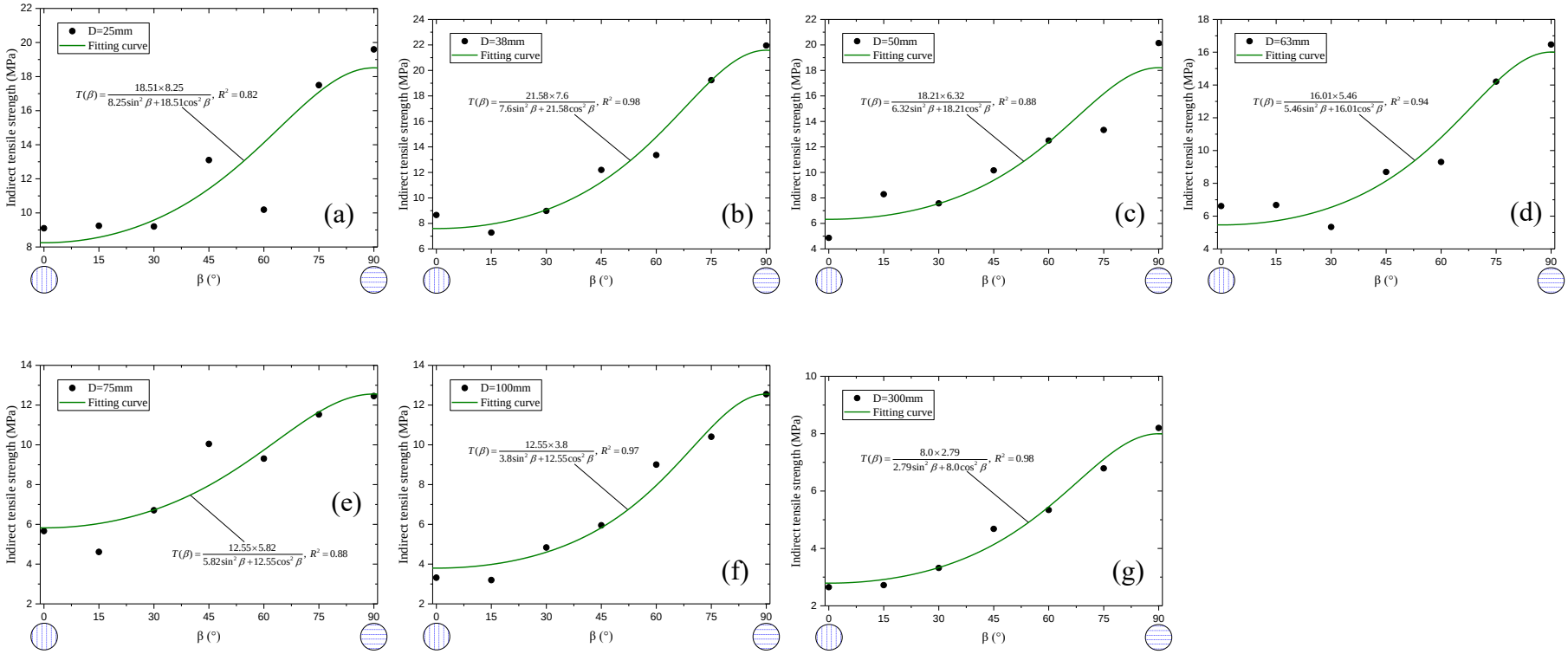

Figure 4.12 Comparison of experimental data or predicted T_{REV} with fitted curves by Eq. (2.15) for the slate specimen of (a) *d*=25mm; (b) *d*=38mm; (c) *d*=50mm; (d) *d*=63mm; (e) *d*=75mm; (f) *d*=100mm and (g) *d*=300mm.

The curve fitted results agree well with the experimental data, with correlation coefficients > 0.82 for various specimen diameters (25-300 mm). In summary, the N-Z criterion is capable of describing the anisotropy of tensile strength of the slate for different sample sizes.

4.4.2.4 Universal equations for size-effect and strength anisotropy

A unified size-effect relation capturing the relationship among tensile strength, sample size and loading direction in transversely isotropic rocks is vital for the correct estimation of the rock strength of a certain specimen size under a given loading direction. As σ_M and σ_0 of Eq. (4.12) and $\bar{\sigma}_0$ of Eq. (4.13) can be replaced by Eq. (2.15), two universal equations describing both size effect and anisotropy in transversely isotropic rocks are proposed in the forms:

(1) Using Eq. (2.15) to substitute σ_M and σ_0 of Eq. (4.12),

$$T_1(d,\beta)=\frac{T_{bM}T_{mM}}{T_{bM}\sin^2\beta+T_{mM}\cos^2\beta}+\frac{\left(\dfrac{T_{b0}T_{m0}}{T_{b0}\sin^2\beta+T_{m0}\cos^2\beta}-\dfrac{T_{bM}T_{mM}}{T_{bM}\sin^2\beta+T_{mM}\cos^2\beta}\right)}{\sqrt{1+\dfrac{d}{\eta}}} \tag{4.15}$$

where $T_1(d,\beta)$ is the tensile strength of specimen with a diameter d and a loading-foliation angle β; T_{b0} and T_{m0} are the tensile strength of weak plane and rock matrix when $d\to 0$, respectively; T_{bM} and T_{mM} represent the tensile strength of the weak plane and rock matrix when $d\to\infty$, respectively; η, as mentioned in Eq. (4.12) denotes a material constant with unit of length (mm).

(2) Using Eq. (2.15) to substitute $\bar{\sigma}_0$ in Eq. (4.13),

$$T_2(d,\beta)=\frac{\bar{T}_{b0}\bar{T}_{m0}}{\bar{T}_{b0}\sin^2\beta+\bar{T}_{m0}\cos^2\beta}\bullet\frac{d^{\frac{d_f-1}{2}}}{\sqrt{1+\dfrac{d}{\eta}}} \tag{4.16}$$

in which, $T_2(d,\beta)$ has the same meaning with $T_1(d,\beta)$; $\overline{T}_{b0}$ and $\overline{T}_{m0}$ represent the tensile strength of weak plane and rock matrix when $d \to 0$, respectively; η is same with that in Eq. (4.15); d_f as mentioned in Eq. (4.13) is the fractal dimension, with dimensionless.

If both ascending and descending trends are observed in experimental data, let $T_1(d_i,\beta) = T_2(d_i,\beta)$, the diameter (d_i) of specimen at which the maximum tensile strength reaches can be determined.

According to the experimental data observed in the slate, Eqs. (4.15) and (4.16) are fitted as Eqs. (4.17) and (4.18) with $R^2 > 0.93$, and the two fitted surfaces are plotted in Figure 4.13.

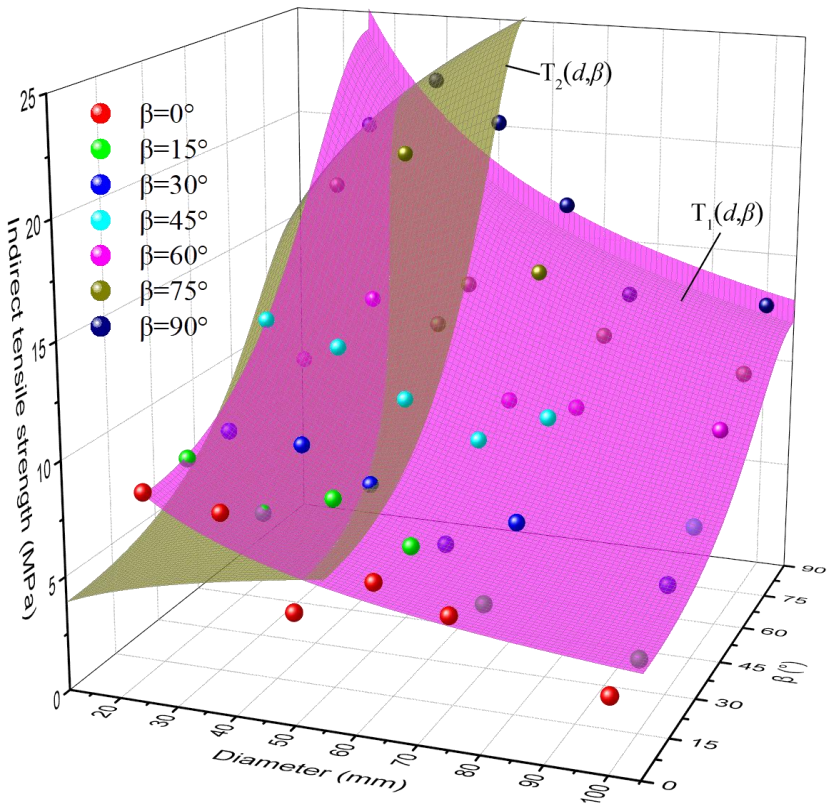

Figure 4.13 Comparison of experimental data with two theoretical surfaces fitted by Eqs. (4.17) and (4.18) for slate specimens of various diameters.

$$T_1(d,\beta)=\frac{1.13\times1.5\times10^{-16}}{1.5\times10^{-16}\sin^2\beta+1.13\cos^2\beta}+\frac{\left(\frac{202.91\times75.61}{75.61\sin^2\beta+202.91\cos^2\beta}-\frac{1.13\times1.5\times10^{-16}}{1.5\times10^{-16}\sin^2\beta+1.13\cos^2\beta}\right)}{\sqrt{1+\frac{d}{0.36}}},\quad R^2=0.931 \tag{4.17}$$

$$T_2(d,\beta)=\frac{12.41\times3.17}{3.17\sin^2\beta+12.41\cos^2\beta}\bullet\frac{d^{\frac{2.61-1}{2}}}{\sqrt{1+\frac{d}{0.36}}},\quad R^2=0.968 \tag{4.18}$$

Combining Eqs. (4.17) and (4.18), d_i for β = 60°, 75° and 90° are 41.0 mm, 35.2 mm and 34.1 mm, respectively. The predicted results are comparable to the experimental results (Figure 4.11b), presenting a downward trend with increasing β . The corresponding maximum tensile strength of the slate for β = 60°, 75° and 90° are 13.32MPa, 18.35 MPa and 21.75 MPa, respectively.

As seen from the discussion, Eqs. (4.15) and (4.16) are providing a method to obtain the tensile strength of slate with sample size and anisotropy varying. Moreover, the characteristic properties of the strength of representative elementary volume, upward and downward size-effect trends and the specimen diameter corresponding to the maximum strength are all combined to enable a systematic description of behaviour to be assessed. Nevertheless, the two equations suffer from the problem that specimens of different sizes and anisotropic angles are needed to determine the parameters in the equations for a certain material. It is also highlighted that more research into this issue is needed to demonstrate the capability of the proposed equations for other transversely isotropic rocks.

4.4.3 Size-effect on the tensile failure pattern

The failure pattern of a slate specimen under the Brazilian test is nearly two-dimensional, mostly being similar in two flat surfaces. Thus, only the failure pattern in one surface is displayed. Figure 4.14 shows the representative fracture patterns of specimens of different sizes after testing. The sketches of fracture patterns are also depicted in Figure 4.15. The failure pattern is closely related to the loading-foliation angle. For different sizes, the slate

specimen under the same loading direction mostly exhibits a similar failure pattern. In total, three types of failure patterns are presented: layer activation failure (type I), mixed failure (type II), and non-layer activation failure (type III).

As seen from Figure 4.15, when β lies from 0 to 30° the disc specimen fails mainly in the type I; when β lies from 45 to 60° the failure pattern of specimen covers all the three types; and when β ranges from 75 to 90° the failure of specimen is mostly manifested by the type III failure mode. This result is consistent with those observed by other researchers **(Dan et al. 2013; Tavallali and Vervoort 2010; Tavallali and Vervoort 2013)**. As for the Type N specimen, it fails by a tensile splitting crack along the loaded diameter accompanying the layer activation as shown in Figure 4.15h.

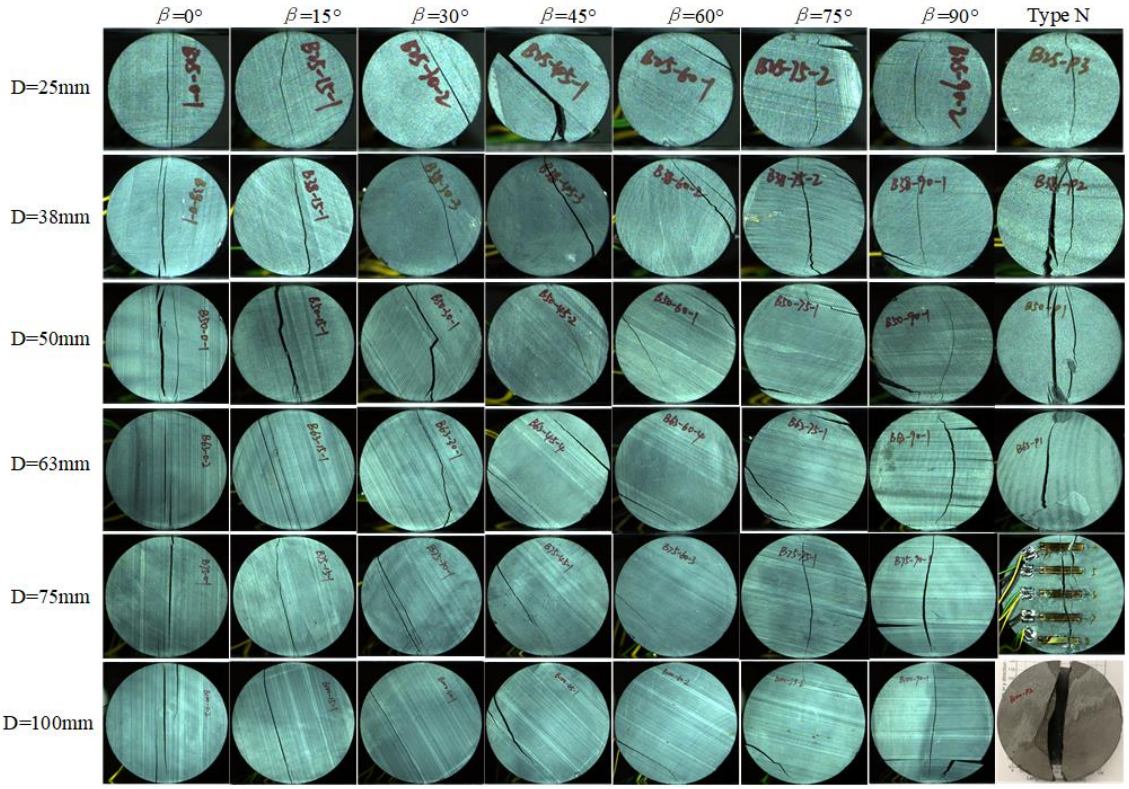

Figure 4.14 The representative fracture patterns of specimens of different sizes after testing.

Further, considering the size-effect, the percentages of the three failure types of specimen under different loading-foliation angles are listed in Table 4.6. For β equal to 0° or 90°, the specimen size has no influence on the failure patterns of specimens. For β varying from 15 to 30°, the failure patterns of specimens include type I and II, and the percentage

of type II increases first and then decreases and then stabilizes with the specimen size increasing. For β increasing from 45 to 60°, the failure patterns of specimens include all the three types, and the percentage of type III increases first and then decreases with the specimen size increasing. For β reaching 75°, the failure patterns of specimens include type II and III, and the percentage of type III increases first and then decreases and then stabilizes with the specimen size increasing.

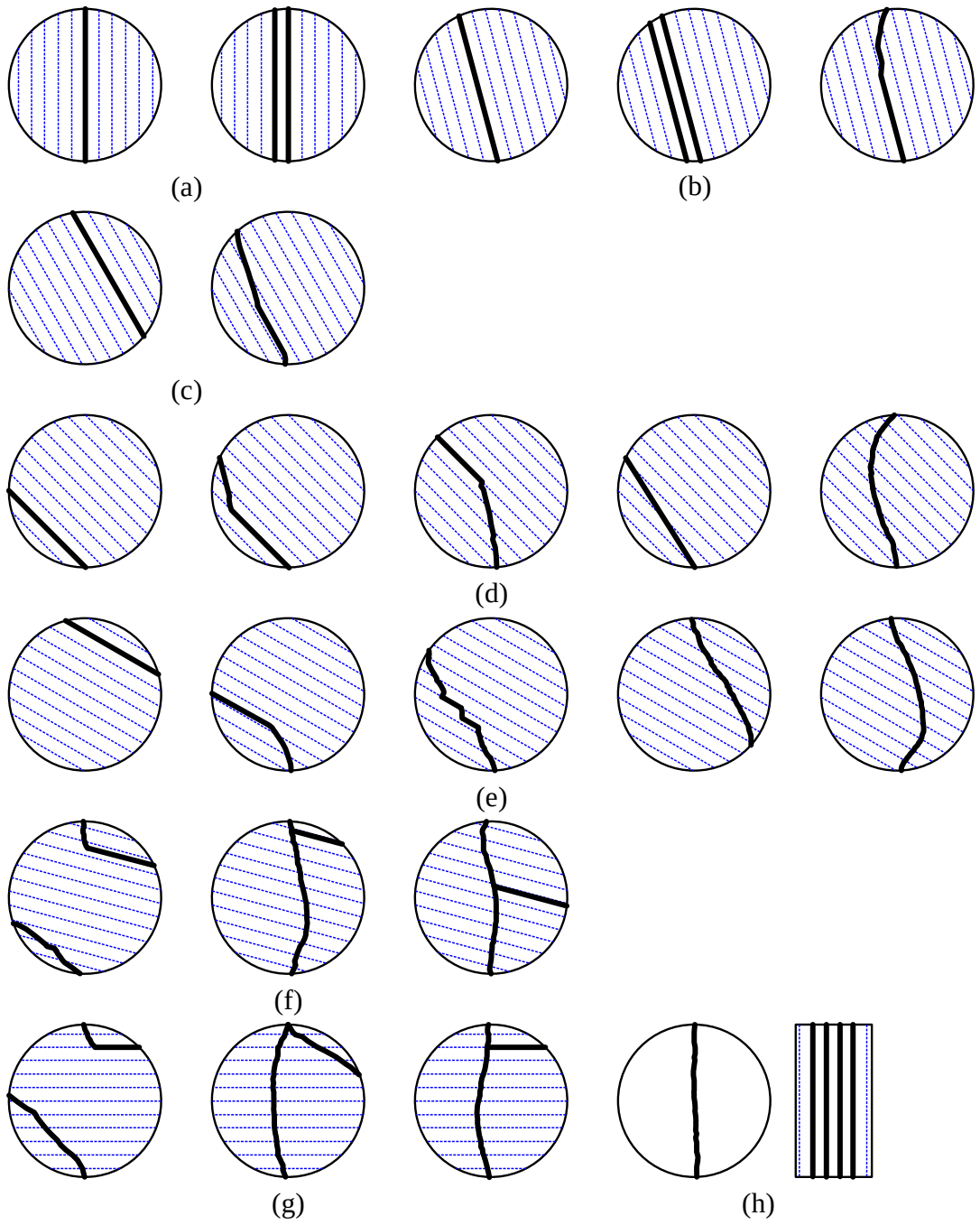

Figure 4.15 The sketches of fracture patterns: (a) β =0°; (b) β =15°; (c) β =30°; (d) β =45°; (e) β =60°; (f) β =75°; (g) β =90° and (h) Type N.

Table 4.6 The percentages of three failure types of slate specimens with different diameters (d) under different loading-foliation angles (β).

d (mm)	β (°)	Fracture patterns			d (mm)	β (°)	Fracture patterns			d (mm)	β (°)	Fracture patterns		
		% of type I	% of type II	% of type III			% of type I	% of type II	% of type III			% of type I	% of type II	% of type III
	0	100	0	0		0	100	0	0		0	100	0	0
	15	67	33	0		15	0	100	0		15	0	100	0
	30	75	25	0		30	0	100	0		30	50	50	0
25	45	25	25	50	50	45	0	33	67	75	45	0	0	100
	60	50	0	50		60	0	0	100		60	0	25	75
	75	0	25	75		75	0	33	67		75	0	0	100
	90	0	0	100		90	0	0	100		90	0	0	100
	0	100	0	0		0	100	0	0		0	100	0	0
	15	0	100	0		15	25	75	0		15	25	75	0
	30	0	100	0		30	25	75	0		30	50	50	0
38	45	0	0	100	63	45	25	50	25	100	45	0	25	75
	60	0	0	100		60	0	100	0		60	0	25	75
	75	0	0	100		75	0	50	50		75	0	33	67
	90	0	0	100		90	0	0	100		90	0	0	100

Generally, the tensile strength of specimen failed by type III is the highest, and that by type II is secondary and that by type I is the lowest. The variation of failure pattern with the specimen size can account for that of tensile strength with specimen size as discussed in section 4.4.2. The percentage of fracture type is also similar to the relative fracture length used in the previous study **(Tavallali and Vervoort 2010; Tavallali and Vervoort 2013)**.

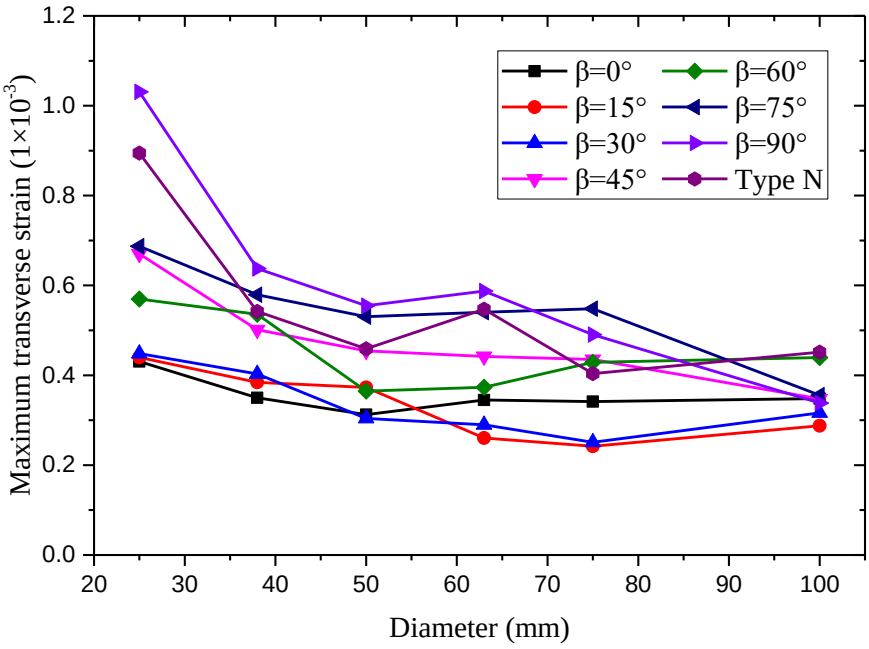

Figure 4.16 The size-effect on the maximum transverse strains of specimens of various diameters. The solid line represents the mean values.

4.4.4Size-effect on the transverse strain

In this study, the maximum transverse strain is defined as the transverse strain measured by the horizontal strain gage of the strain rosette at failure. As shown in Figure 4.16, the specimen size has an effect on the maximum transverse strains of slate specimens under diametral loading. The lowest value of maximum transverse strain occurs at β=0° when the specimen diameter is lower than or equal to 50mm, while it occurs at β=15° when the specimen diameter is larger than 50mm. Moreover, the maximum transverse strains of

specimens under different loading directions generally decrease with the specimen diameter, reaching the minimum value at D=100mm. The result implies that the slate specimens exhibit an increased brittle failure with the specimen diameter increasing, at the transverse strain less than 500 $\mu\varepsilon$ when D=100mm. It is in good agreement with the maximum extension strain of granite under Brazilian tests **(Li et al. 2011)**. Meanwhile, similar to the size-effect on tensile strength, the size-effect on maximum transverse strain is stronger under high loading-foliation angles than low loading-foliation angles, reaching the strongest at the loading-foliation angle of 90°.

In addition, the transverse strain of specimen also presents an anisotropic variation with the loading-foliation angle. As an example, the stress-strain curves and failure modes of 75-mm-diameter slate specimens under different loading directions are shown in Figure 4.17. The transverse strains (No. 4 to No.8) along the loaded diameter of specimen were measured by a series of horizontal strain gages with a length of 20 mm, enough long to capture the fracture initiation point within the specimen. The observed results indicate that the transverse strains measured approximated to the regions of load application are nonsymmetrical with respect to the *Ox*-axis. The experimental transverse strains in most cases except for β =0° or 15° increase with the distance away from the center of specimen. Moreover, based on the measured transverse strains along the loaded diameter, the fracture initiation point can be estimated. For instance, the specimen under β of 0° or 15° tends to fail starting from the disc center, while under other loading-foliation angles the specimen tends to fail starting from the regions of load application. Different from the specimen of Type P, the surfaces of specimen of Type N incline to spall at first from the regions of load application, as illustrated in Figure 4.18.

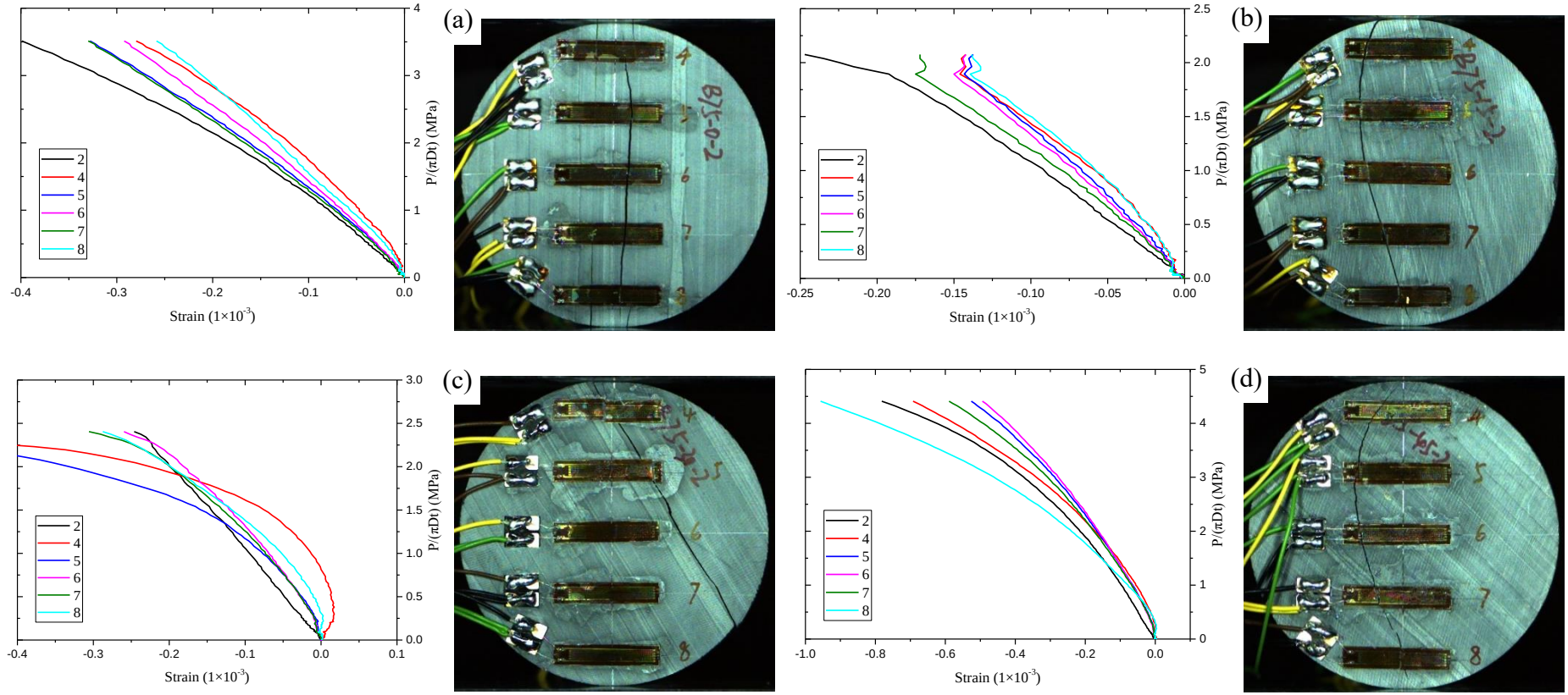

Figure 4.17 The stress-strain curves and failure modes of 75-mm-diameter slate specimens under different loading directions: (a) β =0°; (b) β =15°; (c) β =30°; (d) β =45°; (e) β =60°; (f) β =75°; (g) β =90° and (h) Type N. The No. 2 transverse strain is measured with the horizontal strain gage of the strain rosette glued at the center of specimen in one of its faces as shown in Figure 4.6b. The No. 4 to No. 8 transverse strains are measured with a series of horizontal strain gages glued along the diameter of specimen in the opposite face.

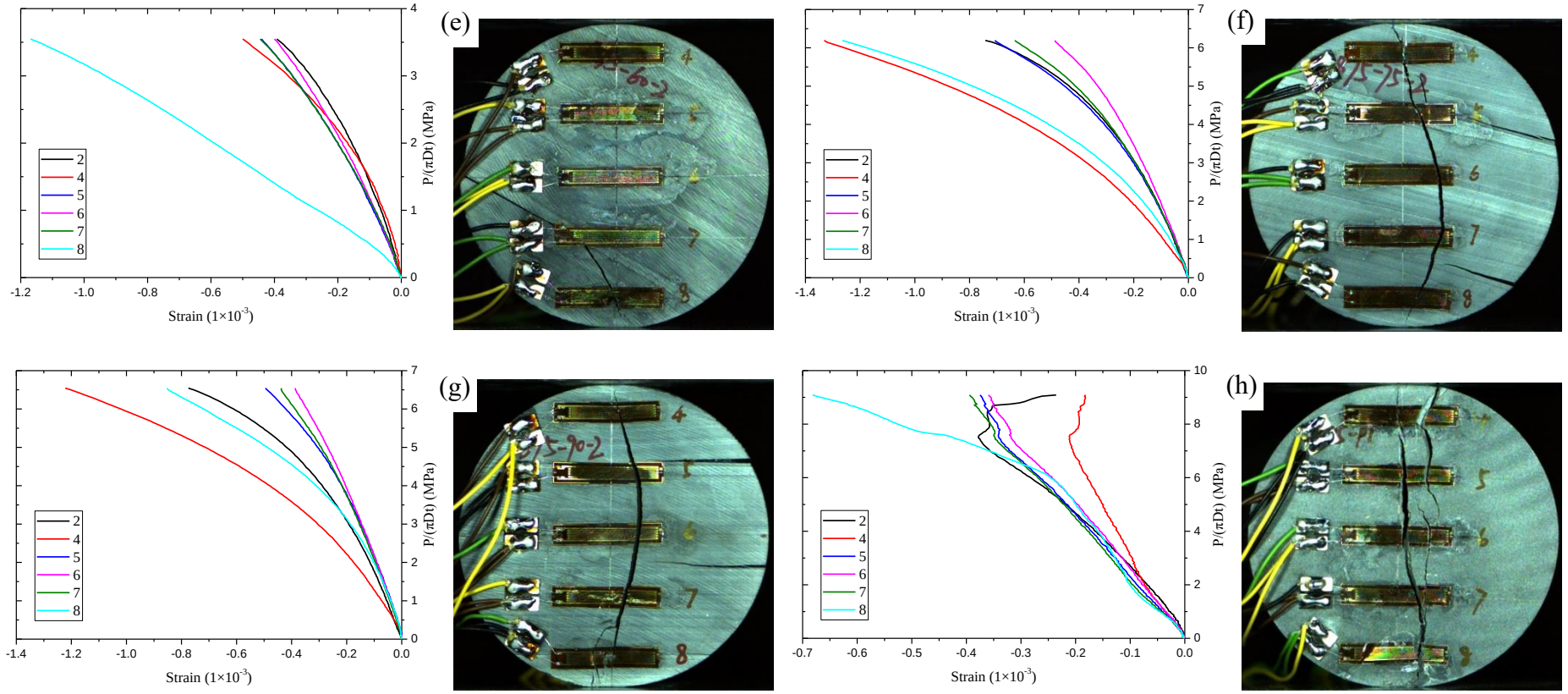

Figure 4.17 (*continued*)

Further, the transverse strain (No. 2) measured by the strain rosette with a length of 3 mm is also drawn in the figure to make a comparison. Except under β =30° or 60°, the transverse strain at the center of specimen measured by the strain gage with a length larger than 10% of the diameter of the specimen underestimates the measured strain with respect to the strain gage of smaller length. This result is opposite to that observed in Dionysos marble by **Exadaktylos and Kaklis (2001)**. Nonetheless, both results support the recommendation given by **Chen et al. (1998)** that the gage length should not exceed 10% of the diameter of specimen. In contrast, under β =30° or 60°, the transverse strains at the center of the disc measured by strain gages of different length are comparable. The reason behind this is that fractures do not pass through the disc center in the two cases and thus strains in the regions close to the center have little change.

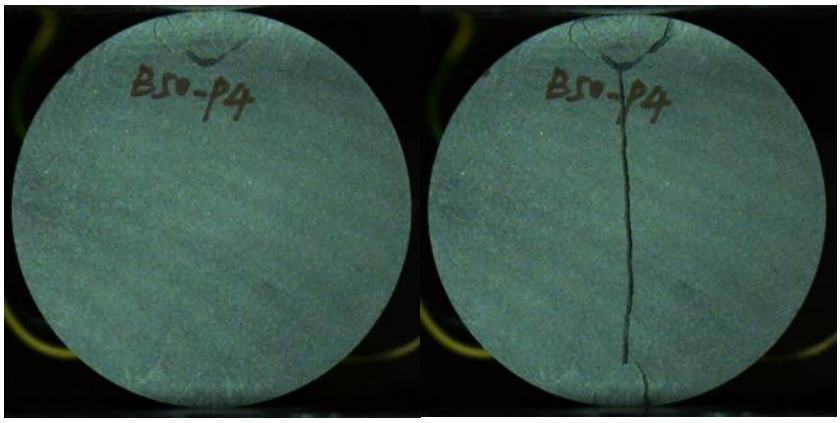

Figure 4.18 The surfaces of slate specimen of Type N close to the regions of load application incline to spall at first.

4.5 Summary

Slate, as a transversely isotropic rock, was employed to investigate the size-effect and anisotropy on its deformation, tensile strength and fracture pattern in this chapter. Disc slate samples of six sizes of 25-100 mm were cored parallel to (Type P) and normal to (Type N) the foliation planes. A series of Brazilian tests were performed on the disc samples with loading-foliation angles of 0°, 15°, 30°, 45°, 60°, 75° and 90°. The main

conclusions are summarised as follows:

(1) Five independent elastic constants of the slate were determined by combining Brazilian test and FLAC3D simulation. The Young's modulus (E) in the transversely isotropic plane presents an increasing trend with specimen diameter, while the Young's modulus (E') and shear modulus (G') perpendicular to the transversely isotropic plane exhibit a reverse size effect. The Poisson's ratios parallel to (ν) and normal to (ν') the transversely isotropic plane do not show an evident size effect. Moreover, the difference between G' obtained from the experiment and the Saint Venant's empirical equation decreases with the specimen diameter, which may arise from the increased brittleness with increasing specimen diameter. Size effects on these elastic properties of the slate can be attributed to the combined influence of foliation planes and near-surface damage during sample preparation.

(2) The principal tension at the disc center considering the elastic anisotropy is recommended as the indirect tensile strength of the slate. The tensile strength variation of slate with loading direction presents an increasing systematically trend (trend III). The N-Z criterion well captures the anisotropy of tensile strength of the slate in different sample sizes.

(3) At loading-foliation angles of 0°-45°, the tensile strength of slate presents a typical descending size-effect. In contrast, at loading-foliation angles of 60°-90°, the tensile strength of slate presents a first ascending and then descending size-effect. The transition of size-effect trends is closely related to the failure mechanism under different loading directions. The degree of descending size-effect on tensile strength increases largely with loading-foliation angle, reaching the strongest when the loading-foliation angle is 90°.

(4) A unified size-effect relation including two equations is first proposed and verified against the experimental data. The size-effect relation captures both the ascending and descending size-effect trends, and reveals the relationship among the tensile strength, specimen size and anisotropic angle. In future, more research into this issue should be done to demonstrate the capability of the proposed unified size-effect law for other transversely isotropic rocks.

(5) Under different loading-foliation angles, there exist three types of failure patterns being presented: layer activation failure (type I), mixed failure (type II), and non-

layer activation failure (type III). As the loading-foliation angle increases, the failure pattern of slate specimen transforms from type I to type III. In general, the tensile strength of specimen failed by type III is the highest, and that by type II is secondary and that by type I is the lowest. With the specimen size increasing, the fracture pattern of specimen at the loading-foliation angle of 0° or 90° does not vary, but at other loading-foliation angles the percentage of fracture type with a higher strength increases first and then decreases.

(6) The maximum transverse strain of slate under the Brazilian test shows a descending size-effect. It implies that the slate specimen exhibits an increased brittle failure with the specimen size increasing, at the transverse strain less than 500 $\mu\varepsilon$. The transverse strains also present an anisotropic variation with the loading-foliation angle, and those measured approximated to the regions of load application are nonsymmetrical. Furthermore, the measured transverse strains along the loaded diameter can estimate the fracture initiation point. The specimen at β of 0° or 15° tends to fail starting from the disc center, while at other loading-foliation angles the specimen tends to fail starting from the regions of load application.

CHAPTER 5 SIZE EFFECT AND ANISOTROPY IN A TRANSVERSELY ISOTROPIC ROCK UNDER COMPRESSIVE CONDITIONS

5.1 Introduction

Size effect is an important characteristic in brittle and semi-brittle materials, e.g., rock and concrete **(Aubertin et al. 2000; Masoumi et al. 2016)**, and the term refers to the influence of sample size on measured mechanical properties **(Masoumi 2013)**. Recently, considering the descending size-effect trend and the strength anisotropy, a universal equation describing the relationship among anisotropic angle, sample size and UCS was put forward by **(Song et al. 2018)** for coal, which can be modelled as an orthotropic material **(Amadei 1996)**. This equation may be extended for transversely isotropic rocks, such as slate, shale, phyllite, schist, gneiss, siltstone, mudstone, sandstone and orthoquartzite. Furthermore, it is found in Chapter 4 that the indirect tensile strength of slate is closely related to the loading-foliation angle and specimen size, which displays a descending size-effect trend when the loading-foliation angle is low to medium (0°-45°), whereas it presents, first, an ascending and then descending size-effect trend when the loading-foliation angle is high (60°-90°). Finally, a unified size-effect relation including two equations was proposed and verified against the experimental data to capture the ascending and descending size-effect trends and the relationship among indirect tensile strength, specimen size and loading-foliation angle. However, to date, there has been no study involving size effect in transversely isotropic rocks under triaxial conditions.

In this chapter, a suite of uniaxial compression tests were conducted on slate samples with six different diameters (19 to 75 mm) and varied foliation orientations relative to the loading direction (0°, 15°, 30°, 45°, 60° and 90°) to explore the influence of specimen

size and anisotropy on the elastic constants and UCS. A series of triaxial compression tests were also performed on slate samples with diameters of 25, 50 and 75 mm and various foliation orientations with respect to the direction of major principal stress (0°, 15°, 30°, 45°, 60° and 90°) under a range of confining pressures between 1 and 20 MPa. The modified Hoek-Brown **(Saroglou and Tsiambaos 2008)** and Saeidi failure criteria **(Saeidi et al. 2014)** were improved in order to incorporate the size effect on both UCS and triaxial compressive strength (TCS), resulting in two size-dependent failure criteria. Additionally, a cohesion loss model **(Peng and Cai 2019)** was modified to capture the anisotropic triaxial residual strength of slate, and two equations providing the upper and lower bounds of the ratio of residual to peak strength were proposed for transversely isotropic rocks.

5.2 Determination of elastic constants under uniaxial compression

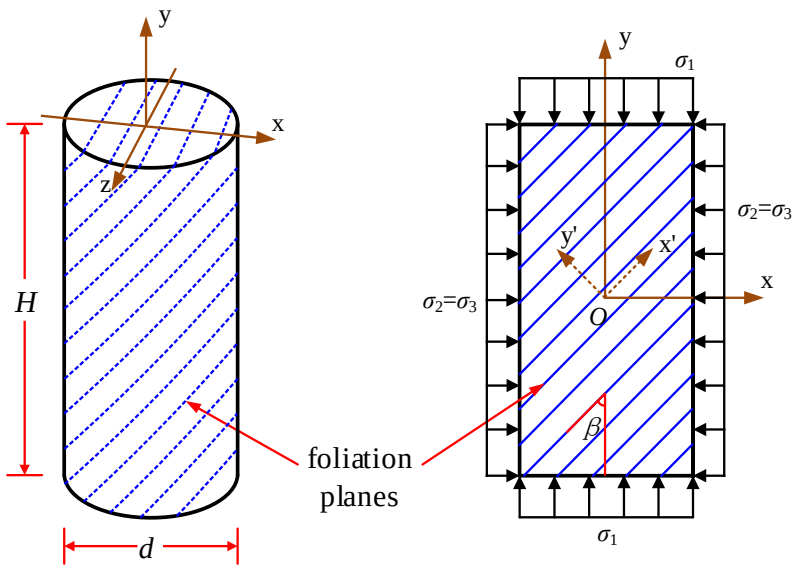

Figure 5.1 The cylindrical geometry of a transversely isotropic material under compression.

As seen from Figure 5.1, the cylinder of a transversely isotropic material under compression has a height of H and a diameter of d. The global co-ordinate system (x, y,

z) is rotated counter-clockwise with an angle of $(\pi/2-\beta)$ relative to the local co-ordinate system (x', y', z'). β is the orientation of foliation with respect to the direction of the major principal stress. The local system is affiliated to the plane of transversely isotropy, with the x'-axis and the y'-axis parallel to and normal to the plane of transverse isotropy, respectively, and the z'-axis coinciding with the z-axis. According to the generalized Hooke's Law, the constitutive model of transversely isotropic media is expressed in global co-ordinates as follows:

$$\begin{Bmatrix} \varepsilon_x \\ \varepsilon_y \\ \varepsilon_z \\ \gamma_{yz} \\ \gamma_{zx} \\ \gamma_{xy} \end{Bmatrix} = \begin{bmatrix} a_{11} & a_{12} & a_{13} & a_{14} & a_{15} & a_{16} \\ a_{21} & a_{22} & a_{23} & a_{24} & a_{25} & a_{26} \\ a_{31} & a_{32} & a_{33} & a_{34} & a_{35} & a_{36} \\ a_{41} & a_{42} & a_{43} & a_{44} & a_{45} & a_{46} \\ a_{51} & a_{52} & a_{53} & a_{54} & a_{55} & a_{56} \\ a_{61} & a_{62} & a_{63} & a_{64} & a_{65} & a_{66} \end{bmatrix} \begin{Bmatrix} \sigma_x \\ \sigma_y \\ \sigma_z \\ \tau_{yz} \\ \tau_{zx} \\ \tau_{xy} \end{Bmatrix} \tag{5.1}$$

After postulating the medium in the direction along the transversely isotropic plane to be linearly elastic, homogeneous and continuous, **Amadei (2012)** deduced the expressions of a_{ij}. The three components of a_{ij} utilised in uniaxial compressive conditions to determine the five independent elastic constants for transversely isotropic rocks are provided as follows:

$$\begin{aligned} a_{12} &= \frac{\varepsilon_x}{\sigma_y} = \frac{\sin^2 2\beta}{4}\left(\frac{1}{E}+\frac{1}{E'}-\frac{1}{G'}\right)-\frac{\nu'}{E'}\left(\sin^4\beta+\cos^4\beta\right) \\ a_{22} &= \frac{\varepsilon_y}{\sigma_y} = \frac{\sin^4\beta}{E'}+\frac{\cos^4\beta}{E}+\frac{\sin^2 2\beta}{4}\left(\frac{1}{G'}-\frac{2\nu'}{E'}\right) \\ a_{32} &= \frac{\varepsilon_z}{\sigma_y} = -\cos^2\beta\frac{\nu}{E}-\sin^2\beta\frac{\nu'}{E'} \end{aligned} \tag{5.2}$$

where E and E' denote the elastic moduli parallel to and perpendicular to the transversely isotropic plane, respectively; ν and ν' represent the Poisson's ratios parallel to and normal to the transversely isotropic plane, respectively; and G' is the shear modulus in the direction normal to the transversely isotropic plane.

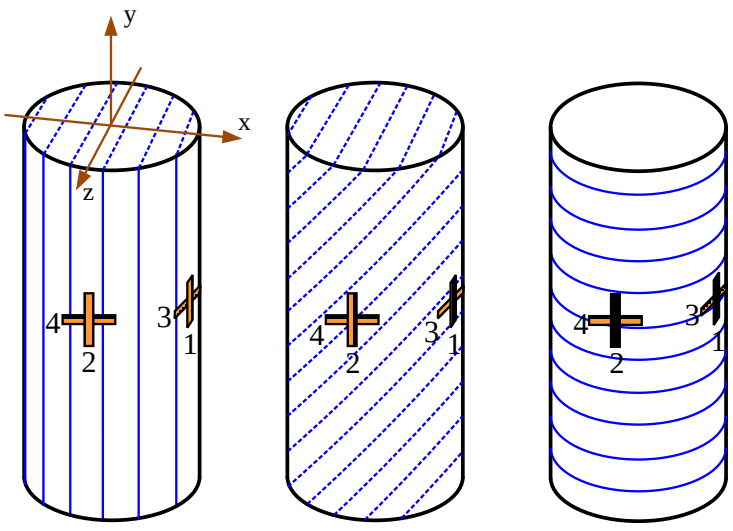

(a) (b) (c)

Figure 5.2 The biaxial strain gages glued on the specimens in uniaxial compression tests with: (a) β =0°; (b) 0°<β<90° and (c) β =90°.

The most frequently-used method for determining the five elastic constants for transversely isotropic rocks under uniaxial compression tests was presented by **Amadei (1996)** and **Cho et al. (2012)**. In this method, at least two specimens (e.g., prismatic, cylindrical) with different foliation orientations (β) are required, provided that one of them is inclined relative to the isotropic plane (0°<β<90°). Figure 5.2 shows the arrangement of biaxial strain gages for specimens with three different foliation orientations. For each specimen, the two biaxial strain gages are mounted at the middle of the specimen with axial gauges (No. 1 and 2) parallel to the cylinder axis (y-axis). Circumferential gauges are glued diametrically perpendicular to axial gauges with each position either in the direction of the dip (No. 3) or the strike (No. 4) of foliation. Substituting the observed stress and strain data from testing into Eq. (5.1), the obtained equations can be summarised into a matrix only containing unknowns E, E', ν, ν' and G'. After that, the five elastic constants are determined through the method of least squares. Despite the fact, in theory, that a minimum of five independent strain measurements is sufficient for the determination of elastic constants for transversely isotropic rocks, the results of Cho et al. showed that more strain measurements can improve the prediction accuracy **(Cho et al. 2012)**.

5.3 Material and methods

5.3.1 Sample preparation

The slate samples, from five blocks collected at the same location in a slate quarry, with different diameters of 19, 25, 38, 50, 63 and 75 mm, were cored at various directions with respect to the foliation plane of 0°, 15°, 30°, 45°, 60° and 90°, as illustrated in Figure 5.3a. All of the samples, part of which are shown in Figure 5.3b, were prepared as per the International Society for Rock Mechanics (ISRM)-suggested method **(ISRM 2007)**. The length-to-diameter ratio of each specimen was fixed at 2:1. A difficult part of the experimentation lies in obtaining good-quality cores with the required length due to the low success rate, particularly for the foliation-normal cores, which are easy to disk off during coring. Moreover, because of the ambiguity and waviness of foliation planes, the actual foliation orientation may deviate within a range of two to three degrees relative to the specified value of foliation orientation. For this experiment, homogeneous samples were carefully selected, having a relatively uniform composition and no macro defects visible to the unaided eye. It is worth pointing out that anisotropic materials can be homogenous, which should not be confused with heterogeneity **(Simpson 2013)**. The slate rock used in this experiment has a well-developed slaty structure and a very fine grain size of 0.01-0.05 mm, and detailed information concerning the petrography and microstructure of which can be found in Chapter 4.

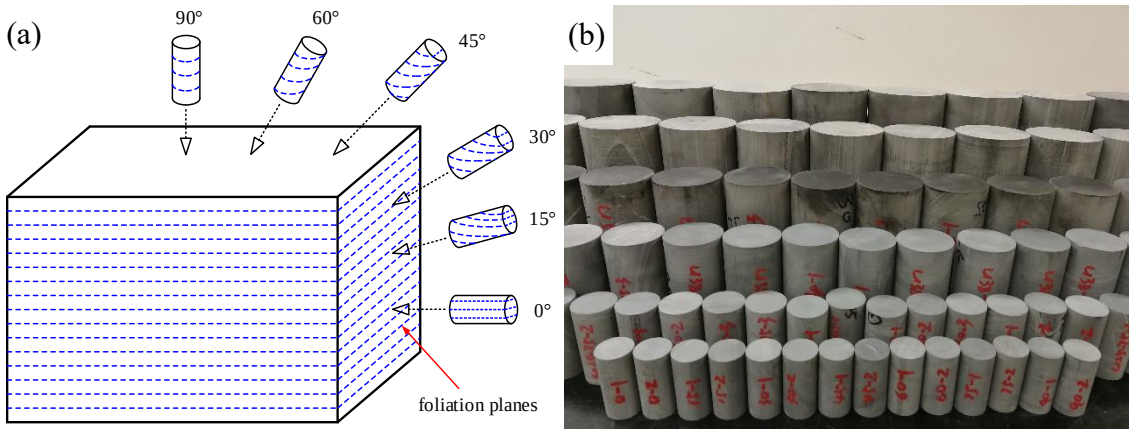

Figure 5.3 Preparation of specimens with different diameters and foliation orientations: (a) coring of specimens with different orientations; (b) part of specimens in each size used in the compression test.

5.3.2 Testing procedure

The laboratory apparatuses for uniaxial and triaxial compression tests are shown in Figure 5.4. Uniaxial compression tests were performed on slate samples with diameters of 19, 25, 38, 50, 63 and 75 mm and loading-foliation angles (β) of 0°, 15°, 30°, 45°, 60° and 90°. To ensure accuracy, a compression machine with a low loading capacity of 100 kN (see Figure 5.4a) was utilised for slate samples with small diameters (19 and 25 mm). As for the samples with larger diameters (38, 50, 63 and 75 mm), a stiff testing machine with 3 MN loading capacity was employed (see Figure 5.4b). The loading rates for uniaxial compression tests were set identically to be 0.5 MPa/s as the ISRM suggests **(ISRM 2007)**. For each specimen, two biaxial strain gages with a length of 5 mm were used, the arrangements of which are shown in Figure 5.2. Throughout the test, the load and strain were simultaneously recorded via a Kyowa datalogger.

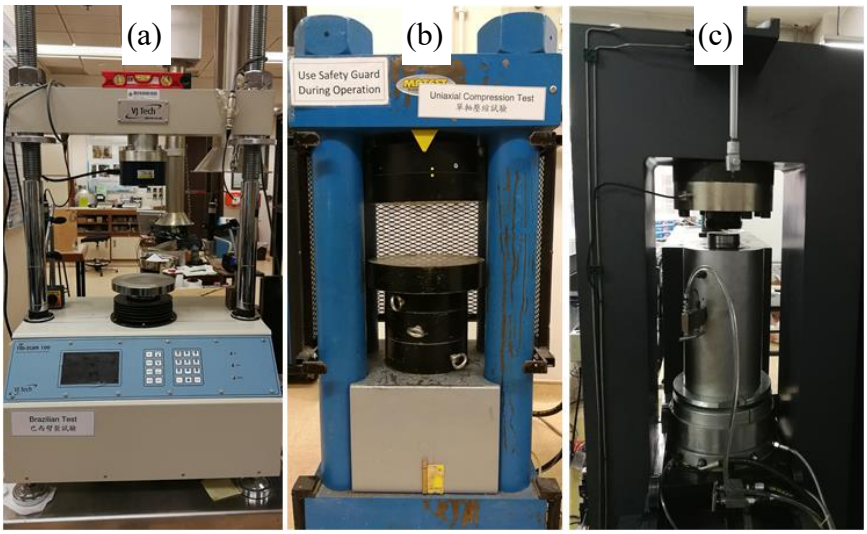

Figure 5.4 The testing equipments for: (a) uniaxial compression tests on 19- and 25-mm-diameter samples and (b) on 38-, 50-, 63- and 75-mm-diameter samples, (c) triaxial compression tests on 25-, 50- and 75-mm-diameter samples.

In addition, triaxial tests were conducted on slate samples with diameters of 25, 50 and 75 mm and foliation orientations relative to the major principal stress (β) of 0°, 15°, 30°, 45°, 60° and 90° using a servo-controlled loading frame system of 2 MN capacity and a triaxial cell capable of generating up to 100 MPa confining pressures (see Figure 5.4c). Three sets of platens incorporating spherical seats of 25, 50, and 75 mm in diameter came with the triaxial cell. Moreover, to adapt for the different diameters of the tested samples,

three sets of extensometers with different sizes were adopted, each of which included an axial extensometer and a circumferential extensometer with measuring ranges of 10 and 5 mm, respectively. The triaxial compression test was performed according to the individual test suggested by **Kovari et al. (1983)**, in which the individual point on the peak or residual strength envelope is obtained from one test. The loading rates of confining pressure and axial stress were controlled at 0.05 and 0.5 MPa/s, respectively, as suggested by the **ISRM (2007)**. In this study, the slate samples were tested with confining pressures ranging from 1 to 20 MPa.

5.4 Results and discussion

5.4.1 Elastic property

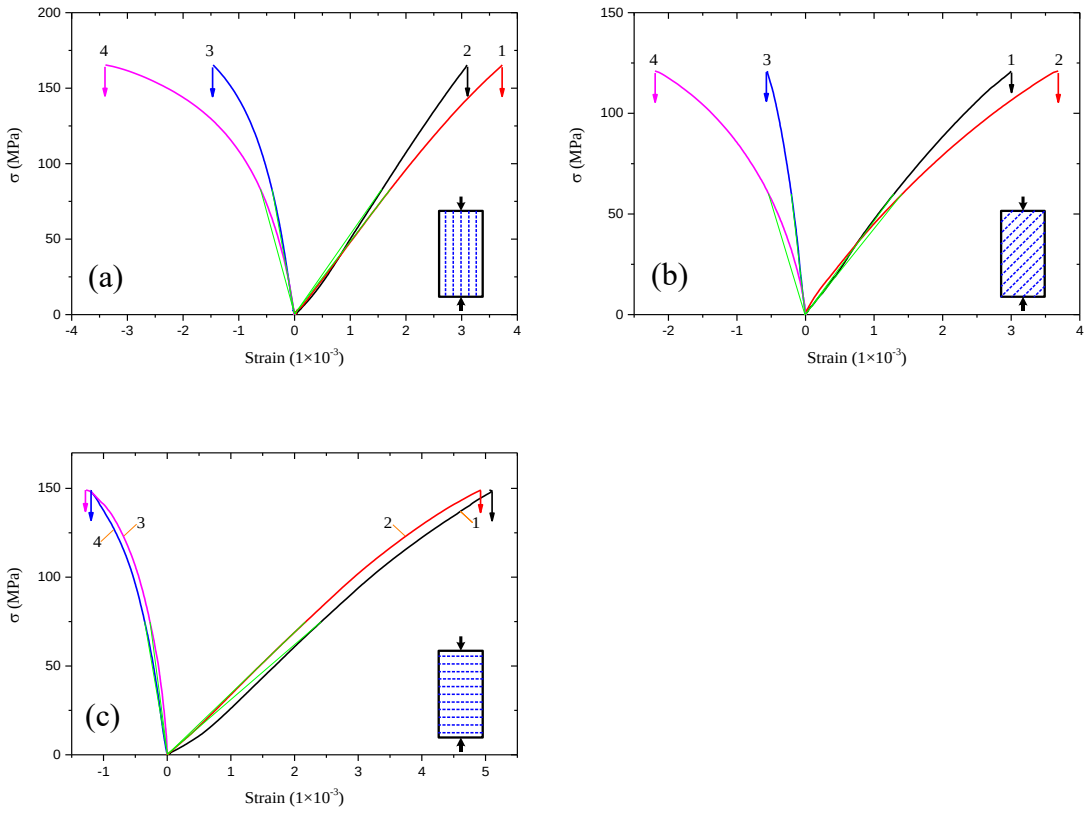

Figure 5.5 Typical stress-strain curves of slate specimens under uniaxial compression tests: (a) β =0°; (b) β =45° and (c) β =90°

As an illustrative example, the typical stress-strain curves of slate samples in uniaxial compression tests are shown Figure 5.5. The stress-strain curves No. 1 to 4 correspond to

the measured strains at different mounting positions as displayed in Figure 5.2. The results show that axial strains obtained at positions No. 1 and 2 are comparable irrespective of β, while the difference in circumferential strains obtained between the directions of dip and strike (No. 3 and 4) is greatly dependent on β. This demonstrates the existence of elastic anisotropy in slate. The ε_x/σ_y, ε_y/σ_y and ε_z/σ_y used in section 5.2.1 to determine the values of E, E', ν, ν' and G' correspond to the secant values at 50% peak stress as represented by the green lines in Figure 5.5.

5.4.1.1 Five elastic constants for the transversely isotropic rock

Table 5.1 The five elastic constants determined on the slate with different specimen diameters using uniaxial compression tests.

Diameter (mm)	Number of gages	E (GPa)	E' (GPa)	ν	ν'	G' (GPa)	w
19	48	58.86	49.29	0.16	0.20	19.01	2.2
25	68	71.58	34.39	0.20	0.16	15.41	2.7
38	48	72.26	25.08	0.21	0.17	17.32	2.7
50	56	71.53	36.40	0.19	0.15	11.82	3.0
63	44	81.43	37.60	0.19	0.18	13.62	3.0
75	52	86.73	33.47	0.17	0.19	18.01	2.8

The five elastic constants determined on slate samples with different sizes in uniaxial compression conditions are listed in Table 5.1, and each group of results were calculated from the corresponding number of strain gage readings, collected from samples with different foliation orientations, using the method of least squares. Taking all of the five elastic constants into consideration, **Kwasniewski (1983)** proposed an anisotropy classification for transversely isotropic materials as follows:

$$\begin{aligned} w &= (2p+q)^{0.5} \\ p &= \left[\left(E/E' - \nu'^2\right)/\left(1-\nu^2\right)\right]^{0.5} \\ q &= \left[E/G' - 2\nu'\left(1+\nu\right)\right]/\left(1-\nu^2\right) \end{aligned} \tag{5.3}$$

According to the anisotropy classification, the slate samples of 19 mm in diameter and of 25 to 75 mm in diameter are classified as the low anisotropic rock ($2.1 < n \leq 2.5$) and the medium anisotropic rock ($2.5 < n \leq 3.0$), respectively.

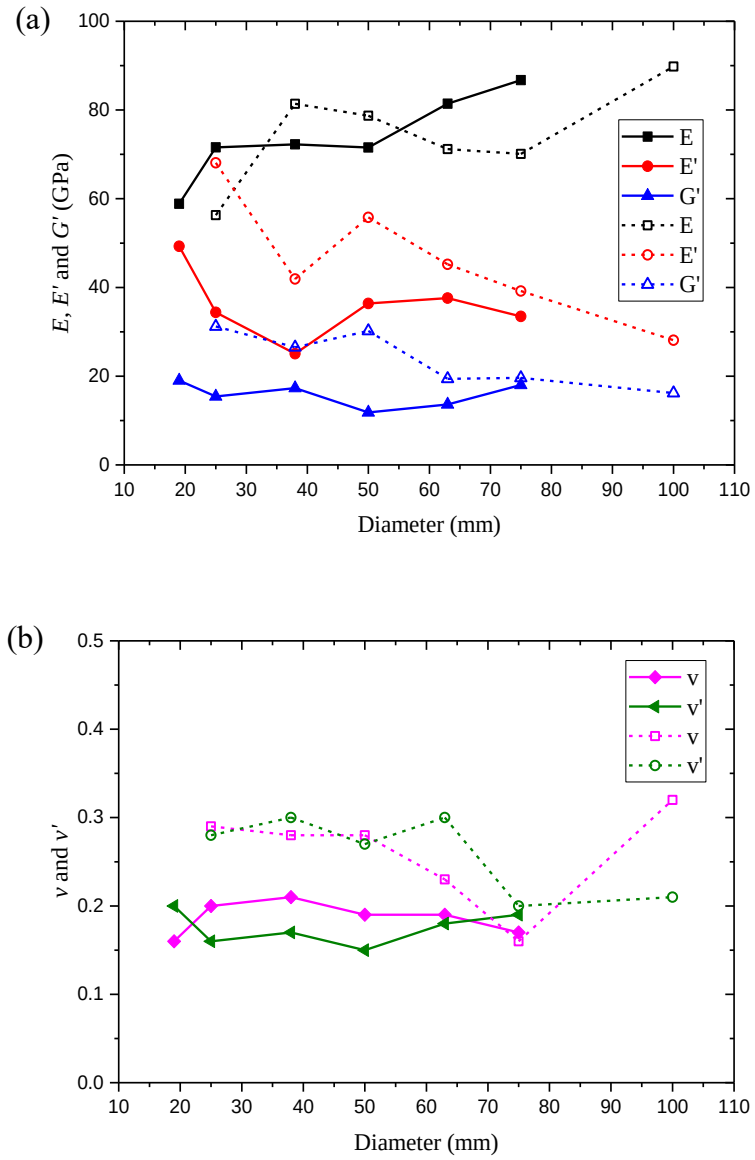

Figure 5.6 Variations of five elastic constants with specimen size, and comparisons between results obtained from uniaxial compression and Brazilian tensile tests in Chapter 4: (a) *E*, *E'*, *G'* and (b) *v*, *v'*. The solid and dashed lines represent the results obtained from uniaxial compression and Brazilian tensile tests, respectively.

Figure 5.6 shows variations of the five elastic constants with the specimen size, as well as comparisons between results obtained from uniaxial compression and Brazilian tensile tests. The Young's modulus parallel to the isotropic plane generally increases, while the Young's modulus perpendicular to the plane of isotropy first decreases and then fluctuates

with the specimen size. Both the shear modulus normal to the foliation plane and Poisson's ratios parallel to and perpendicular to the foliation plane vary little throughout the specimen size range. As analysed in Chapter 4, the combined influence of foliation plane and near-surface damage during sample preparation determines the size effect on the elastic properties in slate.

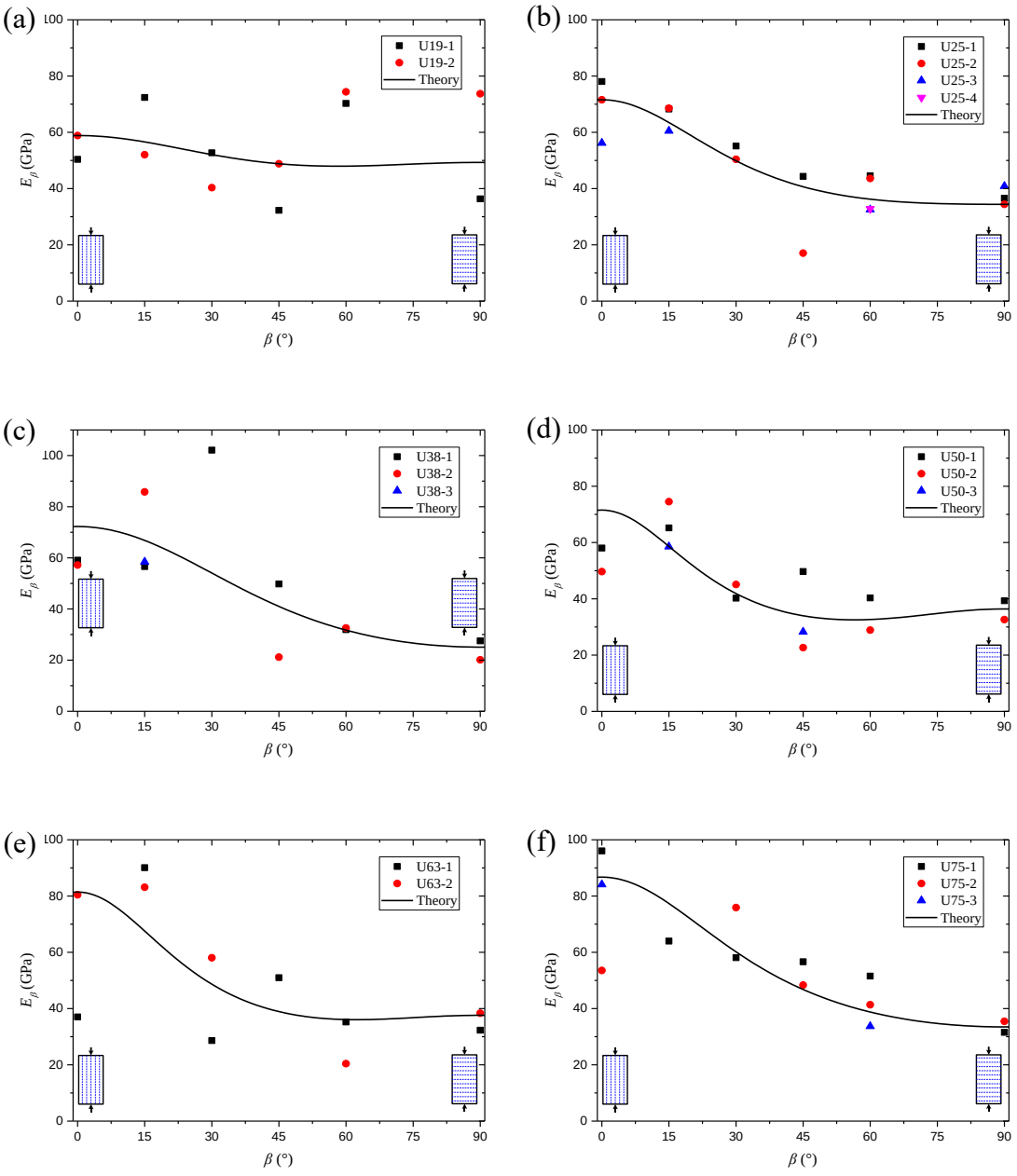

Figure 5.7 Variation of apparent Young's modulus (E_β) and theoretical results from the transversely isotropic solution: (a) *d*=19mm; (b) *d*=25mm; (c) *d*=38mm; (d) *d*=50mm; (e) *d*=63mm and (f) *d*=75mm.

Thus, the outcome of the combined influence for slate in uniaxial compressive conditions is that only the Young's modulus parallel to the isotropic plane presents an increasing size-effect trend, and other elastic constants do not display an evident size-effect trend.

Additionally, with the exception of the Young's modulus parallel to the plane of isotropy, all of the elastic constants obtained by Brazilian tensile tests are higher than those obtained by uniaxial compression tests, regardless of the specimen size. This discrepancy could be attributed to the difference in loading conditions, since rocks have different deformability properties when loaded in tension or compression **(Amadei 1996)**. Further research is needed on this issue, which is outside of the scope of this study.

5.4.1.2 Apparent elastic moduli

In uniaxial compressive condition, the theoretical predications of apparent elastic modulus (E_β) can be calculated as $1/a_{22}$ in the form:

$$\frac{1}{E_\beta}=\frac{\varepsilon_y}{\sigma_y}=\frac{\cos^4\beta}{E}+\frac{\sin^4\beta}{E'}+\frac{\sin^2 2\beta}{4}\left(\frac{1}{G'}-\frac{2\nu'}{E'}\right) \tag{5.4}$$

The apparent elastic moduli for slate samples with different diameters obtained from this experiment are shown in Figure 5.7 with the theoretically predicted results based on the transversely isotropic solution. In general, the apparent elastic modulus decreases gradually, with the foliation orientation relative to the loading direction increasing. In the case of slate samples of 19 mm in diameter, the variation of the apparent elastic modulus with β is less obvious, consistent with the results of anisotropy classification. Furthermore, in order to demonstrate the applicability of the transversely isotropic model to slate, an assessment indicator called mean prediction error (*MPE*) is utilised to compare the measured with the predicted apparent elastic moduli **(Cho et al. 2012; Min and Jing 2003)**, according to

$$MPE=\frac{1}{N}\sum_{i=1}^{N}\left|\frac{y_{i(ex)}-y_{i(th)}}{y_{i(th)}}\right| \tag{5.5}$$

where $y_{i(ex)}$ and $y_{i(th)}$ are the experimental and theoretical values, respectively; and N

represents the number of data points. The calculated *MPE*s of E_β for slate samples with diameters of 19, 25, 38, 50, 63 and 75 mm are 22%, 16%, 22%, 17%, 22% and 13%, respectively. They are within an acceptable range, so the transversely isotropic model is moderately applicable to slate irrespective of specimen size. Therefore, the apparent elastic modulus of slate at any foliation orientation can be estimated using the transversely isotropic solution once relevant elastic constants are determined.

5.4.2 Uniaxial compressive strength

Table 5.2 Uniaxial and triaxial compression test results of slate specimens with different sizes and loading directions (*part 1*).

Diameter (mm)	β =0°			β =15°			β =30°		
	σ_3 (MPa)	σ_1 (MPa)	SD (MPa)	σ_3 (MPa)	σ_1 (MPa)	SD (MPa)	σ_3 (MPa)	σ_1 (MPa)	SD (MPa)
19	0	142.58	11.40	0	129.29	19.18	0	108.83	7.29
	0	129.53	2.92	0	115.59	12.59	0	96.07	11.79
	1	142.06	18.55	1	125.67	—	1	110.15	22.38
25	5	176.75	2.39	5	170.60	3.06	5	135.89	49.27
	10	226.33	12.39	10	203.58	7.20	10	170.67	—
	20	273.19	—	20	232.91	9.42	20	215.67	1.31
38	0	124.31	6.70	0	99.55	10.12	0	86.62	27.99
	0	115.25	0.75	0	95.91	7.45	0	78.77	7.31
	1	132.31	17.44	1	93.88	15.32	1	91.82	3.67
50	5	172.88	45.31	5	131.12	0.63	5	109.68	4.35
	10	199.92	20.98	10	137.74	1.11	10	120.29	2.27
	20	253.09	6.14	20	175.15	2.69	20	164.86	21.74
63	0	102.16	7.03	0	89.52	1.50	0	69.72	10.44
	0	97.29	22.15	0	87.59	14.34	0	73.72	19.59
	1	122.25	0.90	1	95.32	14.68	1	68.93	0.36
75	5	160.37	13.67	5	106.25	9.21	5	88.16	20.04
	10	174.85	1.02	10	130.06	—	10	101.53	3.58
	20	249.85	—	20	161.89	—	20	136.53	—

Table 5.2 Uniaxial and triaxial compression test results of slate specimens with different

sizes and loading directions (*part 2*).

Diameter (mm)	β =45°			β =60°			β =90°		
	σ_3 (MPa)	σ_1 (MPa)	SD (MPa)	σ_3 (MPa)	σ_1 (MPa)	SD (MPa)	σ_3 (MPa)	σ_1 (MPa)	SD (MPa)
19	0	117.12	6.33	0	159.29	11.39	0	190.46	7.66
	0	107.01	7.00	0	147.74	33.61	0	169.14	10.64
	1	121.07	7.41	1	159.06	—	1	176.32	10.69
25	5	150.73	7.89	5	167.56	16.36	5	220.80	1.75
	10	169.37	2.80	10	198.69	16.91	10	240.16	6.67
	20	211.13	37.74	20	251.38	—	20	285.91	—
38	0	99.60	12.51	0	133.01	6.66	0	166.71	16.61
	0	82.51	3.31	0	121.92	6.78	0	157.17	7.40
	1	97.13	3.26	1	130.87	7.63	1	171.74	2.69
50	5	113.76	2.31	5	164.94	3.95	5	207.01	0.16
	10	128.21	22.12	10	189.19	0.21	10	231.60	3.69
	20	155.26	8.96	20	216.28	6.17	20	255.96	2.69
63	0	76.21	28.43	0	115.31	14.34	0	148.38	9.05
	0	82.21	1.39	0	110.84	27.30	0	146.72	0.21
	1	80.94	0.88	1	111.65	18.48	1	167.10	—
75	5	100.23	0.07	5	126.21	14.61	5	168.97	—
	10	100.83	2.19	10	156.10	1.04	10	203.64	—
	20	125.51	0.19	20	184.79	—	20	255.59	—

In order to minimize the influence of heterogeneity, several experiments were carried out on slate samples with each prescribed specimen size and foliation orientation. The mean values of UCS are summarised in Table 5.2 and depicted in Figure 5.9. Based on the experimental results, size effect and anisotropy in the UCS of slate are investigated in this section.

5.4.2.1 Size effect on UCS

Similar to the size effect on tensile strength discussed in Chapter 4 and referring to the experimental results as shown in Figure 5.9, three principles defining the size effect on the UCS of slate should also be followed:

(1) The relationship between UCS and specimen size depends on the mechanical properties of the material.

(2) The variation of UCS with the specimen size shows a descending trend and is closely correlated with the foliation orientation.

(3) For specimens of a prescribed shape, UCS has upper and lower boundaries, with the specimen size varying.

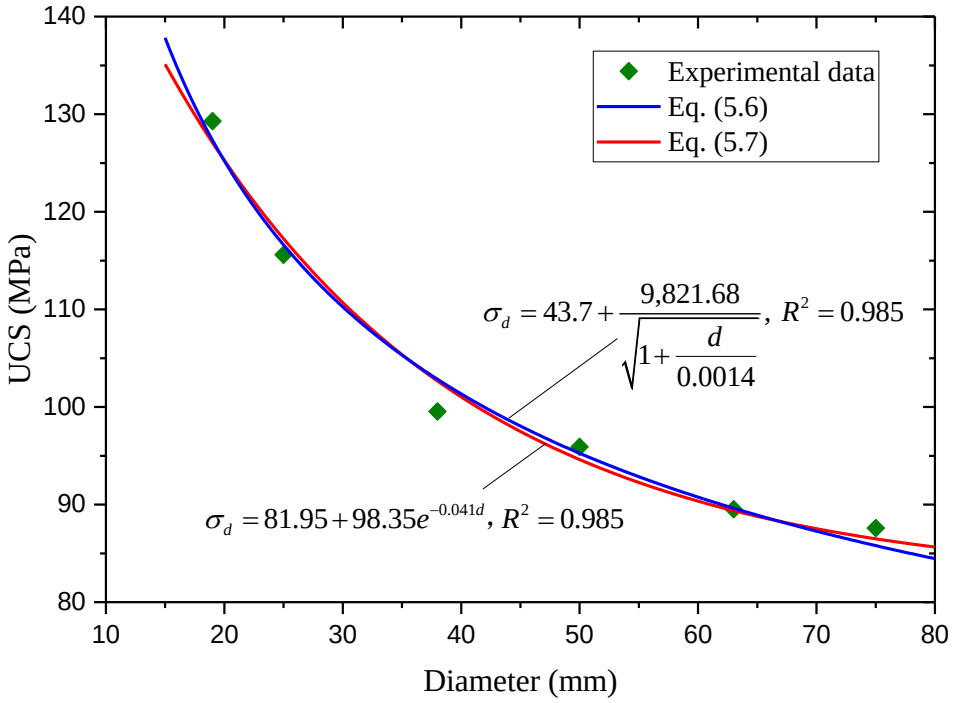

Figure 5.8 Comparison between fitting results of Eqs. (5.6) and (5.7).

As stated in the introduction, classical size-effect models are derived from isotropic materials, but they can be important references for exploring the size-effect model applicable to transversely isotropic materials. Based on the principle (2), the descending size-effect type, including statistical, size-effect law (SEL) and multifractal scaling law (MFSL) models, is considered. Nevertheless, the MFSL model is not able to describe the strength of an infinitesimal sample which is infinite as the sample size approaches zero **(Masoumi et al. 2015)**, violating the principle (3). At this point, introducing both upper and lower boundaries, a transformation of the SEL model expressed as Eq. (5.6) and a statistical model proposed by **(Song et al. 2018)** expressed as Eq. (5.7) are compared, fitting the experimental results as displayed in Figure 5.8. Both equations agree with the experimental data well ($R^2 > 0.98$), but the SEL model does not have a reasonable physical

meaning for the strength of an infinitesimal sample that is at least one order of magnitude larger than the actual value. Thus, the statistical model is adopted.

$$\sigma_d = \sigma_M + \frac{(\sigma_0 - \sigma_M)}{\sqrt{1 + \frac{d}{\lambda d_0}}} \tag{5.6}$$

$$\sigma_d = \sigma_M + (\sigma_0 - \sigma_M)e^{-kd} \tag{5.7}$$

where σ_d represents the UCS of the specimen with a diameter of d; σ_0 and σ_M denote the UCS when $d \to 0$ and $d \to \infty$, respectively; λ and d_0 are same as those in Eq. (2.1); and k is a parameter related to the mechanical properties of the material.

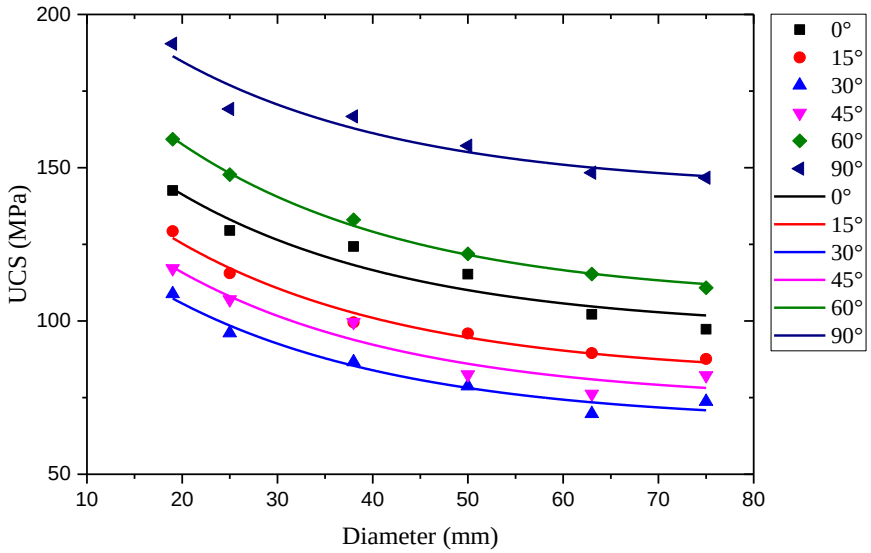

Figure 5.9 Size effects on UCS of slate specimens under different loading-foliation angles.

Figure 5.9 shows variations of the UCS of slate samples with the specimen size as well as fitted results based on Eq. (5.7) under every loading direction. The fitting parameters σ_0, σ_M and k of Eq. (5.7) are listed in Table 5.3. The fitted curves in Figure 5.9 are in agreement with the experimental data with coefficients of determination > 0.92, demonstrating that the UCS of slate follows the descending size-effect trend. The descending size-effect trend is similar to that observed in most isotropic rocks **(Darlington et al. 2011; Hoek and Brown 1980)**, but the severity of size effect on the UCS of slate changes with the loading-foliation angle. To quantify the influence of

anisotropy on the size effect, the derivative of Eq. (5.7) is utilised in the form

$$\sigma_d' = -(\sigma_0 - \sigma_M)ke^{-kd} \tag{5.8}$$

Thus, the severity of size effect is proportional to the magnitude of $(\sigma_0 - \sigma_M)$ since k is positive for the descending size-effect trend. Overall, the influence of size effect is reduced as the specimen size increases. Referring to values of σ_0, σ_M and k as listed in Table 5.3, it is inferred that the strongest and weakest size effects occur at β = 60° and β = 30°, respectively.

Furthermore, for a specified loading direction, σ_0 and σ_M predicted by Eq. (5.7) correspond to the maximum and minimum UCS, respectively, throughout the range of specimen sizes. The estimated UCS of slate ranges between 66.79 and 237.73 MPa, regardless of specimen size and loading direction.

Table 5.3 Fitting parameters in Eq. (5.7) for UCS of slate specimens with different sizes loaded under different loading-foliation angles.

β (°)	0	15	30	45	60	90
σ_0 (MPa)	197.32	180.30	155.16	169.28	222.37	237.73
σ_M (MPa)	97.18	81.95	66.79	73.75	106.70	142.88
$\sigma_0 - \sigma_M$ (MPa)	100.14	98.35	88.37	95.53	115.67	94.85
k	0.041					
R^2	0.929	0.985	0.971	0.935	0.997	0.925

5.4.2.2 Anisotropy of UCS

The experimental data on UCS for specimen diameters of 19, 25, 38, 50, 63 and 75 mm and the predicted data for specimen sizes approaching both 0 and ∞ versus loading-foliation angle are plotted in Figure 5.10, presenting the U-type, different from the undulatory-type and shoulder-type as classified by **Ramamurthy (1993)**. For groups with various sample sizes, the maxima of UCS are located at β = 90°, and the minima of UCS occur at β = 30° close to (45°-φ), where φ is the friction angle along the foliation plane.

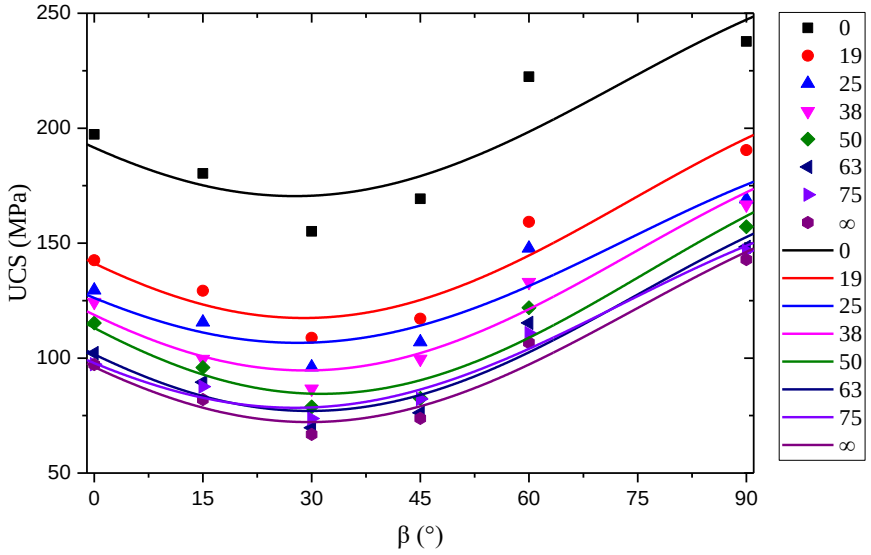

Figure 5.10 Anisotropy in UCS of slate samples with different size.

Numerous approaches have been proposed to describe the relationship between compressive strength and loading direction for transversely isotropic rocks as reviewed in **Duveau et al. (1998)** and **Pei (2008)**. Among these methods, the empirical equation developed initially by **Jaeger (1960)** and improved by **Donath (1961)** is used most commonly in uniaxial compression conditions. The equation is in the form

$$\sigma_\beta = A - D\cos 2(\beta - \beta_{\min}) \tag{5.9}$$

where σ_β is the UCS at the loading-foliation angle of β; $\beta_{\min}$ corresponds to the angle at which UCS is minimum; A and D are two constants. Fitting curves and parameters of both experimental and predicted UCS based on Eq. (5.9) are plotted in Figure 5.10 and summarised in Table 5.4, respectively. Fitting curves agree reasonably well with both the experimental and predicted data. The determined $\beta_{\min}$ fluctuates between 27.7° and 31.3°, with an average angle of 29.2°. The fitting parameter *A* decreases, while D varies little with the specimen size. It is demonstrated that parameter A is correlated to the size effect. The strength anisotropy is usually represented by the following equation **(Ramamurthy 1993)**:

$$R_c = \frac{\sigma_{c(90)}}{\sigma_{c(\min)}} \tag{5.10}$$

where R_c is the degree of anisotropy; $\sigma_{c(90)}$ is the UCS at β = 90°; and $\sigma_{c(\min)}$ is the minimum UCS commonly at β = 30—45°. The values of R_c at specimen diameters approaching 0, equal to 19, 25, 38, 50, 63, 75 mm, and approaching infinite are 1.53, 1.75, 1.76, 1.92, 2.00, 2.13, 1.99 and 2.14, respectively. In general, the degree of strength anisotropy in slate increases with the specimen size, and then stabilizes for samples larger than a critical size. The critical specimen diameter is 63 mm for slate in this analysis.

Table 5.4 Parameters in Eq. (5.9) when the diameter of slate specimen is different.

Diameter (mm)	$d \to 0$	19	25	38	50	63	75	$d \to \infty$
$\beta_{\min}$ (°)	27.7	28.9	28.1	29.2	31.3	29.7	27.7	29.6
A	219.37	168.41	150.83	145.46	137.46	127.15	123.35	121.18
D	48.91	50.97	44.18	50.82	53.00	50.14	44.96	49.01
R^2	0.790	0.907	0.864	0.937	0.930	0.920	0.967	0.955

5.4.2.3 Universal equation for size-effect and anisotropy of UCS

Combining Eqs. (5.7) and (5.9), **Song et al. (2018)** proposed a unified empirical equation describing both the size effect and anisotropy of UCS expressed as

$$\sigma_{c\beta d} = A_M - D_M \cos 2(\beta - \beta_{\min}) + \left[(A_0 - A_M) - (D_0 - D_M)\cos 2(\beta - \beta_{\min})\right] e^{-kd} \qquad (5.11)$$

where $\sigma_{c\beta d}$ is the UCS of specimen with the diameter of d at the loading-foliation angle of β; A_0 and D_0, A_M and D_M are A and D constants for specimen size approaching zero or infinite, respectively; k is a characteristic parameter related to the material as mentions in Eq. (5.7); $\beta_{\min}$ is the average of β at which UCS is minimum.

The fitted equation by Eq. (5.11) is as follow:

$$\sigma_{c\beta d} = 120.84 - 48.58\cos 2(\beta - 29.2) + \left[(220.64\text{-}120.84)\text{-}(50.41\text{-}48.58)\cos 2(\beta - 29.2)\right] e^{-0.041d},\ R^2 = 0.933 \qquad (5.12)$$

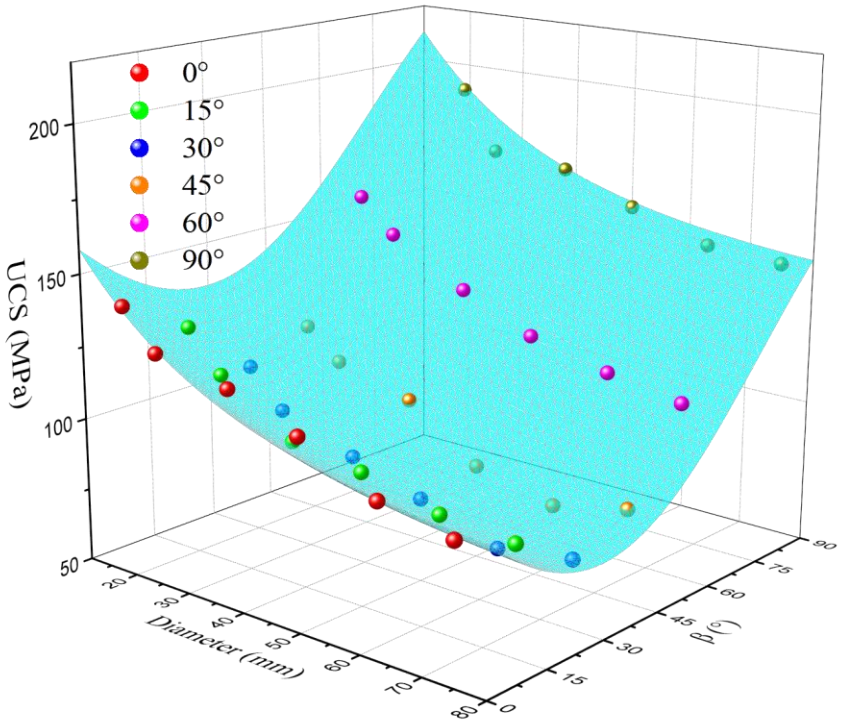

Figure 5.11 Comparison between experimental data and a theoretical surface obtained by Eq. (5.12) for specimens of different diameters at various loading directions.

The experimental data and the fitted surface obtained by Eq. (5.12) for specimens of different diameters at various loading directions are compared as shown in Figure 5.11. The theoretical surface is in agreement with the experimental data with a high reliability (R^2 = 0.933). It demonstrates the applicability of the universal equation to slate, a transversely isotropic rock. Consequently, the universal equation proposed by **Song et al. (2018)** is recommended for describing the relationship among UCS, specimen size and loading direction for the transversely isotropic rock. It is also a basic step for the further study of the size effect of transversely isotropic rocks in triaxial conditions.

5.4.3 Triaxial compressive strength

The triaxial compressive strength (TCS), corresponding to the peak axial stresses in stress-strain curves, is extracted from this experiment. The mean values of the TCS of slate samples with diameters of 25, 50 and 75 mm at different confining pressures and foliation orientations relative to the maximum principal stress are summarised in Table 5.2 and depicted in Figure 5.12.

5.4.3.1 *Size effect on TCS*

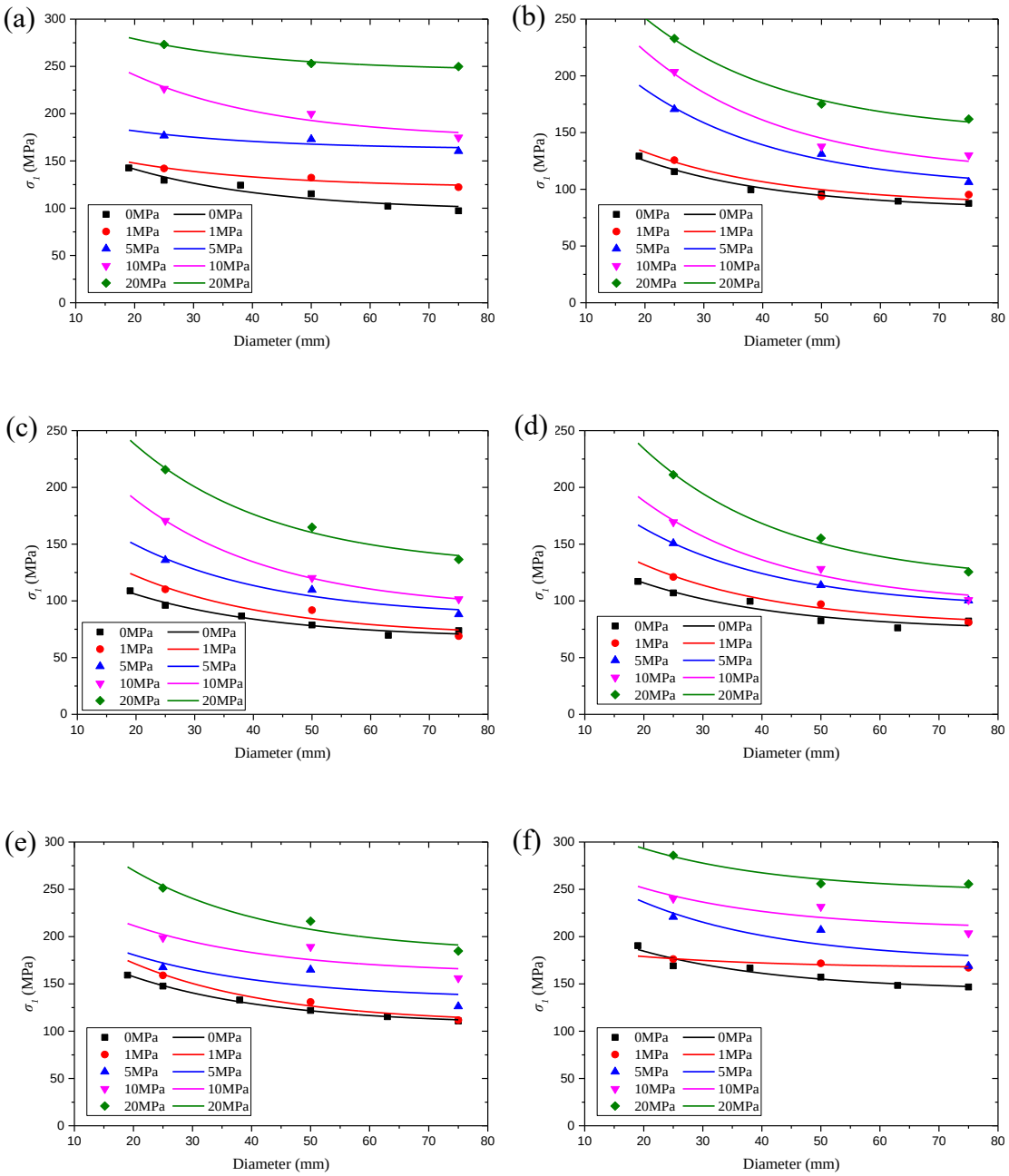

Figure 5.12 Compressive strength versus sample diameter and fitted curves based on Eq. (5.10) at different confining pressures: (a) β =0°; (b) β =15°; (c) β =30°; (d) β =45°; (e) β =60° and (f) β =90°.

As seen in Figure 5.12, variations of both UCS and TCS with the specimen size present a similar trend in line with the observed results in gypsum **(Hunt 1973)** and sandstone **(Masoumi et al. 2016)**. Hence, the descending size-effect model applicable to the UCS

was also utilised to fit the experimental data of TCS. The fitted curves of TCS based on Eq. (5.7) are plotted in Figure 5.12, and fitted parameters are obtained as listed in Table 5.5 with k being a constant of 0.041.

Table 5.5 Comparison of values of $(\sigma_0 - \sigma_M)$ at different confining pressures and foliation orientations.

β (°)			0					15		
σ_3	0	1	5	10	20	0	1	5	10	20
σ_0	197.3	180.6	206.8	326.9	322.3	180.3	192.1	299.1	359.5	381.0
σ_M	97.2	121.7	162.0	173.0	244.9	81.9	86.1	100.7	113.3	148.6
$\sigma_0 - \sigma_M$	100.1	58.9	44.8	153.9	77.4	98.4	106.0	198.4	246.2	232.4
β (°)			30					45		
σ_3	0	1	5	10	20	0	1	5	10	20
σ_0	155.2	189.5	229.9	312.3	374.8	169.3	200.9	254.2	305.9	383.6
σ_M	66.8	68.8	85.6	91.6	128.6	73.8	77.8	92.9	95.4	116.4
$\sigma_0 - \sigma_M$	88.4	120.7	144.3	220.7	246.2	95.5	123.1	161.3	210.5	267.2
β (°)			60					90		
σ_3	0	1	5	10	20	0	1	5	10	20
σ_0	222.4	253.4	240.2	276.5	381.9	237.7	194.3	316.5	307.1	351.4
σ_M	106.7	108.0	134.0	160.7	181.9	142.9	166.8	173.5	207.4	247.3
$\sigma_0 - \sigma_M$	115.7	145.4	106.2	115.8	200.0	94.8	27.5	143.0	99.7	104.1

Furthermore, Eq. (5.8) was employed to quantify the severity of size effect on TCS at different foliation angles and confining pressures. As discussed in section 5.4.2.1, the severity of size effect is proportional to the magnitude of $(\sigma_0 - \sigma_M)$. Based on the values of $(\sigma_0 - \sigma_M)$ in Table 5.5, the influence of confining pressures on the size effect of compressive strength is weak when β = 0°, 60° and 90°, whereas it is strong when β is in the range of 15° to 45°, as also presented in Figure 5.12. When β is located at 15° to 45°, the severity of the size effect on compressive strength increases with the confining pressure, which is contradictory to the viewpoint **(Aubertin et al. 2000)** that confining pressures suppress the size effect in rocks. **Aubertin et al. (2000)** thought that the change

from brittle to ductile behaviour and the closure of microcracks with increasing confinement diminish the size effect. This discrepancy may be attributed to the unique failure mode, viz., sliding failure along the foliations, observed in the slate at β of 15° to 45° and confining pressures of 0 to 20 MPa. There exists a characteristic confining pressure above which size dependency starts to diminish as the confining pressure increases, because the failure mode at β of 15° to 45° is transformed to slide across the foliations, resulting in the change from brittle to ductile failure.

For simplification, in this analysis, size effects on compressive strength at different confining pressures are assumed to be identical when the samples stay within the brittle regime.

5.4.3.2 *Anisotropy of TCS*

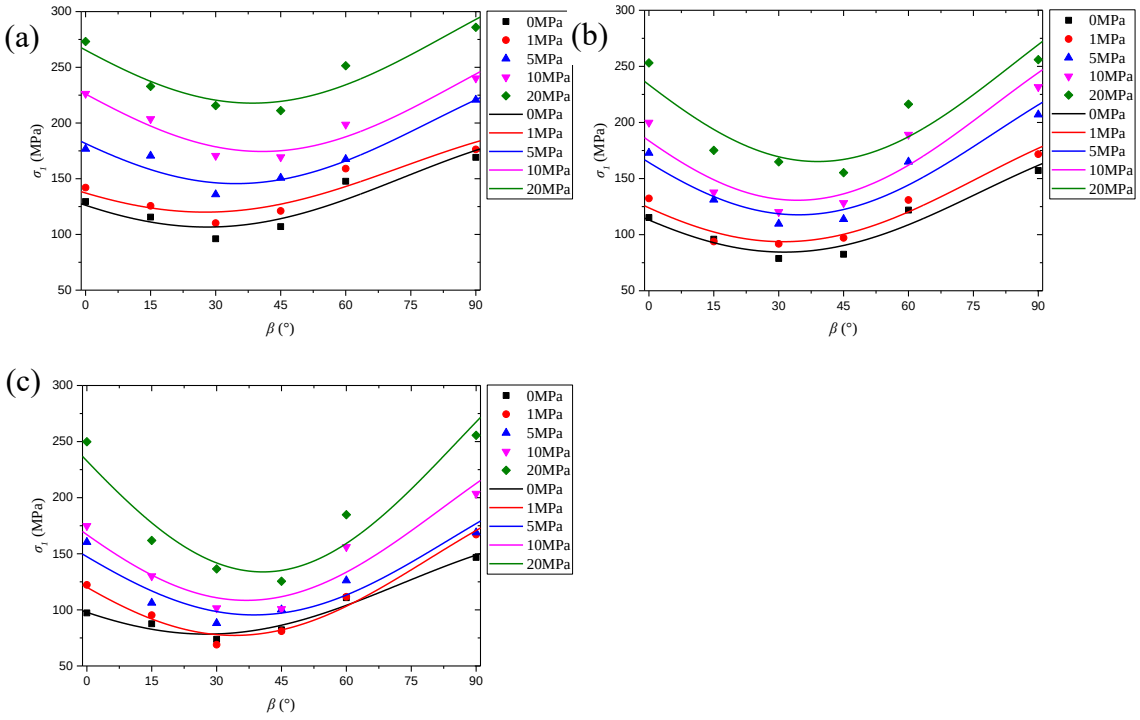

Figure 5.13 Variation of UCS and triaxial compressive strength of slate with different specimen diameters versus β: (a) d=25mm, (b) d=50mm and (c) d=75mm.

Variations in the triaxial compressive strength of slate samples with diameters of 25, 50 and 75 mm at different confining pressures versus foliation orientations are displayed in Figure 5.13, and all the anisotropy curves are U-type. The maxima in anisotropy curves

lie in $\beta = 90°$, but with increasing confining pressure, the maxima are inclined to shift to $\beta = 0°$. The minima of anisotropy curves are found to shift gradually from $\beta = 30°$ to $\beta = 45°$ as the confining pressure increases. Additionally, anisotropy curves are fitted by Eq. (5.9) as shown in Figure 5.13, and the fitted results are summarised in Table 5.6. The results indicate that fitted curves based on Eq. (5.9) agree with the experimental data. The values of parameter A increase as confining pressures increase, while at the same time decreasing with increasing specimen size, and the values of parameter D increase with the confining pressure. It has also been observed that the range of TCS for $\beta = 15°—45°$ at confining pressures between 0 and 20 MPa decreases as the specimen size increases, particularly for the case of $\beta = 45°$. The smaller effect of confining pressure for $\beta = 15°—45°$ can be attributed to the sliding failure along the foliation planes, which is consistent with the observed results in schist **(Duveau et al. 1998)**.

Table 5.6 Parameters in Eq. (5.9) when the slate specimen is loaded at different confining pressures.

Confining pressures (MPa)		0	1	5	10	20
$d = 25$ mm	β_{min} (°)	28.1	27.6	34.7	40.7	38.5
	A	150.83	160.05	201.27	235.02	279.24
	D	44.18	40.01	55.66	60.55	61.38
	R^2	0.864	0.852	0.930	0.933	0.890
$d = 50$ mm	β_{min} (°)	31.33	31.06	34.59	34.33	39.02
	A	137.46	150.47	190.01	214.03	251.50
	D	53.00	56.73	72.31	83.36	86.31
	R^2	0.930	0.940	0.899	0.855	0.809
$d = 75$ mm	β_{min} (°)	27.7	34.1	38.6	36.9	40.7
	A	123.35	145.49	162.18	189.87	250.15
	D	44.96	68.24	66.67	81.38	116.30
	R^2	0.967	0.970	0.886	0.900	0.907

5.4.3.3 Size-dependent modified Hoek-Brown failure criterion

As discussed in the previous section, the size dependencies on the UCS and TCS of slate are similar and are thus postulated to be identical for simplification. The size-effect

relation for UCS, Eq. (5.11), is incorporated into the modified Hoek-Brown criterion, Eq. (2.22), resulting in a size-dependent failure criterion that can comprehensively capture the relationship among the compressive strength, anisotropic orientation, specimen size and confining pressure in the form:

$$\sigma_1 = \sigma_3 + \left\{ A_M - D_M \cos 2(\beta - \beta_{\min}) + \left[(A_0 - A_M) - (D_0 - D_M) \cos 2(\beta - \beta_{\min}) \right] e^{-kd} \right\} \times \left(k_\beta m_i \frac{\sigma_3}{\left\{ A_M - D_M \cos 2(\beta - \beta_{\min}) + \left[(A_0 - A_M) - (D_0 - D_M) \cos 2(\beta - \beta_{\min}) \right] e^{-kd} \right\}} + 1 \right)^{0.5} \quad (5.13)$$

Table 5.7 Parameters in Eqs. (5.13) and (5.14) when the slate specimen is loaded at different confining pressures.

β (°)		0	15	30	45	60	90
Size-dependent modified H-B failure criterion	k_β	1.91	1.09	0.76	0.57	1.14	1.00
	MPE	4.8%	7.9%	7.9%	7.4%	7.4%	4.1%
	R^2	0.980	0.889	0.930	0.882	0.922	0.948
Size-dependent Saeidi failure criterion	α_β	0.96	0.98	1.08	1.07	0.91	1.03
	P	13.73	20.99	11.82	22.82	9.11	16.73
	Q	3.74	9.98	4.96	13.93	3.44	8.23
	MPE	4.5%	5.8%	7.1%	6.6%	4.7%	3.8%
	R^2	0.978	0.939	0.926	0.910	0.945	0.958

Firstly, the values of the parameters in Eq. (5.11) were calibrated based on UCS data, and the resulting parameters for slate are shown in Eq. (5.12). The value of m_i was then obtained by fitting the size-dependent modified Hoek-Brown criterion to the compressive strength data obtained at β = 90°, provided that k_β is 1.0, and was further utilised to determine the values of k_β at other anisotropic orientations. The resulting value of m_i is 10.78 for slate. Fitting parameters in Eq. (5.13) based on uniaxial and triaxial data are summarised in Table 5.7, and the predicted peak stresses versus specimen diameter and confining pressure at different loading directions are plotted as cyan surfaces in Figure 5.14. The fitted value of k_β decreases initially and then increases with the foliation orientation, reaching the maximum and minimum at β = 0° and β = 45°, respectively.

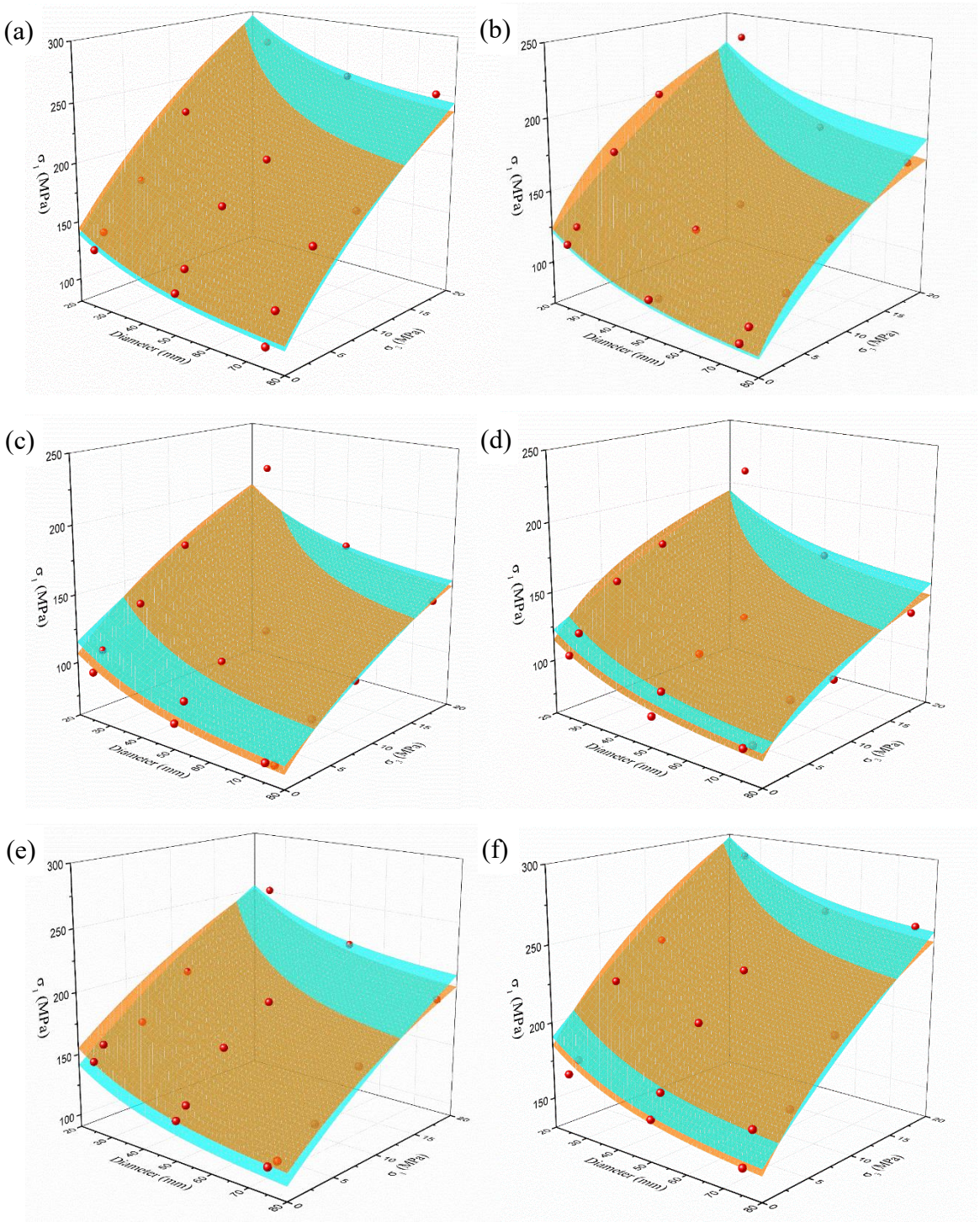

Figure 5.14 Comparison between applicability of proposed size-dependent failure criteria based on the modified Hoek-Brown criterion and the Saeidi criterion to the compressive strength obtained from slate samples with different sizes at different confining pressures and loading directions: (a) β =0°; (b) β =15°; (c) β =30°; (d) β =45°; (e) β =60° and (f) β =90°. The cyan surface represents the size-dependent modified Hoek-Brown failure criterion. The orange surface represents the size-dependent Saeidi failure criterion.

Fitted surfaces are in agreement with the experimental data with coefficients of determination larger than 0.88. The MPEs for the compressive strength of slate samples at different loading directions are lower than 10%, within an acceptable range for practical engineering applications. Consequently, the proposed size-dependent modified Hoek-Brown failure criterion is capable of predicting the peak strength of slate under uniaxial and triaxial conditions regardless of specimen size, foliation orientation or confining pressure. However, inheriting from the basic failure criterion of Hoek–Brown, the size-dependent failure criterion is limited to the brittle regime and neglects the influence of intermediate principal stress.

5.4.3.4 Size-dependent Saeidi failure criterion

Similar to the size-dependent modified Hoek-Brown failure criterion, the size-dependent Saeidi failure criterion is proposed by including size effect in the Saeidi failure criterion, Eq. (2.24). As a result, $\sigma_{c\beta}$ in the Saeidi failure criterion is substituted by Eq. (5.11) according to

$$\sigma_1 = \sigma_3 + \frac{\left\{A_M - D_M \cos 2(\beta - \beta_{\min}) + \left[(A_0 - A_M) - (D_0 - D_M)\cos 2(\beta - \beta_{\min})\right]e^{-kd}\right\} + P\sigma_3}{\alpha_\beta + Q\sigma_3 / \left\{A_M - D_M \cos 2(\beta - \beta_{\min}) + \left[(A_0 - A_M) - (D_0 - D_M)\cos 2(\beta - \beta_{\min})\right]e^{-kd}\right\}} \tag{5.14}$$

After the size-effect model for UCS is calibrated, the triaxial data are fitted by Eq. (5.14). The fitted surfaces are plotted as orange surfaces in Figure 5.14, and fitted parameters are listed in Table 5.7. Compared with fitted results based on Eq. (5.13), the data predicted by Eq. (5.14) agree better with the experimental data with higher R^2 and lower MPEs. As seen from the theoretical surfaces in Figure 5.14, the size-dependent Saeidi failure criterion has fitted the experimental data points well, whereas the size-dependent modified Hoek-Brown failure criterion has overpredicted the strength at high confining pressures and underpredicted it at intermediate confining pressures at every loading direction. It has also overpredicted the strength at low confining pressures for $\beta = 30°$, 45° and 90°. However, the size-dependent Saeidi failure criterion needs more tests performed in order to determine the parameters in the expression relative to the size-dependent modified Hoek-Brown failure criterion. One common drawback of both of the proposed size-dependent failure criteria in this study is that they are incapable of estimating rock

strength in true-triaxial conditions.

Table 5.8 Comparisons between the measured tensile strength by experiment in Chapter 4 and the predicted one by size-dependent failure criteria.

Diameter (mm)	β =0°			β =15°			β =30°		
	σ_t^m (MPa)	σ_t^{p1} (MPa)	σ_t^{p2} (MPa)	σ_t^m (MPa)	σ_t^{p1} (MPa)	σ_t^{p2} (MPa)	σ_t^m (MPa)	σ_t^{p1} (MPa)	σ_t^{p2} (MPa)
25	19.60	6.34	9.07	17.50	9.55	5.27	10.19	12.94	8.59
38	21.95	5.63	8.05	19.23	8.32	4.59	13.36	11.19	7.43
50	20.15	5.24	7.49	13.33	7.65	4.22	12.50	10.22	6.79
63	16.47	4.99	7.13	14.20	7.21	3.98	9.30	9.60	6.37
75	12.45	4.85	6.92	11.53	6.96	3.84	9.30	9.25	6.14
100	12.55	4.70	6.72	10.41	6.72	3.71	9.01	8.90	5.91
Diameter (mm)	β =45°			β =60°			β =90°		
	σ_t^m (MPa)	σ_t^{p1} (MPa)	σ_t^{p2} (MPa)	σ_t^m (MPa)	σ_t^{p1} (MPa)	σ_t^{p2} (MPa)	σ_t^m (MPa)	σ_t^{p1} (MPa)	σ_t^{p2} (MPa)
25	13.10	18.17	4.93	9.20	10.74	13.78	9.10	16.78	10.56
38	12.20	15.86	4.30	8.98	9.56	12.27	8.66	15.41	9.69
50	10.16	14.59	3.96	7.57	8.91	11.43	4.87	14.65	6.21
63	8.69	13.76	3.73	5.34	8.48	10.88	6.61	14.16	8.90
75	10.05	13.30	3.61	6.71	8.25	10.58	5.66	13.88	8.73
100	5.95	12.84	3.48	4.84	8.01	10.28	3.32	13.61	8.56

Additionally, in order to evaluate the applicability of the two size-dependent failure criteria for the estimation of the tensile strength of slate, comparisons between predicted and measured values are made, as listed in Table 5.8. σ_t^{p1} and σ_t^{p2} are the values of tensile strength predicted by the size-dependent modified Hoek-Brown and Saeidi failure criteria, respectively. The results indicate that the size-dependent modified Hoek-Brown failure criterion underestimates and overestimates the tensile strength when β is low (0° and 15°) and high (45° − 90°), respectively, and agrees well with the tensile strength at β = 30°. Nevertheless, the size-dependent Saeidi failure criterion continuously underpredicts the tensile strength as β increases from 0° to 45°, while overpredicting the tensile strength for β = 60° − 90°. Moreover, the tensile strength predicted by the two criteria always presents a descending size-effect trend, but the one observed in the

laboratory exhibits an initially increasing and then decreasing size-effect trend when the loading-foliation angle is high (60°-90°). Overall, the two proposed failure criteria are incapable of predicting rock strength in tensile conditions.

5.4.4 Triaxial residual strength

Since rocks around underground structures (e.g., tunnels, caverns and mining stopes) are still able to sustain certain levels of stress even after they reach the post-peak deformation phase, the residual strength is significant for the safe and optimum design of underground structures **(Gao and Kang 2016; Peng and Cai 2019)**. The residual strength, σ_r, is usually defined as a constant level of stress under which the deformation of existing cracks continues after the peak strength. It can be determined through the flattening trend along the post-failure portion of the stress-strain curve **(Tutluoğlu et al. 2015)**. Due to the extremely brittle nature of the tested slate under uniaxial compression, only the triaxial residual strength (TRS) of specimens with different sizes and foliation orientations was measured under different confining pressures as listed in Table 5.9.

5.4.4.1 Size effect on triaxial residual strength

To evaluate whether the residual strength of slate follows a size-effect trend or not, its variation with the specimen size in three cases of β = 0°, 45° and 90° is shown in Figure 5.15. The observed finding is that the triaxial residual strength of slate does not present an evident size-effect trend irrespective of loading direction and confining pressure, different from the peak strength. It can be explained that a brittle or semi-brittle material, after broken, degrades into the ductile material with the size effect disappearing **(Aubertin et al. 2000)**.

Table 5.9 Triaxial residual strength of slate specimens with different sizes and loading directions.

Diameter (mm)	β =0°			β =15°			β =30°		
	σ_3 (MPa)	σ_r (MPa)	SD (MPa)	σ_3 (MPa)	σ_r (MPa)	SD (MPa)	σ_3 (MPa)	σ_r (MPa)	SD (MPa)
25	1	29.81	0.59	1	23.10	—	1	26.69	3.92
	5	62.73	1.00	5	37.58	1.88	5	37.02	1.13
	10	86.28	1.26	10	75.52	8.39	10	49.74	—
	20	137.65	—	20	126.55	3.72	20	119.99	7.07
50	1	25.36	1.70	1	20.57	2.93	1	23.44	3.46
	5	68.90	—	5	42.12	0.41	5	66.15	—
	10	87.54	—	10	60.31	0.05	10	83.45	2.95
	20	138.92	0.06	20	106.02	3.42	20	88.56	1.27
75	1	24.03	1.93	1	19.92	4.07	1	17.01	2.50
	5	60.34	3.97	5	38.20	7.24	5	34.19	1.98
	10	83.44	4.99	10	58.48	0.55	10	50.17	4.13
	20	128.03	—	20	101.91		20	87.33	—
Diameter (mm)	β =45°			β =60°			β =90°		
	σ_3 (MPa)	σ_r (MPa)	SD (MPa)	σ_3 (MPa)	σ_r (MPa)	SD (MPa)	σ_3 (MPa)	σ_r (MPa)	SD (MPa)
25	1	28.58	2.35	1	20.84	—	1	14.01	1.63
	5	38.05	5.17	5	50.68	—	5	39.60	2.00
	10	64.55	6.24	10	76.85	3.78	10	65.87	1.12
	20	111.59	—	20	113.55	—	20	122.84	—
50	1	19.84	0.74	1	19.73	0.25	1	13.90	—
	5	38.58	6.80	5	38.27	—	5	58.26	—
	10	48.95	2.29	10	68.60	0.25	10	76.30	—
	20	88.67	4.48	20	128.34	4.67	20	100.10	—
75	1	17.61	1.42	1	32.37	1.81	1	12.67	—
	5	33.42	6.57	5	46.82	—	5	35.76	—
	10	59.27	4.38	10	68.79	7.63	10	67.22	—
	20	78.94	0.31	20	—	—	20	102.98	—

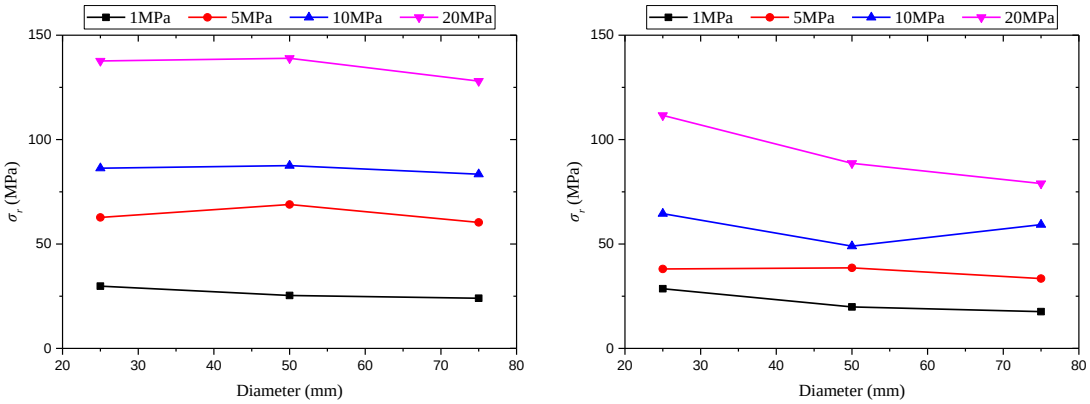

(a) (b)

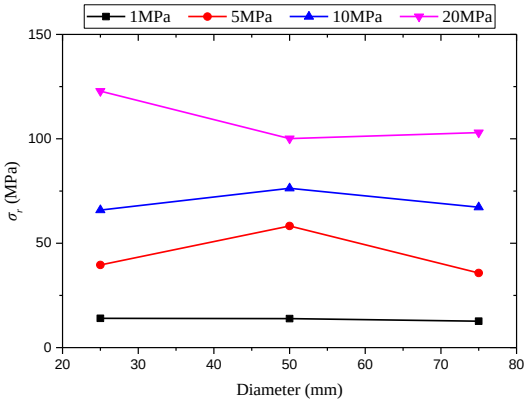

(c)

Figure 5.15 Triaxial residual strength versus sample diameter at different confining pressures: (a) β =0°; (b) β =45°; and (c) β =90°.

5.4.4.2 Anisotropy of triaxial residual strength

As can be seen from Figure 5.16, the anisotropy of the triaxial residual strength of slate is very similar for different specimen sizes. When the applied confining pressure is 1 MPa, the residual strength varies little, fluctuating at approximately 25 MPa. As the confining pressure increases from 5 to 20 MPa, the anisotropy of the residual strength increases and presents a U-shaped curve similar to the findings of **(Liao and Hsieh 1999)** in argillite, with the maxima in the anisotropy curves located at β = 0° and the minima shifting from β = 30° to β = 45°.

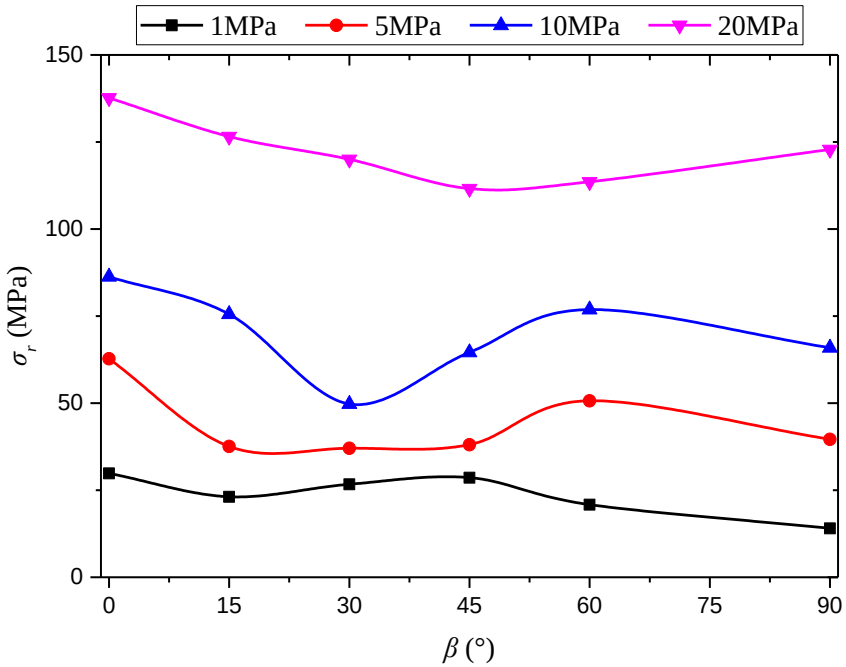

(a)

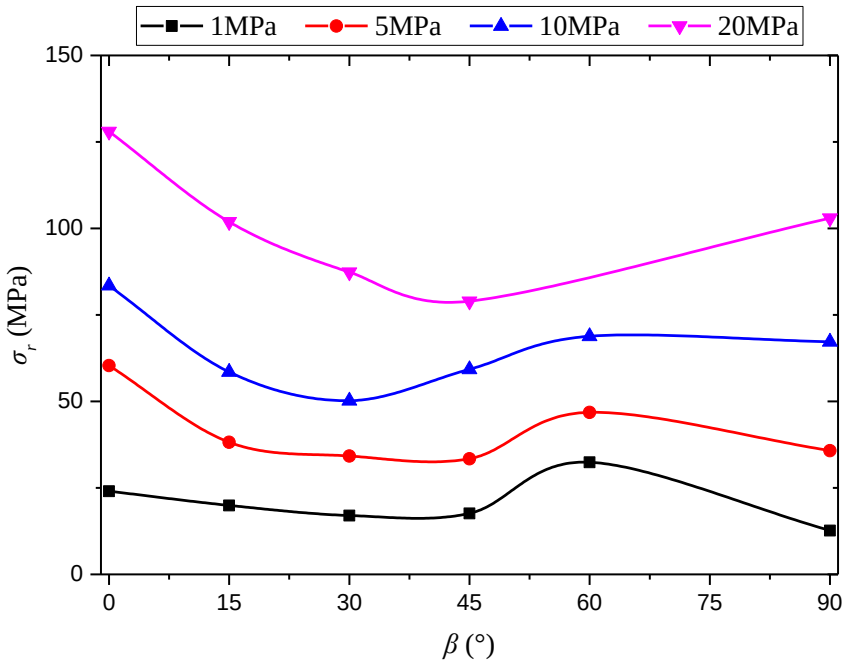

(b)

Figure 5.16 Variation of triaxial residual strength of slate with different specimen diameters versus β: (a) d=25mm and (b) d=75mm.

5.4.4.3 *Modified cohesion loss model*

Most recently, **Peng and Cai (2019)** reviewed various methods including Mohr-Coulomb, Joseph-Barron, Hoek-Brown and GSI-softening models, and proposed a cohesion loss model for estimating the residual strength of intact rocks according to

$$\sigma_1 = \sigma_3 + \left(\lambda_i \sigma_c \sigma_3\right)^{0.5} \tag{5.15}$$

where λ_i is a dimensionless parameter and σ_c represents the UCS of intact rock.

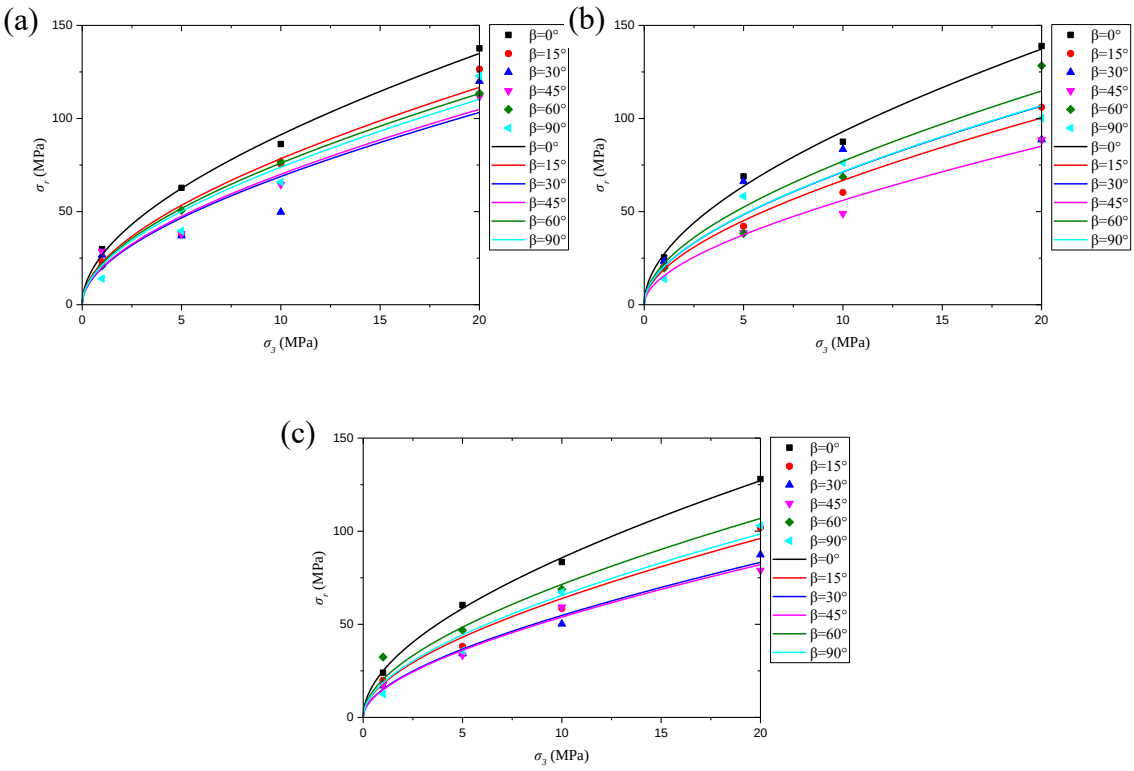

Figure 5.17 Experimental values of triaxial residual strength and fitted curves based on the modified cohesion loss model for slate samples with different sizes: (a) *d*=25mm; (b) *d*=50mm and (c) *d*=75mm.

The cohesion loss model is derived from the generalized Hoek-Brown failure criterion by taking the parameter *s* as zero (the cohesion loss concept) because the value of *s* is very small (<0.01) when GSI $\leqq$ 60. Moreover, the applicability of the cohesion loss model to various types of intact rocks has been validated. The cohesion loss model has the advantage of passing through the origin in the σ_1-σ_3 space, nonlinearity and simple

form, but neglects the influence of the intermediate principal stress and the inherent anisotropy of rock. To extend the model in order to estimate the residual strength of transversely isotropic rocks, a modified cohesion loss model is proposed and given as

$$\begin{cases} \sigma_1 = \sigma_3 + \left(\lambda_\beta \sigma_{c\beta} \sigma_3\right)^{0.5} \\ \lambda_\beta = \lambda_m + \left(\lambda_0 - \lambda_m\right) e^{-g\beta} \end{cases} \tag{5.16}$$

where $\sigma_{c\beta}$ is the UCS at a loading-foliation angle of β; and λ_β is a parameter describing the anisotropy effect as a function of β; λ_0, λ_m and g are constants.

Table 5.10 Fitting parameters of Eq. (5.16) for residual strengths of slate samples under different loading directions.

β (°)		0	15	30	45	60	90
	$\sigma_{c\beta}$	129.5	115.6	96.1	107.0	147.7	169.1
d = 25 mm	λ_β	5.1	4.0	3.6	3.4	3.0	2.4
	R^2	0.99	0.94	0.85	0.94	1.00	0.94
	$\sigma_{c\beta}$	115.2	95.9	78.8	82.5	121.9	157.2
d = 50 mm	λ_β	6.0	3.4	4.8	2.6	3.7	2.4
	R^2	0.99	0.98	0.69	0.97	0.93	0.95
	$\sigma_{c\beta}$	97.3	87.6	73.7	82.2	110.8	146.7
d = 75 mm	λ_β	5.9	3.3	2.7	2.3	3.4	2.1
	R^2	1.00	0.98	0.98	0.98	0.77	0.97

The experimental residual strength of slate with different specimen sizes and loading directions as well as fitted curves based on the modified cohesion loss model are depicted in Figure 5.17, and their fitting parameters are summarised in Table 5.10. The results indicate that the modified cohesion loss model captures the relationship between residual strength and confining pressure well for slate in this study. To the author's knowledge, little research in relation to the residual strength of transversely isotropic rocks takes the anisotropy effect into consideration. Although the residual strength data of argillite were obtained at different confining pressures and anisotropic orientations **(Liao and Hsieh**

1999), the corresponding UCS data were unknown due to the adopted multiple-failure-state test method. Thus, the published data cannot be used to validate the model. In the future, more systematic investigations into the residual behaviour are needed in order to explore the applicability of the modified cohesion loss model to other transversely isotropic rocks.

Additionally, the parameter λ_β varies little with the specimen size, whereas its variation with β is evident as illustrated in Figure 5.18. The parameter λ_β gradually decreases as the β increases, i.e. $\lambda_\beta = 2.73 + (5.56 - 2.73)e^{-0.055\beta}$, attaining the maxima and minima at β = 0° and 90°, respectively. Overall, λ_β for the slate ranges between 2 and 6. The big difference in λ_β demonstrates again that an anisotropy effect on the residual strength of slate exists.

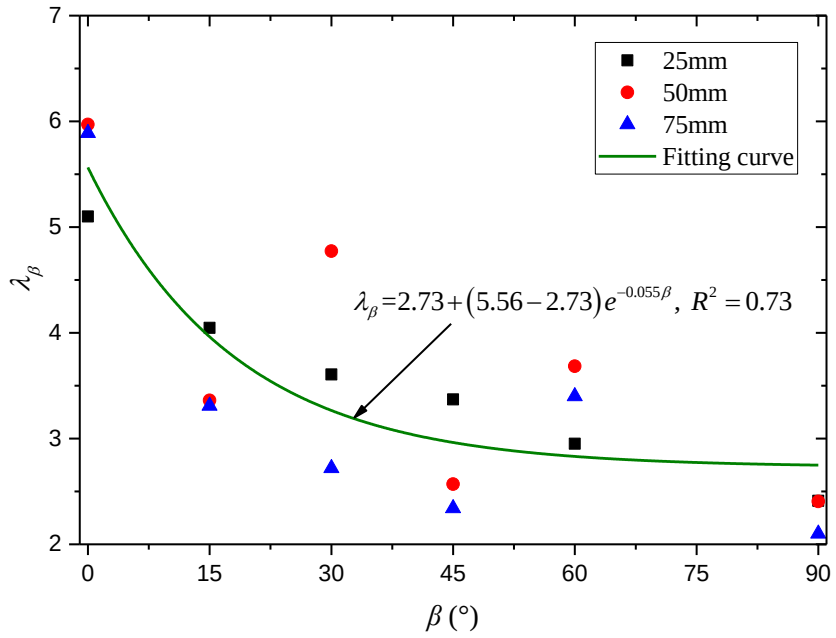

Figure 5.18 Variation of parameters λ_β with β.

5.4.4.4 Ratio between residual and peak strength

The ratio of residual to peak strength (σ_r/σ_p) ranges from 0 to 1, reflecting the transition from a highly brittle state to a plastic state. The variations of σ_r/σ_p of different transversely isotropic rocks, including sandstone **(Gowd and Rummel 1980; Yang et al.**

2012), schist and gneiss **(Kumar et al. 2010)**, mudstone **(Yinlong et al. 2010)**, limestone and marble **(Walton et al. 2015)** as well as slate (this study), with the confining pressure, are compiled and compared as shown in Figure 5.20. The results show that σ_r/σ_p increases as a function of confining pressure for transversely isotropic rocks, following the cohesion-weakening-friction-strengthening (CWFS) model for the brittle failure of rock, as demonstrated and verified by **Hajiabdolmajid et al. (2002)** and **Martin and Chandler (1994)**. The model has also been supported recently by both numerical **(Gao and Kang 2016)** and experimental results **(Rafiei Renani and Martin 2018; Walton et al. 2018)**.

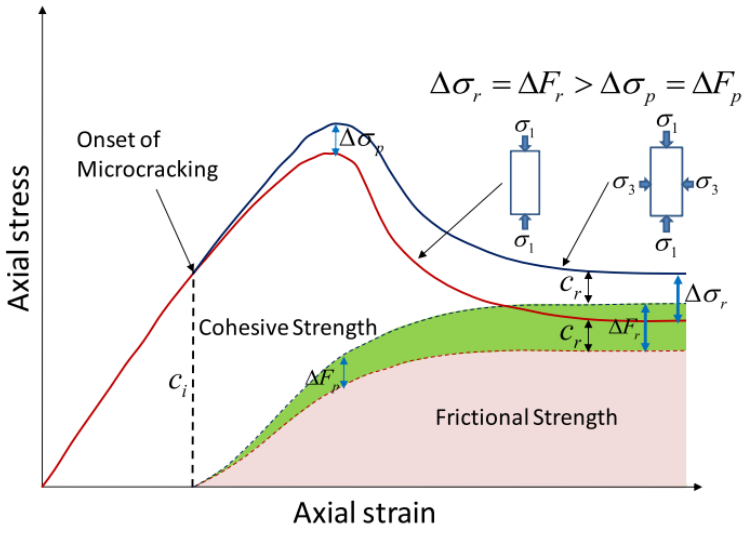

Figure 5.19 Mobilization of the cohesive and frictional strength in the CWFS model, from Ref. **(Gao and Kang 2016)**. c_i and c_r represent the initial and residual cohesive strength, respectively; ΔF_p and ΔF_r denote the increasement in frictional strength due to the increased confinement at the peak and residual stage, respectively; $\Delta\sigma_p$ and $\Delta\sigma_r$ refer to the increased peak and residual strength due to increased confining pressure, respectively.

As illustrated in Figure 5.19, when a rock material is undergoing a triaxial compression test, the cohesive strength is mobilized from an initial state and then decreases from the onset of microcracking to the residual stage with the crack density increasing, while the frictional strength is mobilized at the onset of microcracking and then accumulates until it is fully completed when the macrocracks are formed. After increasing the confining pressure, the mobilization of the cohesive strength displays limited alteration, but that of

the normal stress-dependent frictional strength increases significantly, especially at the residual phase when the frictional strength is fully mobilized. As a result, both the peak and residual strengths accumulate at the higher confining pressure; nevertheless, the residual strength accumulates at a higher rate. It can also account for the importance of support applications in solving the issue of the unstable collapse of underground structures.

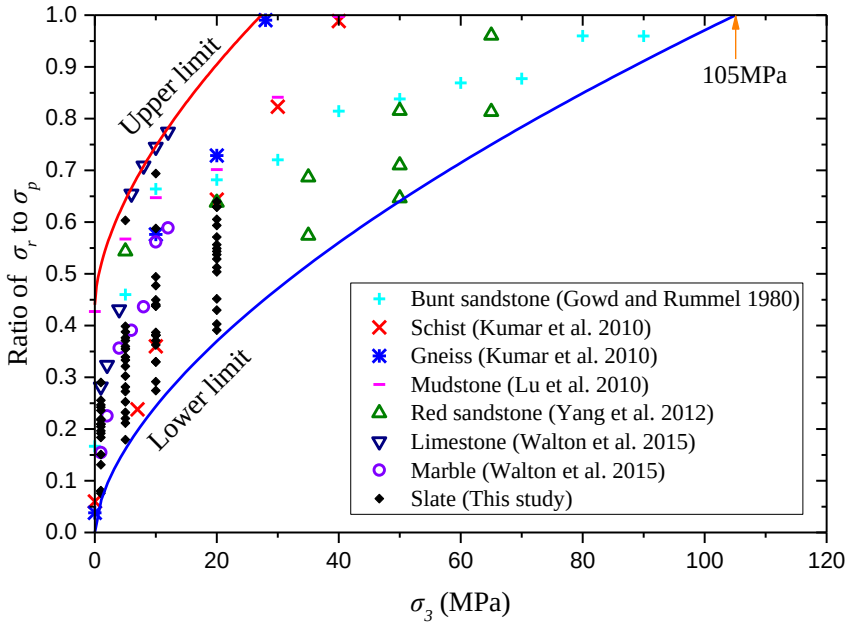

Figure 5.20 Variations of ratios of residual strength to peak strength as a function of confining pressures for transversely isotropic rocks.

Additionally, based on the compiled data as shown in Figure 5.20, the lower and upper limits of relation between σ_r/σ_p and σ_3 for transversely isotropic rocks are put forward by the following two functions.

(1) Lower limit:

$$\frac{\sigma_r}{\sigma_p} = 0.061\sigma_3^{0.6} \tag{5.17}$$

(2) Upper limit:

$$\frac{\sigma_r}{\sigma_p} = 0.077\sigma_3^{0.6} + 0.44 \tag{5.18}$$

It should be noted that the proposed equations are only applicable to rocks in the brittle failure regime. Interestingly, the confining pressure corresponding to the plastic end of the lower limit is approximately 105 MPa, coinciding with the UCS on the brittle end for various rock types **(Tutluoğlu et al. 2015)**. It is in agreement with the statistical analysis of the data from more than 1,100 triaxial tests in **Singh et al. (2011)** that the critical confining pressure for an intact rock can be taken nearly as its UCS.

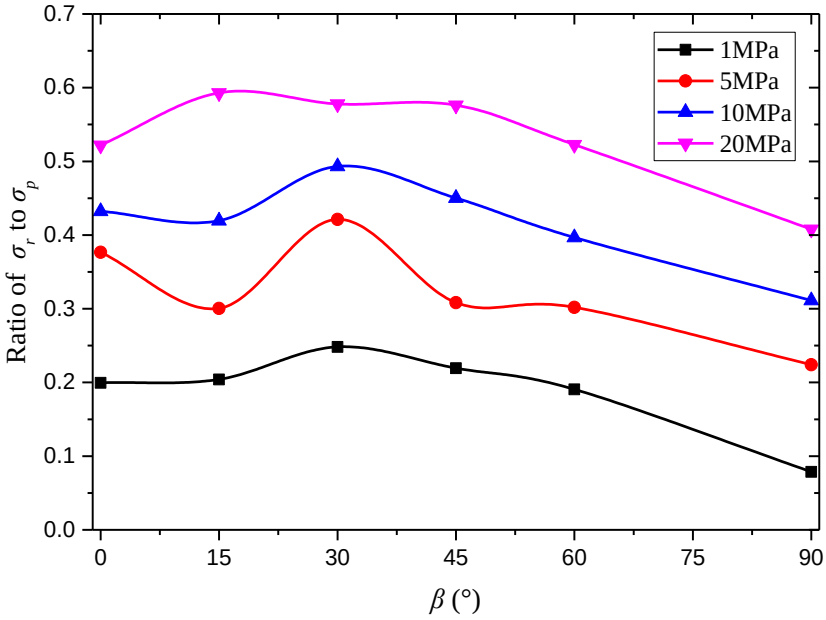

Figure 5.21 Variation of average ratios of residual strength to peak strength with β for slate.

The ratio does not present an evident size effect, and neither does the residual strength. The average of the ratios of residual to peak strength obtained from slate specimens of different sizes was calculated, the variation of which with β is depicted in Figure 5.21. At different confining pressures, the values of σ_r/σ_p generally increase first and then decrease as β increases, exhibiting a reverse U-type shape, with the maxima and minima located at $\beta = 30°$ and 90°, respectively. This implies that the failure of slate specimens at $\beta = 30°$ and $\beta = 90°$ displays the lowest and highest brittleness, respectively, throughout the range of confining pressures.

5.5 Summary

In this chapter, size effect and anisotropy of slate, as a transversely isotropic rock, have been investigated based on compression tests performed on slate samples with different sizes at different confining pressures and foliation orientations with respect to the direction of major principal stress. The main conclusions are summarised as follows:

(1) The Young's modulus parallel to the transversely isotropic plane exhibits an ascending size-effect trend, while the other four elastic constants are insensitive to the specimen size. The anisotropy of the apparent elastic modulus of slate can be captured by the transversely isotropic model with an acceptable error.

(2) A descending size-effect relation developed from coal is extended to slate, which captures the relationship among uniaxial compressive strength, specimen size and loading direction.

(3) The anisotropy of compressive strength is evident, presenting a U-type, which increases with the specimen size and stabilizes for samples larger than a critical size. Also, the anisotropy of compressive strength is captured by a cosine relation.

(4) The size-effect behaviours of uniaxial and triaxial compressive strength are similar. By incorporating the size-effect relation for uniaxial compressive strength into the modified Hoek-Brown and Saeidi failure criteria, two size-dependent failure criteria are proposed and verified against the experimental data of slate. They are capable of describing the relationship among specimen size, confining pressure, foliation orientation and rock strength under uniaxial and triaxial compressive conditions in the brittle regime. The size-dependent Saeidi failure criterion is superior to the size-dependent modified Hoek-Brown failure criterion in terms of prediction accuracy with a higher nonlinearity.

(5) No size effect, but evident anisotropy effect, is observed in the triaxial residual strength of slate. A cohesion loss model is modified to capture the anisotropic residual strength, in which the influence of anisotropy decreases with increasing foliation orientation. Two equations delineating the upper and lower boundaries for the ratio of residual to peak strength are proposed for transversely isotropic rocks.

CHAPTER 6 THREE-DIMENSIONAL DISCRETE ELEMENT SIMULATIONS OF TENSILE FAILURE BEHAVIOUR OF A TRANSVERSELY ISOTROPIC ROCK

6.1 Introduction

Transversely isotropic rocks are widely encountered in civil engineering, mining, petroleum engineering and disposal of radioactive waste **(Blümling et al. 2007; Chen et al. 2017; Meier et al. 2015; Tsang et al. 2012)**. Anisotropy is one of the most distinct characteristics of transversely isotropic rock, such as slate, gneiss, schist, shale, phyllite, limestone and claystone, and should thus be taken into consideration when applied in practical engineering **(Li et al. 2019; Ma et al. 2018)**.

Anisotropy's effect on the tensile behaviour of transversely isotropic rocks has been extensively studied for decades using analytical, experimental and numerical approaches **(Aliabadian et al. 2019; Barla and Innaurato 1973; Celleri et al. 2018; Claesson and Bohloli 2002; Duan and Kwok 2016; Hobbs 1964; Ma et al. 2018; Shang et al. 2018; Tavallali and Vervoort 2010; Wang et al. 2017b; Xu et al. 2018; Yang et al. 2019)**. The published results of such studies have shown that the tensile behaviour of transversely isotropic rocks depends largely on the orientation of weakness planes with respect to the loading direction. The Brazilian test is the most commonly used method of investigating the tensile strength and failure pattern of transversely isotropic rocks. Moreover, in most research, the sample is cored parallel to the orientation of weakness planes and the failure pattern under the Brazilian test is regarded as two-dimensional. In fact, even though the strike of weakness planes coincides with the sample axis, 3D fracture is likely to be observed as illustrated in Figure 6.1. The results observed in slate indicate that failure patterns after testing on both sides of the specimen are distinctly different and that the fracture section presents a 3D structure when the loading-foliation angle (β) is high. The most likely reason for the 3D fracture is deviation of the strike direction of weakness planes from the sample axis, the ripple arrangement of the weakness planes, pyrite inclusion or other imperfections **(Debecker and Vervoort 2009)**. The 3D effect of anisotropy is further demonstrated by the results of Brazilian tests observed in sandstone,

gneiss and slate **(Dan and Konietzky 2014; Dan et al. 2013; Ding et al. 2019)**. The Brazilian tensile strength and energy storage capacity were found to be associated with the orientation of weakness planes with respect to the directions of loading and sample axis.

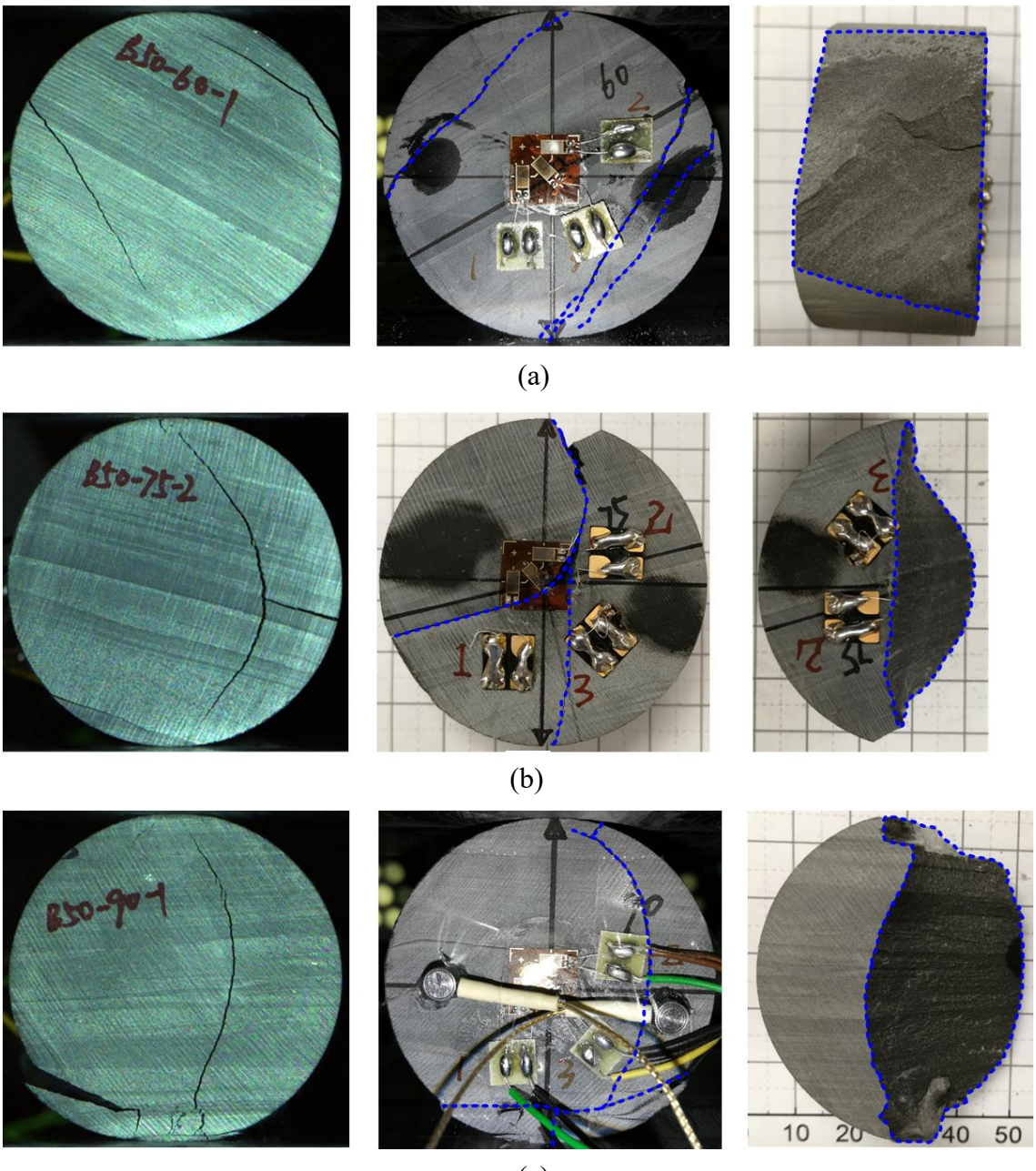

Figure 6.1 Fracture patterns after testing: front surface (left), rear surface (middle) and fracture section (right) of slate samples with different β: (a) 60°; (b) 75° and (c) 90°.

In this chapter, combined with the experimental results as discussed in Chapter 4, the indirect tensile behaviour of transversely isotropic slate was studied with a view to better understanding the 3D effect of anisotropy by means of the particle flow code PFC3D,

which is based on the discrete element method (DEM). The particle-based DEM allows the tracking of crack initiation and propagation and rock failure at both the macro and micro scales **(Duan and Kwok 2015; Fan et al. 2018; Li et al. 2018)**. Different orientations of weakness planes relative to the directions of loading and sample axis were considered.

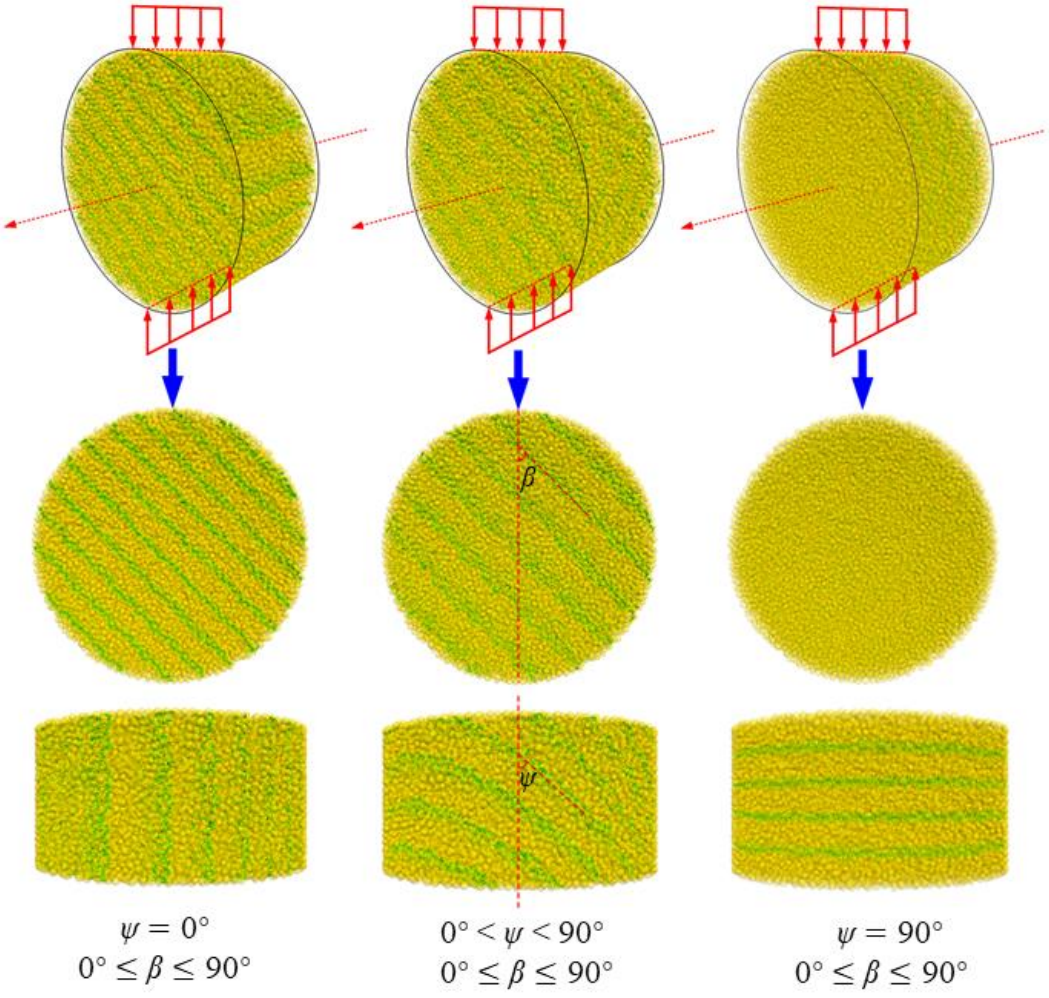

Figure 6.2 The PFC3D models of transversely isotropic rock with different β (angle between loading direction and weak plane) and ψ (angle between sample axis and weak plane) under Brazilian loading conditions: (a) $\psi = 0°$ and $0° \leq \beta \leq 90°$; (b) $0° < \psi < 90°$ and $0° \leq \beta \leq 90°$; and (c) $\psi = 90°$ and $0° \leq \beta \leq 90°$. The weak planes (foliation planes) were denoted by small green cylinders.

6.2 Numerical approach

Recent studies have demonstrated that the strength and deformation behaviour of transversely isotropic rocks can be emulated effectively by 2D DEM models combining bonded-particle and smooth-joint contact models **(Duan and Kwok 2015; Duan and Kwok 2016; Duan et al. 2015; Park and Min 2015; Wang et al. 2016; Xia and Zeng 2018; Xu et al. 2017; Xu et al. 2018; Yang et al. 2019)**. Furthermore, these studies have revealed that the behaviour of weak planes can be emulated by persistent **(Park and Min 2015; Xia and Zeng 2018; Xu et al. 2017; Xu et al. 2018)**, nonpersistent **(Duan and Kwok 2015; Duan and Kwok 2016; Duan et al. 2015)** or a mix of persistent with nonpersistent SJM **(Yang et al. 2019)** according to the microscopic structures of weak planes embedded in the rock matrix. Nevertheless, 2D modelling is still incapable of analysing many practical anisotropic problems, such as borehole instability in oblique wells excavated in anisotropic formations **(Duan et al. 2018; Meier et al. 2015)** and estimation of elastic properties for transversely isotropic rocks **(Min and Thoraval 2012)**, because stress distributions and associated failure cannot necessarily be captured in two dimensions **(Park et al. 2018)**. Consequently, 3D modelling is recommended to comprehensively reproduce the mechanical properties of anisotropic rocks.

To simulate a transversely isotropic rock, two consecutive stages should be carried out: (1) modelling of the isotropic rock matrix and (2) modelling of the transversely isotropic weak planes **(Park and Min 2015; Yang et al. 2019)**. In the particle-based DEM, the rock matrix is represented by an assembly of rigid bonded particles, such as blocks or spheres, in three dimensions **(Potyondy and Cundall 2004)**. Based on the principles laid out in Section 3.2.2, the flat-joint model (FJM) is adopted to simulate the rock matrix in this study, because it overcomes the three intrinsic problems in simulating the hard rock using the contact-bond model (CBM) or parallel-bond model (PBM). A disk-shaped specimen (D = 50 mm and thickness = 25 mm) and a cylindrical specimen (D = 50 mm and L = 100 mm) were generated, comprising 29,290 and 116,029 particles connected by flat-joint (FJ) bonds, respectively. The porosity of both specimens was fixed at 39.21 % using the deletion method **(Ding et al. 2014; Li et al. 2018)** to eliminate the influence of porosity, which produces substantial variations in strength and elasticity **(Schöpfer et al. 2009)**. The particle size distributions of the two specimens were also identical, with a maximum to minimum particle diameter ratio of 1.5. The model resolution, defined as

the average number of particles across the minimum diameter or length of specimen, was controlled by the disk-shaped specimen at 20 based on our previous study **(Li et al. 2018)**. Additionally, the behaviour of weak planes was modelled using the smooth-joint contact model (SJM) developed by Cundall **(Mas Ivars et al. 2008)**. Particles lying on two sides of the SJM plane move across one another by sliding along the discontinuity instead of around each other. As seen from Figure 4.3, the foliation planes in slate are persistent and parallel, so the behaviour of the transversely isotropic slate was modelled by inserting a set of persistent and parallel SJMs with a mean spacing (δ) of 5 mm into the isotropic rock model. For the disk-shaped specimen under Brazilian tests, the angle between the weak plane and the loading direction (β) or the sample axis (ψ) varied from 0° to 90° at intervals of 15°, as shown in Figure 6.2. In contrast, for the cylindrical specimen, with the loading direction coinciding with the sample axis under uniaxial compression tests ($\beta = \psi$), β was chosen to be 0°, 15°, 30°, 45°, 60° and 90°, in line with the experiment in Chapter 5.

6.3 Numerical test

In this section, those microproperties of FJM and SJM relevant for simulating slate were calibrated against the experimental results obtained from the uniaxial compression and Brazilian tests on slate samples having a diameter of 50 mm. In previous 2D modelling, the specimen with $\psi = 90°$ (Figure 6.2c) was treated as isotropic, neglecting the influence of weak planes **(Duan and Kwok 2015; Xu et al. 2018; Yang et al. 2019)**. However, as mentioned in Section 4.4.3, the experimental result indicated the specimen with $\psi = 90°$ after the Brazilian testing split along the loaded diameter accompanying the layer activation, which is different from that for isotropic rocks. Accordingly, development of an appropriate calibration method for the 3D models was necessary.

6.3.1 Calibration procedure

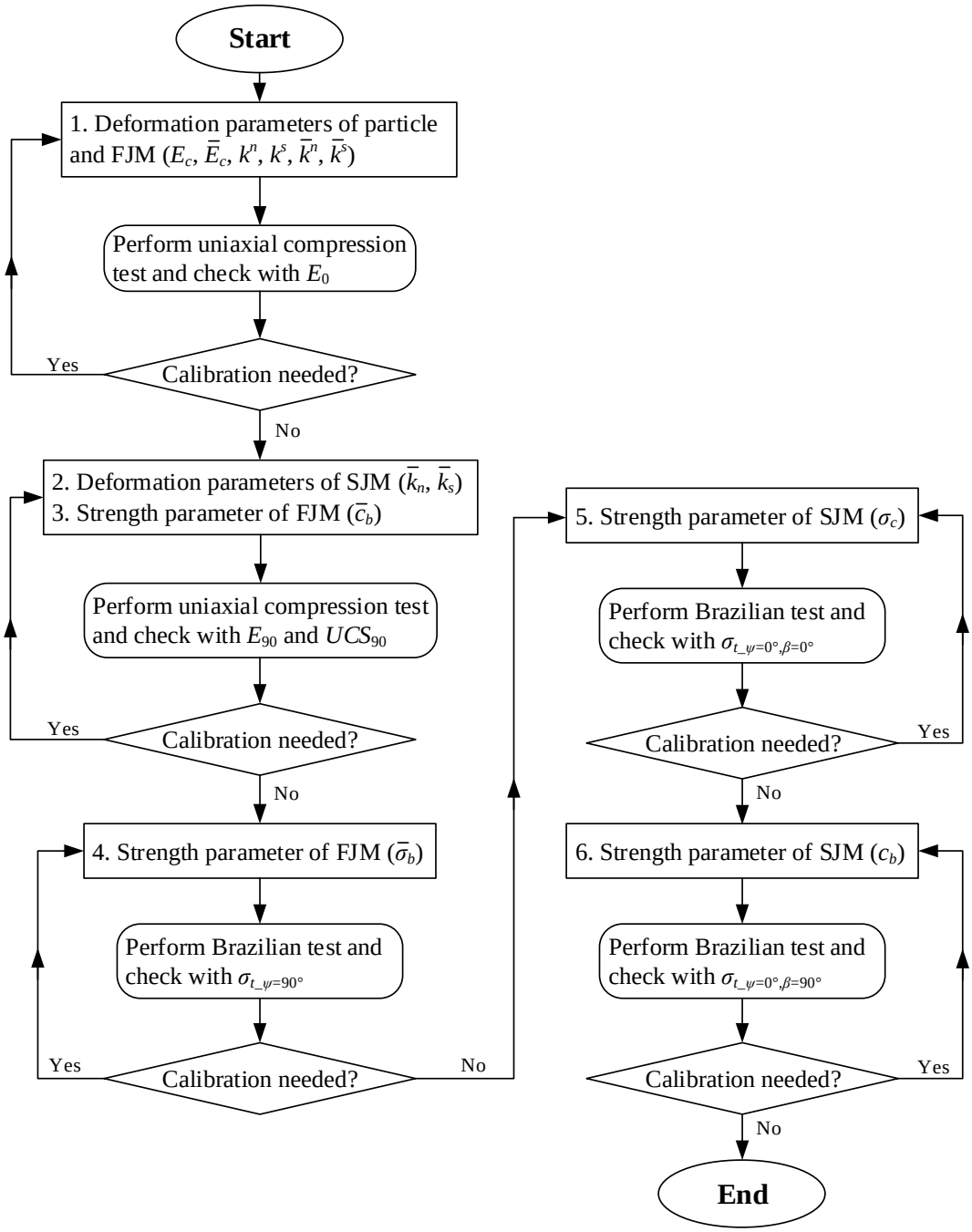

Figure 6.3 The flowchart of calibration process for three-dimensional FJM-SJM models.

The influence of microparameters of FJM and SJM on the macromechanical behaviour of DEM models has been studied by **Xu et al. (2017; 2018)** from a 2D viewpoint. For example, they can be important references with which to develop an appropriate calibration procedure for 3D DEM models, in which both FJM and SJM are employed, for transversely isotropic rock. As shown by the experimental results in Chapter 5,

minimum uniaxial compressive strength (UCS) occurs at β = 30°–45°, and the cohesion and friction angle of the foliation plane of slate are taken as their averages: 23 MPa and 35°, respectively. Hence the first approximations of cohesion (σ_c) and friction coefficient (μ_c) of smooth-joint contacts are 23 MPa and 0.7, respectively. A new calibration procedure is proposed, as shown in flowchart form in Figure 6.3, that can be described by the following steps:

Step 1: The stiffness of smooth-joint contacts has little effect on the Young's modulus (E_0) of the specimen when β = 0° under the uniaxial compressive condition. Thus the deformation parameters ($E_c, \bar{E}_c, k^n, k^s, \bar{k}^n, \bar{k}^s$) of both particle and FJM were adjusted to match E_0 through uniaxial compression tests.

Step 2: When β = 90°, the Young's modulus (E_{90}) of the specimen depends mainly on the stiffness of smooth-joint contacts and the uniaxial compression strength (UCS_{90}) of specimen is well correlated to the cohesion of flat-joint contacts. Hence both E_{90} and UCS_{90} of the specimen were calibrated through adjustment of the deformation parameters ($\bar{k}_n$, $\bar{k}_s$) of SJM and the cohesion ($\bar{c}_b$) of FJM, respectively, by conducting uniaxial compression tests.

Step 3: Because the strength of smooth-joint contacts has little effect on the tensile failure strength ($\sigma_{t\_\psi=90^\circ}$) of a specimen when the specimen axis is perpendicular to the transversely isotropic plane (ψ = 90°), the tensile strength ($\bar{\sigma}_b$) of FJM was iteratively adjusted to match $\sigma_{t\_\psi=90^\circ}$ by Brazilian tests.

Step 4: The tensile failure strength ($\sigma_{t\_\psi=0^\circ,\beta=0^\circ}$) of a specimen at ψ = 0° and β = 0° is largely determined by the tensile strength (σ_c) of SJM, whereas that ($\sigma_{t\_\psi=0^\circ,\beta=90^\circ}$) at ψ = 0° and β = 90° is closely related to the cohesion (c_b) of SJM. Accordingly, two separate series of Brazilian tests for specimens with ψ = 0°, β = 0° and ψ = 0°, β = 90° were performed to calibrate σ_c and c_b, respectively.

6.3.2 Calibration results

Table 6.1 Calibrated micro-parameters of the FJM for simulating the rock matrix of slate.

Micro-parameter	Definition	Value
ρ_v	Bulk density (kg/m^3)	2760
$R_{\min}$	Minimum particle radius (mm)	0.5
$R_{\max} / R_{\min}$	Ratio of maximum to minimum particle radius	1.5
g_{ratio}	Installation gap ratio	0.3
N_r	Number of elements in radial direction	1
N_α	Number of elements in circumferential direction	4
φ_B	Bonded element fraction	0.9
φ_G	Gapped element fraction	0
$\bar{E}_c$	Effective modulus of bond (GPa)	97
$\bar{k}^n / \bar{k}^s$	Ratio of bond normal to shear stiffness	3.0
$\bar{\sigma}_b$	Mean bond tensile-strength ± SD (MPa)	60 ± 12
$\bar{c}_b$	Mean bond cohesion strength ± SD (MPa)	180 ± 36
$\bar{\phi}_b$	Friction angle of bond (degrees)	0
μ	Friction coefficient of bond	0.1
E_c	Effective modulus of particle contact (GPa)	97
k^n / k^s	Ratio of particle normal to shear stiffness	3.0
μ_p	Friction coefficient of particle	0.1

Following the flowchart shown in Figure 6.3, the microparameters of FJM and SJM for simulating the slate were calibrated as listed in Table 6.1 and 6.2. Notably, the slit element fraction ($\varphi_S = 1 - \varphi_B - \varphi_G$), regarded as the quantification of crack density **(Wu and Xu 2016)**, was chosen to be 0.1 so as to take into account the randomly distributed preexisting cracks in the slate. The combination of the number of elements in the radial and circumferential directions ($N_r \times N_\alpha = 1 \times 4$) has been validated to be best suited for calculation efficiency **(Li et al. 2018)**. For simplicity, the normal stiffness and shear stiffness of SJM are set to be equal, as in previous studies **(Duan and Kwok 2016; Duan**

et al. 2015; Shang et al. 2018; Wang et al. 2016; Xu et al. 2017; Xu et al. 2018). The value of the microtensile strength of SJM (3.5 MPa) is lower than the macrotensile strength (6.0 MPa) of the disk-shaped specimen at ψ = 0° and β = 0°, because the microtensile cracks along the SJM contacts were initiated prior to the peak of the macrotensile strength of the specimen, consistent with the findings in **Park and Min (2015)** and **Park et al. (2018)**.

Table 6.2 Calibrated micro-parameters of the SJM for simulating the foliation of slate.

Micro-parameter	Definition	Value
$\bar{k}_n$	Normal stiffness (GPa/m)	5800
$\bar{k}_s$	Shear stiffness (GPa/m)	5800
σ_c	Tensile strength (MPa)	3.5
c_b	Cohesion (MPa)	25
μ_c	Friction coefficient	0.7

The formula for calculating the indirect tensile strength (σ_t) based on Brazilian tests is expressed by Eq. (2.11). Two prerequisites for this formula are that (1) the material be isotropic and (2) the fracture be initiated by tensile crack from the centre of the disk-shaped specimen. For the transversely isotropic rock of interest in this research, the strength obtained from this formula cannot represent the true tensile strength for most cases. Accordingly, the phrase *Brazilian failure strength (BFS)* rather than *Brazilian tensile strength (BTS)* will be used to describe the result of Eq. (2.11). The UCS, apparent Young's modulus, and BFS, which is based on specimens at $\psi = 0°$, obtained from the experimental and numerical tests are compared in Figure 6.4, which indicates that the experimental and numerical results are comparable. Moreover, the BFS of a specimen with $\psi = 90°$ obtained by experiment (22.5 MPa) is comparable to that obtained by numerical simulation (21.4 MPa) at each loading-foliation angle (β).

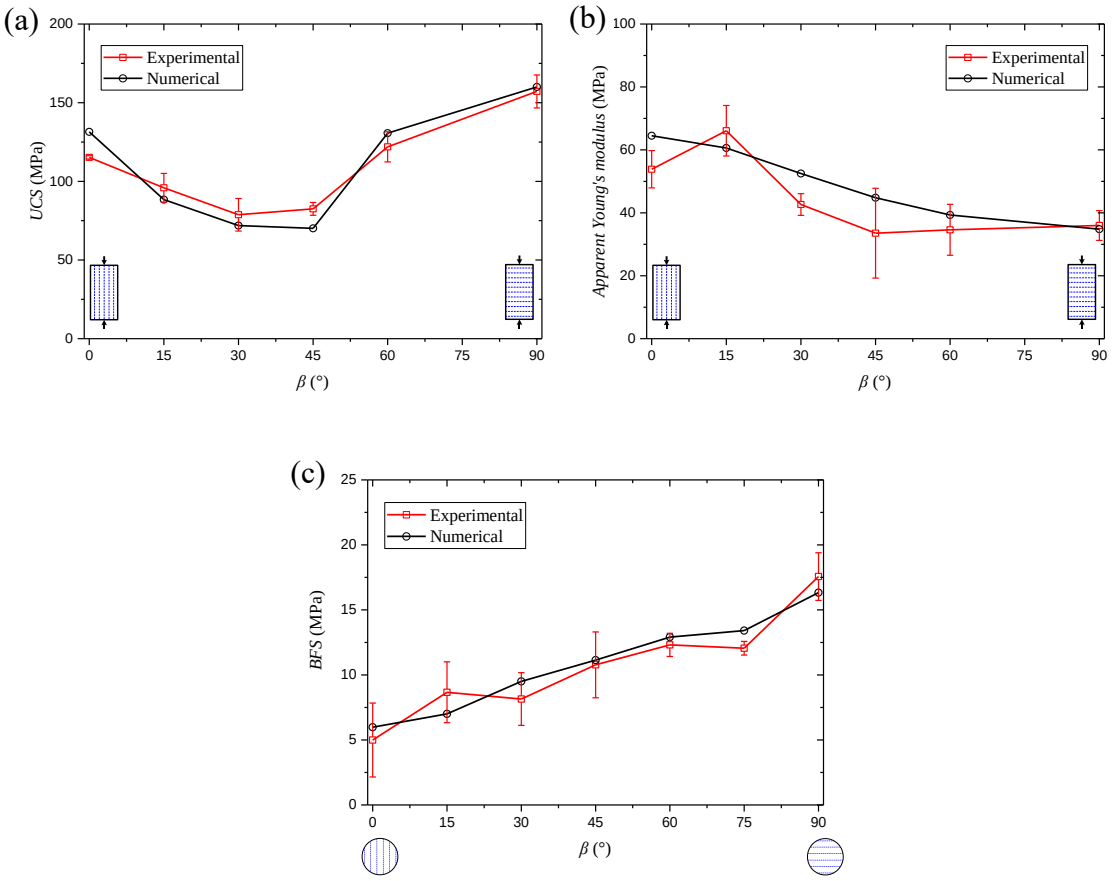

Figure 6.4 The comparisons between experimental and numerical results of specimens with 50-mm-diameter: (a) UCS; (b) apparent Young's modulus and (c) BFS.

6.3.3 Parametric study

Based on the calibrated microparameters, the disk-shaped PFC3D models of slate having different foliation spacings, foliation orientations relative to the loading direction and sample axes were created to investigate their influences on the tensile behaviour by conducting Brazilian tests. The foliation spacings (δ) were chosen to be 2.5 mm, 5.0 mm and 7.5 mm. The foliation orientations relative to the loading direction (β) and the sample axis (ψ) were altered from 0° to 90° at intervals of 15° as shown in Figure 6.2. The loading rate for the Brazilian test simulation was controlled at 0.015 m/s – slow enough to be sure of the specimen's being in a quasistatic equilibrium for each step. The loading platens are frictionless. Additionally, three measurement spheres 5 mm in diameter, containing about 39 particles apiece, were installed at the centre of the disk-shaped specimen along the thickness of specimen. In this way, stresses and strains at the centre of the disk on both surfaces and the middle plane of specimen were monitored throughout the test.

6.4 Numerical results

6.4.1 Effect of foliation spacing on tensile behaviour

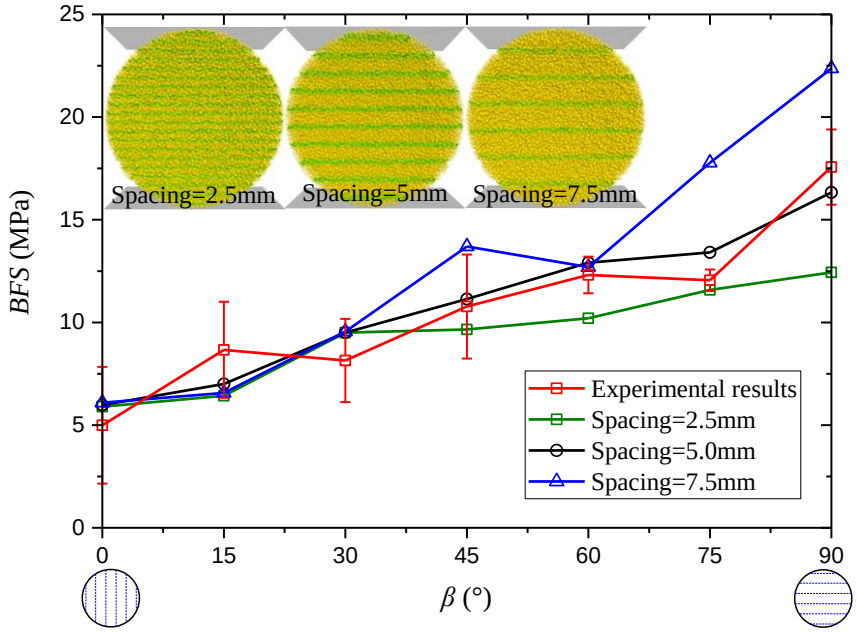

Figure 6.5 The influence of foliation spacing on BFS.

The variation of BFS of specimens at ψ of 0° with different foliation spacings versus the loading-foliation angle is shown in Figure 6.5, which indicates that the influence of foliation spacing on BFS is associated with the loading-foliation angle. At β of 0°–30°, the influence of foliation spacing on BFS is negligible, whereas at β of 45°–90°, the BFS of the specimen is significantly increased by increasing foliation spacing, with a maximum deviation percentage of 80 % at β of 90°. The result is different from those observed in 2D modelling **(Wang et al. 2018)** and in direct tensile modelling in three dimensions **(Shang et al. 2018)**. **Wang et al. (2018)** stated that BFS slightly increased with increases in spacing irrespective of the loading-foliation angle, demonstrating once more that caution should be used when analysing real-world problems in transversely isotropic rocks by means of 2D modelling. **Shang et al. (2018)** concluded that the effect of bedding spacing on direct tensile strength was small and could be ignored. This discrepancy is most likely attributable to the difference in loading conditions, for transversely isotropic rocks fail through different failure mechanisms when loaded in tension or compression-tension. Being in good agreement with the experimental results, the numerical results obtained from specimens with a foliation spacing of 5.0 mm also

demonstrate the feasibility of the adopted microparameters for simulating slate samples.

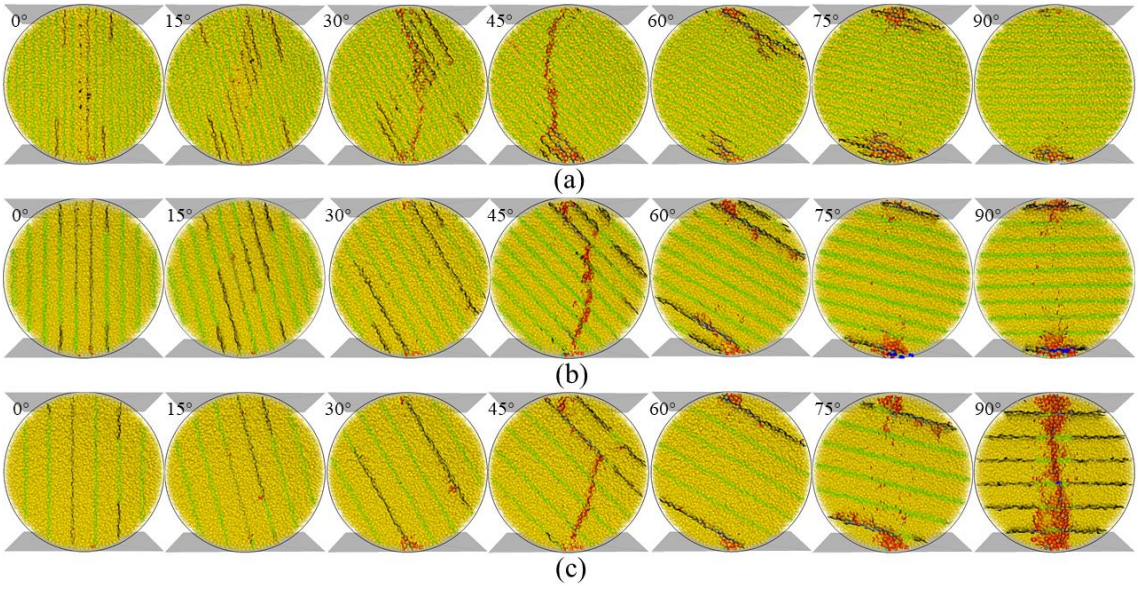

Figure 6.6 The fracture patterns of specimens with different foliation spacings: (a) 2.5 mm; (b) 5.0 mm and (c) 7.5 mm. The small green cylinders denoted the foliation planes. The tensile and shear cracks of smooth-joint (SJ) contacts were marked in black and blue, respectively. The tensile and shear cracks of flat-joint contacts were marked in red and cyan, respectively.

Additionally, the fracture patterns of specimens having different foliation spacings are compared in Figure 6.6. When the loading-foliation angle is low (0°–30°), fracture patterns are similar regardless of foliation spacing. The specimens mainly fail by tensile cracks along the weak plane corresponding to the layer activation failure observed in the experiment in Section 4.4.3, except for the specimen having δ of 2.5 mm at β of 30°. Interestingly, the exception of fracture pattern, which is composed of mixed failures in the weak plane and rock matrix, is not associated with variations in BFS. As analysed at the micro scale, the negligible effect of foliation spacing on BFS can be explained by the invariable percentage of FJ tensile microcracks (see Figure 6.7). Overall, with β increasing from 45° to 90°, failure patterns of specimens transform from mixed failure to nonlayer activation failure. The difference among failure patterns for specimens having different foliation spacings is increasingly obvious, becoming most evident at β = 90°. When spacing is 2.5 mm, the weak planes hinder fracture propagation from the loading points towards the centre of the specimen so that the centre part of the specimen remains

intact after testing – a phenomenon commonly observed in transversely isotropic rocks **(Debecker and Vervoort 2009; Xu et al. 2017)**, as depicted in Figure 6.8. In contrast, when spacing is increased to 7.5 mm, the specimen fails by tensile splitting of the rock matrix accompanying secondary cracks along the weak planes. Similarly, increase in BFS with foliation spacing at β of 45°–90° is attributable to the increased percentage of FJ tensile microcracks, as illustrated in Figure 6.7.

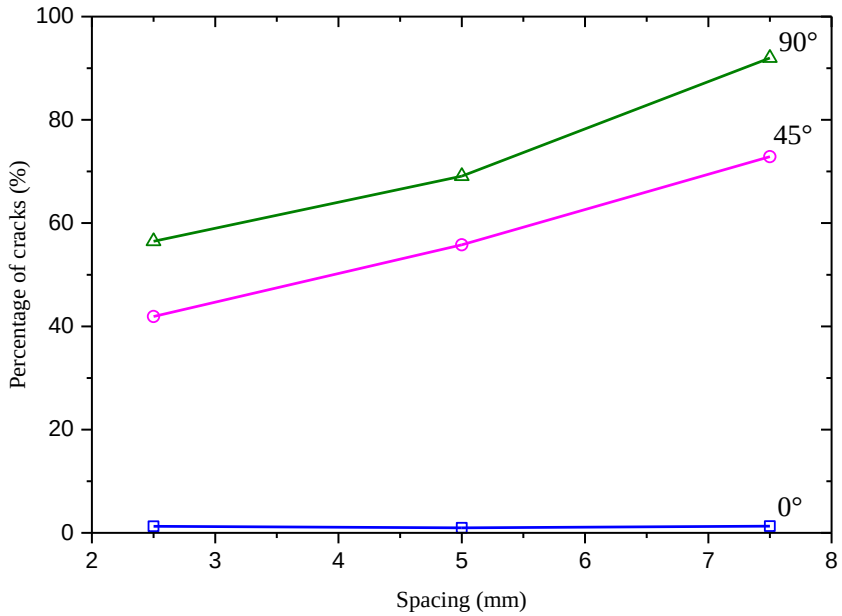

Figure 6.7 Variation of percentage of FJ tensile micro-cracks at failure versus the foliation spacing.

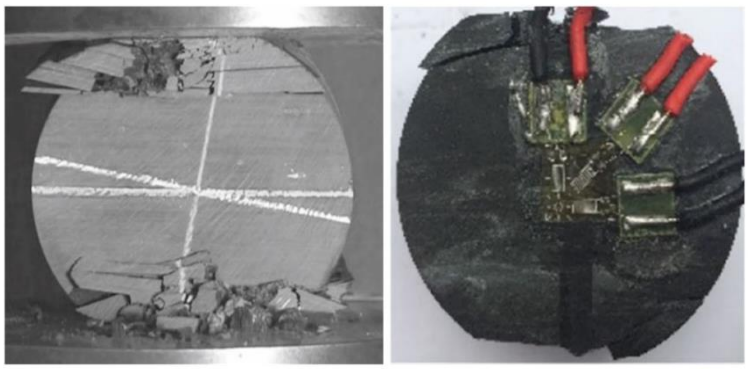

(a) (b)

Figure 6.8 Fracture patterns observed in samples of: (a) slate **(Debecker and Vervoort 2009)** and (b) phyllite **(Xu et al. 2017)** under Brazilian tests.

6.4.2 Effect of three-dimensional foliation orientation on tensile strength

Based on the elastic constants, **Claesson and Bohloli (2002)** put forward a formula for calculating the tensile strength of transversely isotropic rocks as given as Eq. (2.12). Because this formula takes only the angle between loading direction and weak plane (β) into consideration by postulating the strike of weak planes parallel to the sample axis ($\psi = 0°$), the applicability of this formula to transversely isotropic rocks remains open to question when considering the influence of 3D foliation orientation **(Ding et al. 2019)**. Accordingly, further research into this issue is needed that goes beyond the scope of this study.

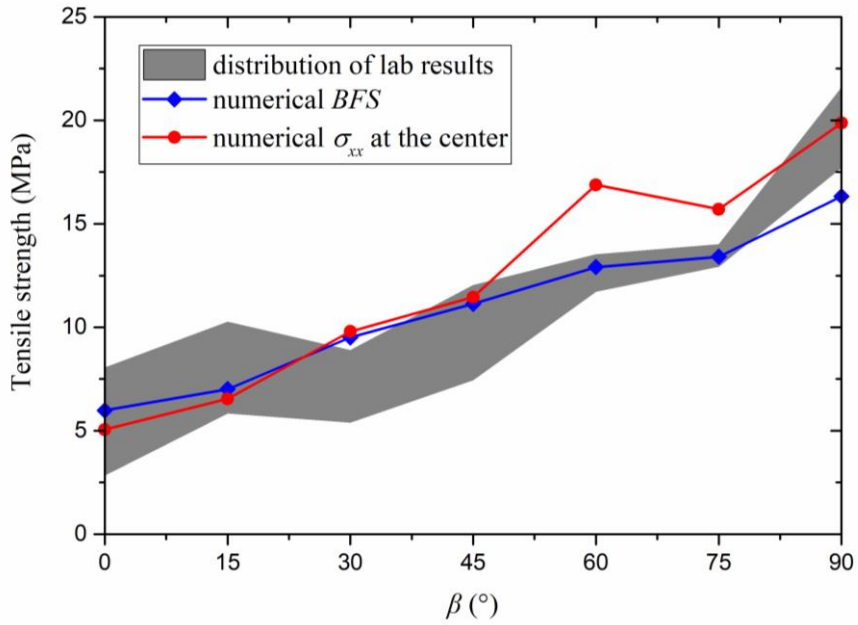

Figure 6.9 Comparison between lab results and numerical results for slate samples at $\psi = 0°$.

The tensile strength of slate samples at ψ of 0° was obtained by Eq. (2.12) based on experimental results in Chapter 4. The distributions of lab results at different β are depicted in Figure 6.9. The tensile stress (σ_{xx}) at the centre of specimen at failure is usually regarded as the tensile strength of a specimen per **Claesson and Bohloli (2002)** and **Yu et al. (2006)**, taking the average of σ_{xx} measured by three measurement spheres installed at the centre in numerical tests. Along with numeric BFS, the distribution of tensile strength and numerical σ_{xx} at the centre as a function of β are compared as shown

in Figure 6.9, indicating that both numerical BFS and σ_{xx} at the centre can reasonably accurately represent the tensile strength of a specimen, with numerical BFS seeming more superior than σ_{xx} at the centre from the viewpoint of the overall trend. Accordingly, BFS based on Eq. (2.11) is used hereinafter to study the influence of 3D foliation orientation on tensile strength.

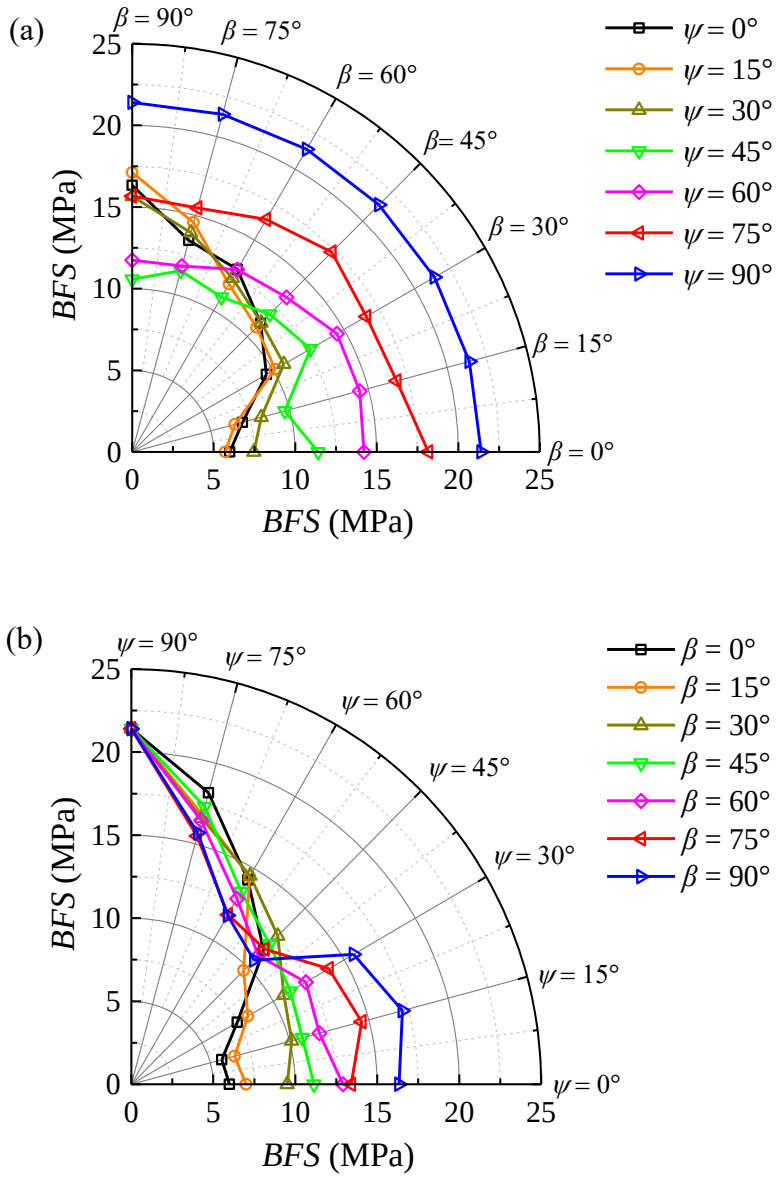

Figure 6.10 Influences of (a) β and (b) ψ on BFS of slate models in PFC3D.

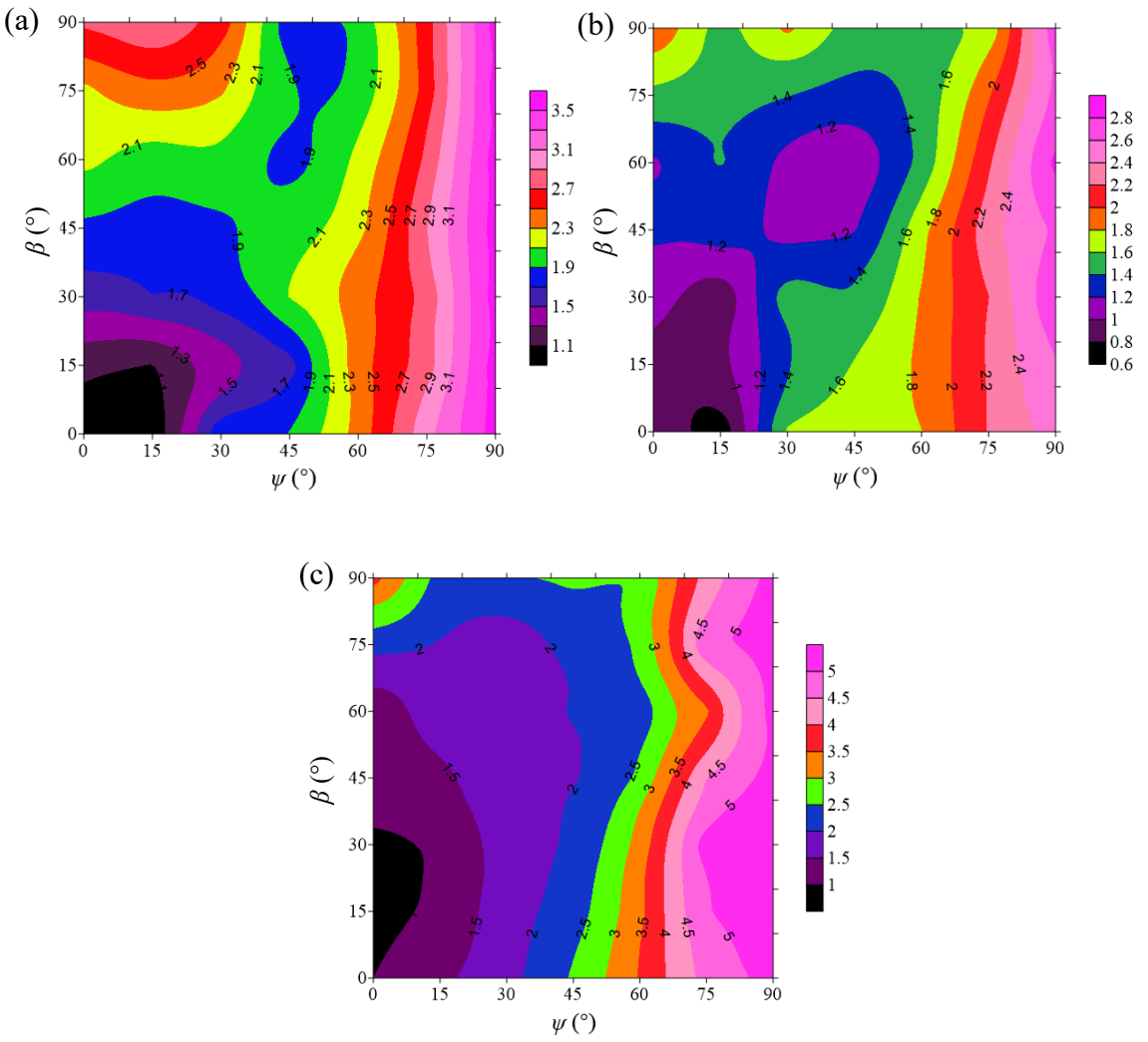

Figure 6.11 Normalized BFS of slate samples with different β and ψ obtained: (a) in this study; (b) by **Ding et al. (2019)** and (c) by **Dan et al. (2013)**.

Figure 6.10 shows the influences of β and ψ on BFS of slate PFC3D models. When $0° \leq \psi \leq 30°$, values of BFS of slate models at each β are very similar, as shown in Figure 6.10a, implying that the BFS of slate models depends primarily on β rather than on ψ, displaying a gradually increasing trend with β. When $45° \leq \psi \leq 90°$, the variation of BFS of slate models is insensitive to β, so that BFS increases linearly with ψ, as illustrated in Figure 6.10b. Furthermore, the effect of β and ψ on the anisotropy of BFS of slate samples is investigated by normalizing the results to 1 at $\psi = 0°$ and $\beta = 0°$. As seen in Figure 6.11, the variation of anisotropy ratios with β and ψ obtained by our numerical study is similar to those obtained in laboratory tests by **Ding et al. (2019)** and **Dan et al. (2013)**, at $45° \leq \psi \leq 90°$, which exhibits an ascending trend with ψ and is nearly independent of β. However, the results are different at $0° \leq \psi < 45°$ in these three

studies. For instance, in our research, the anisotropy ratio of BFS generally increases with β at $0° \leq \psi \leq 30°$, and the coupling effect of β and ψ is evident at $30° \leq \psi < 45°$. For Ding et al.'s results, the coupling effect of β and ψ on the anisotropy ratio of BFS is dominant at this range. In relation to Dan et al.'s results, the anisotropy ratio of BFS grows as ψ increases at $0° \leq \psi < 45°$ and $0° \leq \beta \leq 30°$, whereas the coupling effect plays a role in the rest of β and ψ. Overall, the BFS of slate samples presents evident anisotropic variation, with the values of anisotropy ratio of BFS reaching 3.58, 2.85 and 5.24 for, respectively, this study, **Ding et al. (2019)** and **Dan et al. (2013)**.

6.4.3 Effect of three-dimensional foliation orientation on failure mechanism

In the particle-based DEM, microcracks can be monitored and counted during the fracture process to analyse the damage evolution. When the local stress acting on the contact exceeds the pre-setting strength, it breaks in a tensile or shear fashion and produces one microcrack. In our FJM–SJM modelling, four types of microcracks are generated: FJ tensile crack (FJ-T), FJ shear crack (FJ-S), SJ tensile crack (SJ-T) and SJ shear crack (SJ-S). FJ cracks form only in the rock matrix, whereas SJ cracks form only in the weak planes. Reflecting space limitations, Figure 6.12 shows only the stress and microcrack evolution of slate models at foliation orientations (ψ–β) of 0°–0°, 0°–45°, 0°–90°, 45°–0°, 45°–45°, 45°–90° and 90°–45° under Brazilian tests. Some critical points (*a*, *b*, *c* and *d*) and their corresponding damage location and degree are also displayed in Figure 6.12. In general, three distinct stages are identified based on microcrack number, increase rate and stress–strain curve:

Stage I: There are nearly no microcracks generated in this stage, and the stress–strain curve is in a linear portion.

Stage II: The number of microcracks increases at a relatively low rate, and the stress–strain curve deviates from the linear portion, often accompanied by stress fluctuation, which indicates irreversible damage in the specimen.

Stage III: The number of microcracks accumulates at a relatively high rate to a high level with the formation of macrofractures, and the stress–strain curve presents a descending trend.

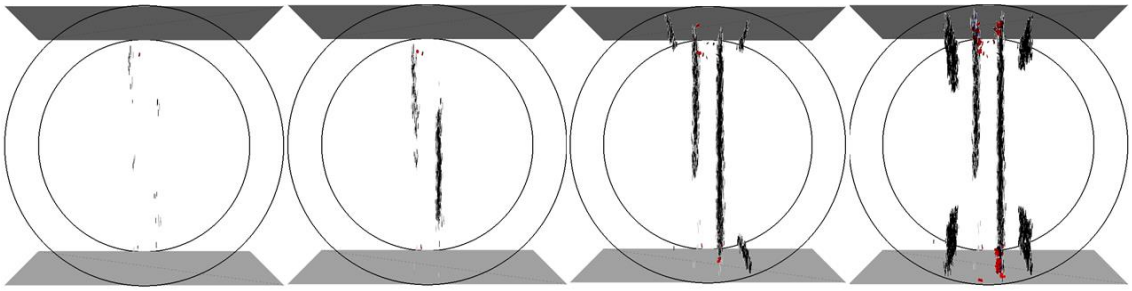

a: 0.55 × 10^{-3} b: 0.58 × 10^{-3} c: 0.6 × 10^{-3} d: 0.63 × 10^{-3}

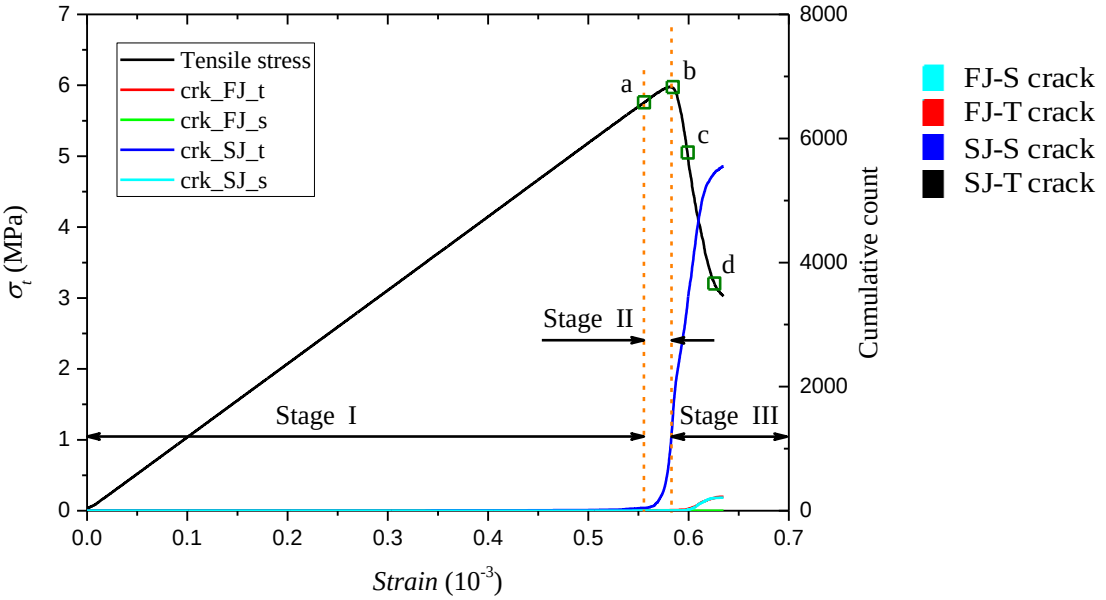

(a)

Figure 6.12 Stress and micro-crack evolution of slate models in PFC3D: (a) 0°—0°; (b) 0°—45°; (c) 0°—90°, (d) 45°—0°; (e) 45°—45°; (f) 45°—90° and (g) 90°—45°.

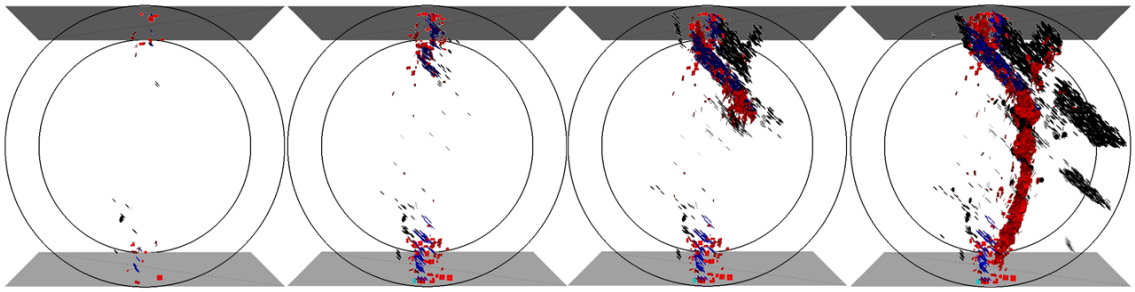

a: 1.0×10^{-3} b: 1.37×10^{-3} c: 1.45×10^{-3} d: 1.55×10^{-3}

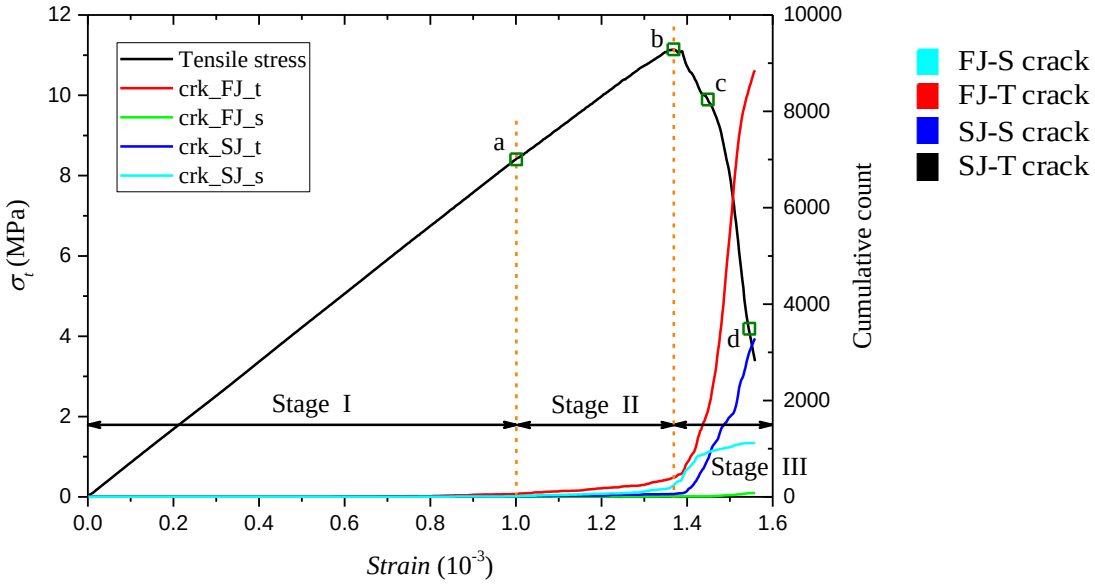

(b)

Figure 6.12 (*continued*)

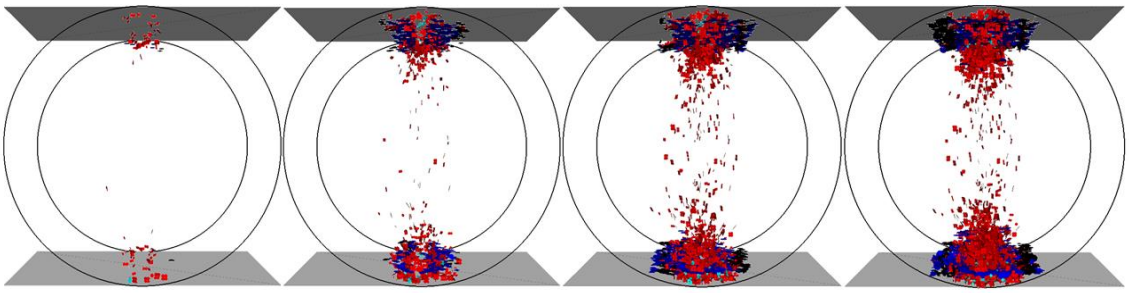

a: 1.4 × 10^{-3} b: 2.48 × 10^{-3} c: 3.53 × 10^{-3} d: 4.86 × 10^{-3}

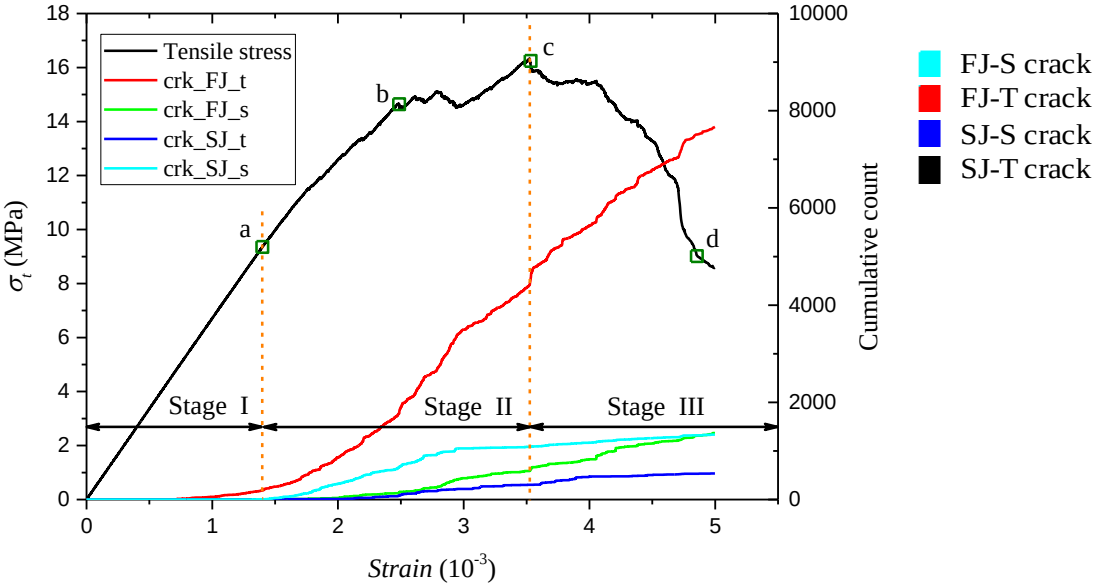

(c)

Figure 6.12 (*continued*)

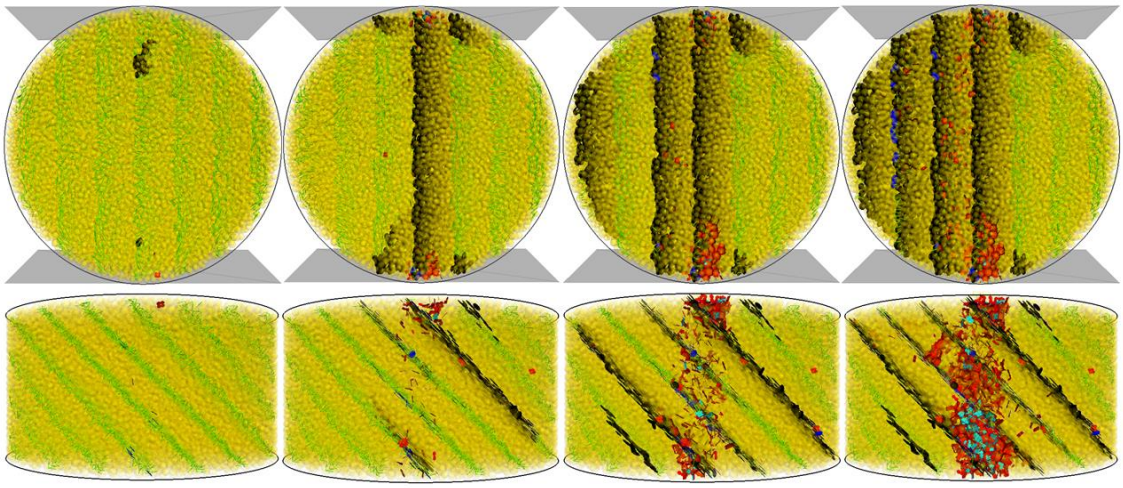

a: 0.75 × 10^{-3} b: 1.03 × 10^{-3} c: 1.52 × 10^{-3} d: 1.98 × 10^{-3}

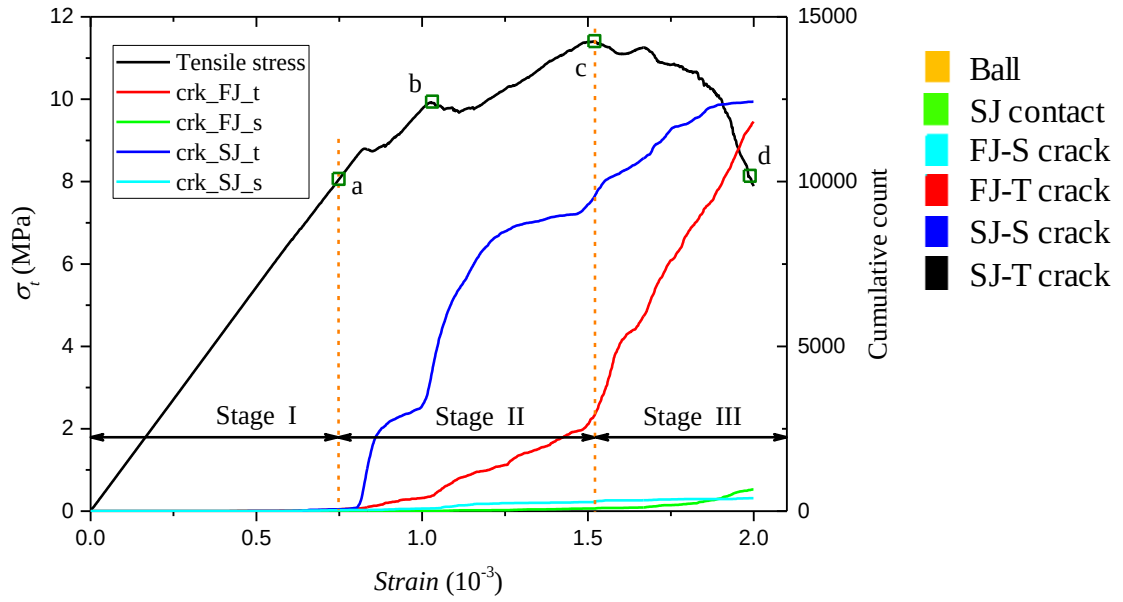

(d)

Figure 6.12 (*continued*)

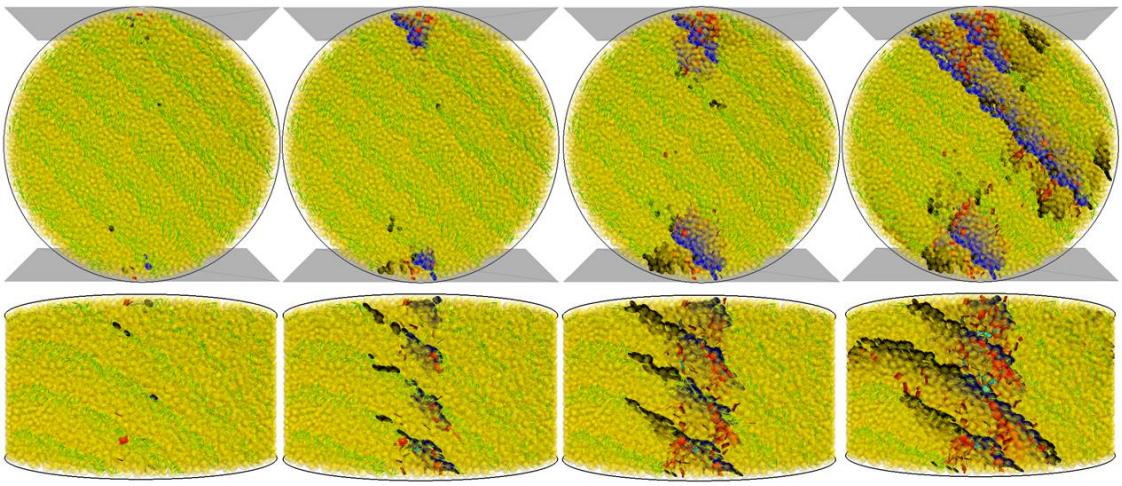

a: 0.86 × 10^{-3} b: 1.19 × 10^{-3} c: 1.57 × 10^{-3} d: 1.85 × 10^{-3}

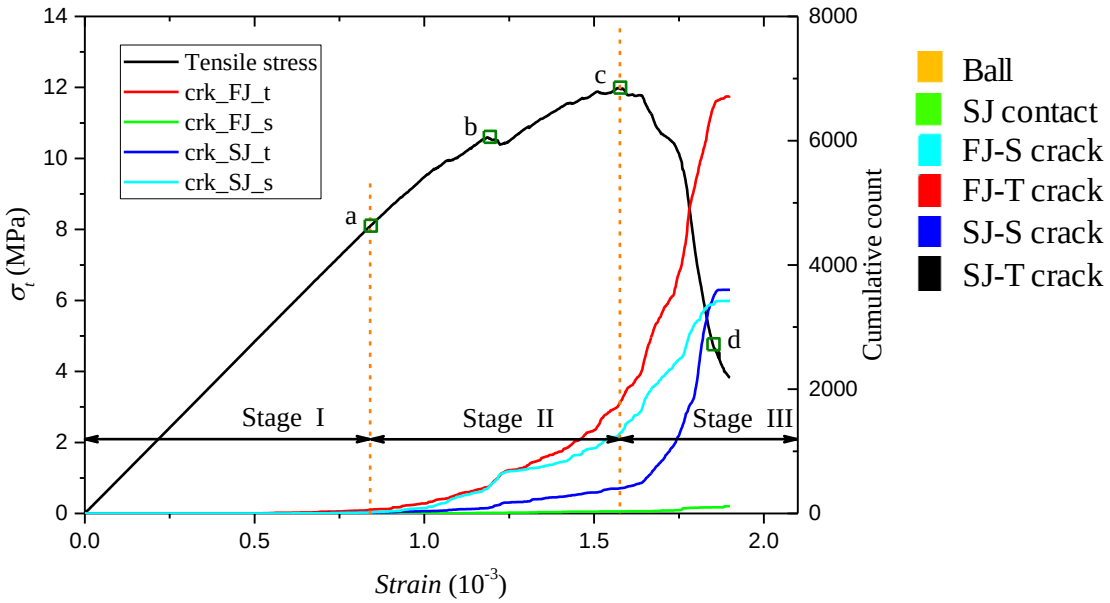

(e)

Figure 6.12 (*continued*)

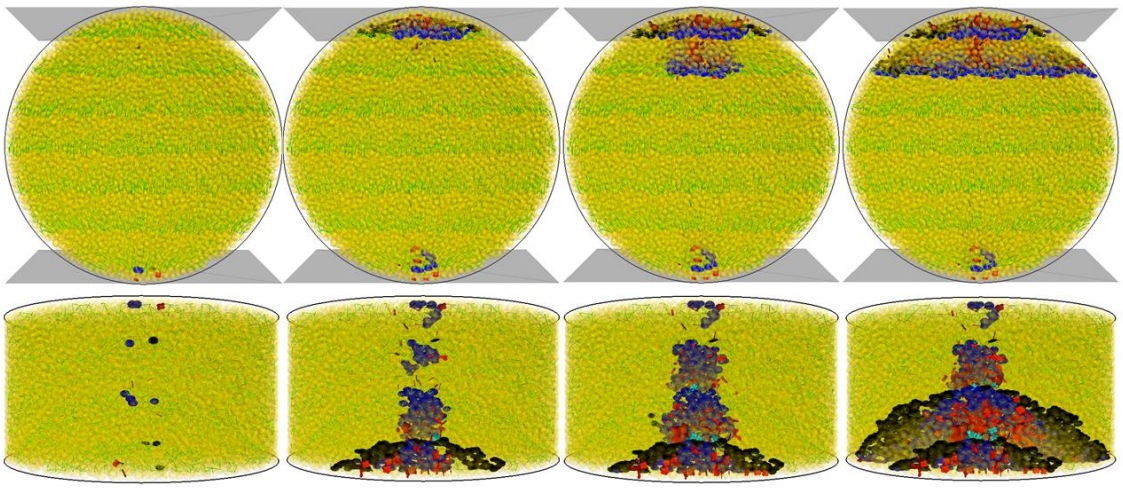

a: 0.87 × 10^{-3} b: 1.22 × 10^{-3} c: 1.6 × 10^{-3} d: 1.8 × 10^{-3}

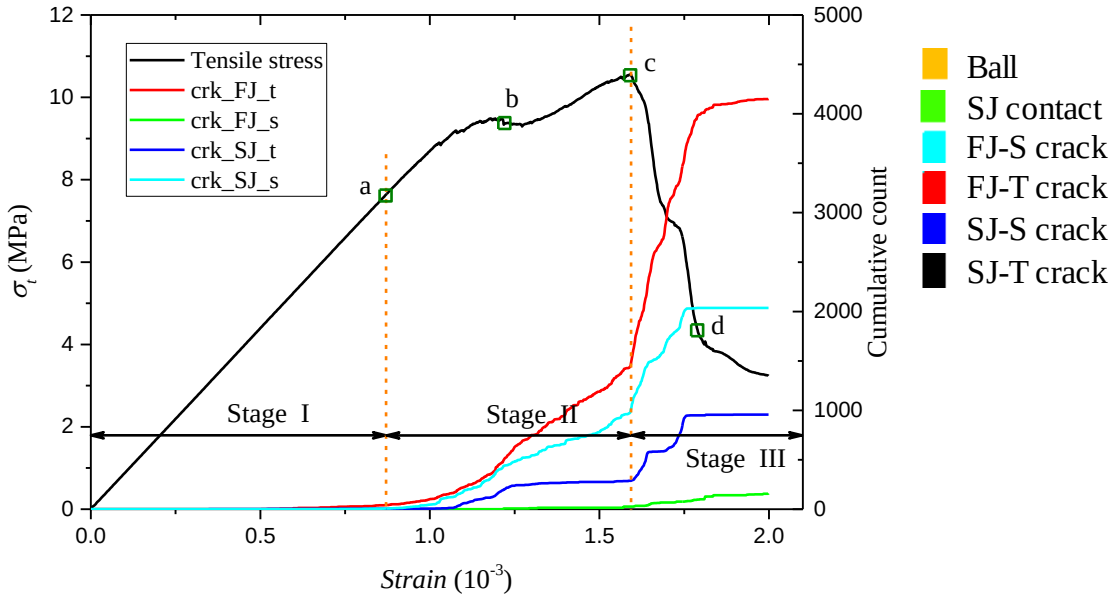

(f)

Figure 6.12 (*continued*)

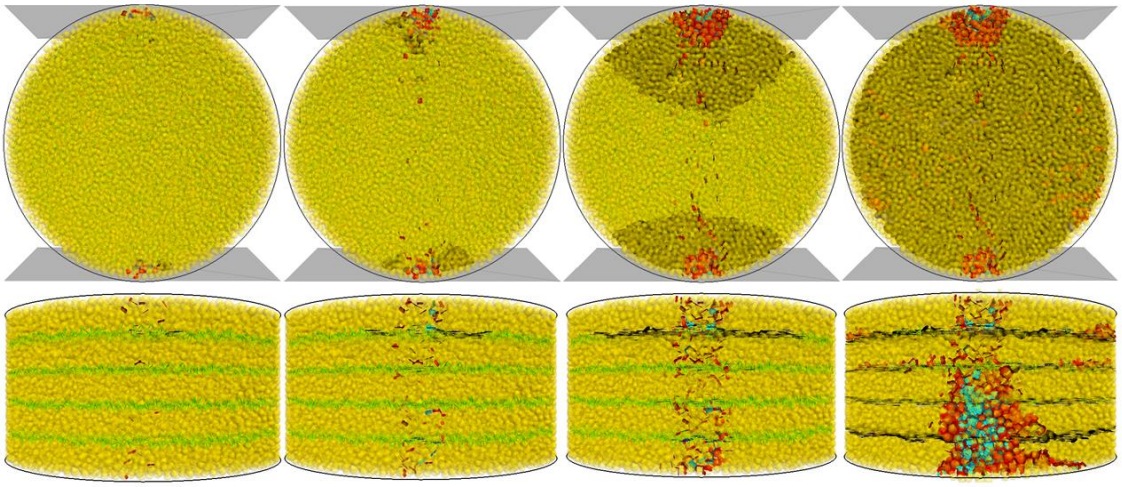

a: 1.0 × 10^{-3} b: 1.4 × 10^{-3} c: 1.93 × 10^{-3} d: 2.44 × 10^{-3}

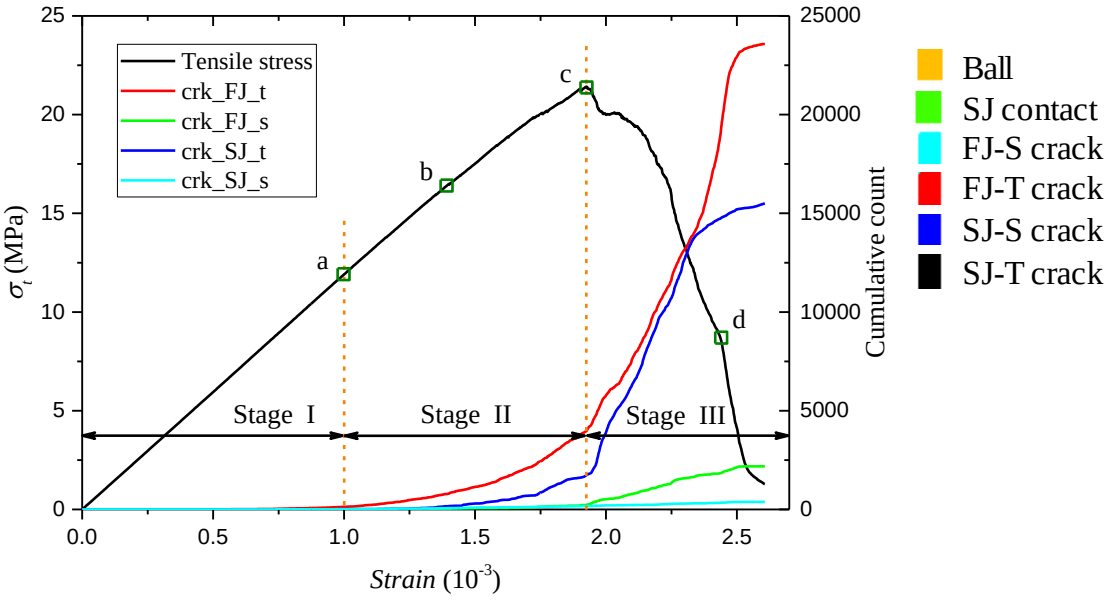

(g)

Figure 6.12 (*continued*).

For ψ–β of 0°–0°, SJ tensile microcracks initiate at the centre (point *a*) and propagate towards the top and bottom loading points; after the peak stress of point *b*, secondary cracks appear near the loading points along the weak planes and grow towards the centre of the disk. The damage of model is dominated by SJ tensile cracks.

For ψ–β of 0°–45°, at stage I, few sporadic microcracks are noticed (point *a*); in stage II,

the FJ tensile and SJ shear cracks increase at the same level, concentrated at the loading ends (point *b*), until stage III, when the FJ and SJ tensile cracks increase rapidly and the SJ tensile cracks exceed the SJ shear cracks. The fracture begins at the loading points and propagates along the weak planes (point *c*), then propagates across the weak planes in the rock matrix, forming an arc-shaped macrofracture (point *d*).

For ψ–β of 0°–90°, at stage II, stress fluctuations (point *b*) occur, with FJ tensile cracks increasing at a high rate and SJ shear cracks increasing at a low rate; fracture of the model starts from the top and bottom loading points and evolves towards the centre of the disk; ultimately the model fails by the tensile cracks through the rock matrix, accompanying secondary cracks along the weak planes concentrated at the loading ends.

When the strike of weak planes coincides with the sample axis (ψ = 0°), the fracture pattern of the model is largely dependent of β and in line with the experimental results. The variation of fracture process with β is also consistent with the laboratory observations as shown in Figure 4.17, which depicts the stress-strain curves and failure patterns of slate specimens at different loading directions. The transverse strains (No. 4 to 8) along the loaded diameter of specimen were measured by a series of horizontal strain gages with a length of 20 mm, enough long to capture the fracture initiation point within the specimen. Accordingly, based on the maximum extension strain criterion **(Li and Wong 2013)**, the fracture process can be estimated as follows: the specimen at β of 0° tends to fail starting from the disc center, while at other β the specimen tends to fail starting from the regions of load application where the largest transverse strain first arrives. Moreover, as β increases, the numerical model tends to fail by tensile failure in the rock matrix, as demonstrated by the increasing percentage of FJ tensile micro-cracks, shown in Figure 6.13a. This also accounts for the increase of BFS with an increase in β.

For ψ–β of 45°–0°, nearly no microcracks appear at stage I, but in stage II the SJ tensile cracks increase rapidly in a stepped fashion and the FJ tensile cracks increase at a relatively low rate; at stage III the SJ tensile cracks increase at a relatively low rate but the FJ tensile cracks increase at a high rate, although both reach the same level by the point of ultimate stress. The fracture of the model starts from the centre of the disk, along the weak planes, and propagates towards the loading points, accompanying cracks forming in the rock matrix near the loading ends (point *c*), after which the cracks in the

rock matrix grow from the two loading points to the centre of the disk. Seen from the top view of the model, the fracture formed in the rock matrix is aligned with the direction of the sample axis, being inclined to the fracture induced in the weak planes (point *d*).

For ψ–β of 45°–45°, the FJ tensile and SJ shear cracks increase at the same level as at stage II; at stage III the FJ tensile, SJ shear and SJ tensile cracks grow at a higher rate. The fracture of model begins at the loading points by simultaneous appearance of shear cracks along the weak planes and of tensile cracks in the rock matrix (point *b*), then propagates towards the centre of the disk (point *c*). At the ultimate stage, a complex 3D fracture is formed in the model (point *d*).

For ψ–β of 45°–90°, the FJ tensile, SJ shear and SJ tensile cracks evolve in a pattern similar to that seen for ψ–β of 45°–45°. However, their fracture patterns are very different. At β of 90°, the fragments of model at the loading ends, which are formed by intersecting cracks along the weak planes with those in rock matrix, are spalled from the model, leaving its centre part still intact after testing.

Finally, ψ of 90° is a special case in which the fracture pattern of the model is independent of β because the loading direction is inherently parallel to the weak planes. Fracture of the model begins simultaneously at the loading points by FJ and SJ tensile cracks and propagates towards the centre of model until the crack coalescence. The cracks in the rock matrix and along weak planes intersect perpendicular to each other, as depicted in Figure 6.12g.

To obtain a better understanding of the influence of microcrack type on fracture pattern, the ratios of the FJ tensile crack, FJ shear crack, SJ tensile crack and SJ shear crack to all cracks are calculated at failure. The proportional variations of microcracks at different ψ and β are shown in Figure 6.13. The results show that the FJ and SJ tensile cracks are the main components of the microcracks, indicating that the slate model fails mainly by tension. The proportional variations of microcracks at ψ of 0°–30° are similar, implying the absence of influence imposed by ψ. The portion of FJ tensile cracks increases continuously with increasing β, and the portion of FJ shear cracks is minimal irrespective of β.

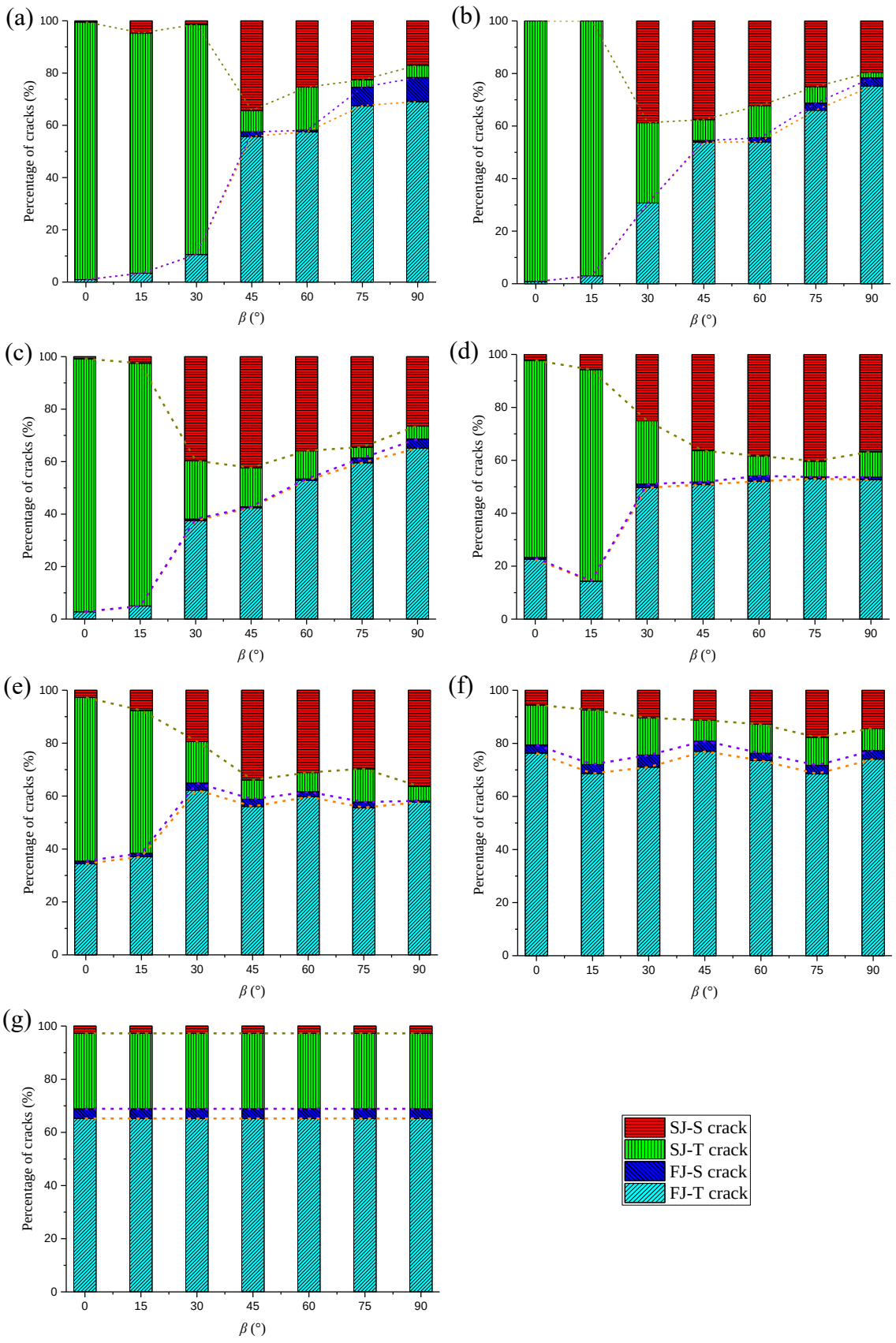

Figure 6.13 Variations of percentage of micro-cracks developed in slate models at different β with varying ψ: (a) 0°; (b) 15°; (c) 30°; (d) 45°; (e) 60°; (f) 75° and (g) 90°.

At low β, the very high portion of SJ tensile cracks indicates that the model fails by tension along the weak plane. With β increasing, the SJ tensile cracks tend to disappear. Meanwhile, the portion of SJ shear cracks decreases as β increases from 45° to 90°, with the tensile fracture in the rock matrix dominating the failure mode of the model. At intermediate β, the portions of FJ tensile and SJ shear cracks are comparable, indicating that the model fails by a mixed shear along the weak plane with tensile across the rock matrix fracture, consistent with laboratory observations.

Additionally, at ψ of 45°–75°, the most distinct difference between proportional variations of microcracks from those at ψ of 0°–30° is that the portions of FJ tensile cracks are nearly constant as β varies in the range 30°–90°. The variations of portions of microcracks with β at each ψ reduce with increasing ψ, almost disappearing at ψ = 75°. This can explain why the BFS of slate model is insensitive to β in this range of ψ. Furthermore, the level of portion of FJ tensile cracks increases with increasing ψ, which is responsible for the increased BFS of model. A ψ of 90° is a special case in which the proportional variation of microcracks is independent of β, with FJ and SJ tensile cracks dominating the failure of the model. Although the portion of FJ tensile cracks at ψ = 90° is not the highest seen, the corresponding BFS is. This can be attributed to a special failure mode in which the model fails by tensile splitting through the rock matrix along the loading direction, behaving like an intact specimen without weak planes. Thus the effective portion of FJ tensile cracks is far higher when excluding SJ cracks.

6.5 Discussion

To further study the effect of weak planes on principal stress distribution, 57 measurement spheres with diameter l = 2.5 mm, containing approximately 5 particles apiece, were installed along the loading plane of the disk-shaped model. As shown in Figure 6.14, these measurement spheres were arranged in three columns, located in the middle plane, near the front and rear surfaces. It should be noted that stress is a continuum variable and does not actually exist anywhere in the particle assembly owing to the discreteness of DEM model **(Fan et al. 2018)**. In essence, the stress at one point is taken as the average in the measurement region. Hence, the diameter of measurement spheres cannot be too large to accurately reproduce the stress at a particular point.

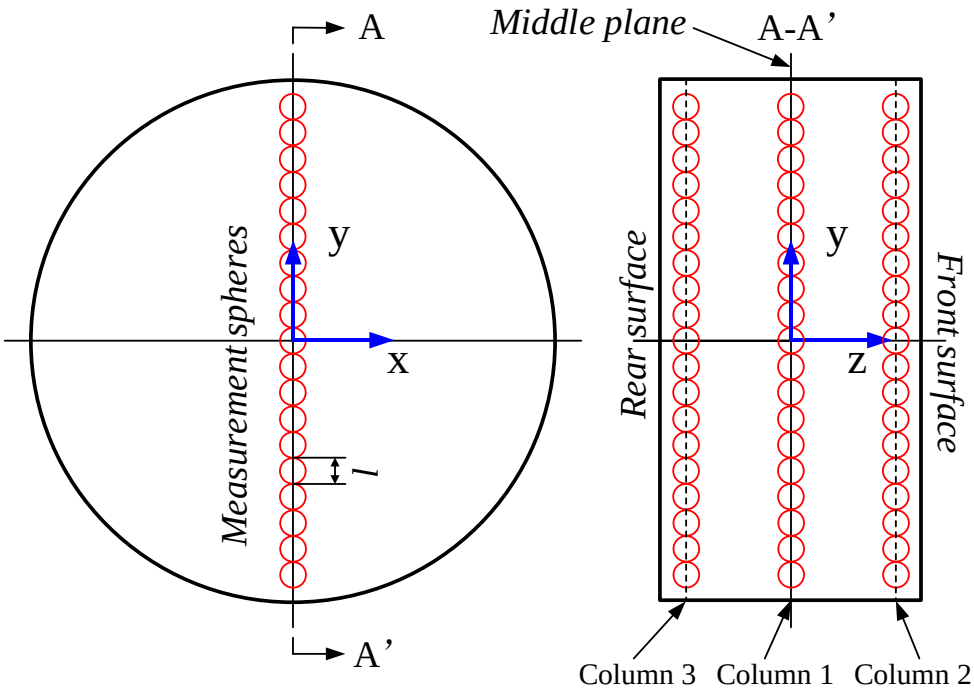

Figure 6.14 Arrangement of measurement spheres along the loading plane in the disc-shaped model under the Brazilian test. Diameter of measurement spheres l = 5 mm.

Based on the assumption that a material is homogeneous, isotropic and linear elastic, **Hondros (1959)** proposed a 2D stress solution for the specimen under the diametric loading over finite arcs according to,

$$\sigma_{\theta\theta}=\frac{P}{\pi Rt\alpha}\left\{\frac{\left[1-(r/R)^2\right]\sin 2\alpha}{1-2(r/R)^2\cos 2\alpha+(r/R)^4}-\tan^{-1}\left[\frac{1+(r/R)^2}{1-(r/R)^2}\tan\alpha\right]\right\} \tag{6.1}$$

$$\sigma_{rr}=-\frac{P}{\pi Rt\alpha}\left\{\frac{\left[1-(r/R)^2\right]\sin 2\alpha}{1-2(r/R)^2\cos 2\alpha+(r/R)^4}+\tan^{-1}\left[\frac{1+(r/R)^2}{1-(r/R)^2}\tan\alpha\right]\right\} \tag{6.2}$$

where $\sigma_{\theta\theta}$ and σ_{rr} represent the tensile and compressive stresses, respectively; P is the exerted force; R and t are the radius and thickness of the disk-shaped specimen, respectively; 2α is the arc over which the force is applied; and r is the distance from the centre of the disk. Notably, tensile stress is regarded as positive. This solution is applicable to conditions of both plane stress and plane strain.

(a)

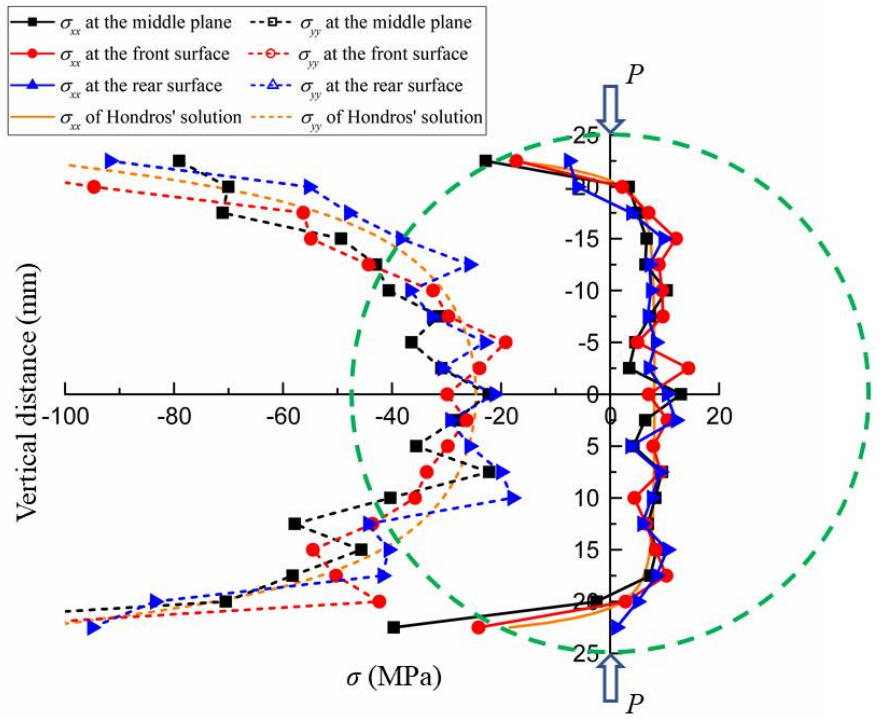

(b)

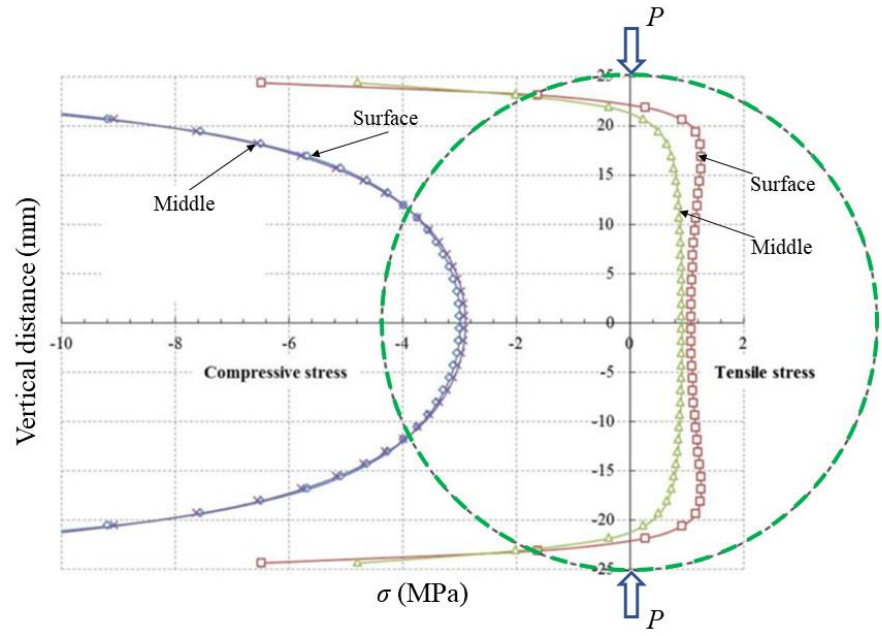

Figure 6.15 Comparison of principal stresses along the compressed diametral line (AA'): (a) between the numerical modeling results and Hondros' solutions at the crack-initiation stress for slate models with $\psi-\beta$ of 45°−45°; and (b) obtained from the continuum method by **Li and Wong (2013)**. The green dashed circle denotes the Brazilian disc specimen.

(a)

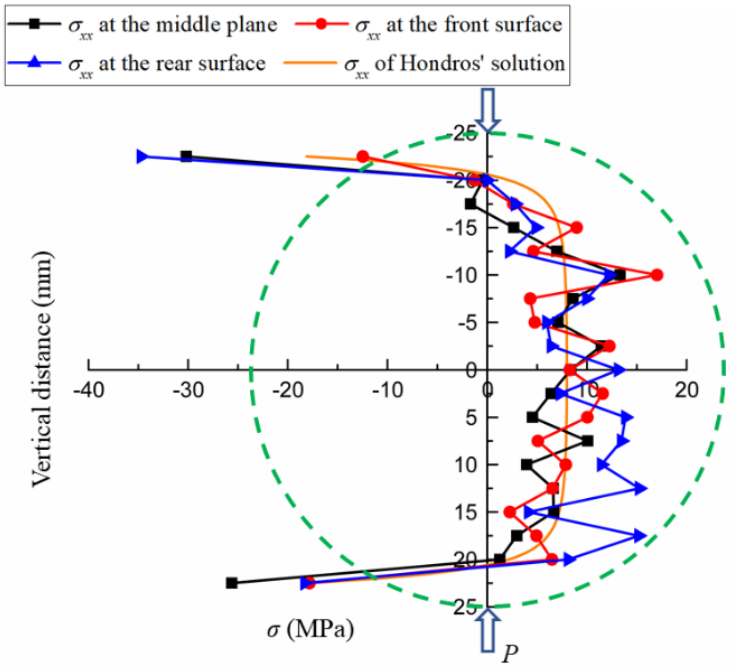

(b)

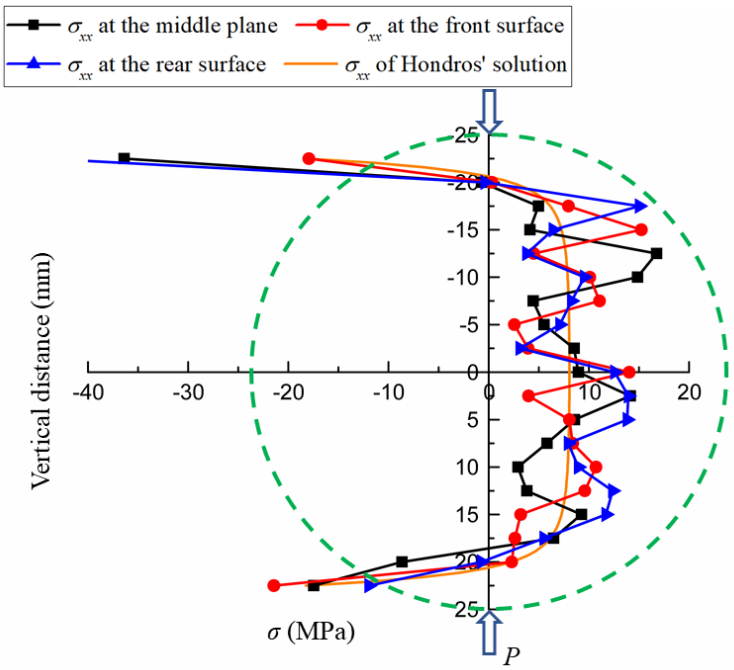

Figure 6.16 Comparison of tensile principal stresses along the compressed diametric line (AA') for slate models with different thicknesses: (a) 50 mm and (b) 100 mm.

As an example, the principal stresses of models at ψ–β of 45°–45° were recorded along the loading plane at the crack-initiation stress (corresponding to point *a* in Figure 6.12e), as illustrated in Figure 6.15a. The principal stresses based on the Hondros solutions (2α = 12°) are also compared with those obtained by the DEM simulation in Figure 6.15a, demonstrating that: (1) the results of numerical modelling follow the overall trend of the

theoretical solution that along the loaded diameter AA′ the vertical stresses (σ_{yy}) are compressive and increase with the distance from the centre of the disk; and (2) the horizontal stresses (σ_{xx}) are tensile in the middle section ($-0.8R < r < 0.8R$) and compressive near the two loading points. However, values of σ_{xx} and σ_{yy} obtained from numerical modelling fluctuate dramatically around those predicted by the Hondros' solution due to the inherent heterogeneity of particle size distribution and the weak planes induced anisotropy. For example, the tensile stress or shear stress at the weak plane does not exceed the micro-tensile strength (3.5 MPa) or cohesion (25 MPa) of SJM, respectively, while those at the rock matrix can be far higher owing to a higher strength of FJM.

In addition, the tensile stress distributions of primary interest in this study on the end surfaces and the middle plane are different, particularly near two loading points, which is to some extent in agreement with that obtained from the continuum method by **Li and Wong (2013)**. As can be seen in Figure 6.15b, the tensile stresses on the surface are higher than those on the middle plane in Li and Wong's results. The variations in tensile stress along the direction of thickness were attributed to the shape effect of the Brazilian disk specimen **(Yu et al. 2006)**. In the isotropic material, the stress distributions on the two end surfaces are symmetrical with respect to the middle plane and taken as identical **(Li and Wong 2013; Yu et al. 2006)**. In contrast, in this transversely isotropic model, there exists a big difference in stress distributions on the two end surfaces because of the existence of weak planes. To get a better understanding of the shape effect of Brazilian disk specimen on the stress distribution, the thickness of the disk specimen is increased to 50 mm ($t = 2R$) and 100 mm ($t = 4R$), and the corresponding tensile stress distributions on the middle plane and end surfaces are compared in Figure 6.16 along with those observed in the specimen with a thickness of 25 mm (Figure 6.15a). The results indicate that with increasing the thickness of specimen, the differences in tensile stress distributions on the end surfaces and middle plane increase, and so do the heterogeneity and the anisotropy of tensile stress distributions. Besides, the deviation between tensile stresses obtained from the numerical modelling and the Hondros' solution accumulates as the thickness of specimen increases. It demonstrates again that the indirect tensile behaviour of transversely isotropic rock is a 3D problem rather than a 2D problem. The increased shape effect further results in the BFS increasing from 12.0 MPa to 14.1 MPa,

which is contradictory to the finding in isotropic rocks that BFS reduces with the thickness of disk-shaped specimen **(Mellor and Hawkes 1971; Yu et al. 2006)**. This discrepancy likely arises from different failure modes. Under Brazilian tensile conditions, isotropic rock is generally failed by a tensile fracture, but the transversely isotropic rock at ψ–β of 45°–45° is failed by a complicated mixed tensile and shear fracture as shown in Figure 6.12e. Accordingly, it is inferred that the shape effect in transversely isotropic rocks is associated with the foliation orientation relative to the loading direction, which has been rarely reported.

6.6 Summary

Two-dimensional modelling is incapable of analysing many practical anisotropic problems, e.g., that of borehole instability in oblique wells excavated in anisotropic formations, estimation of elastic properties for transversely isotropic rocks and 3D fracture after Brazilian testing for transversely isotropic rocks. Thus a 3D model for slate was generated using the embedded FJM and SJM in DEM to investigate the influences of foliation spacing and 3D foliation orientation on the tensile behaviour under indirect tensile conditions. A new calibration procedure was proposed for the DEM modelling of the transversely isotropic rock. Based on the preceding numerical analysis, the following conclusions can be drawn:

(1) At β of 0°–30°, the influences of foliation spacing on tensile strength and failure mode are negligible, but at β of 45°–90°, the tensile strength is significantly increased and failure mode is also impacted by increasing foliation spacing with effects of foliation spacing reaching the maximum at β of 90°.

(2) At $0° \leq \psi \leq 30°$, the tensile strength of slate models is independent of ψ and increases with β, but at $45° \leq \psi \leq 90°$, variations in the tensile strength of slate models are insensitive to β, with tensile strength increasing linearly with ψ. The coupling effect of β and ψ is illustrated by variations in the anisotropy ratio of tensile strength, evident at $30° \leq \psi < 45°$.

(3) The tensile fracture in the rock matrix and along the weak plane are the main fracture patterns of the slate model under Brazilian tests. At low ψ and β, fracture of the slate model begins at the centre of the disk and propagates towards the top and bottom loading points – opposite to the behaviour seen for high ψ and β. The

fracture process is consistent with laboratory observations. Moreover, at intermediate and high ψ, the fracture pattern is 3D and the influence of 3D foliation orientation must be considered.

(4) The proportional variations of micro-cracks at failure with ψ and β well account for the effect of 3D foliation orientation on tensile strength. It is also found that the portion of flat-joint tensile cracks is mainly responsible for the strength of the slate model.

(5) The introduction of weak planes into isotropic rock model increases both heterogeneity and anisotropy of stress distributions, as well as the shape effect in transversely isotropic rock. Contrary to that in isotropic rocks, the shape effect is thought to facilitate the indirect tensile strength of transversely isotropic rock. Considering the 3D anisotropy effect, a more reliable solution to calculate the indirect tensile strength for transversely isotropic rocks can be derived.

CHAPTER 7 CONCLUSIONS AND RECOMMENDATIONS

In this chapter the main findings and conclusions of the present study are summarised and some recommendations for future work are presented.

7.1 Conclusions

This thesis aims to investigate anisotropy and size effect in transversely isotropic rock under different stress conditions, such as indirect tensile, uniaxial and triaxial compressive testing. In particular, this study's main contributions include (1) performing a series of laboratory tests, including indirect tensile, uniaxial and triaxial compressive tests, on slate with different specimen sizes at different anisotropic angles; (2) investigating variations in elastic properties, indirect tensile strength, uniaxial compressive strength, triaxial compressive strength, triaxial residual strength and failure pattern with specimen size and anisotropic angle; (3) incorporating size dependency into the analysis of failure criterion for transversely isotropic rock under triaxial compressive conditions and (4) investigating the effects of model size and particle size distribution on the macro-mechanical properties of isotropic rock using a flat-joint model, so as to further study the effect of three-dimensional anisotropy on tensile behaviour of the transversely isotropic rock using the combined flat-joint and smooth-joint model. Based on these studies, its major contributions and conclusions are as follows:

1. The pure effects of model size and particle size distribution on the macro-mechanical properties of the isotropic rock are revealed by eliminating the influence of porosity. As model size increases, uniaxial compressive strength, crack-initiation stress, Young's modulus and Poisson's ratio first decrease and then stabilize, whereas the indirect tensile strength follows a generalized descending trend best fitted by fracture energy and multifractal size-effect models for which fitting constants are functions of grain size heterogeneity. All the macro-mechanical properties decrease with grain size heterogeneity. Additionally, a commonly accepted standard for the selection of model size and particle size is established for three-dimensional flat-jointed models.
2. Five independent elastic constants are determined by combining indirect tensile test and FLAC3D simulation. The Young's modulus in the transversely isotropic plane

presents an ascending size effect, whereas the Young's modulus and shear modulus perpendicular to the transversely isotropic plane exhibit a reverse size effect. The Poisson's ratios parallel to and normal to the transversely isotropic plane do not show an evident size effect. The size effects on the elastic properties can be attributed to the combined influence of weak planes and near-surface damage during sample preparation. Moreover, the values of elastic properties obtained from compressive tests are different than those obtained from indirect tensile tests. The anisotropy of the apparent elastic modulus follows the transversely isotropic model with an acceptable degree of error.

3. The size effect and anisotropy in the indirect tensile strength are correlated with each other. At the low loading–foliation angle, the indirect tensile strength presents a typical descending size effect, whereas at the high loading–foliation angle it presents an initially ascending and then descending size effect. The transition of size-effect trends is closely associated with the failure mechanism at different loading directions. Furthermore, a unified size-effect relation including two equations is proposed and validated against the experimental data to capture the relationship among indirect tensile strength, specimen size and loading–foliation angle.

4. The indirect tensile strength of slate is associated with not only the loading–foliation angle but also the foliation orientation relative to the sample axis. The indirect tensile strength is independent of the foliation orientation and increases with loading–foliation angle at foliation orientations of 0° to 30°, whereas at foliation orientations of 45° to 90° it is insensitive to the loading–foliation angle and increases with foliation orientation. The coupling effect of loading–foliation angle and foliation orientation is illustrated by the variation of anisotropy ratio of indirect tensile strength, most evident at the foliation orientation of 30° to 45°. Furthermore, the proportional variations of micro-cracks at failure account for the effect of three-dimensional foliation orientation on the indirect tensile strength at the microscale.

5. The tensile fracture in the rock matrix and along the weak plane are the main fracture pattern of slate specimen under indirect tensile conditions. At low loading–foliation angle and foliation orientation, the fracture initiates at the centre of the disc and then propagates towards the top and bottom loading points, the reverse of what is seen at other loading–foliation angles and foliation orientations. It is also found that the horizontal strain along the compressed diameter can be used to estimate the fracture

initiation point in the laboratory test. The fracture processes observed in numerical and experimental tests are consistent. Moreover, at low foliation orientation, the fracture pattern is approximately two-dimensional, whereas at the intermediate or high foliation orientation the fracture pattern is three-dimensional and rather complex.

6. A size-effect relation developed from an orthotropic rock, coal, is extended to a transversely isotropic rock, slate, which captures the relationship among uniaxial compressive strength, specimen size and loading–foliation angle. The anisotropy of compressive strength follows a cosine relation, with the degree of anisotropy being dependent on both specimen size and confining pressure.

7. The size-effect behaviours of uniaxial and triaxial compressive strengths are found to be similar. Through incorporation of the size-effect relation for uniaxial compressive strength into the modified Hoek–Brown and Saeidi failure criteria, two size-dependent failure criteria are proposed and verified against the experimental data of slate. They are capable of describing the relationship among specimen size, anisotropic angle, confining pressure and rock strength under uniaxial and triaxial compressive conditions. The size-dependent Saeidi failure criterion is superior to the size-dependent modified Hoek–Brown failure criterion in terms of the prediction accuracy with a higher nonlinearity. Moreover, the former one can be applicable to both brittle and ductile regimes, whereas the latter one is limited in the brittle regime. However, both size-dependent failure criteria are not applicable to the transversely isotropic rock in the tensile stress condition.

8. Evident anisotropy, but no size effect, exists in the triaxial residual strength of slate. A cohesion loss model is improved to capture the anisotropic residual strength, in which the influence of anisotropy decreases with increasing anisotropic angle. The ratio of residual to peak strength increases as a function of confining pressure for transversely isotropic rocks, following the cohesion-weakening–friction-strengthening model for the brittle failure of rock. Two equations delineating the range for the ratio of residual to peak strength are proposed for transversely isotropic rocks.

7.2 Recommendations for future works

Although some progress has been made in proposing size-effect models and size-

dependent failure criteria for the analysis of size effect and anisotropy in transversely isotropic rocks and investigating the effect of three-dimensional anisotropy on indirect tensile behaviour in the present study, certain limitations do leave room for further improvement:

1. The size effect on macro-mechanical properties for isotropic rock is investigated without introducing the discrete fracture network in Chapter 3, because the pre-existing flaws or pores within the specimen are unknown. To accurately reproduce the size effect in numerical modelling, a quantitative analysis of microstructure by means of X-ray computed tomography scan should be conducted.
2. Although the proposed size-effect relation in Chapter 4 can capture the relationship among indirect tensile strength, specimen size and loading–foliation angle, it is only suitable for the transversely isotropic rock when the strike of weak planes coincides with the sample axis. This is because the adopted formula for calculating the tensile strength is applicable only to the two-dimensional problem. Accordingly, considering the three-dimensional anisotropy effect, a more capable solution for indirect tensile strength in transversely isotropic rocks is necessary that can further develop a size-effect model for three-dimensional analysis of transversely isotropic rocks under the indirect tensile condition.
3. Although two size-dependent failure criteria are proposed and validated against the experimental data of slate in Chapter 5, an underlying assumption should not be neglected – that the severity of size effect on compressive strength is independent of confining pressure. The observed results indicate that the severity of size effect increases with confining pressure when sliding failure along the weak planes, contrary to the common viewpoint that confining pressures suppress the size effect in rocks. A critical confining pressure for transversely isotropic rocks must exist below which the confining pressure facilitates the size effect but beyond which it reverses when sliding failure along the weak planes occurs. Accordingly, a wide range of confining pressures is suggested for future size-effect study in transversely isotropic rocks so as to incorporate the influence of confining pressure on size effect into the size-dependent failure criterion.
4. The two proposed size-dependent failure criteria are applicable only to transversely isotropic rock in conventional triaxial conditions. However, the three principal

stresses are usually not the same in the practical engineering, and the intermediate principal stress plays an important role in the strength of rock. Hence study of the size effect and anisotropy in transversely isotropic rocks subject to a true triaxial stress state is also a meaningful research topic.

5. The effect of three-dimensional anisotropy in transversely isotropic rocks has been studied only under indirect tensile tests in Chapter 6. It should be applied in real-world projects, such as to address stability problems in boreholes, tunnels or caverns excavated obliquely in anisotropic formations. Considering the effects of far-field stress anisotropy, rock anisotropy, shape and size of underground structures, a three-dimensional numerical study is recommended that would use a hybrid continuum/dicontinuum method.

6. In this study, the applicability of the findings focused on elastic property, indirect tensile strength, uniaxial and triaxial compressive strength and triaxial residual strength have been validated only for slate, because data on various tests of transversely isotropic rocks considering the size effect are scarce in the literature. It is suggested that a systematic study of size effect and anisotropy should be carried out on different types of anisotropic rocks, including sedimentary rocks and metamorphic rocks, and that the proposed relation or criterion be calibrated against all the data. A database of representative values of model parameters for various rocks should be established.

REFERENCES

Abad I, Nieto F, Gutiérrez-Alonso G (2003) Textural and chemical changes in slate-forming phyllosilicates across the external-internal zones transition in the low-grade metamorphic belt of the NW Iberian Variscan Chain. Swiss Bulletin of Mineralogy and Petrology 83:63-80

Akazawa T (1943) New test method for evaluating internal stress due to compression of concrete (the splitting tension test)(part 1). 29:777-787

Aliabadian Z, Zhao G-F, Russell AR (2019) Crack development in transversely isotropic sandstone discs subjected to Brazilian tests observed using digital image correlation. International Journal of Rock Mechanics and Mining Sciences 119:211-221

Aliabadian Z, Zhao GF, Russell AR (2017) An Analytical Study of Failure of Transversely Isotropic Rock Discs Subjected to Various Diametrical Loading Configurations. Procedia Engineering 191:1194-1202

Amadei B (1996) Importance of anisotropy when estimating and measuring in situ stresses in rock. International Journal of Rock Mechanics and Mining Sciences & Geomechanics Abstracts 33:293-325

Amadei B (2012) Rock anisotropy and the theory of stress measurements. vol 2. Springer Science & Business Media.

ASTM (2014) Standard Test Methods for Compressive Strength and Elastic Moduli of Intact Rock Core Specimens under Varying States of Stress and Temperatures. ASTM International, West Conshohocken, PA.

ASTM (2016) Standard Test Method for Splitting Tensile Strength of Intact Rock Core Specimens. ASTM International, West Conshohocken, PA.

Aubertin M, Li L, Simon R (2000) A multiaxial stress criterion for short- and long-term strength of isotropic rock media. International Journal of Rock Mechanics and Mining Sciences 37:1169-1193

Bagi K (2005) An algorithm to generate random dense arrangements for discrete element simulations of granular assemblies. Granular Matter 7:31-43

Bahrani N, Kaiser PK (2016) Numerical investigation of the influence of specimen size on the unconfined strength of defected rocks. Computers and Geotechnics 77:56-67

Bai Q-S, Tu S-H, Zhang C (2016) DEM investigation of the fracture mechanism of rock disc containing hole(s) and its influence on tensile strength. Theoretical and Applied Fracture Mechanics 86:197-216

Barla G, Innaurato N (1973) Indirect tensile testing of anisotropic rocks. Rock mechanics 5:215-230

Barron K Brittle fracture initiation in and ultimate failure of rocks: part II—Anisotropic rocks: theory. In: International Journal of Rock Mechanics and Mining Sciences & Geomechanics Abstracts, 1971. vol 6. Elsevier, pp 553-563.

Bažant ZP (1984) Size effect in blunt fracture: concrete, rock, metal. Journal of Engineering Mechanics 110:518-535

Bažant ZP (1997) Scaling of quasibrittle fracture: hypotheses of invasive and lacunar fractality, their critique and Weibull connection. International Journal of Fracture 83:41

Benz T, Schwab R, Kauther RA, Vermeer PA (2008) A Hoek–Brown criterion with intrinsic material strength factorization. International Journal of Rock Mechanics and Mining Sciences 45:210-222

Blümling P, Bernier F, Lebon P, Derek Martin C (2007) The excavation damaged zone in clay formations time-dependent behaviour and influence on performance assessment. Physics and Chemistry of the Earth, Parts A/B/C 32:588-599

Brace W, Paulding B, Scholz C (1966) Dilatancy in the fracture of crystalline rocks. Journal of Geophysical Research 71:3939-3953

Broch E, Franklin JA (1972) The point-load strength test. International Journal of Rock Mechanics and Mining Sciences & Geomechanics Abstracts 9:669-676

Cai M (2010) Practical estimates of tensile strength and Hoek–Brown strength parameter mi of brittle rocks. Rock Mechanics and Rock Engineering 43:167-184

Cai M, Kaiser PK (2004) Numerical Simulation Of The Brazilian Test And The Tensile Strength Of Anisotropic Rocks And Rocks With Pre-Existing Cracks. International Journal of Rock Mechanics and Mining Sciences 41:478-483

Carneiro F A new method to determine the tensile strength of concrete. In: Proceedings of the 5th meeting of the Brazilian Association for Technical Rules, 1943. vol 16. pp 126-129.

Carpinteri A, Chiaia B, Ferro G (1995) Size effects on nominal tensile strength of concrete structures: multifractality of material ligaments and dimensional transition from order to disorder. Materials and Structures 28:311

Castro-Filgueira U, Alejano LR, Arzúa J, Ivars DM (2017) Sensitivity Analysis of the Micro-Parameters Used in a PFC Analysis Towards the Mechanical Properties of Rocks. Procedia Engineering 191:488-495

Celleri HM, Sánchez M, Otegui JL (2018) Fracture behaviour of transversely isotropic rocks with discrete weak interfaces. International Journal for Numerical and Analytical Methods in Geomechanics 42:2161-2176

Chen C-S, Hsu S (2001) Measurement of indirect tensile strength of anisotropic rocks by the ring test. Rock mechanics and rock engineering 34:293-321

Chen C-S, Pan E, Amadei B (1998) Determination of deformability and tensile strength of anisotropic rock using Brazilian tests. International Journal of Rock Mechanics and Mining Sciences 35:43-61

Chen P-Y (2017) Effects of Microparameters on Macroparameters of Flat-Jointed Bonded-Particle Materials and Suggestions on Trial-and-Error Method. Geotech Geol Eng:1-15

Chen Z, He C, Wu D, Xu G, Yang W (2017) Fracture evolution and energy mechanism of deep-buried carbonaceous slate. Acta Geotechnica:1-18

Cheng Y, Wong LNY, Zou C (2015) Experimental study on the formation of faults from en-echelon fractures in Carrara Marble. Engineering Geology 195:312-326

Cho J-W, Kim H, Jeon S, Min K-B (2012) Deformation and strength anisotropy of Asan gneiss, Boryeong shale, and Yeoncheon schist. International Journal of Rock Mechanics and Mining Sciences 50:158-169

Cho N, Martin CD, Sego DC (2007) A clumped particle model for rock. International Journal of Rock Mechanics and Mining Sciences 44:997-1010

Chou YC, Chen CS (2008) Determining elastic constants of transversely isotropic rocks using Brazilian test and iterative procedure. International journal for numerical and analytical methods in geomechanics 32:219-234

Claesson J, Bohloli B (2002) Brazilian test: stress field and tensile strength of anisotropic rocks using an analytical solution. International Journal of Rock Mechanics and Mining Sciences 39:991-1004

Cundall PA, Strack OD (1979) A discrete numerical model for granular assemblies. Geotechnique 29:47-65

Dan DQ, Konietzky H (2014) Numerical simulations and interpretations of Brazilian tensile tests on transversely isotropic rocks. International Journal of Rock Mechanics and Mining Sciences 71:53-63

Dan DQ, Konietzky H, Herbst M (2013) Brazilian tensile strength tests on some anisotropic rocks. International Journal of Rock Mechanics and Mining Sciences 58:1-7

Darbor M, Faramarzi L, Sharifzadeh M (2018) Size-dependent compressive strength properties of hard rocks and rock-like cementitious brittle materials. Geosystem Engineering:1-14

Darlington WJ, Ranjith PG, Choi SK (2011) The Effect of Specimen Size on Strength and Other Properties in Laboratory Testing of Rock and Rock-Like Cementitious Brittle Materials. Rock Mechanics and Rock Engineering 44:513

Debecker B, Vervoort A (2009) Experimental observation of fracture patterns in layered slate. International Journal of Fracture 159:51-62

Desai CS (1976) Finite element residual schemes for unconfined flow. International Journal for Numerical Methods in Engineering 10:1415-1418

Desai CS (2016) Disturbed state concept as unified constitutive modeling approach. Journal of Rock Mechanics and Geotechnical Engineering 8:277-293

Ding C, Hu D, Zhou H, Lu J, Ma D, Zhang Y (2019) Brazilian splitting tests of slate considering three-dimensional foliation effect. Chinese Journal of Rock Mechanics and Engineering 38:301-312

Ding X, Zhang L, Zhu H, Zhang Q (2014) Effect of Model Scale and Particle Size Distribution on PFC3D Simulation Results. Rock Mechanics and Rock Engineering 47:2139-2156

Donath FA (1961) Experimental study of shear failure in anisotropic rocks. Geological Society of America Bulletin 72:985-989

Donzé F, Harthong B, Scholtès L DEM modeling of jointed rock slopes. In: 47th US Rock Mechanics/Geomechanics Symposium, 2013. American Rock Mechanics Association.

Duan K, Kwok CY (2015) Discrete element modeling of anisotropic rock under Brazilian test conditions. International Journal of Rock Mechanics and Mining Sciences 78:46-56

Duan K, Kwok CY (2016) Evolution of stress-induced borehole breakout in inherently anisotropic rock: Insights from discrete element modeling. Journal of Geophysical Research: Solid Earth 121:2361-2381

Duan K, Kwok CY, Pierce M (2015) Discrete element method modeling of inherently anisotropic rocks under uniaxial compression loading. International Journal for Numerical and Analytical Methods in Geomechanics:n/a-n/a

Duan K, Wu W, Kwok CY (2018) Discrete element modelling of stress-induced

instability of directional drilling boreholes in anisotropic rock. Tunnelling and Underground Space Technology 81:55-67

Duveau G, Shao J, Henry J (1998) Assessment of some failure criteria for strongly anisotropic geomaterials. Mechanics of Cohesive-frictional Materials 3:1-26

Elkadi AS, Van Mier JGM, Sluys LJ (2006) Multiaxial failure of low-cohesive frictional materials: fracture behaviour and size dependency. Philosophical Magazine 86:3137-3159

Esmaieli K, Hadjigeorgiou J, Grenon M (2010) Estimating geometrical and mechanical REV based on synthetic rock mass models at Brunswick Mine. International Journal of Rock Mechanics and Mining Sciences 47:915-926

Exadaktylos GE, Kaklis KN (2001) Applications of an explicit solution for the transversely isotropic circular disc compressed diametrically. International Journal of Rock Mechanics and Mining Sciences 38:227-243

Fairhurst C Fundamental considerations relating to the strength of rock. In: Colloquium on rock fracture, Ruhr University, Bochum, Germany, Veröff. Inst. Bodenmechanik und Felsmechanik (Karlsruhe). 1971. Citeseer, pp 1-56.

Fairhurst C, Hudson J (1999) Draft ISRM suggested method for the complete stress-strain curve for intact rock in uniaxial compression. International Journal of Rock Mechanics and Mining Sciences 36:279-289

Fan X, Li K, Lai H, Xie Y, Cao R, Zheng J (2018) Internal stress distribution and cracking around flaws and openings of rock block under uniaxial compression: A particle mechanics approach. Computers and Geotechnics 102:28-38

Fu H, Zhang J, Huang Z, Shi Y, Chen W (2018) A statistical model for predicting the triaxial compressive strength of transversely isotropic rocks subjected to freeze–thaw cycling. Cold Regions Science and Technology 145:237-248

Gao FQ, Kang HP (2016) Effects of pre-existing discontinuities on the residual strength of rock mass – Insight from a discrete element method simulation. Journal of

Structural Geology 85:40-50

Gingold RA, Monaghan JJ (1977) Smoothed particle hydrodynamics: theory and application to non-spherical stars. Mon Not Roy Astron Soc 181:375-389

Goodman RE (1989) Introduction to rock mechanics. vol 2. Wiley New York.

Gowd T, Rummel F Effect of confining pressure on the fracture behaviour of a porous rock. In: International Journal of Rock Mechanics and Mining Sciences & Geomechanics Abstracts, 1980. vol 4. Elsevier, pp 225-229.

Hajiabdolmajid V, Kaiser PK, Martin CD (2002) Modelling brittle failure of rock. International Journal of Rock Mechanics and Mining Sciences 39:731-741

Hawkins AB (1998) Aspects of rock strength. Bulletin of Engineering Geology and the Environment 57:17-30

Hobbs D Rock tensile strength and its relationship to a number of alternative measures of rock strength. In: International Journal of Rock Mechanics and Mining Sciences & Geomechanics Abstracts, 1967. vol 1. Elsevier, pp 115-127.

Hobbs DW (1964) The tensile strength of rocks. International Journal of Rock Mechanics and Mining Sciences & Geomechanics Abstracts 1:385-396

Hoek E, Brown ET (1980) Underground excavations in rock. Institution of Mining and Metallurgy, Spon Press, Hertford, London.

Hoek E, Brown ET (1997) Practical estimates of rock mass strength. International Journal of Rock Mechanics and Mining Sciences 34:1165-1186

Hofmann H, Babadagli T, Yoon JS, Zang A, Zimmermann G (2015) A grain based modeling study of mineralogical factors affecting strength, elastic behaviour and micro fracture development during compression tests in granites. Engineering Fracture Mechanics 147:261-275

Hondros G (1959) The evaluation of Poisson's ratio and the modulus of materials of low tensile resistance by the Brazilian (indirect tensile) test with particular reference to

concrete. Australian J Appl Sci 10:243-268

Hu S, Tan Y, Zhou H, Guo W, Hu D, Meng F, Liu Z (2017) Impact of Bedding Planes on Mechanical Properties of Sandstone. Rock Mechanics and Rock Engineering 50:2243-2251

Hudson JA, Harrison JP (2000) Engineering rock mechanics: an introduction to the principles. Elsevier, Amsterdam.

Hunt DD (1973) The influence of confining pressure on size effect., Massachusetts Institute of Technology

Imani M, Nejati HR, Goshtasbi K (2017) Dynamic response and failure mechanism of Brazilian disk specimens at high strain rate. Soil Dynamics and Earthquake Engineering 100:261-269

Inglis CE (1913) Stresses in a plate due to the presence of cracks and sharp corners. 55:219-241

ISRM (1978) Suggested methods for determining tensile strength of rock materials. International Journal of Rock Mechanics and Mining Sciences & Geomechanics Abstracts 15:99-103

ISRM (2007) The complete suggested methods for rock characterization, testing and monitoring: 1974–2006. Compilation Arranged by the ISRM Turkish National Group, Ankara, Turkey.

Itasca Consulting Group I (2014) PFC (particle flow code in 2 and 3 dimensions), version 5.0 [User's manual]. Minneapolis, ICG.

Jaeger J (1960) Shear failure of anistropic rocks. Geological Magazine 97:65-72

Jaeger JC, Cook NG, Zimmerman R (2009) Fundamentals of rock mechanics. John Wiley & Sons.

Jing L (2003) A review of techniques, advances and outstanding issues in numerical modelling for rock mechanics and rock engineering. International Journal of Rock

Mechanics and Mining Sciences 40:283-353

Ju Y, Yang YM, Peng RD, Mao LT (2013) Effects of Pore Structures on Static Mechanical Properties of Sandstone. Journal of Geotechnical and Geoenvironmental Engineering 139:1745-1755

Karampinos E, Hadjigeorgiou J, Hazzard J, Turcotte P (2015) Discrete element modelling of the buckling phenomenon in deep hard rock mines. International Journal of Rock Mechanics and Mining Sciences 80:346-356

Kelly D, Peck D, James R (1994) Petrography of granitic samples from the 420 m level of the Underground Research Laboratory. Pinawa, Manitoba, report, Laurentian Univ, Sudbury, Ont, Canada

Khanlari G, Rafiei B, Abdilor Y (2015) An experimental investigation of the Brazilian tensile strength and failure patterns of laminated sandstones. Rock Mechanics and Rock Engineering 48:843-852

Komurlu E, Kesimal A (2015) Evaluation of indirect tensile strength of rocks using different types of jaws. Rock Mechanics and Rock Engineering 48:1723-1730

Kovari K, Tisa A, Einstein H, Franklin J (1983) Suggested methods for determining the strength of rock materials in triaxial compression: revised version. Intl J of Rock Mech & Mining Sci & Geomechanic Abs 20

Koyama T, Jing L (2007) Effects of model scale and particle size on micro-mechanical properties and failure processes of rocks—a particle mechanics approach. Engineering analysis with boundary elements 31:458-472

Kumar R, Sharma KG, Varadarajan A (2010) Post-peak response of some metamorphic rocks of India under high confining pressures. International Journal of Rock Mechanics and Mining Sciences 47:1357-1362

Kundu J, Mahanta B, Sarkar K, Singh TN (2018) The Effect of Lineation on Anisotropy in Dry and Saturated Himalayan Schistose Rock Under Brazilian Test Conditions. Rock Mechanics and Rock Engineering 51:5-21

Kwasniewski M (1983) Anisotropy of elasticity of rocks and its effect on the magnitude and distribution of stresses around underground openings. Proceedings of the 8th Plenary Scientific Session of the International Bureau of Strata Mechanics: Application of Rock Mechanics to Planning and Design Prior to Mining:5-37

Lan H, Martin CD, Hu B (2010) Effect of heterogeneity of brittle rock on micromechanical extensile behaviour during compression loading. Journal of Geophysical Research: Solid Earth 115

Lee Y-K, Pietruszczak S (2008) Application of critical plane approach to the prediction of strength anisotropy in transversely isotropic rock masses. International Journal of Rock Mechanics and Mining Sciences 45:513-523

Lee Y-K, Pietruszczak S (2015) Tensile failure criterion for transversely isotropic rocks. International Journal of Rock Mechanics and Mining Sciences 79:205-215

Li D, Li CC, Li X (2011) Influence of Sample Height-to-Width Ratios on Failure Mode for Rectangular Prism Samples of Hard Rock Loaded In Uniaxial Compression. Rock Mechanics and Rock Engineering 44:253-267

Li D, Wong LNY (2013) The Brazilian Disc Test for Rock Mechanics Applications: Review and New Insights. Rock Mechanics and Rock Engineering 46:269-287

Li KH, Cao P, Zhang K, Zhong YF (2015) Macro and meso characteristics evolution on shear behaviour of rock joints. Journal of Central South University 22:3087-3096

Li K, Cheng Y, Fan X (2018) Roles of model size and particle size distribution on macro-mechanical properties of Lac du Bonnet granite using flat-joint model. Computers and Geotechnics 103:43-60

Li K, Cheng Y, Yin Z, Han D, Meng J (2019) Size effects in a transversely isotropic rock under Brazilian tests: laboratory testing. Rock Mechanics and Rock Engineering

Li L, Aubertin M Un critère de rupture multiaxial pour les roches avec une anisotropie planaire. In: Compte-Rendu., 53 ème Conf. Can. Géotech, 2000. pp 15-18.

Li L, Aubertin M (2002) A crack-induced stress approach to describe the tensile strength

of transversely isotropic rocks. 39:1-13

Li S, Liu WK (2002) Meshfree and particle methods and their applications. Applied Mechanics Reviews 55:1-34

Liao J, Hsieh H Triaxial residual strength of an anisotropic rock. In: Vail Rocks 1999, The 37th US Symposium on Rock Mechanics (USRMS), 1999. American Rock Mechanics Association.

Liao JJ, Yang M-T, Hsieh H-Y (1997) Direct tensile behaviour of a transversely isotropic rock. International Journal of Rock Mechanics and Mining Sciences 34:837-849

Liu G, Cai M, Huang M (2018) Mechanical properties of brittle rock governed by micro-geometric heterogeneity. Computers and Geotechnics

Liu X, Liu Q, Kang Y, Pan Y (2017) Improved Nonlinear Strength Criterion for Jointed Rock Masses Subject to Complex Stress States. International Journal of Geomechanics 18:04017164

Loureiro-Pinto J Determination of the elastic constants of anisotropic bodies by diametral compression tests. In: 4th ISRM Congress, 1979. International Society for Rock Mechanics.

Lu YY, Belytschko T, Gu L (1994) A new implementation of the element free Galerkin method. Computer Methods in Applied Mechanics and Engineering 113:397-414

Ma T, Peng N, Zhu Z, Zhang Q, Yang C, Zhao J (2018) Brazilian Tensile Strength of Anisotropic Rocks: Review and New Insights. Energies 11:304

Ma T, Zhang QB, Chen P, Yang C, Zhao J (2017) Fracture pressure model for inclined wells in layered formations with anisotropic rock strengths. Journal of Petroleum Science and Engineering 149:393-408

Manchao H, Leal e Sousa R, Müller A, Vargas E, Ribeiro e Sousa L, Xin C (2015) Analysis of excessive deformations in tunnels for safety evaluation. Tunnelling and Underground Space Technology 45:190-202

Markides CF, Kourkoulis SK (2012) The Stress Field in a Standardized Brazilian Disc: The Influence of the Loading Type Acting on the Actual Contact Length. Rock Mechanics and Rock Engineering 45:145-158

Martin C, Chandler N (1994) The progressive fracture of Lac du Bonnet granite. International Journal of Rock Mechanics and Mining Sciences & Geomechanics Abstracts 31:643-659

Martin CD (1993) The strength of massive Lac du Bonnet granite around underground openings., University of Manitoba

Martin CD (1997) Seventeenth Canadian geotechnical colloquium: the effect of cohesion loss and stress path on brittle rock strength. Canadian Geotechnical Journal 34:698-725

Mas Ivars D, Potyondy D, Pierce M, Cundall P (2008) The smooth-joint contact model. Proceedings of WCCM8-ECCOMAS 2008:8th

Masoumi H (2013) Investigation into the mechanical behaviour of intact rock at different sizes. Doctor of Philosophy thesis, University of New South Wales, Sydney

Masoumi H, Roshan H, Hagan PC (2016) Size-Dependent Hoek-Brown Failure Criterion. International Journal of Geomechanics 17:04016048

Masoumi H, Roshan H, Hedayat A, Hagan PC (2018) Scale-Size Dependency of Intact Rock under Point-Load and Indirect Tensile Brazilian Testing. International Journal of Geomechanics 18:04018006

Masoumi H, Saydam S, Hagan PC (2015) Unified size-effect law for intact rock. International Journal of Geomechanics 16:04015059

Masoumi H, Serati M, Williams DJ, Alehossein H Size dependency of intact rocks with high brittleness: A potential solution to eliminate secondary fractures in Brazilian test. In: 51st US Rock Mechanics/Geomechanics Symposium, 2017. American Rock Mechanics Association.

Medhurst TP, Brown ET (1998) A study of the mechanical behaviour of coal for pillar

design. International Journal of Rock Mechanics and Mining Sciences 35:1087-1105

Meier T, Rybacki E, Backers T, Dresen G (2015) Influence of Bedding Angle on Borehole Stability: A Laboratory Investigation of Transverse Isotropic Oil Shale. Rock Mechanics and Rock Engineering 48:1535-1546

Mighani S, Sondergeld CH, Rai CS (2016) Observations of tensile fracturing of anisotropic rocks. SPE Journal 21:1,289-281,301

Min K-B, Jing L (2003) Numerical determination of the equivalent elastic compliance tensor for fractured rock masses using the distinct element method. International Journal of Rock Mechanics and Mining Sciences 40:795-816

Min K-B, Thoraval A (2012) Comparison of two-and three-dimensional approaches for the numerical determination of equivalent mechanical properties of fractured rock masses. Tunnel and Underground Space 22:93-105

Nicksiar M, Martin C (2014) Factors affecting crack initiation in low porosity crystalline rocks. Rock mechanics and rock engineering 47:1165-1181

Nishimatsu Y, Yamagushi U, Motosugi K, Morita M (1969) The size effect and experimental error of the strength of rocks. Journal of the Society of Materials Science, Japan 18:1019-1025

Nova R, Zaninetti A An investigation into the tensile behaviour of a schistose rock. In: International Journal of Rock Mechanics and Mining Sciences & Geomechanics Abstracts, 1990. vol 4. Elsevier, pp 231-242.

Oda M (1977) Co-ordination number and its relation to shear strength of granular material. Soils and Foundations 17:29-42

Park B, Min K-B (2015) Bonded-particle discrete element modeling of mechanical behaviour of transversely isotropic rock. International Journal of Rock Mechanics and Mining Sciences 76:243-255

Park B, Min K-B, Thompson N, Horsrud P (2018) Three-dimensional bonded-particle

discrete element modeling of mechanical behaviour of transversely isotropic rock. International Journal of Rock Mechanics and Mining Sciences 110:120-132

Pei J (2008) Strength of transversely isotropic rocks. Massachusetts Institute of Technology

Pei J, Einstein HH, Whittle AJ (2018) The normal stress space and its application to constructing a new failure criterion for cross-anisotropic geomaterials. International Journal of Rock Mechanics and Mining Sciences 106:364-373

Peng J, Cai M (2019) A cohesion loss model for determining residual strength of intact rocks. International Journal of Rock Mechanics and Mining Sciences 119:131-139

Peng J, Wong LNY, Teh CI (2017a) Effects of grain size-to-particle size ratio on micro-cracking behaviour using a bonded-particle grain-based model. International Journal of Rock Mechanics and Mining Sciences 100:207-217

Peng J, Wong LNY, Teh CI (2017b) Influence of grain size heterogeneity on strength and microcracking behaviour of crystalline rocks. Journal of Geophysical Research: Solid Earth 122:1054-1073

Pestman BJ, Van Munster JG (1996) An acoustic emission study of damage development and stress-memory effects in sandstone. International Journal of Rock Mechanics and Mining Sciences & Geomechanics Abstracts 33:585-593

Pierce M, Gaida M, DeGagne D Estimation of rock block strength. In: Proceedings of the 3rd Canada–US rock mechanical symposium, Toronto, 2009.

Potyondy D A flat-jointed bonded-particle material for hard rock. In: 46th US rock mechanics/geomechanics symposium, 2012. American Rock Mechanics Association.

Potyondy D (2016) Flat-Joint Contact Model [version 1]. Itasca Consulting Group, Inc., Minneapolis, MN, Technical Memorandum 5-8106:16TM47.

Potyondy D Simulating perforation damage with a flat-jointed bonded-particle material. In: 51st US Rock Mechanics/Geomechanics Symposium, 2017. American Rock

Mechanics Association.

Potyondy DO (2015) The bonded-particle model as a tool for rock mechanics research and application: current trends and future directions. Geosystem Engineering 18:1-28

Potyondy DO, Cundall PA (2004) A bonded-particle model for rock. International Journal of Rock Mechanics and Mining Sciences 41:1329-1364

Quiñones J, Arzúa J, Alejano LR, García-Bastante F, Mas Ivars D, Walton G (2017) Analysis of size effects on the geomechanical parameters of intact granite samples under unconfined conditions. Acta Geotechnica

Rafiai H (2011) New empirical polyaxial criterion for rock strength. International Journal of Rock Mechanics and Mining Sciences 48:922-931

Rafiei Renani H, Martin CD (2018) Cohesion degradation and friction mobilization in brittle failure of rocks. International Journal of Rock Mechanics and Mining Sciences 106:1-13

Ramamurthy T (1993) Strength and modulus responses of anisotropic rocks. Comprehensive rock engineering 1:313-329

Rocco C, Guinea GV, Planas J, Elices M (1999a) Size effect and boundary conditions in the Brazilian test: Experimental verification. Materials and Structures 32:210

Rocco C, Guinea GV, Planas J, Elices M (1999b) Size effect and boundary conditions in the brazilian test: theoretical analysis. Materials and Structures 32:437

Rong G, Peng J, Yao M, Jiang Q, Wong LNY (2018) Effects of specimen size and thermal-damage on physical and mechanical behaviour of a fine-grained marble. Engineering Geology 232:46-55

Saeidi O, Rasouli V, Vaneghi RG, Gholami R, Torabi SR (2014) A modified failure criterion for transversely isotropic rocks. Geoscience Frontiers 5:215-225

Saeidi O, Vaneghi RG, Rasouli V, Gholami R (2013) A modified empirical criterion for

strength of transversely anisotropic rocks with metamorphic origin. Bulletin of Engineering Geology and the Environment 72:257-269

Saint Venant B (1863) Sur la distribution des élasticités autour de chaque point d'un solide ou d'un milieu de contexture quelconque, particulièrement lorsqu'il est amorphe sans être isotrope. Journal de Math Pures et Appliquées 8:257-430

Saroglou H, Tsiambaos G (2008) A modified Hoek–Brown failure criterion for anisotropic intact rock. International Journal of Rock Mechanics and Mining Sciences 45:223-234

Scholtès L, Donzé F-V (2013) A DEM model for soft and hard rocks: Role of grain interlocking on strength. Journal of the Mechanics and Physics of Solids 61:352-369

Scholtès L, Donzé F-V, Khanal M (2011) Scale effects on strength of geomaterials, case study: Coal. Journal of the Mechanics and Physics of Solids 59:1131-1146

Schöpfer MP, Abe S, Childs C, Walsh JJ (2009) The impact of porosity and crack density on the elasticity, strength and friction of cohesive granular materials: insights from DEM modelling. International Journal of Rock Mechanics and Mining Sciences 46:250-261

Sesetty V, Ghassemi A (2018) Effect of rock anisotropy on wellbore stresses and hydraulic fracture propagation. International Journal of Rock Mechanics and Mining Sciences 112:369-384

Setiawan NB, Zimmerman RW (2018) Wellbore breakout prediction in transversely isotropic rocks using true-triaxial failure criteria. International Journal of Rock Mechanics and Mining Sciences 112:313-322

Sewell R (2000) The pre-quaternary geology of Hong Kong. Hong Kong Geological Survey.

Shang J, Duan K, Gui Y, Handley K, Zhao Z (2018) Numerical investigation of the direct tensile behaviour of laminated and transversely isotropic rocks containing incipient

bedding planes with different strengths. Computers and Geotechnics 104:373-388

Shang J, Hencher SR, West LJ (2016) Tensile Strength of Geological Discontinuities Including Incipient Bedding, Rock Joints and Mineral Veins. Rock Mechanics and Rock Engineering 49:4213-4225

Shi X, Yang X, Meng Y, Li G (2016) Modified Hoek–Brown failure criterion for anisotropic rocks. Environmental Earth Sciences 75:995

Simpson N, Stroisz A, Bauer A, Vervoort A, Holt R Failure mechanics of anisotropic shale during Brazilian tests. In: 48th US Rock Mechanics/Geomechanics Symposium, 2014. American Rock Mechanics Association.

Simpson NDJ (2013) An analysis of tensile strength, fracture initiation and propagation in anisotropic rock (gas shale) using Brazilian tests equipped with high speed video and acoustic emission., Institutt for petroleumsteknologi og anvendt geofysikk

Singh M, Raj A, Singh B (2011) Modified Mohr–Coulomb criterion for non-linear triaxial and polyaxial strength of intact rocks. International Journal of Rock Mechanics and Mining Sciences 48:546-555

Singh M, Samadhiya NK, Kumar A, Kumar V, Singh B (2015) A nonlinear criterion for triaxial strength of inherently anisotropic rocks. Rock Mechanics and Rock Engineering 48:1387-1405

Soga K, Alonso E, Yerro A, Kumar K, Bandara S (2016) Trends in large-deformation analysis of landslide mass movements with particular emphasis on the material point method. Géotechnique 66:248-273

Song H, Jiang Y, Elsworth D, Zhao Y, Wang J, Liu B (2018) Scale effects and strength anisotropy in coal. International Journal of Coal Geology 195:37-46

Tavallali A, Vervoort A (2010) Failure of Layered Sandstone under Brazilian Test Conditions: Effect of Micro-Scale Parameters on Macro-Scale Behaviour. Rock Mechanics and Rock Engineering 43:641-653

Tavallali A, Vervoort A (2013) Behaviour of layered sandstone under Brazilian test

conditions: Layer orientation and shape effects. Journal of Rock Mechanics and Geotechnical Engineering 5:366-377

Thuro K, Plinninger R Scale effects in rock strength properties. Part 2: Point load test and point load strength index. In: Rock Mechanics-A Challenge for Society.-881 p., Proceedings of the ISRM Regional Symposium Eurock, 2001. pp 175-180.

Thuro K, Plinninger R, Zäh S, Schütz S (2001) Scale effects in rock strength properties. Part 1: Unconfined compressive test and Brazilian test. EUROCK 2001: Rock Mechanics-A Challenge for Society:169-174

Togashi Y, Kikumoto M, Tani K (2017) An Experimental Method to Determine the Elastic Properties of Transversely Isotropic Rocks by a Single Triaxial Test. Rock Mechanics and Rock Engineering 50:1-15

Tsang CF, Barnichon JD, Birkholzer J, Li XL, Liu HH, Sillen X (2012) Coupled thermo-hydro-mechanical processes in the near field of a high-level radioactive waste repository in clay formations. International Journal of Rock Mechanics and Mining Sciences 49:31-44

Tsidzi K (1997) Propagation characteristics of ultrasonic waves in foliated rocks. Bulletin of the International Association of Engineering Geology:103-114

Tutluoğlu L, Öge İF, Karpuz C (2015) Relationship Between Pre-failure and Post-failure Mechanical Properties of Rock Material of Different Origin. Rock Mechanics and Rock Engineering 48:121-141

Vallejos JA, Salinas JM, Delonca A, Mas Ivars D (2016) Calibration and Verification of Two Bonded-Particle Models for Simulation of Intact Rock Behaviour. International Journal of Geomechanics:06016030

Vervoort A et al. (2014) Failure of transversely isotropic rock under Brazilian test conditions. International Journal of Rock Mechanics and Mining Sciences 70:343-352

Vutukuri V, Lama R, Saluja S (1974) Handbook on mechanical properties of rocks. Trans

Tech Publications, Bay Village, OH.

Wallace MI, Ng KC (2016) Development and application of underground space use in Hong Kong. Tunnelling and Underground Space Technology 55:257-279

Walton G (2017) Scale Effects Observed in Compression Testing of Stanstead Granite Including Post-peak Strength and Dilatancy. Geotech Geol Eng

Walton G, Alejano LR, Arzua J, Markley T (2018) Crack Damage Parameters and Dilatancy of Artificially Jointed Granite Samples Under Triaxial Compression. Rock Mechanics and Rock Engineering

Walton G, Arzúa J, Alejano LR, Diederichs MS (2015) A Laboratory-Testing-Based Study on the Strength, Deformability, and Dilatancy of Carbonate Rocks at Low Confinement. Rock Mechanics and Rock Engineering 48:941-958

Wang B, Martin U, Rapp S (2017a) Discrete element modeling of the single-particle crushing test for ballast stones. Computers and Geotechnics 88:61-73

Wang P, Cai M, Ren F (2018) Anisotropy and directionality of tensile behaviours of a jointed rock mass subjected to numerical Brazilian tests. Tunnelling and Underground Space Technology 73:139-153

Wang P, Yang T, Xu T, Cai M, Li C (2016) Numerical analysis on scale effect of elasticity, strength and failure patterns of jointed rock masses. Geosciences Journal 20:539-549

Wang Y, Li C, Hu Y, Mao T (2017b) Brazilian Test for Tensile Failure of Anisotropic Shale under Different Strain Rates at Quasi-static Loading. Energies 10:1324

Weibull W (1951) A statistical distribution function of wide applicability. Journal of applied mechanics 18:293-297

Wilson AH (1983) The stability of underground workings in the soft rocks of the Coal Measures. International Journal of Mining Engineering 1:91-187

Witherspoon P, Cook N, Gale J (1981) Geologic Storage of Radioactive. Science 211:894-

900

Wittke W (2014) Rock mechanics based on an anisotropic jointed rock model (AJRM). John Wiley & Sons.

Wu S, Xu X (2016) A study of three intrinsic problems of the classic discrete element method using flat-joint model. Rock Mechanics and Rock Engineering 49:1813-1830

Xia L, Zeng Y (2018) Parametric study of smooth joint parameters on the mechanical behaviour of transversely isotropic rocks and research on calibration method. Computers and Geotechnics 98:1-7

Xu G, He C, Chen Z, Su A (2017) Transverse Isotropy of Phyllite Under Brazilian Tests: Laboratory Testing and Numerical Simulations. Rock Mechanics and Rock Engineering

Xu G, He C, Chen Z, Wu D (2018) Effects of the micro-structure and micro-parameters on the mechanical behaviour of transversely isotropic rock in Brazilian tests. Acta Geotechnica 13:887-910

Xu X, Wu S, Gao Y, Xu M (2016) Effects of Micro-structure and Micro-parameters on Brazilian Tensile Strength Using Flat-Joint Model. Rock Mechanics and Rock Engineering 49:3575-3595

Yang S-Q, Jing H-W, Wang S-Y (2012) Experimental Investigation on the Strength, Deformability, Failure Behaviour and Acoustic Emission Locations of Red Sandstone Under Triaxial Compression. Rock Mechanics and Rock Engineering 45:583-606

Yang S-Q, Yin P-F, Huang Y-H (2019) Experiment and Discrete Element Modelling on Strength, Deformation and Failure Behaviour of Shale Under Brazilian Compression. Rock Mechanics and Rock Engineering

Yinlong L, Lianguo W, Feng Y, Yujie L, Haimin C (2010) Post-peak strain softening mechanical properties of weak rock. Chinese Journal of Rock Mechanics and

Engineering 29:640-648

Yoshinaka R, Osada M, Park H, Sasaki T, Sasaki K (2008) Practical determination of mechanical design parameters of intact rock considering scale effect. Engineering Geology 96:173-186

Yu Y, Yin J, Zhong Z (2006) Shape effects in the Brazilian tensile strength test and a 3D FEM correction. International Journal of Rock Mechanics and Mining Sciences 43:623-627

Zhang Q, Zhu H, Zhang L, Ding X (2011) Study of scale effect on intact rock strength using particle flow modeling. International Journal of Rock Mechanics and Mining Sciences 48:1320-1328

Zhang X-P, Wong LNY (2012) Cracking processes in rock-like material containing a single flaw under uniaxial compression: a numerical study based on parallel bonded-particle model approach. Rock Mechanics and Rock Engineering 45:711-737

Zheng Y, Chen C, Liu T, Song D, Meng F (2019) Stability analysis of anti-dip bedding rock slopes locally reinforced by rock bolts. Engineering Geology 251:228-240

Zhou J, Zhang L, Yang D, Braun A, Han Z (2017) Investigation of the Quasi-Brittle Failure of Alashan Granite Viewed from Laboratory Experiments and Grain-Based Discrete Element Modeling. Materials 10:835